Theoretical studies of the dynamics of gas-phase and gas/surface atom+alkane reactions and of the structure and dynamics of water confined between hydrophobic surfaces

Joshua Parker Layfield

Dissertation submitted to the faculty of the Virginia Polytechnic Institute and State
University in partial fulfillment of the requirements for the degree of

Doctor of Philosophy
In
Chemistry

Diego Troya
T. Daniel Crawford
Edward F. Valeev
Louis A. Madsen
John R. Morris

26 January 2011
Blacksburg, VA

Keywords: potential-energy surface derivation, quasi-classical trajectory simulations, self-assembled monolayers, gas/organic-surface interactions, hydrophobic effect

Theoretical studies of the dynamics of gas-phase and gas/surface atom+alkane reactions and of the structure and dynamics of water confined between hydrophobic surfaces

Joshua Parker Layfield

(ABSTRACT)

Comprehension of reactive chemical dynamics in the gas phase and at the gas/organic-surface interface and non-reactive dynamics at the interface between hydrophobic surfaces and water requires an understanding of the fundamental atomic and molecular interactions that undergird these important phenomena. In an effort to study these regimes of chemical interaction, we have performed computational simulations that probe the dynamics of chemical systems that exemplify each of these domains. To study gas-phase chemical dynamics, we reparametrized semiempirical Hamiltonians so that they can accurately describe the potential energy surfaces for two distinct atom+alkane reactions. In addition to their demonstrated accuracy, these methods possess the attractive quality of being computationally inexpensive enough to afford extensive direct-dynamics trajectory studies. Our results on the dynamics of atom+alkane hydrogen-abstraction reactions have shown good agreement with experimental metrics that are as diverse as product velocity distributions, excitation functions, angular distributions and rovibrational state distributions for diatomic products of the abstraction. We have demonstrated that our reparametrized Hamiltonians are suitable for investigating gas-phase reactions with up to 15 (5 heavy) atoms and that they are appropriate for studying reactions beyond the gas phase, especially gas/surface reactions.

By employing our semiempirical methods within a quantum-mechanics/molecular-mechanics hybrid scheme we are able to examine hydrogen-abstraction reactions of fluorine atoms with alkanethiolate self-assembled monolayers. Our simulations reproduce the general trends of experimental results for the cousin F+squalane reaction. Our simulations also probe the role that secondary collisions play in determining the final internal and translational energy of the product HF molecules. For instance, we determined that very few interactions with the SAM surface were required to cool rotational and translational modes of the HF product, while its vibrational energy remains unchanged on the time scale that HF molecules trap on the SAM surface.

Moving beyond the gas/organic surface interface, we have also performed molecular-dynamics simulations of thin water films confined between hydrophobic SAM surfaces. These simulations illuminated the structural and dynamics behavior induced in the water films by confinement in hydrophobic environments. While most effects of the surface do not penetrate deep into the water layers we have noted that enhanced lateral diffusion of water molecules can persist in these films with > 1 nm length scales. We have elucidated a possible mechanistic precursor for the attractive forces seen in experimental measurement of the hydrophobic effect.

Acknowledgments

Tremendous thanks go to my advisor, Dr. Diego Troya for his tireless efforts to train and challenge me in my work over the past four and half years. Your passion for chemistry is a true inspiration to me in my vocational pursuits.

Thanks also go to my committee members, Dr. Daniel Crawford, Dr. Ed Valeev, Dr. Lou Madsen, and Dr. John Morris for their support and guidance throughout my graduate school career.

Will Alexander, Uros Tasic, Paula Weiss, Andrew Sweeney, and Ben Cherniawski for their mentorship and camaraderie throughout my time in the "Troya Lifestyle Center."

I thank my parents for their constant support and encouragement throughout my entire life and specifically during my graduate school career. I also want to thank my sister for her support of my endeavor and her example to me of perseverance throughout the past few years.

Finally, I would like to thank my fiancée, Corrie for her love and support of me during the final years of my graduate school career. I would like to particularly thank her for providing more productive support to me while I have written my thesis than I did for her while she was writing hers.

J. P. L., January 2011, Blacksburg, VA

Attribution

Several advisors and group mates have aided this author in the development of the research presented and the preparation of the manuscripts throughout the chapters of this document.

Prof. Diego Troya (Department of Chemistry, Virginia Tech) is my research advisor and committee chair. He has provided guidance and support for all of the work presented throughout this dissertation. He has additionally provided editorial oversight for all of the chapters of this dissertation.

Specifically, the research in the manuscript presented in Chapter 3 was done almost entirely by me and only a nominal (less than 10%) amount of work on the initial *ab initio* calculations was performed by Matthew D. Owens. Most of the manuscript was written by Dr. Troya, after data and figures were prepared by this author. This work was published in the *Journal of Chemical Physics* as “Theoretical study of the dynamics of $H+CH_4$ and $H+C_2H_6$ reactions using a specific-reaction-parameter semiempirical Hamilonian” by Joshua P. Layfield, Matthew D. Owens and Diego Troya.

The comparative dynamics study of the H+alkane family of reactions presented in Chapter 4 was done entirely by me with the oversight of Dr. Troya. The manuscript was completed by Dr. Troya after a full draft was written by this author. This work was published in *Chemical Physics Letters* as “Theoretical study of the dynamics of H+alkane reactions” by Joshua P. Layfield and Diego Troya.

The direct-dynamics study of the F+alkane reaction class presented in Chapter 5 was almost entirely completed by me, with Andrew Sweeney performing some *ab initio* calculations of the larger alkanes studied in the project. The manuscript was prepared by Dr. Troya after a rough draft was written by this author. The work was published in the *Journal of Physical Chemistry A* as “Direct-Dynamics Study of the F+ CH_4, C_2H_6, C_3H_8, and *i*-C_4H_{10} Reactions” by Joshua P. Layfield, Andrew F. Sweeney, and Diego Troya.

The QM/MM study of the F+SAM reactions in Chapter 6 was performed mostly by me (> 75%) after significant work was done by Dr. Troya to ensure that proper initial conditions for the SAM surface were implemented. The manuscript was compiled by Dr. Troya after a full draft was written by this author. This work was published in the

Journal of Chemical Physics as “Theoretical study of the dynamics of F-alkanethiol self-assembled monolayer hydrogen-abstraction reactions” by Joshua Layfield and Diego Troya.

The work to study the hydrophobic effect by molecular-dynamics simulations of water confined in hydrophobic environments in Chapter 7 was performed mainly by me after preliminary calculations were performed by Dr. Troya. The manuscript was written by Dr. Troya after a full draft was prepared by this author.

Table of Contents

List of Figures

List of Tables

Chapter 1
Introduction

1.1 Thesis Statement

The goal of the research presented in this document is to investigate the dynamics of the reactions of atomic radicals with both gas-phase alkanes and at the gas/organic-surface and to study the structure and dynamics of confined water to elucidate the mechanisms of the hydrophobic effect.

1.2 Motivation

Elementary elastic, inelastic, and chemically reactive collisions between atoms and molecules are the fundamental processes that undergird the macroscopic properties of chemical reactions and many biological systems. The field of computational molecular dynamics uses theoretical methods to investigate the specific elementary interactions that lead to chemical reaction and the rich diversity of interfacial behavior that governs a plethora of biochemical activity.

These molecular interactions result in the fundamental processes responsible for a vast array of applications. Reactions studied in the gas phase are important in a variety of applications ranging from the combustion of fossil fuels[1] to the development of chemical lasers.[2] The degradation of polymeric coverings on satellites[3] and the regulation of ozone in the atmosphere by organic aerosols[4] are just two examples of problems that are governed by the reactions that occur at the interface between organic surfaces and the surrounding atmosphere. Non-reactive attraction of hydrophobic surfaces in aqueous environments, dominate many protein-folding mechanisms[5] and have important application to nanofluidics.[6]

We have sought to use computational molecular dynamics techniques to study each of these three physical regimes: 1) gas-phase chemical reactions 2) reactive gas/organic-surface collisions and 3) non-reactive liquid/solid interfaces. The rest of this introduction is organized as follows. First, we present a review of the literature relevant to the two different atom+alkane gas-phase reaction classes studied in this work. Then we provide an introduction to the gas/organic surface reactive scattering experiments and calculations. Finally, we will present an extended introduction to investigations of the hydrophobic effect through experimental and computational investigations of the nature of water confined in hydrophobic environments.

1.3 H+Alkanes

Chapters 3 and 4 of this dissertation will show our work on the simulations of the reaction of hydrogen atoms with alkane molecules. Here, we provide a brief literature review of these reactions that focuses those chapters.

Due to the small number of electrons involved and the relatively simple profile of the potential-energy surface, H + alkane reactions are turning out to be benchmark systems[7, 8] for studying the dynamics of atom-polyatom chemical reactions.

Before discussing the state-to-state experiments for H+alkane reactions, there are two dynamics concepts that need to be fully understood: the impact parameter and the opacity function. The impact parameter, as shown in Figure 1.1, is defined as the distance between the initial velocity vector of the impinging hydrogen atom and a parallel line that passes through the center of mass of the target molecule. In an experiment, collisions between reagents occur at different impact parameters. Small impact parameters imply a "hard" hit between reagents, while large impact parameters imply a peripheral approach of reagents and a tangential collision. The opacity function is related to the impact parameter, and can be defined as a measure of the reaction probability as a function of the impact parameter.[9] The shape of the opacity function can give some insight into the "reactive size" and shape of the target molecule as well as the reactive mechanisms that contribute to the formation of products.

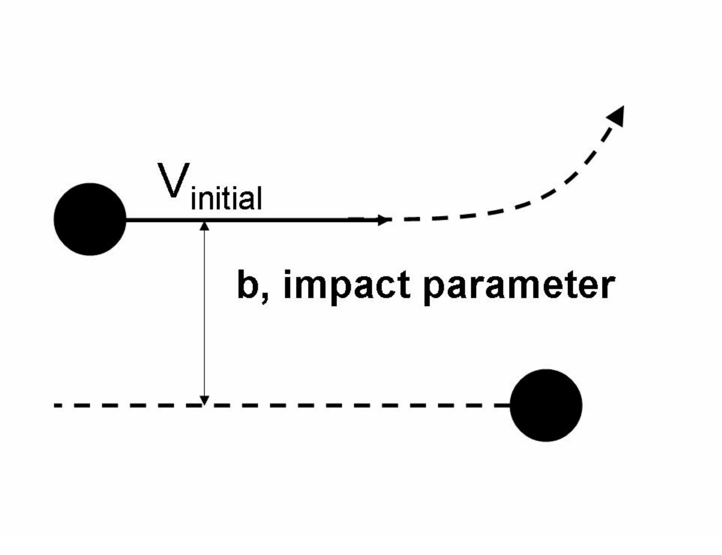

Figure 1.1: A schematic representation of the impact parameter

1.3.1 H+methane → H_2/HD + methyl

The importance of the H + alkane class of reactions can be exemplified by the intense experimental and theoretical research activity surrounding the simplest reaction of the family, H+methane → H_2+methyl. The importance of this reaction goes beyond H + alkane chemistry, as it represents the simplest chemical reaction at a tetrahedral carbon center.[10]

The rate constants for the forward and reverse reactions have been reported[11] and there have also been a few state-to-state dynamics experiments completed.[3, 5, 7, 8] State-to-state dynamics experiments study the energy partitioning in a chemical reaction starting with a well-defined set of initial reactant states and collision energies into the product degrees of freedom. The analysis of these dynamics studies usually involves the determination of the relative populations of the vibrational and rotational states of one or all of the products.

The first state-to-state experiments on the $H + CD_4 \rightarrow HD + CD_3$ reaction were reported in 1991 by Germann *et al.*[7] using a pump-probe technique called Coherent Anti-Stokes Raman Spectroscopy (CARS).[12] This technique allowed them to probe the nascent rotational and vibrational state distributions of the diatomic product, HD, with a careful selection of experimental conditions to approximate closely single collision conditions. They chose to study the $H+CD_4$ system as a logical progression from their previous studies on the $H + HCl \rightarrow H_2 + Cl$ reaction,[13-15] due to the fact that both reactions are nearly thermoneutral, $\Delta H_{HCD4} = 0.087$ eV and $\Delta H_{H+HCl} = -0.046$ eV[13] and they have somewhat similar classical reaction barriers, 0.21 eV for H + HCl[16, 17] and 0.54 eV for $H + CD_4$. Additionally both reactions exhibit light + light-heavy → light-light + heavy kinematics, which allows for certain simplifications to be made in the analysis and mechanistic determination.[14]

In the experiments, the H atoms were created by the photolysis of hydrogen iodide (HI) resulting in H atoms with two different translational energies. This bimodal energy distribution corresponds to the non-degenerate spin-orbit iodine states, $I(^2P_{3/2})$, and $I(^2P_{1/2})$. In the $H+CD_4$ center of mass, the collision energies are $E_{coll}=1.53\pm0.15$ eV and $E_{coll}=0.65\pm0.10$ eV respectively.

Two major results were published in this study. First, the authors reported vibrational state distributions for the HD product is $HD(\nu'=0):HD(\nu'=1) = 4:1$, with no population in the $\nu'=2$ or $\nu'=3$ states, even though both states are energetically accessible up the $J'=10$ and $J'=5$ rotational states, respectively. The other major, and much more surprising, result reported was that in the HD(ν'= 1) vibrational state, the rotational state distribution was distinctly more excited than the HD(ν'=0) state.[3, 19] In the ν'=1 state, 0.17 eV is the average HD rotational energy, which represents 17% of the available energy, where $E_{available} = E_{total} - E_{vibrational}(HD(\nu'))$. However, the average HD rotational energy in HD(ν'=0) was only found to be 0.13 eV, which represents only 9% of the available energy. The authors compared these findings to their benchmark reaction H + HCl → H_2 + Cl, which results in an average rotational energy in ν=0 of 0.35 eV, while in the ν'=1 state the average rotational energy is only 0.13 eV, a decrease from 21% of available energy to 8%. The authors concluded that this discrepancy between the benchmark polyatomic reaction and other atom-diatom bimolecular collisions that had been studied previously was a result of the increased dimensionality of the H + CD_4 system.[7] These results indicated that popular reduced-dimensionality models commonly used to understand the dynamics of polyatomic reactions, *e.g.* approximating the CD_4 molecule to a simple pseudodiatomic analog D-(CD_3), are not valid for a complete description of the dynamics of the system.

In 2003, Camden *et al.* analyzed the nascent products of the H+CD_4 reaction at E_{coll}=1.95eV using resonance enhanced multi-photon ionization (REMPI). They reported the vibrational and rotational states for the CD_3 product as well the **kk'** angular distributions. The **kk'** angular distribution is a measure of the scattering angle between the initial relative velocity vector pointing from the H atom to the CD_4 (**k**) and the final relative velocity vector pointing from the CD_3 product to the center of mass of the HD product (**k'**), as shown in Figure 1.2. A reactive collision that has a small scattering angle (**kk'**~0°) is described as forward scattering because the HD product continues in roughly the same direction as the impinging hydrogen atom. These "stripping" collisions usually occur at larger impact parameters. Collisions with large scattering angles (**kk'**~180°) are referred to as backward scattering and are

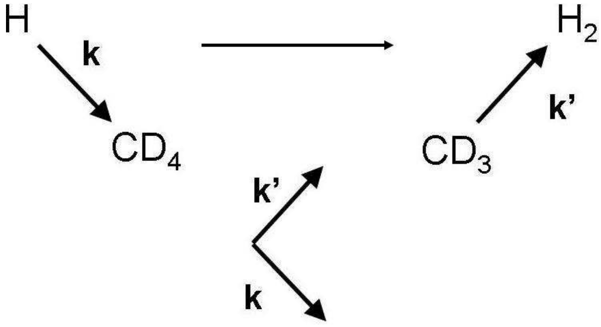

Figure 1.2 A schematic representation of the kk' scattering angle for the H+CD_4→HD+CD_3 reaction

said to proceed by a rebound mechanism. Backward scattering collisions usually occur at smaller impact parameters.

The reported REMPI spectra showed that there were approximately equal populations in the ground and first-excited vibrational states of the CD_3 umbrella-bending mode. This result confirms the earlier claims of Hermann *et al.*[7] that it is an invalid approximation to assume that methane acts as a pseudo-diatomic molecule D-(CD_3) if we want to fully understand the dynamics of this reaction, since the excitation of CD_3 bending modes is a non-negligible channel for energy partitioning.

The measured **kk'** angular distribution shows an average CD_3 scattering angle of $\cos\theta = -0.20 \pm 0.09$, where θ = **kk'** angle when averaged over all CD_3 vibrational and rotational states. This average scattering angle for the CD_3 product indicates that backward-sideways scattering dominates, and this leads to a new understanding of the possible reaction mechanisms. All previous theoretical studies[18-20] as well as the benchmark system used by Camden *et al.*, $H + D_2 \rightarrow HD + D$,[21] had shown a reaction mechanism that proceeded via a rebound mechanism, in which the HD product recoils in the direction of the incoming H atom (*i.e.*, backwards) and therefore, the CD_3 co-product scatters forward. This unexpected backward angular distribution of CD_3 led to the conclusion that there exists a competition between the rebound and stripping mechanisms. The former prevails at low impact parameters, while the latter dominates at high impact parameters.

Camden *et al.* further investigated the $H+CD_4$ hydrogen abstraction reaction at E_{coll}=1.20eV with experimental and theoretical techniques to further elucidate the details of the reaction dynamics.[10] Their communication reports a **kk'** angular distribution that shows that the most probable reactive scattering angle corresponds to $\cos\theta = -0.07$, which indicates that even at relatively low collision energies sideways and backward scattering of the CD_3 product occurs preferentially.

The theoretical aspects of the study by Camden *et al.* show that the hard-sphere collision model used in this and earlier studies is a good approximation. Trajectory calculations indicate an excellent correlation between the impact parameter and the scattering angle for the hard-sphere model and two different theoretical potential energy surfaces.[10]

Study of the $H + CD_4 \rightarrow HD + CD_3$ reaction by Camden *et al.* was augmented by two complementary papers published in 2005.[22, 23] There are two major experimental results in these two papers, 1) the excitation function, 2) the lab-frame speed distribution of the CD_3 product. The excitation function is a measure of the reactivity, expressed as a reactive cross section, as a function of E_{coll}. The measurements reveal that the reaction cross section decreases by about 40% from E_{coll}=1.48eV to 2.36eV.[22] The CD_3 lab-speed distribution is an indication of the energy released into relative translation of the product species. At E_{coll}=1.20eV, the CD_3 speed distribution ranges from 300 to 1950 m/s and shows a maximum at 1250 m/s. At E_{coll}=1.95eV, the maximum occurs at 1550 m/s and the distribution spans the 250 m/s – 2550 m/s range.

On the theoretical side, the first modern surface created for the $H + CH_4$ reaction was reported by Jordan and Gilbert (JG) in 1995.[24] This analytical surface was based upon functional forms proposed in 1987 by the Truhlar group.[25] The major advancement made in the new JG surface was the introduction of a four-fold symmetry that treated all of the hydrogen atoms originally bonded to the carbon atom in methane as equivalent. All previous attempts at describing this reaction had at most 3-fold symmetry, which only treated the three methyl hydrogen atoms as equivalent. The addition of four-fold symmetry increases the complexity of the analytical PES, but allows for important advances in describing the exchange reaction, $H + CD_4 \rightarrow CHD_3 + D$, as well as a more accurate treatment of the abstraction channel, $H + CD_4 \rightarrow HD + CD_3$.[24]

The next major advancement in the way of analytical surfaces for the $H+CH_4$ reaction was made by Espinosa-Garcia in 2002 (EG PES).[26] This surface made an improvement by treating all of the 5 hydrogen atoms as equivalent (*i.e.*, permutation of any two atoms in the PES does not alter the potential energy). In addition, the surface was fit considering new experimental and *ab initio* data. The EG surface was followed by an *ab initio* based analytical PES reported by the Manthe group in 2006.[27] This surface was based on the Shepard Interpolation approach,[28-32] and used fully quantum-mechanical thermal rate constant calculations as a criterion for accuracy.

The most advanced analytical surface that has been derived to date for the $H + CH_4$ reaction was produced by the Bowman group at Emory University.[33] This PES was created by covering the geometrically accessible configurations that resulted from a series of *ab initio* based direct dynamics calculations at the MP2 / aug-cc-pVDZ level of theory. The energies of the geometries of the 20,728 points resulting from these trajectory calculations were then calculated at the coupled cluster level of theory with a more substantial basis set and method (RCCSD(T)/aug-cc-pVTZ)[33] and these energies were used to map the global PES. This map was then fit to a series of invariant polynomials that were originally developed by the Bowman group to study other reactive systems.[37, 38] This surface has been used to perform quasi-classical trajectory calculations with various levels of vibrational excitation in the CH_4 reactant.[34]

1.3.1.1 $H + CD_4 \rightarrow CHD_3 + D$

Another possible reaction mechanism for the $H + CD_4$ system is a homolytic second-order substitution (S_H2) reaction, resulting in $D + CHD_3$ products. This reactive channel has been studied in much less detail than the competing abstraction reaction. In the experiment, the S_H2 inversion mechanism has been confirmed by Chattopadhyay and co-workers.[35] The angular distribution of the D atom product relative to the initial H atom velocity vector was measured using a pump-probe technique. It was determined that the D atoms were mostly parallel to the initial H atom velocity vector, leading the conclusion that an S_N2-like inversion mechanism was responsible for the exchange reaction. Using electronic structure methods, the barrier to the exchange reaction has been calculated to be 1.62eV at the CCSD(T)/aug-cc-pvqz//MP2/aug-cc-pvdz level of theory.

1.3.2 $H + C_2D_6 \rightarrow HD + C_2D_5$ / $H + C_3D_8 \rightarrow HD + C_3D_7$

The majority of investigation of the dynamics of H+alkane reactions has focused on the H+methane, reaction but limited work has sought to measure the dynamics of larger systems in the family. In 1992, the Valentini group continued their work by publishing a study of the $H + C_2D_6$ and $H + C_3D_8$ reactions.[36] The experimental setup is largely the same as their studies of $H + CD_4$.[7] The photolysis of HI in their experiments were resulted in collision energies of 1.56eV±0.13 eV and 1.58±0.13 eV for $H+C_2D_6$ and $H+C_3D_8$, respectively.

Valentini and co-workers also measured absolute reactive cross sections of 1.5±0.5 and 2.9±0.8 $Å^2$, for the $H + C_2D_6$ and $H + C_3D_8$ reactions, respectively. This increase in the reactive cross section seems to reflect the increasing size of the molecules and not necessarily an increase in reactivity. The HD vibrational distributions in both reactions show a 4:1 ratio for the ground state and the first excited states (ν'= 0:1) with no significant population of the HD($\nu' \geq 2$) states, which matches the H + CD_4 results.

HD product rotational state distributions were also reported for the ν'=0 and the ν'= 1 states for both reactions. Both reactions have the same type of positive correlation between HD vibrational and rotational energy seen in their H + CD_4 experimental measurements (*i.e.* there is a larger rotational excitation in the HD(ν'=1) than in the HD(ν'=0) vibrational state). Overall, for $H + C_2D_6 \rightarrow HD + C_2D_5$, the HD average rotational energy for the ν'=1 state is 0.30eV (16% of $E_{available}$) compared to 0.20eV (11% of $E_{available}$) for the HD(ν'=0) state. For the $H + C_3D_8 \rightarrow HD(\nu',J') + C_3D_7$ reaction the average HD rotational energy in the ν'=1 state is 0.35eV (27% of $E_{available}$) and for the ν'=0 state is 0.22eV (12% of $E_{available}$).

Oldershaw and Gould have also investigated the $H+C_2D_6 \rightarrow HD+C_2D_5$ reaction by irradiating HI and HBr over a range of wavelengths in the presence of C_2D_6.[37] The reaction mixture was analyzed by mass-spectrometry and the excitation function for the reaction was reported. These authors report a threshold for reaction occurring around 55 kJ mol^{-1} and a maximum reactivity occurring around 125 kJ mol^{-1}.

1.4 F+Alkanes

After the discussion of H+alkane reactions in Chapters 3 and 4 of this dissertation, additional studies of the cousin F+alkane reactions are presented in Chapter 5. Here, we provide a brief literature review of F+alkane reactions that is intended to put in perspective the simulations of that chapter.

1.4.1 $F+CH_4 \rightarrow HF+CH_3$

The reaction of fluorine atoms reacting with alkane molecules represents a step of increased complexity in the study of atomic-radical+alkanes. Interest in the $F+CH_4$ reaction has been motivated by the potential exploitation of this system to develop a chemical laser[2, 38] and for the fundamental understanding of reactions with small reactive barriers and large exothermicities.

The dynamics of the $F+CH_4 \rightarrow HF+CH_3$ reaction has been extensively studied also for fundamental reasons. In 1990, Sugawara *et al.* showed that there is some slight excitation in the umbrella-bending mode of the CH_3 radical product but no population inversion exists, even with the ~34 kcal mol^{-1} reaction exothermicity.[39] These authors report relative vibrational distributions of $CD_3(\nu_2'=0,1,2)$ = 1.0 : 0.36 : 0.15 and found this result to be consistent with the $F+ClH_3 \rightarrow IF+CH_3$ reaction. The Nesbitt group has studied the title reaction and published both HF rovibrational state distributions[40] and angular distributions.[41] Their analysis of the nascent HF vibrational state distributions shows strong population inversion with the $HF(\nu')$ distribution being peaked at $\nu'=2$ and roughly 10% of the population residing in $HF(\nu'=3)$. In 2001, the Nesbitt group showed that there is a strong propensity for HF forward and backward scattering with a strong suppression of HF scattering in the sideways regime. This result indicates the bifurcation of reaction mechanisms that occur between rebound and stripping dynamics.

The Liu group has studied both the $F+CH_4$ and isotopically substituted $F+CD_4$ reaction.[42-44] The first major result from these studies is the positive correlation between forward-scattering and vibrational excitation in the DF products. The authors suggest that this unexpected result is evidence of a quantum-mechanical reactive resonance. Additionally, the Liu group published an excitation function for the $F+CH_4$ reaction. They show that the threshold for reaction occurs around ~0.5 kcal mol^{-1} and that that maximum reactivity occurs at ~2.6 kcal mol^{-1}.

Several theoretical reaction-dynamics studies of the $F+CH_4$ system based on analytical surfaces,[45-47] interpolated surfaces,[48] and a specific-reaction-parameters Hamiltonian[49] have emerged recently, providing different levels of agreement with experiment.

1.4.2 $F+C_2H_6 \rightarrow HF+C_2H_5$

Going beyond the extensive investigation of the $F+CH_4$ reaction, analogous studies for the next member of the F+alkane family, $F+C_2H_6 \rightarrow HF+C_2H_5$, are decidedly available. The Nesbitt group have studied the nascent rovibrational state distributions of the HF products in the $F+C_2H_6$ reaction. The vibrational distributions measured for $HF(\nu'=3:2:1:0)=0.28:0.43:0.12:0.16$. The rotational state distributions are statistically consistent with the available energy in each vibrational manifold. No direct comparison exists between calculated vibrational distributions of the HF product arising from a full-dynamics study and those measured by Nesbitt and co-workers. This fact is likely due to the difficulty in deriving analytic potential-energy surfaces for systems of this size.

After presenting our work on atom+alkane reactions in Chapters 3-5, this dissertation will move to our efforts in the simulation of gas/alkane surface reaction dynamics in Chapter 6. The change from gas-phase to gas/surface dynamics is significant, and the following section of the introduction is intended to give an overview of the relevant work done on the field of gas/organic surface dynamics prior to the computational work on F+alkane surface reaction shown in Chapter 6.

1.5 Gas/Organic Surface Scattering

1.5.1 Gas/Organic Liquids

While the vast majority of investigation into dynamics at the gas/surface interfaces has traditionally lied in the field of gas/metal scattering, there is a growing interest in the inelastic and reactive scattering of gas-phase species from organic surfaces. Early work in the field of gas/organic surface scattering focused on the inelastic collisions of closed-shell molecules with organic liquids, such as squalane (2,6,10,15,19,23-Hexamethyltetracosane). Over the past 20 years, these studies have progressed to investigate not only gas/polymer interfaces but also the scattering of gas-phase projectiles from alkanethiolate self-assembled-monolayer surfaces (SAMs).

1.5.1.1 Inelastic Scattering

Early experimental inelastic scattering experiments by Nathanson showed the importance of effective surface mass for energy transfer in the collisions of rare gases and sulfur hexafluoride with both squalane and perfluorinated polyether (PFPE).[50] Using time-of-flight mass spectrometry, the authors analyzed arrival time profiles of scattered products. The time-of-flight distributions can be separated into two components, a fast one, which is surmised to emerge from direct gas phase-like interaction of the gas and the surface and is termed impulsive scattering, and a slow one, which originates from the products that are desorbed from the surface after thermal accommodation and is termed trapping desorption.[51] They conclude that the bifurcation of the two main collision mechanisms, impulsive scattering and trapping desorption, is sensitive to the composition of the organic liquid.

McCaffery and co-workers used laser-induced fluorescence (LIF) techniques to probe the internal modes of molecular iodine scattering from a wide range of organic liquids.[52] The authors presented vibrational state distributions for inelasitcally scattered

I_2 molecules and determined that liquids which present C-H bonds at the surface are much more effective than C-F bonds at converting I_2 translational energy into I_2 vibrations, thereby increasing the fraction of gas molecules which trap on the surface. The work of the McCaffery group however analyzed all of the I_2 molecules that passed through their laser beam and did not provide any information on the angular distributions of scattering products.

More recently, the Nesbitt group has probed the inelastic scattering behavior of CO_2 from a constantly refreshed PFPE surface.[53] The authors investigated the rovibrational state distributions of scattering CO_2 molecules as a function of both initial and final scattering angle. They showed that the impulsively scattered molecules recoil predominantly in the forward direction for non-normal collisions and that there is a strong correlation between large scattering angles (as measured from the surface normal) and rotationally excited CO_2 molecules.

Computational studies of inelastic scattering from liquid organic surfaces have lagged behind the extensive experimental investigation of these interactions. The McKendrick group has used molecular-dynamics techniques to study the interface of the vacuum/squalane interface.[54] These simulations showed that the methyl groups on the squalane molecules are preferentially pointing toward the vacuum. However, they also estimate that reactions with impinging oxygen atoms can also occur at more interior sites of that liquid alkane.

A more complete study of the inelastic scattering of Ne atoms from a squalane surface was performed by the Hase group.[55] Analyzing the collisions of Ne with initial translational energy of 10 kcal mol^{-1} and an incident angle of 45° relative to the surface normal, they report product angular scattering and translational energy distributions. Using a similar molecular-mechanics model to govern the surface dynamics as the McKendrick group and an analytical potential for the neon/squalane interactions, the authors determine that energy transfer to the surface is effectively achieved within only a few collisions of the gas with the surface.

1.5.1.2 Reactive Scattering

As the field of gas/organic surface scattering dynamics has matured, the ability to probe not only inelastic scattering but also reactive scattering events has become possible. Using hyperthermal beams (up to 5 eV translational energy) and time-of-flight detection, the Minton group investigated the dynamics of reactions of $O(^3P)$ atoms with the surface of liquid squalane.[56-58] The atomic-oxygen species can either scatter inelastically, abstract a single hydrogen to form hydroxyl radicals, or abstract two hydrogen atoms to form water. The authors present energy-transfer distributions for inelastic encounters, and translational-energy and angular distributions for OH products.

In a series of complementary experiments, McKendrick and co-workers have studied O+squalane reactions using a different experimental set-up.[59-63] They produce low-energy (~3.4 kcal mol^{-1} average collision energy) $O(^3P)$ atoms via photodissociation of NO_2, and measure the internal-state distributions of the nascent OH product using LIF. Alkane liquids other than squalane have also been investigated by the McKendrick group to understand the role of surface composition and organization on interfacial reaction dynamics.[63]

Of particular interest to the work presented in this dissertation are the experiments the Nesbitt group on the reactions of fluorine radicals with liquid squalane.[64, 65] High-resolution infrared absorption measurements of the HF product have revealed detailed rovibrational-state distributions. The energetics of reaction for the F+squalane system are dramatically different than the previously studied O+squalane reactions. Although the collision energy in the F+squalane experiments (0.7 ± 0.3 kcal mol^{-1}) is substantially smaller than in the O+squalane experiments, the product HF vibrational distributions are notably more excited than the OH product distributions.

Another important result from the F+squalane experiments is the presence of a strong positive correlation between product HF rotational and translational excitation across all accessible HF vibrational states.[64, 65] This correlation points to the role of secondary collisions in the microscopically rough squalane surface in cooling the rotational and translational HF degrees of freedom for products that do not impulsively recoil from the surface immediately after reaction.

As in the case for inelastic scattering, there have been only a few computational investigations of the reactions occurring at the gas/organic liquid surface interface. However, the problem for reactive scattering calculations is exacerbated by the fact that reactive potential energy surfaces for such large systems are hard to describe in a computationally manageable way. These simulations are challenging due to the hundreds of atoms that need to be taken into account for an accurate description of an organic surface. Hybrid quantum-mechanics/molecular-mechanics (QM/MM) schemes have been shown to provide a workable technique to investigate gas/organic surface reactive scattering. These schemes balance the needs for a reactive PES to describe bond breaking and forming at the interface and a computationally feasible method to describe the non-reactive surface dynamics. QM/MM approaches to gas/surface scattering divide the organic surface into a reactive region, where the radical reactions take place, and an inactive region, that provides structural support to the reactive region.[66]

Recently, Radak *et al.*[67] have used this approach to investigate the reactions of fluorine atoms with squalane in an attempt to complement the measurements by Nesbitt.[64, 65] The large computational expenditure associated with the calculations forced the authors to propagate trajectories at much higher collision energies (11.53 and 23.06 kcal mol^{-1}) than experiment (0.7±0.3 kcal mol^{-1}), making it difficult to establish quantitative comparisons between theory and experiment. Even with these limitations, the calculations captured the major experimental trends, including an inverted HF vibrational distribution, which is peaked at HF($\nu'=2$) and has roughly equal population in $\nu'=1$ and $\nu'=3$, and the quenching of HF rotational excitation as a function of its residence time on the surface prior to desorption. The Schatz group has also used a similar methodology to study the reactions of oxygen collisions with both squalane[68] and ionic liquids.[69]

1.5.2 Gas/SAM Scattering

While squalane has been a benchmark liquid alkane surface in many experimental and some of the few computational scattering studies available, hydrocarbon self-assembled monolayers have recently emerged as an attractive alternative organic surface for inelastic and reactive scattering experiments and simulations. Self-assembled monolayers are paradigmatic semi-crystalline organic surfaces, which are smooth and highly-ordered.[70, 71] These surfaces represent a chemically similar surface but provide a physical contrast with the molecularly rough liquid surfaces. Additionally, the ordered, regular nature of these SAM surfaces increases their attractiveness for computational scattering simulations and a much larger body of computational work exists probing the nature of gas/SAM dynamics.

1.5.2.1 Inelastic Scattering

In 1987, Cohen *et al.* published a study of rare gas atomic and molecular scattering from SAM surfaces.[72] As in the case of gas/organic liquid scattering, these authors found that impinging rare gases and molecular oxygen transfer significantly more translational energy to hydrocarbon SAM surfaces than to similar SAM surfaces that are fluorinated.

As previously mentioned, inelastic scattering simulations from SAM surfaces have been reported by a number of research groups. The first simulations of gas-phase species scattering from SAM surfaces were performed by Bosio and Hase a decade after the first experiments.[73] This work studied the collisions of neon atoms with hexanethiolate SAM surfaces over a range of collision energies and angles of incidence. They showed that trapping collisions were favored by impinging Ne atoms with low collision energies and near-normal angles of incidence.

The investigation of the mechanisms that lead to trapping behavior on SAMs was extended by joint experimental and theoretical efforts of the Sibener and Hase groups that attempted to separate the impulsive-scattering and trapping-desorption components of the product translational-energy distribution.[74] They found that efficient energy transfer from the neon atoms to the SAM surface that leads to thermalization of the gas can occur in a single collision event, and does not necessitate the long-trapping idea that had been commonly hypothesized. Collision geometries that excite the torsional C-C-C modes and low-frequency chain-wagging modes of the surface facilitate energy transfer and thermalization of the impinging atoms. The thermalized Ne atoms would then desorb the surface with a Boltzmann translational-energy distribution at the surface temperature that is seen in the experiment.

More recently the Morris and Troya groups have studied inelastic scattering collisions with both atomic and molecular gases with SAMs.[75-80] The theoretical scattering calculations have shown the importance of properly describing the interaction potential between the impinging gas and the SAM surface. These potentials are commonly obtained by fitting analytic Buckingham potentials to high-level *ab inito* data and are subsequently used in molecular-dynamic simulations of the gas/surface collisions.[78] These authors have also reported that for various rare gas (Ne, Ar, Kr) /

SAM (-CH_3 and -CF_3 terminated) combination, the relative mass of the colliding partners governs the extent of interfacial energy transfer.[75]

Moving beyond atomic scattering into the molecular gas realm, the Troya and Morris groups have investigated the collisions of N_2 and CO molecules with both –CH_3 and –CF_3 terminated SAMs. While the internal ro-vibrational state of scattering diatomic molecules cannot be assessed with their experimental technique, the translational energy profiles reveal that a pseudo-monoatomic approximation of the colliding gas cannot accurately describe the scattering dynamics. Alexander and Troya extended these studies to investigate the role that rovibrational excitation of the diatomic gas has on the scattering processes.[76] In that work, the authors also presented a stereodynamic investigation of the role that rotational and vibration dynamics of CO molecules have on the mechanism of the collisions and the properties of the desorbed gas.

1.5.2.2 Reactive Gas/SAM scattering

Much as in the case of gas/organic liquid scattering, recent work has investigated the reactions of gas-phase species with SAM surfaces. In 2005, the Morris group showed an example of the types of reactions that can occur at the gas/SAM interface.[81] They exposed a vinyl-terminated SAM surface to ozone, and monitored the reflection-absorption infrared spectra (RAIRS) as a function of exposure time. After ozone exposure, the signal peaks associated with the double bond of the SAM disappear and the C-H methylene stretching peaks broaden and shift to the blue. These results indicate that the ozone molecules react with the vinyl terminus of the SAM chains and increase the disorder of the surface. The authors comment that even under extended exposure and washing with water, the SAM surfaces are not consumed as they were for alkanethiolate SAM surfaces. This suggests cross-linking between the termini of adjacent SAM chains that protects the underlying region of the surface.

More recently, the McKendrick group have studied the dynamics of $O(^3P)$ collisions with alkanethiol SAMs.[70, 71] A key finding in this experimental study is that the relatively smooth SAM surfaces are not as effective as the rougher squalane surface in thermalizing the nascent OH product under identical initial conditions. A conclusion stemming from this study is that product species generated in reactions with the rough liquid have a larger probability to experience subsequent collisions with the surface.

These secondary collisions are not as likely on the atomically smooth SAMs and the corresponding product-energy distributions do not show thermalization nearly to the degree that they do on squalane. Using selectively deuterated SAMs, these authors have shown that the topmost methylene (-CH_2-) group of the SAM chains is the most reactive site (even more than the terminal –CH_3 group) and that penetration and reaction can occur up to 6 carbon atoms deep into the surface.[70]

By implementing a QM/MM approach similar to the ones described in the previous section, both the Hase[82] and the Schatz[83, 84] groups have studied the reactions of oxygen atoms with SAMs. The simulation of reactions of at the gas/surface interface has proven to exhibit a rich diversity of reaction mechanisms and post-collisional dynamics. The interfaces presented thus far have all involved impinging gas molecules reacting with a condensed phase. The work showed in Chapter 6 of this dissertation describes progress in the simulation of gas/SAM reaction dynamics by reporting a study of the reactions of F atoms with SAM surfaces.

1.6 Hydrophobic Interactions

After showing our work on atom+SAM surface reactions in Chapter 6, we finalize our dissertation by presenting simulations on the structure and dynamics of water in the vicinity of hydrophobic surfaces in Chapter 7. This work is a radical departure from the reaction-dynamics studies that form the body of this dissertation in Chapters 3 to 6, and the following is a brief introduction expected to focus our work the field of hydrophobic interactions.

1.6.1 Motivation

The interactions experienced by hydrophobic solutes and extended surfaces in an aqueous environment have wide-ranging implications in a variety of fields. Many phenomena related to essential biological processes are dominated by the properties of water confined in hydrophobic environments. For instance, hydrophobic amino acid residues appear prominently in protein-folding mechanisms in aqueous environments.[5, 85, 86] Moreover, non-polar pockets in proteins have been shown to be responsible for tremendous protein stability over a large range of pressures (up to 2000 atm),[87, 88] and temperatures (up to 400 K).[89] In fact, the non-polar regions in the native conformations of membrane proteins on thermophilic bacteria serve to facilitate optimal cellular growth under extreme conditions.[90] Furthermore, it has been recently shown that intervening thin films of water between hydrophobic surfaces are crucial to the adhesion of the spatulae of geckos to many different chemical substrates.[91]

1.6.2 Experimental Results

The mutual structural and dynamics effects that water and hydrophobic surfaces have on one another have lent themselves to extensive experimental and theoretical investigation. The first direct experimental evidence of the length scale and magnitude of the interaction between hydrophobic surfaces in water was shown by Israelachvili and Pashley in 1982,[92] who reported an attractive force acting at distances as long as 10-15 nm. A subsequent key study by Parker *et al.*[93] showed that the magnitude of the attraction between hydrophobic species in water is much larger than what is predicted from models solely accounting for electrostatic and van der Waals forces acting between the two surfaces.[94, 95] The inability of traditional inter-surface forces to reproduce the strength of the hydrophobic attraction therefore led to the conclusion that the effects that the solute and solvent have on one another need to be explicitly considered.

More recently, a large number of studies using modern surface-force apparatus (SFA) and atomic-force microscopy (AFM) techniques have measured hydrophobic attraction at surface separation distances ≥100 nm.[96-116] While there are numerous experimental accounts of the strength and range of the hydrophobic interaction, a definitive mechanism for the measured long-range attraction has not been confirmed. The difficulty in unequivocally determining the mechanism of the interaction is due in part to the dramatic dependence of the force on the type of hydrophobic surface present. For instance, the type of binding of the surfactant molecules to the substrate (covalent bonding *vs*. physisorption) seems to have a major effect on the hydrophobic interaction.[117]

1.6.3 Mechanisms of the Hydrophobic Effect

Some of the major mechanisms proposed to describe the attraction of hydrophobic plates in water include: 1) capillary evaporation of the intervening water film, which leads to a collapse of the plates,[118] 2) turbulent and unstable water forming gaseous bubbles that bridge the surfaces and serve as precursor states to complete evaporation as the surfaces approach one another,[93] and 3) increased water structuring induced by hydrophobic confinement, which results in attraction between the confining surfaces.[119]

To illuminate the mechanism involved in the long-range attraction of surfaces in aqueous environments and investigate the nature of the confined water, extensive work has been done using molecular-dynamics (MD) simulations. The simulations clearly reveal that the strength of solvent-solute interactions control the properties of solvent molecules near the surface. Strong water-surface interactions, such as those afforded by a hydrophilic surface with hydrogen-bonding moieties, result in complete and persistent hydration of the surface.[120, 121 122] On the other hand, a gaseous depletion layer is formed for surface-solvent interfaces with solvent-solute interactions weaker than the solvent self interactions, such as is the case in hydrophobic surfaces.[123]

1.6.4 Molecular Dynamics Simulation

MD studies of confined water in hydrophobic environments have been a fruitful area of study over the past few years. Early MD simulations focused on non-atomistic hydrophobic plates that were modeled as Lennard-Jones particles and thus limited quantitative comparison between theory and experiment.[123, 124] In an effort to characterize the proposed capillary-evaporation mechanism for hydrophobic attraction, Huang *et al.* suggested that the critical distance at which capillary evaporation of the intervening water film occurs (dewetting) depends strongly on the cross sectional area and shape of hydrophobic plates.[118] This result is important because atomistic simulations rarely can tackle the hydrophobic-plate sizes used in macroscopic experiments. Giovambattista *et al.* have also contributed a series of papers describing the effects that pressure, temperature, and surface topology have on the critical dewetting distance for water in between two silica-based hydrophobic plates.[125-127] The calculations show that as the temperature increases and the external pressure decreases, the critical dewetting distance becomes larger. At pressures of 1 bar and 300 K, the largest inter-surface separation at which dewetting is observed in the simulations is < 0.8 nm during the simulation times studied, which are all at most 1 ns. This body of work also indicated that water at distances larger than just 1 nm from a hydrophobic surface showed behavior that was essentially the same as bulk water.

As the experimentally-determined forces exist on much longer distances (up to 100 nm) than the simulations predict, a dewetting mechanism as the one pursued in the simulations does not seem to be solely responsible for the hydrophobic effect. Other signatures that distinguish water confined between hydrophobic surfaces and bulk water must extend well beyond the length scale seen in the simulations mentioned above. The work presented in Chapter 7 of this document seeks to provide an understanding of the mechanisms responsible for the hydrophobic effect using a series of MD simulations to probe the structural and dynamical properties of water under hydrophobic confinement.

References

1. W. C. Gardiner Jr., D.B. Olson Annual Review of Physical Chemistry **31**, 377 (1980).
2. J. F. Hon and J. R. Novak, Appl. Phys. Lett. **24** (4), 202-204 (1974).
3. D. Troya and G. C. Schatz, Int. Rev. Phys. Chem. **23** (3), 341-373 (2004).
4. S. K. Friedlander, *Smoke, dust, and haze : fundamentals of aerosol dynamics*. (Oxford University Press, New York, 2000).
5. P. Z. Luo and R. L. Baldwin, PNAS **96** (9), 4930-4935 (1999).
6. M. Majumder, N. Chopra, R. Andrews and B. J. Hinds, Nature **438** (7064), 44-44 (2005).
7. G. J. Germann, Y.-D. Huh and J. J. Valentini, The Journal of Chemical Physics **96** (3), 1957-1966 (1992).
8. T. V. Albu, J. Espinosa-Garcia and D. G. Truhlar, Chem. Rev. **107** (11), 5101-5132 (2007).
9. R. D. Levine and R. B. Berstein, *Molecular Reaction Dynamics and Chemical Reactivity*. (Oxford University Press, Oxford, 1987).
10. J. P. Camden, H. A. Bechtel, D. J. A. Brown, M. R. Martin, R. N. Zare, W. Hu, G. Lendvay, D. Troya and G. C. Schatz, J. Am. Chem. Soc. **127** (34), 11898-11899 (2005).
11. M. G. Bryukov, I. R. Slagle and V. D. Knyazev, J. Phys. Chem. A **105** (13), 3107-3122 (2001).
12. J. J. Valentini, in *Spectrometric Methods*, edited by G. A. Vanasse (Academic Press, London, 1985), Vol. IV, pp. 1-62(62).
13. P. M. Aker, G. J. Germann and J. J. Valentini, The Journal of Chemical Physics **90** (9), 4795-4808 (1989).
14. P. M. Aker and J. J. Valentini, Israel Journal of Chemistry **30** (1-2), 157-178 (1990).
15. P. M. Aker and J. J. Valentini, International Reviews in Physical Chemistry **12** (2), 363-390 (1993).
16. J. T. H. Dunning, The Journal of Chemical Physics **66** (6), 2752-2753 (1977).
17. D. W. Schwenke, S. C. Tucker, R. Steckler, F. B. Brown, G. C. Lynch, D. G. Truhlar and B. C. Garrett, The Journal of Chemical Physics **90** (6), 3110-3120 (1989).
18. P. J. Kuntz, E. M. Nemeth, J. C. Polanyi and W. H. Wong, The Journal of Chemical Physics **52** (9), 4654-4674 (1970).
19. L. M. Raff, The Journal of Chemical Physics **60** (6), 2220-2244 (1974).
20. T. Valencich and D. L. Bunker, The Journal of Chemical Physics **61** (1), 21-29 (1974).
21. F. Fernández-Alonso, B. D. Bean, J. D. Ayers, A. E. Pomerantz, R. N. Zare, L. Bañares and F. J. Aoiz, Angewandte Chemie International Edition **39** (15), 2748-2752 (2000).
22. J. P. Camden, W. Hu, H. A. Bechtel, D. J. A. Brown, M. R. Martin, R. N. Zare, G. Lendvay, D. Troya and G. C. Schatz, J. Phys. Chem. A **110** (2), 677-686 (2006).

23. W. Hu, G. Lendvay, D. Troya, G. C. Schatz, J. P. Camden, H. A. Bechtel, D. J. A. Brown, M. R. Martin and R. N. Zare, J. Phys. Chem. A **110** (9), 3017-3027 (2006).
24. M. J. T. Jordan and R. G. Gilbert, The Journal of Chemical Physics **102** (14), 5669-5682 (1995).
25. T. Joseph, R. Steckler and D. G. Truhlar, The Journal of Chemical Physics **87** (12), 7036-7049 (1987).
26. J. Espinosa-Garcia, The Journal of Chemical Physics **116** (24), 10664-10673 (2002).
27. T. Wu, H.-J. Werner and U. Manthe, The Journal of Chemical Physics **124** (16), 164307-164312 (2006).
28. J. Ischtwan and M. A. Collins, The Journal of Chemical Physics **100** (11), 8080-8088 (1994).
29. M. J. T. Jordan, K. C. Thompson and M. A. Collins, The Journal of Chemical Physics **102** (14), 5647-5657 (1995).
30. M. J. T. Jordan, K. C. Thompson and M. A. Collins, The Journal of Chemical Physics **103** (22), 9669-9675 (1995).
31. M. J. T. Jordan and M. A. Collins, The Journal of Chemical Physics **104** (12), 4600-4610 (1996).
32. R. P. A. Bettens and M. A. Collins, The Journal of Chemical Physics **111** (3), 816-826 (1999).
33. X. Zhang, B. J. Braams and J. M. Bowman, The Journal of Chemical Physics **124** (2), 021104-021104 (2006).
34. Z. Xie, J. M. Bowman and X. Zhang, The Journal of Chemical Physics **125** (13), 133120-133128 (2006).
35. A. Chattopadhyay, S. Tasaki, R. Bersohn and M. Kawasaki, The Journal of Chemical Physics **95** (2), 1033-1036 (1991).
36. G. J. Germann, Y.-D. Huh and J. J. Valentini, The Journal of Chemical Physics **96** (8), 5746-5757 (1992).
37. G. A. Oldershaw and P. L. Gould, J. Chem. Soc., Faraday Trans. 2 **81** (81), 1507-1516 (1985).
38. J. H. Parker and G. C. Pimentel, J. Chem. Phys. **51** (1), 91-96 (1969).
39. K.-i. Sugawara, F. Ito, T. Nakanaga, H. Takeo and C. Matsumura, J. Chem. Phys. **92** (9), 5328-5337 (1990).
40. W. W. Harper, S. A. Nizkorodov and D. J. Nesbitt, J. Chem. Phys. **113** (9), 3670-3680 (2000).
41. W. W. Harper, S. A. Nizkorodov and D. J. Nesbitt, Chem. Phys. Lett. **335** (5-6), 381-387 (2001).
42. W. Shiu, J. J. Lin, K. Liu, M. Wu and D. H. Parker, J. Chem. Phys. **120** (1), 117-122 (2004).
43. J. J. Lin, J. Zhou, W. Shiu and K. Liu, Science **300** (5621), 966 (2003).
44. J. Zhou, J. J. Lin, W. Shiu, S.-C. Pu and K. Liu, J. Chem. Phys. **119** (5), 2538-2544 (2003).
45. J. Espinosa-Garcia, J. Phys. Chem. A **111** (18), 3497-3501 (2007).
46. D. Troya, J. Millan, I. Banos and M. Gonzalez, J. Chem. Phys. **120** (11), 5181-5191 (2004).

47. G. Czako, B. C. Shepler, B. J. Braams and J. M. Bowman, Journal of Chemical Physics **130** (8) (2009).
48. J. F. Castillo, F. J. Aoiz, L. Banares, E. Martinez-Nunez, A. Fernandez-Ramos and S. Vazquez, J. Phys. Chem. A **109** (38), 8459-8470 (2005).
49. D. Troya, J. Chem. Phys. **123** (21), 214305-214311 (2005).
50. M. E. Saecker, S. T. Govoni, D. V. Kowalski, M. E. King and G. M. Nathanson, Science **252** (5011), 1421-1424 (1991).
51. C. T. Rettner, E. K. Schweizer and C. B. Mullins, The Journal of Chemical Physics **90** (7), 3800-3813 (1989).
52. A. J. Kenyon, A. J. McCaffery, C. M. Quintella and M. D. Zidan, Faraday Discuss **96**, 245-254 (1993).
53. B. G. Perkins and D. J. Nesbitt, Journal of Physical Chemistry A **112** (39), 9324-9335 (2008).
54. S. P. K. Köhler, S. K. Reed, R. E. Westacott and K. G. McKendrick, The Journal of Physical Chemistry B **110** (24), 11717-11724 (2006).
55. Y. Peng, L. Liu, Z. Cao, S. Li, O. A. Mazyar, W. L. Hase and T. Yan, The Journal of Physical Chemistry C **112** (51), 20340-20346 (2008).
56. D. J. Garton, T. K. Minton, M. Alagia, N. Balucani, P. Casavecchia and G. G. Volpi, J Chem Phys **112** (13), 5975-5984 (2000).
57. J. M. Zhang, D. J. Garton and T. K. Minton, Journal of Chemical Physics **117** (13), 6239-6251 (2002).
58. J. M. Zhang, H. P. Upadhyaya, A. L. Brunsvold and T. K. Minton, J Phys Chem B **110** (25), 12500-12511 (2006).
59. H. Kelso, S. P. K. Kohler, D. A. Henderson and K. G. McKendrick, J Chem Phys **119** (19), 9985-9988 (2003).
60. S. P. K. Kohler, M. Allan, H. Kelso, D. A. Henderson and K. G. McKendrick, J Chem Phys **122** (2), 024712 (2005).
61. S. P. K. Kohler, M. Allan, M. L. Costen and K. G. McKendrick, J Phys Chem B **110** (6), 2771-2776 (2006).
62. M. Allan, P. A. J. Bagot, S. P. K. Kohler, S. K. Reed, R. E. Westacott, M. L. Costen and K. G. McKendrick, Phys Scripta **76** (3), C42-C47 (2007).
63. M. Allan, P. A. J. Bagot, R. E. Westacott, M. L. Costen and K. G. McKendrick, J Phys Chem C **112** (5), 1524-1532 (2008).
64. A. M. Zolot, W. W. Harper, B. G. Perkins, P. J. Dagdigian and D. J. Nesbitt, J Chem Phys **125** (2), 021101 (2006).
65. A. M. Zolot, P. J. Dagdigian and D. J. Nesbitt, J Chem Phys **129** (19), 194705 (2008).
66. D. Troya and G. C. Schatz, Esa Sp Publ **540**, 121-128
743 (2003).
67. B. K. Radak, S. Yockel, D. Kim and G. C. Schatz, J Phys Chem A **113** (26), 7218-7226 (2009).
68. D. Kim and G. C. Schatz, J. Phys. Chem. A **111** (23), 5019-5031 (2007).
69. B. H. Wu, J. M. Zhang, T. K. Minton, K. G. McKendrick, J. M. Slattery, S. Yockel and G. C. Schatz, J Phys Chem C **114** (9), 4015-4027 (2010).
70. C. Waring, P. A. J. Bagot, M. W. P. Bebbington, M. T. Raisanen, M. Buck, M. L. Costen and K. G. McKendrick, J. Phys. Chem. Lett. **1** (13), 1917-1921 (2010).

71. C. Waring, P. A. J. Bagot, M. T. Raisanen, M. L. Costen and K. G. McKendrick, J. Phys. Chem. A **113** (16), 4320-4329 (2009).
72. S. R. Cohen, R. Naaman and J. Sagiv, Physical Review Letters **58** (12), 1208-1211 (1987).
73. S. B. M. Bosio and W. L. Hase, Journal of Chemical Physics **107** (22), 9677-9686 (1997).
74. T. Y. Yan, N. Isa, K. D. Gibson, S. J. Sibener and W. L. Hase, Journal of Physical Chemistry A **107** (49), 10600-10607 (2003).
75. W. A. Alexander, B. S. Day, H. J. Moore, T. R. Lee, J. R. Morris and D. Troya, Journal of Chemical Physics **128** (1), - (2008).
76. W. A. Alexander, J. R. Morris and D. Troya, Journal of Physical Chemistry A **113** (16), 4155-4167 (2009).
77. W. A. Alexander, J. R. Morris and D. Troya, Journal of Chemical Physics **130** (8), - (2009).
78. W. A. Alexander and D. Troya, Journal of Physical Chemistry A **110** (37), 10834-10843 (2006).
79. M. E. Bennett, W. A. Alexander, J. W. Lu, D. Troya and J. R. Morris, J Phys Chem C **112** (44), 17272-17280 (2008).
80. B. S. Day, J. R. Morris, W. A. Alexander and D. Troya, Journal of Physical Chemistry A **110** (4), 1319-1326 (2006).
81. L. R. Fiegland, M. M. Saint Fleur and J. R. Morris, Langmuir **21** (7), 2660-2661 (2005).
82. G. Li, S. B. M. Bosio and W. L. Hase, J Mol Struct **556** (1-3), 43-57 (2000).
83. D. Troya and G. C. Schatz, J Chem Phys **120** (16), 7696-7707 (2004).
84. D. Kim and G. C. Schatz, J Phys Chem A **111** (23), 5019-5031 (2007).
85. R. Parthasarathy, S. Chaturvedi and K. Go, PNAS **87** (3), 871-875 (1990).
86. H. A. Scheraga, J. Biomolec. Struc. & Dyn. **16** (2), 447-460 (1998).
87. M. D. Collins, M. L. Quillin, G. Hummer, B. W. Matthews and S. M. Gruner, J Mol Biol **367** (3), 752-763 (2007).
88. M. D. Collins, G. Hummer, M. L. Quillin, B. W. Matthews and S. M. Gruner, Proceedings of the National Academy of Sciences of the United States of America **102** (46), 16668-16671 (2005).
89. J. Peters, W. Baumeister and A. Lupas, J Mol Biol **257** (5), 1031-1041 (1996).
90. H. Yin, G. Hummer and J. C. Rasaiah, Journal of the American Chemical Society **129** (23), 7369-7377 (2007).
91. G. Huber, H. Mantz, R. Spolenak, K. Mecke, K. Jacobs, S. N. Gorb and E. Arzt, Proceedings of the National Academy of Sciences of the United States of America **102** (45), 16293-16296 (2005).
92. J. Israelachvili and R. Pashley, Nature **300** (5890), 341-342 (1982).
93. J. L. Parker, P. M. Claesson and P. Attard, J. Phys. Chem. **98** (34), 8468-8480 (1994).
94. E. J. Verwey and J. T. G. Overbeek, *Theory of the Stability of Lyophobic Colloids* (Elsevier, New York, 1947).
95. B. Derjaguin and L. Landau, Prog Surf Sci **43** (1-4), 30-59 (1993).
96. H. K. Christenson, P. M. Claesson and R. M. Pashley, P Indian as-Chem Sci **98** (5-6), 379-389 (1987).

97. Y. I. Rabinovich and B. V. Derjaguin, Colloid Surface **30** (3-4), 243-251 (1988).
98. P. Kekicheff and O. Spalla, Phys. Rev. Lett. **75** (Copyright (C) 2010 American Chemical Society (ACS). All Rights Reserved.), 1851-1854 (1995).
99. J. Wood and R. Sharma, Langmuir **11** (Copyright (C) 2010 American Chemical Society (ACS). All Rights Reserved.), 4797-4802 (1995).
100. M. L. Fielden, R. A. Hayes and J. Ralston, Langmuir **12** (Copyright (C) 2010 American Chemical Society (ACS). All Rights Reserved.), 3721-3727 (1996).
101. M. Hato, J. Phys. Chem. **100** (Copyright (C) 2010 American Chemical Society (ACS). All Rights Reserved.), 18530-18538 (1996).
102. M. E. Karaman, B. W. Ninham and R. M. Pashley, J. Phys. Chem. **100** (Copyright (C) 2010 American Chemical Society (ACS). All Rights Reserved.), 15503-15507 (1996).
103. J. Tamayo and R. Garcia, Langmuir **12** (Copyright (C) 2010 American Chemical Society (ACS). All Rights Reserved.), 4430-4435 (1996).
104. V. V. Yaminsky, B. W. Ninham, H. K. Christenson and R. M. Pashley, Langmuir **12** (Copyright (C) 2010 American Chemical Society (ACS). All Rights Reserved.), 1936-1943 (1996).
105. V. Yaminsky, C. Jones, F. Yaminsky and B. W. Ninham, Langmuir **12** (Copyright (C) 2010 American Chemical Society (ACS). All Rights Reserved.), 3531-3535 (1996).
106. G. Bar, Y. Thomann, R. Brandsch, H. J. Cantow and M. H. Whangbo, Langmuir **13** (Copyright (C) 2010 American Chemical Society (ACS). All Rights Reserved.), 3807-3812 (1997).
107. A. Kuhle, A. H. Sorensen and J. Bohr, J. Appl. Phys. **81** (Copyright (C) 2010 American Chemical Society (ACS). All Rights Reserved.), 6562-6569 (1997).
108. A. Carambassis, L. C. Jonker, P. Attard and M. W. Rutland, Phys. Rev. Lett. **80** (Copyright (C) 2010 American Chemical Society (ACS). All Rights Reserved.), 5357-5360 (1998).
109. V. S. J. Craig, B. W. Ninham and R. M. Pashley, Langmuir **14** (Copyright (C) 2010 American Chemical Society (ACS). All Rights Reserved.), 3326-3332 (1998).
110. M. Preuss and H.-J. Butt, Langmuir **14** (Copyright (C) 2010 American Chemical Society (ACS). All Rights Reserved.), 3164-3174 (1998).
111. R. F. Considine, R. A. Hayes and R. G. Horn, Langmuir **15** (Copyright (C) 2010 American Chemical Society (ACS). All Rights Reserved.), 1657-1659 (1999).
112. V. S. J. Craig, B. W. Ninham and R. M. Pashley, Langmuir **15** (Copyright (C) 2010 American Chemical Society (ACS). All Rights Reserved.), 1562-1569 (1999).
113. G. Haugstad and R. R. Jones, Ultramicroscopy **76** (Copyright (C) 2010 American Chemical Society (ACS). All Rights Reserved.), 77-86 (1999).
114. N. Ishida, M. Sakamoto, M. Miyahara and K. Higashitani, Langmuir **16** (Copyright (C) 2010 American Chemical Society (ACS). All Rights Reserved.), 5681-5687 (2000).
115. N. Ishida, N. Kinoshita, M. Miyahara and K. Higashitani, J. Colloid Interface Sci. **216** (Copyright (C) 2010 American Chemical Society (ACS). All Rights Reserved.), 387-393 (1999).

116. N. Ishida, T. Inoue, M. Miyahara and K. Higashitani, Langmuir **16** (Copyright (C) 2010 American Chemical Society (ACS). All Rights Reserved.), 6377-6380 (2000).
117. H. K. Christenson and P. M. Claesson, Adv Colloid Interfac **91** (3), 391-436 (2001).
118. X. Huang, C. J. Margulis and B. J. Berne, PNAS **100** (21), 11953-11958 (2003).
119. J. C. Eriksson, S. Ljunggren and P. M. Claesson, J Chem Soc Farad T 2 **85**, 163-176 (1989).
120. G. Hummer, J. C. Rasaiah and J. P. Noworyta, Nature **414** (6860), 188-190 (2001).
121. N. Choudhury and B. M. Pettitt, Journal of the American Chemical Society **129** (15), 4847-4852 (2007).
122. S. Romero-Vargas Castrillón, N. s. Giovambattista, I. A. Aksay and P. G. Debenedetti, The Journal of Physical Chemistry B **113** (23), 7973-7976 (2009).
123. C.-Y. Lee, J. A. McCammon and P. J. Rossky, The Journal of Chemical Physics **80** (9), 4448-4455 (1984).
124. S. H. Lee and P. J. Rossky, The Journal of Chemical Physics **100** (4), 3334-3345 (1994).
125. N. Giovambattista, P. J. Rossky and P. G. Debenedetti, Phys. Rev. E **73** (4) (2006).
126. N. Giovambattista, P. J. Rossky and P. G. Debenedetti, Phys. Rev. Lett. **102** (5) (2009).
127. N. Giovambattista, P. J. Rossky and P. G. Debenedetti, J. Phys. Chem. B **113** (42), 13723-13734 (2009).

Chapter 2
Computational Methods

2.1 Introduction

For almost a century it has been known that quantum mechanics (QM) governs the movement of electrons, atoms, and molecules in reactive and inelastic collisions. To fully characterize gas-phase reaction dynamics using computational methods, all degrees of freedom of each particle should be studied using a full quantum-mechanics-based description. For all but the simplest reactive molecular systems, a full QM treatment is computationally intractable and therefore simplifications must be taken into consideration.

This chapter describes the (quasi-) classical-trajectory method which is used in all subsequent gas-phase and gas/surface reactive-scattering simulations of this Thesis. The classical-trajectory method separates the electronic and nuclear motions of a chemical-dynamics simulation into the quantum and classical realms, respectively. The theoretical basis for this simplification is the Born-Oppenheimer (BO) approximation, which argues that nuclear and electronic motions are separable based on the differing timescales of their motions.[1] The BO approximation states that only one electronic configuration plays a role for a given set of nuclear positions, and thus the nuclear motions occur in an equilibrated electronic configuration. The approximation is valid for systems that do not have low-lying excited electronic states and for chemical systems where the nuclei are moving at exceedingly large velocities. When the nuclei approach the speed of the electrons (translational energies of this magnitude are beyond those studied in this body of work), the Born-Oppenheimer becomes invalid.

Under the BO approximation, nuclear motion is separable from electronic motion and the forces acting on the nuclei can be calculated for any given molecular configuration independent of the nuclear motions. The classical trajectory method treats the nuclei as classical particles where Newton's Second Law of Motion governs their dynamics. The classical trajectory approximation has been shown to be valid for a wide range of chemical reactions and with a high quality description of the potential energy of the system can provide quantitative agreement with both quantum simulations and experiment.[2]

Newton's Second Law can be expressed as Equation 2.1:

$$\vec{F} = m\vec{a} = \frac{md\vec{v}}{dt} = \frac{md^2\vec{r}}{dt^2} \tag{2.1}$$

Under the BO approximation the potential energy of the molecular system is only a function of the nuclear positions and the force acting on each of the nuclei is related to the potential energy by Equation 2.2:

$$\vec{F} = \frac{-dU(\vec{r})}{d\vec{r}} \tag{2.2}$$

where $U(\vec{r})$ is the potential energy as a function of the nuclear coordinates. Equation 2.2 assumes that the system studied is not affected by any external forces and that there is no time-dependence on the potential energy, which is the case for gas-phase reactions under single collision conditions. Such conditions exist for most modern crossed molecular-beam experiments, particularly under ultra-high vacuum conditions. Setting Equation 2.1 and Equation 2.2 equal to each other we get Equation 2.3:

$$\frac{-dU(\vec{r})}{d\vec{r}} = \vec{F} = \frac{md^2r}{dt^2} \tag{2.3}$$

Equation 2.3 is the basis for the classical trajectory method, and it also raises three requirements needed for a full treatment of the time-evolution of the nuclei. The first requirement is a proper description of the potential energy for the given system to be studied, which is commonly called the potential energy surface (PES). The second requirement needed to implement the classical trajectory method is a proper description of the initial conditions for the reactants, including the initial positions and velocities of each nucleus. And finally, since Equation 2.3 is first-order with respect to position and second-order with respect to time, no closed-form analytical solution to the differential equation exists. Therefore, the classical trajectory method requires a suitable numerical integration scheme that must balance the need for precision with the computational demands required for implementation. In the following, we address each of the three requirements to propagate classical trajectories for a chemical system.

2.2 Potential Energy Surfaces

High-quality potential energy surfaces are an essential component to performing accurate and predictive chemical dynamics simulations. PESs can take many forms, which will be described below. The major requirement needed for an effective PES is that it can provide an accurate potential energy for molecular configurations in the regions of space explored in a dynamics simulation. Modern studies of gas-phase molecular dynamics require the evaluation of upwards of 10^7 energy and energy gradients.[3] Therefore, the PES must be able to provide these calculations on a time-scale that allows the simulations to be completed in a reasonable amount of time.

2.2.1 Analytical Potential Energy Surfaces

The most common technique used to describe the PES has been the use of analytic functions which can be parametrically fit to either high-level theoretical or experimental data. For simple systems with relatively few degrees of freedom, functional forms can be used which provide the convenient situation where the adjustable, empirical parameters retain some physical meaning. As an example, the London-Eyring-Polanyi-Sato (LEPS) potential energy function has been widely used and the adjustable parameters can be linearly adjusted to fit different regions of the PES to be studied with either the classical trajectory method or quantum scattering calculations.[4, 5] While the LEPS function has been used extensively as the functional form for the study of triatomic reactions, it lacks the flexibility to properly describe the PES of all triatomic reactions and a number of other forms based on other empirical relationships have been developed.[6, 7] While simple functions with physically meaningful parameters may be used for triatomic reactions, the development of a PES for systems larger than a few atoms requires significant effort to define appropriate functional forms.

Early attempts to move beyond these LEPS-type functions resulted in PESs which did not possess the proper permutationally invariant symmetry required (i.e. inverting the position of two identical atoms yields two different energies).[8] Braams and Bowman have developed a series of permutationally invariant polynomial functions that they have used to properly describe the PES for systems up to 10 atoms.[9, 10] A trade-off for these symmetry-corrected functional forms is the loss of physical relevance of the fitted parameters and the non-linear ways in which they describe the PES. Additionally, the number of *ab initio* electronic structure points needed to properly describe the increases dramatically as the size of the system grows. As an example, Czako *et al.* recently published a PES for the $F+CH_4 \rightarrow HF+CH_3$ reaction, which uses the previously described polynomials as the functional form.[11] To properly account for all the degrees of freedom for this six-atom reaction they needed to calculate ~20,000 single point energies at the CCSD(T)/aug-cc-pVTZ level of theory. Additionally, these more complex functional forms are computationally more expensive the simple LEPS functions and increase the time needed to perform a classical trajectory study for a given reaction. Furthermore, these potential energy functions lack analytical derivatives. Therefore, numerical differentiation needs to be implemented to obtain energy gradients for each coordinate, and this is computationally demanding for systems with more than a few atoms. The final limitation of the analytical function description is that a new PES must be derived for each different system to be studied.

2.2.2 Direct Dynamics

An attractive alternative to an analytical description of the PES is the use of direct dynamics.[12] Direct dynamics is performed by calling an electronic structure program at each step along a classical trajectory to calculate the potential energy and the forces acting on the atomic nuclei. The use of direct-dynamics simulation has recently come into vogue and it is philosophically attractive for a number of reasons. The first major attraction to the use of direct dynamics is the generality with which it can be applied to any chemical system of interest without the need to derive appropriate functional forms or focus on specific regions of the PES. Secondly, the quality of the dynamics results should be directly tied to the quality of the electronic-structure-method/basis-set pair used in the dynamics. Therefore any limitations in the accuracy of the dynamics should be tied to either the physics of the electronic structure method or the assumptions made in the type of dynamics performed (e.g. classical *vs.* quantum) and not to an error in the analytical functions resulting, for instance, from insufficient coverage of the relevant regions of the PES. Finally, one can attempt to study processes that involve more than one electronic state smoothly using multireference methods that provide the potential energy surfaces and their couplings, as needed in surface-hopping methods such as Tully's.[13, 14]

A major limitation of direct-dynamics simulations is the computational expense associated with the calculation of energies and gradients along each step of the trajectory. To achieve a full description of the dynamics for a reactive system one would ideally run upwards of 1000 trajectories for each system and set of conditions under consideration. As previously stated, depending on the initial collision energies and reactive mechanisms for a given system, $>10^7$ energy and gradient calculations may need to be performed. This fact dramatically limits the type of electronic structure methods and basis sets that can be reasonably used for a full-dynamics classical-trajectory study. Limited numbers of trajectories reduce the precision with which dynamics properties can be calculated and reduce the effectiveness of direct dynamics methods.

2.2.3 Specific-Reaction-Parameters Semiempirical Hamiltonians

To ameliorate this limitation in the direct-dynamics method, a strategy has emerged that makes used of specific-reaction-parameters (SRP) semiempirical Hamiltonians. Semiempirical methods are based on the same quantum mechanical foundation as Hartree–Fock theory, however some of the more computationally expensive electronic integrals are approximated by the use of empirical parameters[15] such as orbital exponents, ionization energies, and pseudo-potentials for non-valence electrons.[16] The empirical parameters are usually derived so that calculations of several molecular properties agree with experiments or the thermochemistry of a large test set of molecules.[15]

The specific-reaction-parameters semiempirical Hamiltonian method was first proposed by Don Truhlar and co-workers in 1991 to perform dynamics calculations on a nucleophilic substitution reaction.[17] Their results showed that a SRP Hamiltonian provided results that improved upon the best analytical PES available at that time for the specific chemical reaction that they investigated.

The technique involves taking a standard semiempirical method, which contains a number of empirical parameters, and varying these parameters, using a non-linear least squares fitting technique, in such a way as to match a set of *ab initio* data specific to the reaction(s) under consideration. In this method, there is a need for an accurate *ab initio* map, which sufficiently covers the relevant regions of the PES. This map requires substantial computational effort as well as chemical understanding of the accessible regions of the PES. The SRP strategy has been shown to be applicable to studying the reactive dynamics of a varied number of chemical systems by our group[18-25] and others.[26-31]

Our reaction dynamics simulations have all used the SRP method to explore the dynamics of not just a single chemical reaction but two different series of homologous chemical reactions, namely the hydrogen abstraction reactions of the H+alkane[3, 32] and F+alkane[33, 34] families. For both reaction classes, we have employed a modification of the Intermediate Neglect of Differential Overlap-1 (INDO1) semiempirical Hamiltonian[35-37] called the modified symmetrically orthogonalized intermediate neglect of differential overlap (MSINDO) semiempirical Hamiltonian.[16, 38]

MSINDO was chosen because it provided the most accurate description of the intrinsic reaction coordinate for the $H+CH_4$ and $H+C_2H_6$ reactions[3] and the $F+CH_4$ reaction[39] when compared with other semiempirical methods such as AM1[40] and PM3.[41, 42] The MSINDO Hamiltonian provides a set of parameters (4 empirical parameters for H, 9 parameters for C and F, and a specific binding term for each atom-type pair) that give the Hamiltonian sufficient flexibility for the SRP process.

Generally speaking, the SRP process requires the calculation of a number of single point energies in relevant regions of the PES using a high-level electronic structure method and a sufficiently large basis set. These calculated points then serve as the basis for reparameterization of the SRP Hamiltonian. Since the specific regions of the PES that are important for a proper treatment of the dynamics are system-dependent, their choice will be discussed in the subsequent chapters that detail the individual reaction classes studied. We have shown that the SRP process can predict the barriers for hydrogen-abstraction reactions within 1 kcal mol^{-1} and reaction energies that are within 1-2 kcal mol^{-1} compared with coupled-cluster *ab initio* calculations. Similar calculations performed with both second-order Moller-Plesset and density-functional theory have shown average deviations of ~5 kcal mol^{-1} in both the reactive barriers and energies. To exemplify the dramatic increase in speed that the SRP-Hamiltonians, we present the example of a quasi-classical trajectory study of the $F+CH_4$ reaction. A sizable batch of 30,000 trajectories calculated at E_{coll}=1.8 kcal mol^{-1} with optimized initial conditions for reaction (initial separation reactant separation and impact parameter sampling) require the evaluation of ~$9x10^8$ energy gradients. To perform these calculations using the SRP-MSINDO method with 10 processors, the full dynamics study can be completed in 2-3 days. To calculate the same number of trajectories using the aug-cc-pVDZ basis set, the

B3LYP method would require approximately seven years to complete the calculations and second-order Moller-Plessett perturbation (MP2) theory would take approximately eleven years. Additionally, the SRP-MSINDO Hamiltonian scales as N^3, meaning that doubling the number of basis functions will result in a factor of eight increase in computational time. Density-functional methods such as B3LYP scale as N^4, and MP2 scales as N^5, which means that as the size of the system increases the computational cost advantages with the SRP-MSINDO method are magnified.

Now that we have introduced the SRP process and we have laid out the general process for the construction of a suitable Hamiltonian that can be used for direct-dynamics calculations, we next present the details for (quasi-)classical gas-phase and gas/surface reactive scattering calculations.

2.3 Gas-Phase Initial Conditions

The quasi-classical trajectory method requires well-defined initial conditions (atomic coordinates and velocities) that correspond to quantum vibrational and rotational states of reagent molecules. A known limitation of the classical trajectory method is the presence of internal vibrational energy redistribution (IVR).[43] As a polyatomic molecule propagates through time governed by classical mechanics, energy is repartitioned through different vibrational and rotational modes and during long trajectories complete energy scrambling occurs.[44]

In a full quantum-mechanical treatment of the nuclear motion, energy that is deposited into a specific vibrational mode remains in that mode until the molecule is perturbed by a physical collision or interaction with an external field. (There are a few exceptions to this rule which include molecules that have a Fermi resonance, which occurs when two different vibrational modes in the same molecule have similar energy transitions and the transitions are members of the same irreducible representation. Such resonances should not occur in the vibrational manifolds of the molecules pertinent to this work as they have been shown to exist in molecules such as water[10] and those that have carbonyl functionalities, such as CO_2[31] and ketones.[45, 46])

Since IVR is time dependent, it is important to prepare molecules that correspond to the proper vibrational quantum states and then optimize the conditions of that trajectory to ensure that the polyatomic molecules react while they still correspond to the desired quantum states as faithfully as possible. This section will be organized in two parts: 1) the preparation of polyatomic molecules in initial states that correspond to the proper quantum states to be studied and 2) the preparation of radical-molecule initial conditions for quasi-classical trajectories which are then integrated to investigate the dynamics.

2.3.1 Polyatomic Molecule Preparation

Polyatomic molecular species have a number of degrees of freedom that need to be properly accounted for to give correct initial conditions for the quasi-classical trajectories. We make use of a modified version of the VENUS96 computer program[47, 48] which has been interfaced with the MSINDO and SRP-MSINDO electronic-structure methods to provide proper initial conditions. Due to the scope of this document, we will not review here all of the techniques that can be employed to map molecular rovibrational states into atomic coordinates and momenta. However, we will provide a limited description of the process employed in our studies and we refer the reader to the original work developing these techniques[49-51] and also to the VENUS code documentation[47, 48] for a more thorough review of these techniques.

Since all experimental comparisons are made with polyatomic molecules in supersonically expanded molecular beams, we assume that the molecules are all located in the vibrational ground state. Supersonically expanded molecular beam experiments result in rotational temperatures that are significantly depressed. As an approximation to these conditions, we start all of our polyatomic reactants in the rotational ground state. We input the equilibrium geometry for the alkane molecules and the Hessian matrix from an electronic-structure calculation with the appropriate method. The MSINDO Hamiltonian, and thus also the SRP-MSINDO, has been shown to overestimate the frequencies of molecular species by ~20%. To account for this known limitation of the Hamiltonian the vibrational frequencies are scaled by a factor of 0.8 relative to the frequencies found in the Hessian matrix.

All of the *n* normal modes for the alkane molecules are treated as harmonic oscillators with energies described by Equation 2.4:

$$E_i = \left[E_v^0 - \sum_j^{i-1} E_j \right] \left[1 - R_i^{1/(n-i)} \right] \tag{2.4}$$

where E_i is the energy in each normal mode *n*, R_i is a vector of *n* random numbers between 0 and 1, and $E_v^o = \sum_i^n E_i$, which is the total energy. The normal mode amplitudes, A_i, are calculated from the Hessian matrix by the relationship in Equation 2.5:

$$A_i = \frac{(2E_i)^{1/2}}{\omega_i} \tag{2.5}$$

where $\omega_i = 2\pi\nu_i$ where ν_i are the harmonic normal-mode vibrational frequencies . From these amplitudes and the R_i vector, the normal mode coordinates and velocities can be computed as Equation 2.6:

$$\begin{aligned} Q_i &= A_i \cos(2\pi R_i) \\ V_i &= -\omega_i A_i \sin(2\pi R_i) \end{aligned} \tag{2.6}$$

These normal mode coordinates are transformed into Cartesian coordinates by:

$$\begin{aligned} [x] &= [L_x][Q] + [x_0] \\ [p_x] &= [M][L_x][V] \end{aligned} \tag{2.7}$$

Where $[L_x]$ is the transform matrix from normal-mode coordinates to mass-weighted Cartesian coordinates in the x dimension, $[x_0]$ is a matrix that contains the equilibrium coordinates in the x direction and [M] is a diagonal matrix whose elements are the atomic masses. Equation 2.7 can be generalized for all spatial directions. This process introduces additional angular momentum into the molecule due to the approximate nature of normal mode sampling for finite displacements. Since we have decided to produce the polyatomic alkane molecules in the rotational ground state the total angular momentum for the system should be zero. To correct for this approximation, the energy of the system, E, is calculated using the appropriate Hamiltonian (SRP-MSINDO) and the coordinates and momenta are scaled as in Equation 2.8:

$$\begin{aligned} x_i^{'} &= (x_i - x_i^0)(E^0/E)^{1/2} + x_i^0 \\ p_{x_i}^{'} &= p_{x_i}(E^0/E)^{1/2} \end{aligned} \tag{2.8}$$

Where p_{x_i} is the momentum of atom i in the x direction and $E^0 = E_v^0$, which was previously calculated. When E and E^0 agree to within 0.1% the process in complete and then molecules are ready to be used for quasi-classical trajectories.

2.3.2 Trajectory Initial Conditions

As previously stated, the conditions for the trajectories are important to properly simulate experiments. To obtain the trajectory initial conditions, the polyatomic hydrocarbon molecule is placed at the center of a Cartesian coordinate system and the center-of-mass velocity is subtracted so that the molecule is stationary as shown in Figure 2.1. Three Euler angles are selected to randomly orient the atomic reactant around the hydrocarbon molecule. The random orientation of the two reactants allows for a complete sampling of the phase-space of the reaction if sufficient trajectories are generated. There are a number of other parameters that must be defined in order to ensure that all possible approaches of the atom to the molecule are properly investigated.

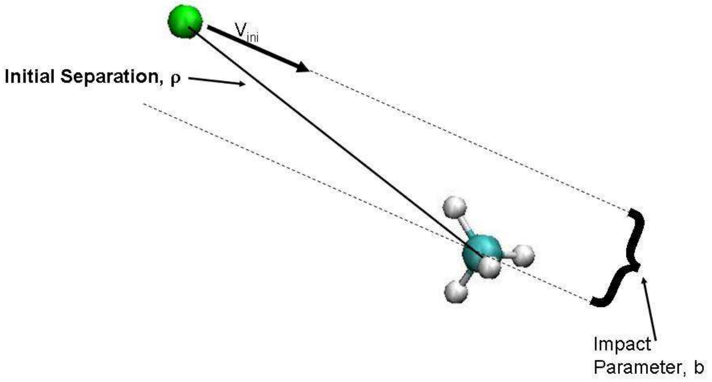

Figure 2.1: Schematic representation of the initial conditions for a gas-phase quasi-classical trajectory

The initial separation of the impinging atom from the center of mass of the target molecule, ρ, needs to be optimized. This distance should be long enough that there are no intermolecular forces between the two colliding reactants at the beginning of the trajectory. However, the distance should also be as short as possible to reduce the computational time and improve the survivability of the quasi-quantum state for the hydrocarbon molecule, as described in the previous section.

A second important initial condition parameter is the impact parameter, which measures the ‘direct-ness’ with which a molecular collision occurs. The impact parameter, b, is defined as the perpendicular distance between two parallel lines drawn in the direction of the initial velocity vector of the atomic reactant and passing through the center of mass for each reactant. Since the crossed-molecular beams used in experiments have a width that is dramatically greater than the molecular diameter all possible impact parameters are sampled. Therefore, to reproduce the experiment all impact parameters for which reaction is possible must be sampled. The maximum sampling impact parameter (b_{max}) has to be long enough that all possible reactive approaches are included in the trajectories, but short enough that non-reactive trajectories due to an excessively long impact parameter are minimized.

The final parameter to be defined for a gas-phase quasi-classical trajectory is the collision energy. The initial collision energy is defined by the relative momentum of the atomic reactant and the center of mass of the hydrocarbon. The collision energy is typically chosen to match the experiments with which the calculations are compared. While many of the considerations explained here for gas-phase reactions need to be taken into account for the considerably more complicated case of gas/surface reactions, we will now describe the differences and similarities between these two types of reactions.

2.4 Gas/surface Trajectory Calculations

Simulations of gas/surface reactions are significantly more complex than their analogous calculations in the gas phase. The first challenge is to build an organic surface that is simultaneously physically relevant and computationally feasible. Our choice for the reactive organic surface to be studied is an alkanethiolate self-assembled monolayer (SAM). SAMs are attractive organic surfaces due their regular structure and the ease with which they can be modeled computationally. Of course, SAM surfaces have also been utilized in experimental[52-60] and theoretical[61-69] studies of gas/surface reactions. SAM surfaces can also act as a model for liquid squalane surfaces which have been used extensively in gas/liquid scattering investigations.[70-82]

2.4.1 SAM Model

The main difficulty in simulating gas/SAM reactions is in the sheer size of the system, which contains literally hundreds of atoms. Numerous quantum-mechanical calculations of energy gradients for a system of such size is prohibitive, even if semiempirical Hamiltonians are used. To alleviate the computational expense of these simulations, end we have employed a hybrid quantum-mechanics/molecular-mechanics (QM/MM) technique, which divides the alkanethiolate SAM surface into a non-reactive, structural region and a reactive region. In the rest of this section, we first describe the molecular-mechanics potential used for the SAM system, and then present the mechanical-embedding procedure used to define the interface between the structural and reactive sections of the SAM surface.

2.4.1.1 Molecular-Mechanics Model

Simulation of atom/SAM reactions requires a computational model which can accurately mimic the behavior of real systems. To this end we have built upon the wealth of inelastic gas/SAM scattering calculations that have been performed in our group.[64-68, 83] The SAM potentials are modeled using the optimized potentials for liquid simulations (OPLS) force field developed by the Jorgensen group.[84] The OPLS force field treats all bond stretches and angular bending terms as harmonic potentials with equilibrium values defined for each atom pair involved. The dihedral angular terms are defined as a summation of cosine terms with specific parameters for each four-atom group. Non-bonded interactions are modeled as the summation of Coulombic and 6-12 Lennard-Jones (L-J) interaction terms. The structural SAM potential takes the final from:

$$U(r,\theta,\phi,R) = \sum_{stretches} \tfrac{1}{2}k_r(r-r_0)^2 + \sum_{angles} \tfrac{1}{2}k_\theta(\theta-\theta_0)^2 + \sum_{dihedrals}\sum_{n=1}^{3} \tfrac{1}{2}k_n[1+\cos(n\phi-\phi_n)] + \sum_{Coulombic} \frac{q_i q_j}{4\pi\varepsilon_0 R} + \sum_{L-J} 4\varepsilon\left[\left(\frac{\sigma}{R}\right)^{12} - \left(\frac{\sigma}{R}\right)^{6}\right] \tag{2.9}$$

where r is the bond distance for all bonded pairs of atoms, θ is the angle formed by all three bonded atoms, ϕ is the dihedral angle for all four consecutively bound atoms and R is the distance between each atom and every other atom that is either more than three bonds away or a part of other SAM chains. The terms r_o and θ_o are the equilibrium bond distances and bond angles for each two and three atom pair, while k_r and k_θ represent harmonic stretching and bending force constants, respectively. The k_n terms are the torsional force constants expanded around equilibrium dihedral angle, ϕ_n. Regarding non-bonding interactions, in the Coulombic term, q_i and q_j are the partial charges on each atomic center ε_0 is the permittivity of vacuum and R is the through-space distance between atomic centers. The models used for gas/SAM reactive scattering do not have any partial charges associated with the atoms in the SAM or the impinging atomic gases and therefore the Coulombic term is zero for all steps in the simulation. The L-J potential for each atom pair is defined by two different atom-type specific parameters. The depth of the attractive well is ε and the distance at which the pair's intermolecular energy becomes zero is σ. Table 2.1 shows the interaction parameters for all of the relevant atomic interactions in the OPLS force field.

Table 2.1: The empirical parameters used to define the OPLS intermolecular potential for the F+SAM system.

Interactions	Parameters
Bond Stretches[a]	
C-H	k_r=340.0 r_o=1.090
C-C	k_r=268.0 r_0=1.529
S-C	k_r=222.0 r_0=1.810
Angular Bends[b]	
H-C-H	k_q=33.0 θ_0=107.8
C-C-H	k_q=77.0 θ_0=109.1
C-C-C	k_q=63.0 θ_0=112.4
S-C-C	k_q=50.0 θ_0=112.4
Dihedral Torsions[c]	
H-C-C-H, C-C-C-H	k_3=0.3 ϕ_3=0.0
C-C-C-C, S-C-C-C	k_3=2.0 ϕ_3=0.0
Lennard-Jones[d]	
H	σ=2.50 ε=0.030
C	σ=3.50 ε=0.066
S	σ=3.905 ε=0.118

[a] Stretching parameters (k_r) units are $(x10^3)K \cdot Å^{-2}$, and the equilibrium bond lengths (r_o) units are Å.

[b] Bending parameters (k_θ) units are $(x10^3)K \cdot rad^{-2}$ and the equilibrium angles are in degrees

[c] k_1 and k_2 are both zero, reducing the dihedral terms to a simple cosine function, k_x torsional bending parameters units are kcal mol^{-1} and the equilibrium angles are in degrees

[e] Equlibrium bond length (σ) units are Å and the well depths (ε) are in kcal mol^{-1}.

Past simulations of SAM surfaces have investigated the role that explicitly modeling the hydrogen atoms have on the structure and scattering behavior of SAM surfaces. Early SAM models used a united-atom model, which averages the hydrogen atoms into the nearest heavy atom.[61, 85] This simplification dramatically reduces the number of interactions that must be calculated and reduces the computational times for SAM simulations. While this united-atom approach yields relatively accurate results, the Hase group has shown that explicitly modeling the hydrogen atoms with the OPLS force field yields a SAM surface which not only predicts the correct chain tilt angle but also has the chain-tilt pointing toward the second nearest neighbor and not the nearest neighbor as united-atom models predict.[62] Previous work in our group has shown a hybrid approach can also provide a compromise which maintains most of the gain in computational expense of the united-atom approach while matching the accuracy of the all-atom approach.[66-68, 86, 87]

Our choice of force field is motivated by the correlation between SAM surfaces modeled with OPLS and experimentally measurable surface parameters. A tilt angle of ~30º from normal has been measured experimentally[88] and work in our group shows that the average tilt angle 29.9±2.2º.

Our gas/surface reaction cell consists of 25 octanethiolate SAM chains arranged in a hexagonal lattice with sulfur-sulfur separations of 4.98Å. The sulfur atoms are frozen during the simulation in a configuration that is consistent with the equilibrium position of sulfur atoms on a Au(111) surface.[89] Previous studies have explicitly modeled the gold surface, but fixing the sulfur atoms in the equilibrium positions they would have on a gold surface does not affect the scattering dynamics calculations and greatly reduces the computational expense associated with explicitly modeling the gold atoms. Additionally, the regular nature of the SAM allows for another computational simplification to be made. Periodic boundary conditions are implemented in the x- and y-directions to create an infinite two-dimensional surface as implemented in the TINKER program suite.[90]

2.4.1.2 Mechanical Embedding Procedure

The harmonic stretching terms in the OPLS molecular mechanics force field do not allow for the possibility of bond forming and breaking. To study the reactions of atomic radicals with organic surfaces, we have added a second component to our system which is based upon the same SRP-MSINDO Hamiltonian that we used in our gas-phase classical trajectory calculations.

Figure 2.2 shows a schematic breakdown of the structural and reactive regions of the SAM surface for the F+SAM reaction.[69] The interface between the reactive and structural regions of the SAM surface is treated using a common technique called the mechanical embedding procedure (MEP).[91] In the MEP, the potential energy of the entire surface is calculated using a molecular-mechanics method. Then the potential energy of the reactive region is calculated with the force field and subtracted from the prior energy. Finally, the gas-phase SRP-Hamiltonian is used to calculate the potential energy of the reactive region and this term is added back into the total system energy. Equation 2.10 expresses the mathematical representation of the mechanical embedding procedure:

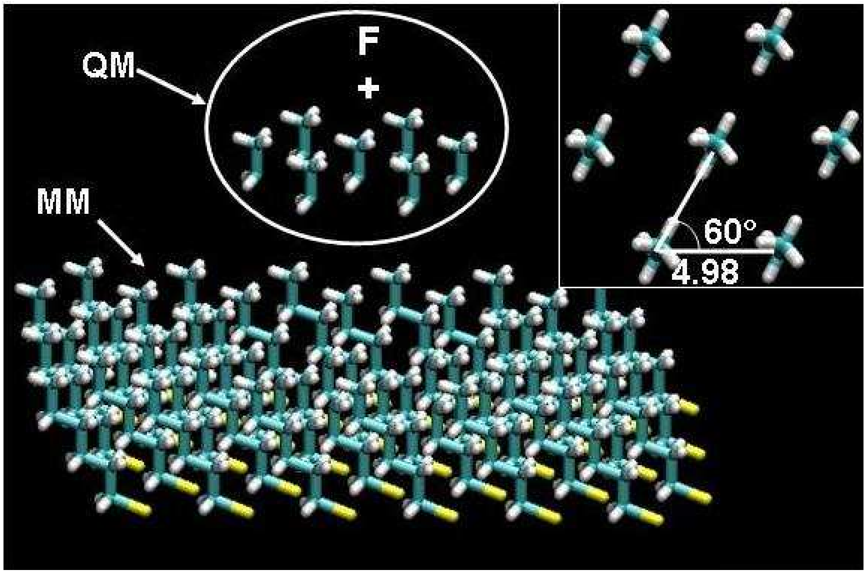

Figure 2.2: A description of the QM/MM regions for the SAM surfaces with the mechanical embedding procedure

$$E_{QM/MM} = E_{reactive+structural}(MM) - E_{(reactive)}(MM) + E_{(reactive)}(QM) \quad (2.10)$$

A similar recipe is used to calculate the forces (energy gradients) acting on each of the atomic centers that are necessary to propagate classical trajectories.

In our investigation of the F+SAM system, the reactive region consists of the ethyl-terminus of a central SAM chain and the ethyl-termini of the six nearest-neighbor chains in the hexagonally-packed SAM surface. The impinging fluorine atom and these seven ethyl-terminated SAM chains (50 atoms) represent the entire reactive region. Capping hydrogen atoms are added to the ethyl moieties to saturate the valence shell of each of the ethyl temini and facilitate the QM calculations. The total SRP-MSINDO calculation of energy and gradients involves 56 atoms and 105 electrons.

The size of the reactive region and the choice to only model the ethyl termini with SRP-MSINDO is justified by the results of our dynamics calculations which show that

<2% of impinging fluorine atoms either trap on the surface or react with the sub-terminal carbon atom for all initial conditions investigated. Earlier computational investigations involving higher collision energies and systems that are less reactive (O+SAMs) found it necessary to model *n*-butyl chains to account for all of the reactivity in experimental conditions.[63]

2.4.2 Initial Conditions

2.4.2.1 Surface Structure

While SAM surfaces are highly regular, the perfect SAM depicted in Figure 2.2 does not accurately represent the structural disorder induced by thermal motion in reactive scattering experiments above 0 K. To create a physically relevant surface we have simulated a SAM surface in the canonical ensemble [constant temperature, constant volume] at 300K for 10ns. We then take the equilibrated surface and run an additional 1ns simulation of in the canonical ensemble. The momentary atomic positions and velocities of snapshots of this second simulation are taken and used as the initial surface conditions for our gas/surface scattering calculations.

2.4.2.2 Reactive Region

Classical, molecular-mechanics simulations provide surface conditions that correspond to the temperature chosen in the simulation, but there is no guarantee that that total energy will be correctly located in the proper vibrational manifolds of the reactive region of the surface. To address this issue, we have adapted a hybrid technique that assures that our impinging atomic gas interacts SAM chains having zero-point energy.

Our technique involves a three step process which involves first simulating isolated gas-phase ethane molecules with the proper zero-point vibrational motions, orienting the ethane molecules properly according to their positions in the surface and finally integrating these molecules into the SAM surface. Ethane molecules are simulated using similar techniques to those described above in section 2.3.1.1 for polyatomic reactant molecules in the gas phase. We have again simulated the molecules with 80% of the zero-point energy predicted by the Hessian matrix of an electronic-structure calculation using SRP-MSINDO and then completed the process exactly as described above.

The second step in the initial condition generation process involves obtaining the Euler angles that rotate the molecule from its orientation in the gas-phase calculation that determines proper coordinates and momenta for zero-point motion to their orientation in the SAM surface. Once the Euler angles for rotation are determined, we must finally place the ethane molecules into the SAM surface. To properly incorporate the ethane molecules in the surface, we begin by placing the sub-terminal carbon atom coincident with one of the carbon atoms in the ethane molecule. Using that carbon atom as the origin, we apply the rotation based upon the previously determined Euler angles. We rotate the positions and momentum of the rest of the ethane molecule to match the positions of the ethyl-terminus for each of the seven SAM chains. Since an ethane molecule is being placed in the SAM to replace an ethyl moiety, one of the hydrogen atoms must be deleted and the C-H bond is substituted with the C-C bond that bridges the QM/MM interface.

2.4.2.3 Initial Gas Conditions

The preparation of the impinging atomic gas is simpler than the surface preparation due to the lack of internal degrees of freedom. Figure 2.3 shows a schematic representation of the initial conditions of an F+SAM trajectory. Connecting our dynamics simulations with the experimental work done on analogous systems involves defining a few parameters of the system. The three relevant spatial parameters are the initial separation of the atom from the surface, the angle of incidence, θ_I, which is defined as the angle formed between the initial velocity vector of the atomic species, **k**, and the surface normal, and the azimuthal angle ϕ_i, which is defined as the angle between the vector **k** and the SAM chains tilt vector. Molecular-beam experiments

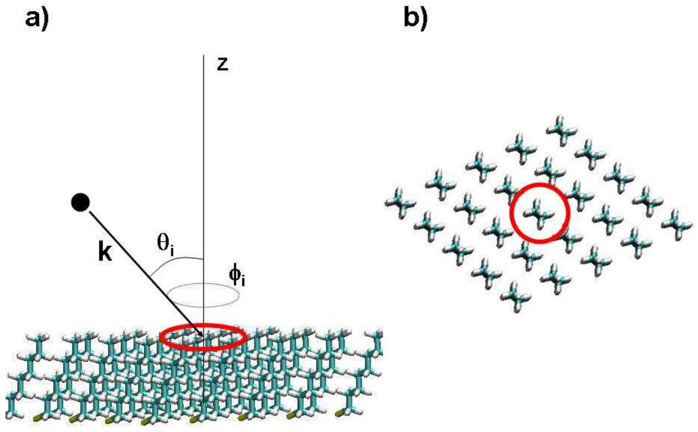

Figure 2.3: A schematic representation of the initial conditions for the gas/SAM classical trajectories. a) A side-on view showing the scattering angle and azimuthal angle. b) A top-down view of the SAM surface showing the circular target area

use the angle of incidence as an experimental parameter. Thus, we select this angle in our simulations to make direct connection with the experiments. The size of the molecular beam cross-section used in experiments is distinctly larger than individual rotational domains of an alkanethiolate SAM surface, and thus all of the different azimuthal angles are sampled. To make the connection with experiments, we have consequently sampled the azimuthal angles randomly.

The surface target area is defined as the area where the gas-phase atom would first make contact with the top of the SAM surface assuming that there are no inter-atomic forces acting on the impinging gas. We define our target area as a circle around the central SAM chain in the reactive region, which has an area equal to the size of the unit cell. The unit cell is defined as the rhombus formed between four adjacent SAM chains. SAMs formed on a Au(111) surface are arranged as a $\sqrt{3} \,\mathrm{x}\, \sqrt{3}$ R30º lattice with 4.98Å nearest-neighbor spacing. These parameters result in a target with a ~21.5 Å^2 area, and thus a radius of 2.61Å. We sample this target area by generating two random numbers, with the first representing a radial component and the second an angular component for the target area. The first random number is sampled quadratically from 0.0→2.61Å and the second number is sampled linearly from 0→360º. The initial height of the impinging atomic gas above the SAM surface is fixed so that there are no interactions between the gas and the surface. These three parameters coupled with this height fixed define the location of initial gas atom.

The final parameter we need to define is the initial collision energy of the impinging gas. Whereas in the gas-phase conditions we define the collision energy as a function of the relative velocity and the reduced mass of the system, in the gas/surface regime we define the collision energy only by the translational energy of the impinging atomic species. Reactive scattering experiments are typically performed on a constantly-refreshed organic surface where the reactant gas is formed in a molecular beam and delivered to the surface with a very narrow translational energy distribution.[81] In an effort to match the experimental energy profiles, we select our initial impinging gas energy to be equal to the center of the translational energy profile used in the experiments. We also vary the initial collision energy to probe the differences role that the initial translational energy profiles have on the dynamics that occur at surfaces.

2.5 Trajectory Propagation

Once the initial conditions and the potential-energy surface for reaction have been defined for either the SRP Hamiltonian in the gas phase or the QM/MM mechanical-embedding procedure for gas/surface reactions, a propagation method must be chosen to accurately describe the evolution of the nuclei through time. As previously stated, there is no closed-form solution possible for the differential Equation (2.3) since the left-hand side is first-order with respect to time and the right-hand side is second-order with respect to position. The trajectory propagation must be solved by using one of a number of numerical integration methods. All of these numerical methods are based around the understanding that if the potential is known, a Taylor Series expansion about the time t_0 can provide the updated nuclear coordinates for a given time step Δt, as expressed in Equation 2.11:

$$y(t_0+\Delta t) = y(t_0) + f'(t_0)\Delta t + f''(t_0)\frac{\Delta t^2}{2!} + f^{(3)}(t_0)\frac{\Delta t^3}{3!} + \ldots + f^{(n)}(t_0)\frac{\Delta t^n}{n!} \tag{2.11}$$

where y(t) is the coordinate vector at time, t, and f'(t), f''(t), and $f^{(n)}$(t) are the first-, second-, and nth-derivatives of the nuclear positions at time t. The most popular method for numerical integration is the fourth-order Runge-Kutta method, which is based on a series of four terms across the time step. The propagation method is described by the following series of equations, denoted 2.12:[92]

$$\begin{aligned}
y(t_{n+1}) &= y(t_n + \Delta t) = y(t_n) + \tfrac{(\Delta Y_1 + 2\Delta Y_2 + 2\Delta Y_3 + \Delta Y_4)}{6} \\
\Delta Y_1 &= \Delta t * f'(t_n, y_n) \\
\Delta Y_2 &= \Delta t * f'(t_n + \frac{\Delta t}{2}, y_n + \frac{\Delta Y_1}{2}) \\
\Delta Y_3 &= \Delta t * f'(t_n + \frac{\Delta t}{2}, y_n + \frac{\Delta Y_2}{2}) \\
\Delta Y_4 &= \Delta t * f'(t_n + \Delta t, y_n + \Delta Y_3)
\end{aligned} \tag{2.12}$$

where ΔY_n represents the change in position at different points along the time step.

The term "fourth order" means that the error in each individual step is on the order of $(\Delta t)^5$ and the overall accumulated error in the position is on the order of Δt^4. The Runge-Kutta method represents a relatively simple improvement to one of the most simple integration methods, the Euler method, which depends only on the first derivative at the time t_n and not the more complicated calculation of the slope at time $(t_n + \left(\frac{\Delta t}{2}\right))$ and also at time $(t_n + \Delta t)$. One of the advantages of the Runge-Kutta method is that it is self-starting, which means that it does not need any information about the t_{n-1} position or velocities.[93] Another advantage of this method is that it can be used to "back integrate" each trajectory as a check of accuracy by taking the velocities of each of the atoms and reversing each of them and check that the trajectory returns to the same position as the initial conditions of the original trajectory, within a given tolerance.

Our simulation methods implement a more sophisticated Predictor-Corrector (P-C) algorithm, which is based upon the Gear fifth-order predictor, sixth-order corrector algorithm.[94] The first step in the P-C algorithm involves predicting the updated positions of the nuclei based upon an extrapolation of the velocities of the past four steps in the simulation:

$$\begin{aligned} y(t+\Delta t) &= y(t) + \Delta t(\beta_1 v(t) + \beta_2 v(t-\Delta t) + \beta_3 v(t-2\Delta t) \\ &+ \beta_4 (v(t-3\Delta t) + \beta_5 (v(t-4\Delta t)) \end{aligned} \tag{2.13}$$

where the β_i terms are defined by the order of the integration and the specific implementation of the P-C algorithm. From this prediction step, the velocity, $v(t+\Delta t)$ is calculated by evaluating the potential with the new calculated atomic positions. This new atomic velocity is plugged into the sixth-order corrector step as in Equation 2.14:

$$\begin{aligned} y(t+\Delta t) &= y(t) + \Delta t(\beta_0 v(t+\Delta t) + \beta_1 v(t) + \beta_2 (v-\Delta t) + \\ &\beta_3 (v-2\Delta t) + \beta_4 (v-3\Delta t) + \beta_5 (v-4\Delta t)) \end{aligned} \tag{2.14}$$

After this step the corrector step, the energy derivatives are calculated at the new $y(t+\Delta t)$, the velocities are saved, and the array of velocities is updated for the next P-C step.

Successive trajectory steps are propagated using the P-C algorithm until termination conditions are met. In the case of gas-phase calculations, these termination criteria are based upon separation distances between different atomic centers which determine products. Alternatively, in gas/surface reactions, the trajectory is completed when the impinging gas atom reaches a certain distance above the SAM surface where there are no gas-surface interactions after collision.

2.6 Analysis

During the trajectory runs, the instantaneous coordinates and momenta for certain atomic nuclei and the total kinetic and potential energy are recorded and printed for analysis. From the reagent and product coordinate and momenta we have calculated a number of experimentally measurable quantities such as: rotational and vibrational actions (classical analog of quantum state) for diatomic molecules, distributions of the angle formed by the initial and final relative velocity vectors, opacity functions, which are a measure of reactivity as a function of impact parameter or the 'direct-ness' of the collision, and excitation functions, which are measures of reactivity in terms of cross section as a function of collision energy.

For gas/surface calculations, final translational energy, scattering angle, vibrational and rotational actions of diatomic products, are all calculated and compared with related experimental results. By printing the coordinates and momenta for all of the atoms in the reactive region at intermediate time steps, we also analyzed the collisions mechanism. In particular, we studied the role that post-reaction collisions of freshly-generated products with the surface play in the final state distributions. These post-reaction secondary collisions were analyzed in terms of hops (changes in the z-component of the linear momentum of the gas species), kicks (changes in the sign of any of the components of the linear momentum of the diatomic product after formation), and angular-momentum reversals of the diatomic product.

References

1. M. Born and R. Oppenheimer, Ann. Phys. **84** (20), 457 (1927).
2. H. Mayne, International Reviews in Physical Chemistry (1991).
3. J. P. Layfield, M. D. Owens and D. Troya, J. Chem. Phys. **128** (19), 194302-194312 (2008).
4. S. Sato, The Journal of Chemical Physics **23** (3), 592-593 (1955).
5. P. J. Kuntz, E. M. Nemeth, J. C. Polanyi, S. D. Rosner and C. E. Young, The Journal of Chemical Physics **44** (3), 1168-1184 (1966).
6. N. C. Blais and D. L. Bunker, The Journal of Chemical Physics **37** (11), 2713-2720 (1962).
7. K. S. Sorbie and J. N. Murrell, Molecular Physics **31** (3), 905-920 (1976).
8. M. J. T. Jordan and R. G. Gilbert, The Journal of Chemical Physics **102** (14), 5669-5682 (1995).
9. X. Huang, B. J. Braams and J. M. Bowman, The Journal of Chemical Physics **122** (4), 044308-044312 (2005).
10. A. Sokołowska and Z. Kęcki, Journal of Raman Spectroscopy **17** (1), 29-33 (1986).
11. G. Czako, B. C. Shepler, B. J. Braams and J. M. Bowman, The Journal of Chemical Physics **130** (8), 084301-084319 (2009).
12. K. Bolton, W. Hase and G. Peslherbe, in *Multidimensional Molecular Dynamics Methods*, edited by D. Thompson (World Scientific Publishing, Inc London, 1998), pp. 143-189.
13. J. C. Tully and R. K. Preston, The Journal of Chemical Physics **55** (2), 562-572 (1971).
14. J. R. Schmidt, P. V. Parandekar and J. C. Tully, The Journal of Chemical Physics **129** (4), 044104-044106 (2008).
15. J. Pople and D. L. Beveridge, *Approximate Molecular Orbital Theory*. (McGraw-Hill, New York, 1970).
16. B. Ahlswede and K. Jug, Journal of Computational Chemistry **20** (6), 563-571 (1999).
17. A. Gonzalez-Lafont, T. N. Truong and D. G. Truhlar, J. Phys. Chem. **95** (12), 4618-4627 (1991).
18. U. Tasic, P. Hein and D. Troya, Journal of Physical Chemistry A **111** (18), 3618-3632 (2007).
19. J. P. Camden, W. Hu, H. A. Bechtel, D. J. A. Brown, M. R. Martin, R. N. Zare, G. Lendvay, D. Troya and G. C. Schatz, J. Phys. Chem. A **110** (2), 677-686 (2006).
20. D. Troya, Journal of Chemical Physics **123** (21) (2005).
21. D. Troya, Journal of Physical Chemistry A **109** (26), 5814-5824 (2005).
22. D. Troya and E. Garcia-Molina, Journal of Physical Chemistry A **109** (13), 3015-3023 (2005).
23. D. Troya, R. Z. Pascual, D. J. Garton, T. K. Minton and G. C. Schatz, Journal of Physical Chemistry A **107** (37), 7161-7169 (2003).
24. D. Troya and P. J. E. Weiss, Journal of Chemical Physics **124** (7) (2006).
25. T. Yan, C. Doubleday and W. L. Hase, J. Phys. Chem. A **108** (45), 9863-9875 (2004).

26. G. H. Peslherbe and W. L. Hase, Journal of Chemical Physics **104** (20), 7882-7894 (1996).
27. G. H. Peslherbe, H. B. Wang and W. L. Hase, Journal of the American Chemical Society **118** (9), 2257-2266 (1996).
28. C. Doubleday, K. Bolton and W. L. Hase, Journal of Physical Chemistry A **102** (21), 3648-3658 (1998).
29. O. Roberto-Neto, E. L. Coitino and D. G. Truhlar, Journal of Physical Chemistry A **102** (24), 4568-4578 (1998).
30. Y. Y. Chuang, M. L. Radhakrishnan, P. L. Fast, C. J. Cramer and D. G. Truhlar, Journal of Physical Chemistry A **103** (25), 4893-4909 (1999).
31. J. Z. Pu and D. G. Truhlar, Journal of Chemical Physics **116** (4), 1468-1478 (2002).
32. J. P. Layfield and D. Troya, Chemical Physics Letters **467** (4-6), 243-248 (2009).
33. J. P. Layfield, A. F. Sweeney and D. Troya, J. Phys. Chem. A. **113** (16), 4294-4304 (2009).
34. G. Czako, B. C. Shepler, B. J. Braams and J. M. Bowman, Journal of Chemical Physics **130** (8) (2009).
35. K. Jug and D. N. Nanda, Theoretica Chimica Acta **57** (2), 107-130 (1980).
36. K. Jug and D. N. Nanda, Theoretica Chimica Acta **57** (2), 131-144 (1980).
37. D. N. Nanda and K. Jug, Theoretica Chimica Acta **57** (2), 95-106 (1980).
38. B. Ahlswede and K. Jug, Journal of Computational Chemistry **20** (6), 572-578 (1999).
39. D. Troya, J. Chem. Phys. **123** (21), 214305-214316 (2005).
40. M. J. S. Dewar, E. G. Zoebisch, E. F. Healy and J. J. P. Stewart, J. Am. Chem. Soc. **107** (13), 3902-3909 (1985).
41. J. P. S. James, Journal of Computational Chemistry **10** (2), 209-220 (1989).
42. J. P. S. James, Journal of Computational Chemistry **10** (2), 221-264 (1989).
43. D. J. Nesbitt and R. W. Field, The Journal of Physical Chemistry **100** (31), 12735-12756 (1996).
44. J. Ortigoso and J. T. Hougen, Journal of Chemical Physics **112** (23), 10212-10220 (2000).
45. V. Rodriguez-Garcia, S. Hirata, K. Yagi, K. Hirao, T. Taketsugu, I. Schweigert and M. Tasumi, The Journal of Chemical Physics **126** (12), 124303-124306 (2007).
46. K. Noack, Spectrochimica Acta **18** (6), 697-708 (1962).
47. W. L. Hase, R. J. Duchovic, X. Hu, A. Komornicki, K. Lim, D. Lu, G. H. Peslherbe, K. N. Swamy, S. R. Vande Linde, A. J. C. Varandas, H. Wang and R. J. Wolf, (1996), pp. 55.
48. X. Hu, W. L. Hase and T. Pirraglia, Journal of Computational Chemistry **12** (8), 1014-1024 (1991).
49. S. Chapman and D. L. Bunker, Journal of Chemical Physics **62** (7), 2890-2899 (1975).
50. C. S. Sloane and W. L. Hase, Journal of Chemical Physics **66** (4), 1523-1533 (1977).
51. W. L. Hase, D. M. Ludlow, R. J. Wolf and T. Schlick, J Phys Chem-Us **85** (8), 958-968 (1981).

52. L. R. Fiegland, M. M. Saint Fleur and J. R. Morris, Langmuir **21** (7), 2660-2661 (2005).
53. T. M. D'Andrea, X. Zhang, E. B. Jochnowitz, T. G. Lindeman, C. Simpson, D. E. David, T. J. Curtiss, J. R. Morris and G. B. Ellison, Journal of Physical Chemistry B **112** (2), 535-544 (2008).
54. L. R. Fiegland, J. R. Morris and B. S. Day, Abstr Pap Am Chem S **231**, 515-COLL (2006).
55. C. Waring, P. A. J. Bagot, M. T. Raisanen, M. L. Costen and K. G. McKendrick, J. Phys. Chem. A **113** (16), 4320-4329 (2009).
56. C. Waring, P. A. J. Bagot, M. W. P. Bebbington, M. T. Raisanen, M. Buck, M. L. Costen and K. G. McKendrick, J. Phys. Chem. Lett. **1** (13), 1917-1921 (2010).
57. H. Fairbrother, Abstr Pap Am Chem S **231**, 516-COLL (2006).
58. J. Gorham, B. Smith and D. H. Fairbrother, J Phys Chem C **111** (1), 374-382 (2007).
59. J. M. Gorham, A. K. Stover and D. H. Fairbrother, J Phys Chem C **111** (50), 18663-18671 (2007).
60. A. J. Wagner, G. M. Wolfe and D. H. Fairbrother, Journal of Chemical Physics **120** (8), 3799-3810 (2004).
61. S. B. M. Bosio and W. L. Hase, Journal of Chemical Physics **107** (22), 9677-9686 (1997).
62. T. Y. Yan and W. L. Hase, Journal of Physical Chemistry B **106** (33), 8029-8037 (2002).
63. D. Troya and G. C. Schatz, Proceedings of the 9th International Symposium on Materials in a Space Environment **540**, 121-128 (2003).
64. W. A. Alexander and D. Troya, J. Phys. Chem. A **110**, 10834-10843 (2006).
65. B. S. Day, J. R. Morris, W. A. Alexander and D. Troya, J. Phys. Chem. A **110** (4), 1319-1326 (2006).
66. W. A. Alexander, B. S. Day, H. J. Moore, T. R. Lee, J. R. Morris and D. Troya, Journal of Chemical Physics **128** (1), - (2008).
67. W. A. Alexander, J. R. Morris and D. Troya, Journal of Physical Chemistry A **113** (16), 4155-4167 (2009).
68. W. A. Alexander, J. R. Morris and D. Troya, Journal of Chemical Physics **130** (8), - (2009).
69. J. P. Layfield and D. Troya, The Journal of Chemical Physics **132** (13), 134307 (2010).
70. M. E. Saecker and G. M. Nathanson, J. Chem. Phys. **99** (9), 7056-7075 (1993).
71. H. Kelso, S. P. K. Kohler, D. A. Henderson and K. G. McKendrick, J. Chem. Phys. **119** (19), 9985-9988 (2003).
72. S. P. K. Kohler, M. Allan, H. Kelso, D. A. Henderson and K. G. McKendrick, J. Chem. Phys. **122** (2), 24712-24721 (2005).
73. S. P. K. Kohler, M. Allan, M. L. Costen and K. G. McKendrick, J. Phys. Chem. B **110** (6), 2771-2776 (2006).
74. S. P. K. Kohler, S. K. Reed, R. E. Westacott and K. G. McKendrick, J. Phys. Chem. B **110** (24), 11717-11724 (2006).
75. J. Zhang, H. P. Upadhyaya, A. L. Brunsvold and T. K. Minton, J. Phys. Chem. B **110** (25), 12500-12511 (2006).

76. A. M. Zolot, W. W. Harper, B. G. Perkins, P. J. Dagdigian and D. J. Nesbitt, J. Chem. Phys. **125** (2), 21101-21105 (2006).
77. M. Allan, P. A. J. Bagot, M. L. Costen and K. G. McKendrick, J. Phys. Chem. C **111** (40), 14833-14842 (2007).
78. D. Kim and G. C. Schatz, J. Phys. Chem. A **111** (23), 5019-5031 (2007).
79. M. Allan, P. A. J. Bagot, R. E. Westacott, M. L. Costen and K. G. McKendrick, J. Phys. Chem. C **112** (5), 1524-1532 (2008).
80. P. A. J. Bagot, C. Waring, M. L. Costen and K. G. McKendrick, J. Phys. Chem. C **112** (29), 10868-10877 (2008).
81. A. M. Zolot, P. J. Dagdigian and D. J. Nesbitt, J. Chem. Phys. **129** (19), 194705-194711 (2008).
82. B. K. Radak, S. Yockel, D. Kim and G. C. Schatz, J. Phys. Chem. A **113** (26), 7218-7226 (2009).
83. M. E. Bennett, W. A. Alexander, J. W. Lu, D. Troya and J. R. Morris, J Phys Chem C **112** (44), 17272-17280 (2008).
84. W. L. Jorgensen, D. S. Maxwell and J. Tirado-Rives, J. Am. Chem. Soc. **118** (45), 11225-11236 (1996).
85. J. Hautman and M. L. Klein, Journal of Chemical Physics **91** (8), 4994-5001 (1989).
86. W. A. Alexander and D. Troya, Journal of Physical Chemistry A **110** (37), 10834-10843 (2006).
87. B. S. Day, J. R. Morris, W. A. Alexander and D. Troya, Journal of Physical Chemistry A **110** (4), 1319-1326 (2006).
88. C. D. Bain, H. A. Biebuyck and G. M. Whitesides, Langmuir **5** (3), 723-727 (1989).
89. N. Camillone, C. E. D. Chidsey, P. Eisenberger, P. Fenter, J. Li, K. S. Liang, G. Y. Liu and G. Scoles, J. Chem. Phys. **99** (1), 744-747 (1993).
90. J. W. Ponder and F. M. Richards, J. Comp. Chem. **8** (7), 1016-1024 (1987).
91. D. Bakowies and W. Thiel, J. Phys. Chem. **100** (25), 10580-10594 (1996).
92. J. I. Steinfeld, J. S. Francisco and W. L. Hase, *Chemical Kinetics and Dynamics*. (Prentice-Hall, United States, 1989).
93. M. Baer, *Theory of Chemical Reaction Dynamics*. (CRC Press, United States, 1985).
94. C. W. Gear, *Numerical initial value problems in ordinary differential equations*. (Prentice-Hall, Englewood Cliffs, N.J., 1971).

Chapter 3
Theoretical study of the dynamics of the $H+CH_4$ and $H+C_2H_6$ reactions using a specific-reaction-parameters semiempirical Hamiltonian

Reprinted with permission from J. P. Layfield, M. D. Owens and D. Troya, J. Chem. Phys. 128 (19), 194302 (2008). Copyright 2008, American Institute of Physics.

3.1 Introduction

Over the last two decades, calculations of the dynamics properties of various low-dimensionality chemical reactions have shown quantitative agreement with experiment.[1-3] The success of these reaction-dynamics calculations has enabled the characterization of chemical reactions with a level of detail not commonly available from the experiment. A natural step forward in our understanding of the dynamics of chemical reactions would be to extend the accuracy shown by these simulations to reactions of larger dimensionality, including gas/surface reactions. There are two major problems limiting quantitative studies of the dynamics of large chemical reactions. First, quantum-dynamics calculations for multidimensional chemical reactions are prohibitive, particularly if many heavy atoms are involved. Second, accurate analytic potential-energy surfaces required for quantitative dynamics calculations are difficult to derive for reactions with many active degrees of freedom.

One of the most popular approaches to circumvent the need to derive an analytic or interpolated potential-energy surface for state-to-state dynamics calculations is to perform direct-dynamics calculations.[9] In direct-dynamics simulations, the potential energy and derivatives required to evolve the chemical system in time are obtained directly from electronic-structure calculations whenever needed. A major problem of the direct-dynamics approach is that literally millions of energy gradient are commonly required to obtain reaction-dynamics properties with statistical significance using the quasiclassical-trajectory method. This requirement poses strict limitations in the types of methods and basis sets that can be used in the ‘on-the-fly’ electronic-structure calculations, particularly for large chemical systems.

Due to their minimal computational demand, semiempirical Hamiltonians have been used in past direct-dynamics calculations of various chemical reactions for which first-principle methods were prohibitive.[10-15] A serious drawback with this approach is that standard semiempirical Hamiltonians generally do not possess the level of accuracy necessary for predictive reaction-dynamics studies. Truhlar and co-workers pioneered an elegant solution to this problem, which consists of developing new sets of parameters for semiempirical Hamiltonians that are specific to each chemical reaction under consideration.[16] Drawing inspiration from that idea, dynamics studies of various chemical reactions have been recently carried out using specific-reaction-parameters (SRP) semiempirical Hamiltonians.[7, 17-23]

In this work, we use direct-dynamics in combination with an SRP Hamiltonian to study the reaction of hydrogen atoms with the methane and ethane molecules. This study represents a step forward in the development of SRP Hamiltonians because while in the above-mentioned efforts SRP Hamiltonians have usually been derived for one specific reaction, here we present an SRP Hamiltonian to investigate both the H+methane and H+ethane reactions. Future work will determine if this Hamiltonian is accurate for homologous H+alkane reactions.

Our choice of the H+alkane family of reactions to perform this study is based on the availability of a number of experiments and accurate theoretical calculations that can be used to calibrate the accuracy of our approach. In particular, H+methane is turning out to be a benchmark reaction in the progress of the reaction-dynamics field toward polyatomic reactions. Two main sets of experiments have provided important information about the dynamics of the hydrogen-abstraction channel of the H+methane reaction. First, Valentini and co-workers reported the rotational distributions of the HD product produced in the $H+CD_4$ reaction and the absolute cross section at 1.5 eV collision energy.[5, 24, 25] Second, the Zare group has measured the CX_3 product speed distributions of the $H+CX_4$ reaction (X=H,[8] D[7, 23]), the relative excitation function of the $H+CD_4 \rightarrow HD+CD_3$ reaction,[7] and the cross-section enhancement ratio due to excitation in the asymmetric C-H stretching mode of methane in the $H+CH_4 \rightarrow H_2+CH_3$ and $H+CHD_3$ reaction.[26] The hydrogen-exchange channel ($H+CD_4 \rightarrow D+HCD_3$) has also been detected experimentally at a collision energy near 2 eV.[27] The experimental information is more limited for the $H+C_2H_6 \rightarrow H_2+C_2H_5$ reaction. The Valentini group measured the rotational distribution of the H_2 product, and the absolute reaction cross section at 1.6 eV collision energy.[6, 24, 25] In addition, Oldershaw and Gould measured the excitation function of the $H+C_2D_6 \rightarrow HD+C_2D_5$ reaction in the 0.7-1.5 eV range.[4]

In regards to theory, while there have been a plethora of detailed studies of the dynamics of the $H+CH_4$ reaction and isotopomers, reaction-dynamics studies for the homologous $H+C_2H_6$ reaction are still lacking. All of the significant theoretical work on the $H+CH_4$ reaction and isotopic derivatives until 2007 has been extensively reviewed by Albus et al.,[28] so we refer the reader to that reference for work not mentioned here. Of particular interest to this paper is the work by the Espinosa-Garcia,[29-33] Schatz[7, 23, 34] and Bowman[35-37] groups. The Espinosa-Garcia group have used their own analytical potential-energy surface[29] to calculate angular distributions[30] and product energy partitioning[31] in the $H+CD_4 \rightarrow HD+CD_3$ reaction. Quasiclassical-trajectory studies of the angular distribution provided results in sharp contrast with experiment, but the agreement was improved when the distributions were calculated using reduced-dimensionality quantum-dynamics methods.[30] The energy partitioning to the HD product was well described by the trajectory estimates. [31] That same group also studied the dynamics of the $H+CH_4$[32] and $H+CHD_3$[33] reactions with initial vibrational excitation in the reagent molecule. Calculated CH_3 product speed distributions were notably more excited than experiment.

Schatz and co-workers carried out direct-dynamics calculations of the of the $H+CD_4 \rightarrow HD+CD_3$ reaction at the B3LYP/6-31G* level, and with a specific-reaction-parameters semiempirical Hamiltonian. The density-functional-theory based direct-dynamics calculations yielded good agreement with experiment in most cases.[7, 23, 34] Finally, Bowman and co-workers have constructed a potential-energy surface based on several thousand *ab initio* points calculated at the RCCSD(T)/aug-cc-pVTZ level, and used it to calculate cross sections and energy partitioning in products for the $H+CD_4 \rightarrow HD+CD_4$ reaction, and the effect of initial vibration on the $H+CH_4 \rightarrow H_2+CH_3$ and $H+CHD_3$ reactions.[36-38]

In contrast with this wealth of detailed dynamics studies for the H+methane reaction, work on H+ethane has been more limited. Kerkeni and Clary recently used quantum-scattering calculations to calculate the thermal rate constants for the $H+C_2H_6 \rightarrow H_2+C_2H_5$ reaction.[39, 40] Truhlar and coworkers developed a hybrid valence-bond/molecular-mechanics potential-energy surface to investigate thermal rate constants and kinetic isotope effects.[41] However, neither of these studies investigated reaction properties unrelated to the dynamics along the minimum-energy reaction path that can be compared with the experiments of Valentini and co-workers[4, 6] and Oldershaw and Gould.[27]

In this work, we perform high-quality *ab initio* calculations of the various channels of the H+CH_4 and H+C_2H_6 reactions to obtain an accurate description of the potential-energy surfaces of these systems. The *ab initio* calculations are used to develop a specific-reaction-parameters semiempirical Hamiltonian that is suitable for both reactions. Quasiclassical-trajectory calculations are then evolved with the SRP Hamiltonian using direct dynamics. The results of the calculations are critically compared with experiments and earlier calculations to calibrate the accuracy of the SRP Hamiltonian.

The rest of this paper is organized as follows: Section 3.2 shows the *ab initio* calculations, Section 3.3 describes the development of the SRP semiempirical Hamiltonian, Section 3.4 is for the quasiclassical-trajectory results, and Section 3.5 presents a summary and conclusions.

3.2 Ab Initio Calculations

We have characterized the most important stationary points of the potential-energy surface of the H+CH_4 and H+C_2H_6 reactions using high-quality electronic-structure methods. Geometry optimization and frequency analysis of reagents, products, and transition states have been performed mainly using second-order Möller-Plesset (MP2) perturbation theory with the correlation-consistent double-zeta basis set of Dunning augmented with diffuse functions (MP2/aug-cc-pVDZ). Our best calculations of the reaction energy and barrier have been carried out using coupled-cluster calculations with single, double, and perturbative triple excitations (CCSD(T)) with basis sets up to aug-cc-pVQZ. All of the calculations have used an unrestricted reference, and have been carried out using the Gaussian03 package of programs.[42]

Table 3.1 shows the reaction energies and barriers for the hydrogen-abstraction channel, H+RH → H_2+R (R=CH_3, C_2H_5), calculated at various levels of theory and basis sets. For the H+CH_4 → H_2+CH_3 reaction, B3LYP calculations overestimate the reaction exothermicity by more than 2 kcal mol^{-1}, while MP2 results are about 3 kcal mol^{-1} more endothermic than experiment.[43] CCSD(T) calculations are within 1 kcal mol^{-1} of the experiment, as expected. Regarding the barriers, we see that the B3LYP estimates are ~5 kcal mol^{-1} below the CCSD(T) results. Conversely, MP2 calculations provide reaction barriers 5 kcal mol^{-1} above the more accurate CCSD(T) data. The results of this comparison between B3LYP, MP2, and CCSD(T) energies follow what previously reported in related cousin radical+methane systems.[19, 20]

An important result in Table 3.1 is that dual-level CCSD(T) calculations using geometries and harmonic frequencies calculated at the MP2/aug-cc-pVDZ level match to within 0.3 kcal mol^{-1} the results of CCSD(T) calculations in which geometries and harmonic frequencies have been calculated at the same CCSD(T) level. For instance, the reaction energy and barrier calculated at the CCSD(T)/aug-cc-pVDZ//MP2/aug-cc-pVDZ level are within 0.22 kcal mol^{-1} of the ‘pure’ CCSD(T)/aug-cc-pVDZ results. Analogous results are obtained for CCSD(T) calculations with the aug-cc-pVTZ basis set. This finding is important because geometry optimizations and harmonic-frequency calculations for the H+C_2H_6 and larger homologous reactions are overly demanding if one wants to use CCSD(T) calculations with large basis sets. Therefore, the fact that MP2/aug-cc-pVDZ geometries and frequencies are sufficient to capture the CCSD(T) results will enable us to accurately characterize the energetics of the H+C_2H_6 reaction by performing single-point energy calculations at the CCSD(T) level using MP2/aug-cc-pVDZ geometries and harmonic frequencies.

To further investigate the adequacy of dual-level calculations in H+alkane reactions, we show in Table 3.2 representative geometrical parameters of the transition state (C_{3v} symmetry) of the H+CH_4 → H_2+CH_3 reaction. All of the first-principles calculations predict very similar transition-state geometries. In particular, we see that the lengths of the bonds that are breaking and forming at the MP2/aug-cc-pVDZ level are within 0.03 Å of the CCSD(T) estimates with the aug-cc-pVDZ and aug-cc-pVTZ basis sets. This result lends further confidence to the use of dual-level CCSD(T)//MP2 calculations in this work.

Table 3.1 Reaction energetics for the H+RH → H_2+R (R=CH_3, C_2H_5) abstraction reactions.[a,b]

	$H + CH_4 \rightarrow H_2 + CH_3$		$H + C_2H_6 \rightarrow H_2 + C_2H_5$	
Method/Basis set	Reaction energy	Barrier	Reaction energy	Barrier
B3LYP/aug-cc-pVDZ	-0.47 (2.45)	8.31 (9.50)	-5.21 (-1.92)	4.81 (6.41)
B3LYP/aug-cc-pVTZ	-2.21 (0.79)	8.26 (9.58)	-7.17 (-3.89)	4.91 (6.57)
B3LYP/aug-cc-pVQZ	-2.28 (0.74)	8.23 (9.56)	-7.24 (-3.95)	4.89 (6.56)
MP2/aug-cc-pVDZ	4.98(7.89)	18.54 (19.84)	2.21 (5.32)	15.37 (16.97)
MP2/aug-cc-pVTZ	3.80 (6.86)	18.21 (19.60)	0.77 (3.91)	15.06 (16.69)
MP2/aug-cc-pVQZ	3.78 (6.79)	18.20 (19.59)	0.59 (3.73)	
CCSD(T)/aug-cc-pVDZ	0.42 (3.48)	13.25 (14.73)	-2.51 (0.58)	
CCSD(T)/aug-cc-pVTZ	-0.37 (2.80)	13.15 (14.71)		
CCSD(T) / aug-cc-pVDZ // MP2 / aug-cc-pVDZ	0.59 (3.51)	13.47 (14.77)	-2.51 (0.60)	10.36 (11.95)
CCSD(T) / aug-cc-pVTZ // MP2 / aug-cc-pVDZ	-0.10 (2.82)	13.33 (14.62)	-3.61 (-0.49)	10.19 (11.78)
CCSD(T) / aug-cc-pVQZ // MP2 / aug-cc-pVDZ	-0.10 (2.82)	13.37 (14.67)	-3.72 (-0.60)	10.21 (11.80)
MSINDO	-4.84 (-1.07)	26.63 (28.58)	-14.74 (-11.17)	22.71 (24.91)
SRP-MSINDO	-1.08 (2.37)	15.88 (16.82)	-3.89 (-0.25)	11.90 (13.53)
Exp.[c]	0.7±0.2		-3.2±0.4	

[a] Energies are in kcal/mol

[b] Values between parentheses correspond to classical energies, i.e. not corrected by the zero-point energy.

[c] Experimental reaction energies calculated from the heats of formation at 298 K as reported in Ref. [43]

Table 3.2 Representative geometrical parameters of the transition states of the H+RH → H_2+R (R=CH_3, C_2H_5) abstraction reactions.[a]

Method / Basis set	R(H-H') / Å	R(C-H') / Å	∠H-H'-C / °
	$H+CH_4 \rightarrow H_2+CH_3$		
B3LYP / aug-cc-pVDZ	0.888	1.451	180
B3LYP / aug-cc-pVTZ	0.892	1.412	180
B3LYP / aug-cc-pVQZ	0.892	1.409	180
MP2 / aug-cc-pVDZ	0.882	1.426	180
MP2 / aug-cc-pVTZ	0.875	1.404	180
MP2 / aug-cc-pVQZ	0.873	1.404	180
CCSD(T) / aug-cc-pVDZ	0.905	1.417	180
CCSD(T) / aug-cc-pVTZ	0.898	1.398	180
MSINDO	0.932	1.272	180
SRP-MSINDO	0.870	1.396	180
	$H+C_2H_6 \rightarrow H_2+C_2H_5$		
B3LYP/aug-cc-pVDZ	0.920	1.394	177.6
B3LYP/aug-cc-pVTZ	0.927	1.360	177.8
B3LYP/aug-cc-pVQZ	0.929	1.358	177.7
MP2/aug-cc-pVDZ	0.896	1.403	176.2
MP2/aug-cc-pVTZ	0.890	1.382	176.0
MSINDO	0.989	1.403	176.2
SRP-MSINDO	0.910	1.343	173.6

[a] H is the approaching hydrogen atom, H' is the hydrogen atom being abstracted, and C is the carbon atom bonded to the hydrogen atom undergoing abstraction.

A second point of interest is that the reaction energy and barrier are only weakly dependent on the basis set for all of the electronic-structure methods explored in this work (B3LYP, MP2, and CCSD(T)). This is particularly true for the reaction barrier, with aug-cc-pV*N*Z (*N* = D, T, Q) estimates being well within 0.5 kcal mol^{-1} of one another for each method. The importance of this result is that large basis sets do not seem necessary to accurately capture the details of the potential-energy surface for the H+CH_4 reaction to within 1 kcal mol^{-1} accuracy. This fact will facilitate the study of the H+C_2H_6 and larger H+alkane reactions.

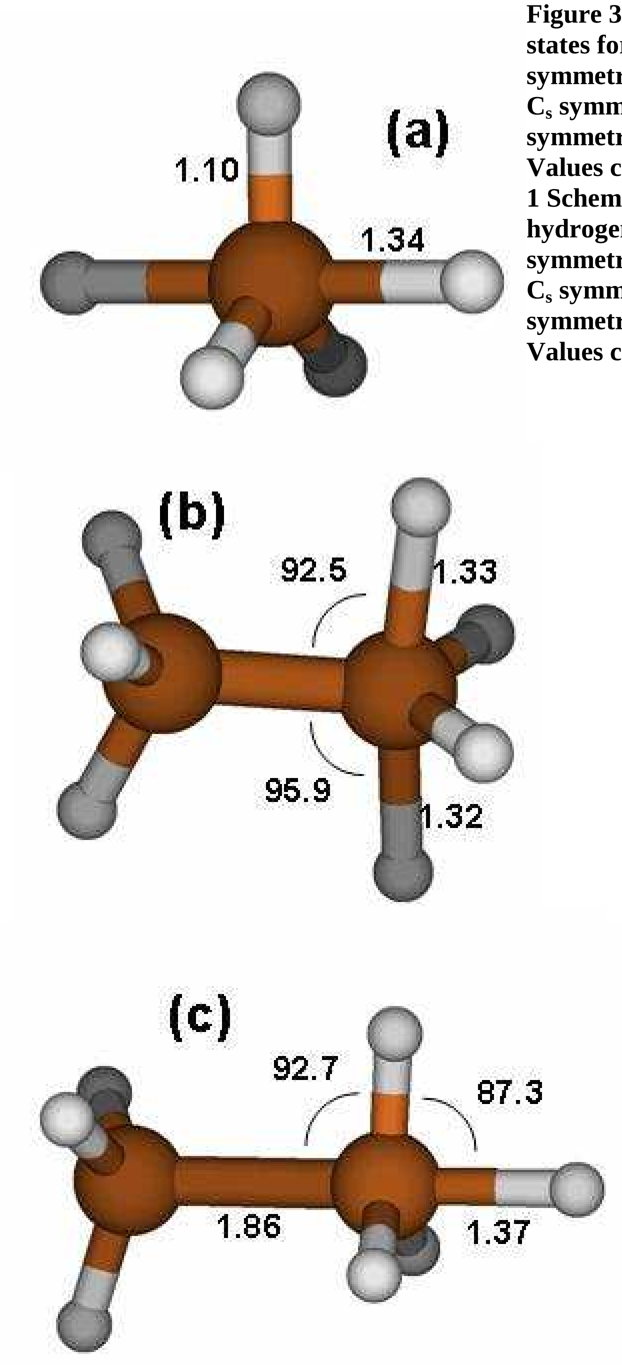

Figure 3.1: Schematic representations the transition states for hydrogen-atom exchange in $H+CH_4$ ((a), D_{3h} symmetry), hydrogen-atom exchange in $H+C_2H_6$ ((b), C_s symmetry), and C—C breakage in $H+C_2H_6$ ((b), C_{3v} symmetry). Distances are in Å, and angles in degrees. Values correspond to MP2/aug-cc-pVDZ calculations.

1 Schematic representations the transition states for hydrogen-atom exchange in $H+CH_4$ ((a), D_{3h} symmetry), hydrogen-atom exchange in $H+C_2H_6$ ((b), C_s symmetry), and C—C breakage in $H+C_2H_6$ ((b), C_{3v} symmetry). Distances are in Å, and angles in degrees. Values correspond to MP2/aug-cc-pVDZ calculations.

Table 3.1 also shows the reaction energy and barrier for the $H+C_2H_6 \rightarrow H_2+C_2H_5$ reaction calculated with most of the same techniques used for the $H+CH_4$ reaction. The trends of the changes in the reaction energy and barrier with the electronic-structure method and basis set parallel what was discussed before for $H+CH_4$. B3LYP overestimates the reaction exothermicity and underestimates the reaction barrier predicted by CCSD(T), and MP2 results go in exactly the opposite direction. CCSD(T) reaction energies are within 1 kcal mol^{-1} of the experiment. The weak dependence of the reaction energetics on the basis set discussed before for $H+CH_4$ is also seen in $H+C_2H_6$. The reaction energy at the CCSD(T)/aug-cc-pVDZ level agrees very well with CCSD(T)/aug-cc-pVDZ//MP2/aug-cc-pVDZ dual-level calculations. Unfortunately, we could not afford to locate the transition state at the CCSD(T)/aug-cc-pVDZ level to further test the dual-level approximation, but the results described before for the $H+CH_4$ reaction show compelling evidence for the legitimacy of this approach to predict the reaction barrier in H+alkane reactions. Representative geometrical parameters of the $H+C_2H_6 \rightarrow H_2+C_2H_5$ transition state (C_s symmetry) are listed in Table 3.2. A salient feature of this transition state is that the breaking and forming bonds are not collinear. In all of the calculations, the C—C—H'—H dihedral angle (where H' is the hydrogen atom undergoing abstraction) is 0°.

Comparison of the $H+CH_4$ and $H+C_2H_6$ CCSD(T) energies reveals that the larger reaction is about ~3.5 kcal mol^{-1} more exothermic and has a barrier that is 3 kcal mol^{-1} smaller than the $H+CH_4$ reaction. The increased stabilization of products and transition state with increasing alkane chain length agrees with what recently reported for $O(^3P)$+alkane → OH+alkyl reactions.[44] Comparison of transition-state geometries for both abstraction reactions indicates that the transition state is slightly more reagents-like in the $H+C_2H_6 \rightarrow$

$H_2+C_2H_5$ reaction than in the $H+CH_4 \rightarrow H_2+CH_3$ reaction (i.e., the forming bond is slightly longer and the breaking bonds is slightly shorter in $H+C_2H_6$). This trend in the reaction energetics and transition-state structures of homologous reactions agrees well with the prediction of Hammond's postulate[45] and has been described in detail for similar hydrogen-abstraction reactions.[44]

Until now, we have discussed the energetics of the $H+RH \rightarrow H_2+R$ ($R=CH_3$, C_2H_5) hydrogen abstraction reactions. However, other reaction channels are possible under the conditions of the dynamics experiments by Zare and co-workers, which reach collision energies of approximately 2.4 eV (~55 kcal mol^{-1}). In fact, the hydrogen-exchange reaction has been observed experimentally using isotopic substitution, $H+CD_4 \rightarrow D+CHD_3$, at energies of about 2 eV.[27] Table 3.3 shows the barriers of this hydrogen-exchange reaction calculated at various levels of electronic-structure theory. Our best estimate, CCSD(T)/aug-cc-pVQZ//MP2/aug-cc-pVDZ, predicts a reaction barrier well within the range of energies explored in Zare group's experiments. Figure 3.1(a) shows the transition-state structure for this reaction channel (D_{3h} symmetry), and reveals that the hydrogen-exchange reaction is formally a second-order homolytic substitution (SH_2) reaction. Interestingly, we find the same weak dependence of the results on the basis sets explored, so this seems to be a general trend in H+alkane calculations. Much as in the abstraction channel, MP2 calculations overestimate the CCSD(T) reaction barrier and B3LYP

Table 3.3 Energetics of the hydrogen-exchange H*+RH→ H*+RH (R=CH_3, C_2H_5) and H+C_2H_6 → CH_3+CH_4 reactions. [a,b,c]

	H*+CH_4 → H+CH_3H*	H*+C_2H_6→ H+C_2H_5H*	H+C_2H_6 → CH_4+CH_3	
	Barrier	Barrier	Reaction energy	Barrier
B3LYP/aug-cc-pVDZ	31.36 (31.49)	33.98 (34.52)	-17.16 (-17.09)	32.21 (31.49)
MP2/aug-cc-pVDZ	42.03 (41.99)	43.87 (44.22)	-9.71 (-9.75)	43.80 (42.78)
CCSD(T)/aug-cc-pVDZ[d]	37.66 (37.62)	39.59 (39.94)	-14.54 (-14.57)	37.68 (36.66)
CCSD(T)/aug-cc-pVTZ[d]	37.50 (37.46)	39.20 (39.55)	-15.51 (-15.54)	37.09 (36.07)
CCSD(T)/aug-cc-pVQZ[d]	37.23 (37.19)	38.97 (39.32)	-15.36 (-15.39)	37.04 (36.02)
MSINDO	52.02 (52.20)	54.74 (55.06)	-18.53 (-18.47)	54.74 (55.06)
SRP-MSINDO	31.45 (32.01)	32.46 (32.59)	-10.85 (-10.66)	26.10 (27.60)

[a] Energies are in kcal/mol

[b] Values between parentheses correspond to classical energies, i.e. not corrected by the zero-point energy.

[c] The reaction energy of the hydrogen-exchange reaction is 0 kcal/mol.

[d] Single-point calculations based on geometries and harmonic frequencies obtained at the MP2/aug-cc-pVDZ.

underestimate it. The hydrogen-exchange reaction pathway in the H+C_2H_6 reaction has a slightly larger barrier than in H+CH_4 (Table 3.3), but is still within the range of collision energies provided by hot H atoms emerging from HI or HBr photolysis. Figure 3.1(b) shows a schematic for the transition-state structure of the H-exchange reaction in H+C_2H_6

(C_s symmetry). Note that the breaking and forming bonds are not collinear (angle = 171.6° at the MP2/aug-cc-pVDZ level), presumably due to the steric hindrance of the neighboring ‘inactive’ CH_3 moiety. This steric hindrance is likely also the cause of the slight increase of the hydrogen-exchange barrier with respect to H+CH_4.

Finally, a third reaction pathway that is open at the energies of the experiment is $H+C_2H_6 \rightarrow CH_3+CH_4$. This channel is another SH_2 process consisting of concomitant H-addition/C-C breakage (we shall refer to this pathway as C-C breakage, hereafter). The reaction is notably exothermic, and our best estimate of the reaction energy (CCSD(T)/aug-cc-pVQZ//MP2/aug-cc-pVDZ, Table 3.3) agrees well with the experimental value, -14.8±0.2 kcal/mol.[43] The barrier for this process is about 3 kcal mol^{-1} less than that for H-exchange, and the transition state structure (C_{3v} symmetry) shows collinear breaking and forming bonds (Figure 3.1(c)).

The results of our calculations for high-energy reaction channels (H-exchange in H+CH_4 and H+C_2H_6 and C-C breakage in H+C_2H_6) indicate that photolytic hot H atoms have enough energy to surmount the barriers for all these channels. Of special interest might be the C-C breakage channel, as one of the products, CH_3, can be detected experimentally using techniques analogous to those used by the Zare group in their H+CH_4 studies.

3.3 Specific-Reaction-Parameters Hamiltonian

The *ab initio* study above shows that state-of-the-art electronic-structure methods can provide reaction energies in quantitative agreement with experiment. However, a problem with these accurate methods is that they are computationally prohibitive in direct-dynamics calculations. Even methods of moderate accuracy, such as MP2/aug-cc-pVDZ become restrictive in direct-dynamics studies of a reaction as large as H+C_2H_6. In fact, earlier direct-dynamics calculations of the H+CD_4 reaction were forced to use the relatively inexpensive B3LYP/6-31G* level of theory, and even then, the number of trajectories that could be calculated was limited.[7, 23, 34] As mentioned in the introduction, specific-reaction-parameters semiempirical Hamiltonians are gaining attention as affordable and potentially accurate methods for extensive direct-dynamics studies. In this section, we describe the development of a SRP Hamiltonian that is suitable for the H+CH_4 and H+C_2H_6 reactions.

Tables 3.1-3.3 show the predictions of reaction energy, barrier, and transition-state structures of the MSINDO Hamiltonian[46] for the $H+CH_4$ and $H+C_2H_6$ reactions in comparison with the estimates of first-principles methods. The performance of the MSINDO Hamiltonian is typical of standard low-cost semiempirical methods for open-shell systems. The reaction energies are 5-10 kcal mol^{-1} below experiment, and the reaction barriers are 10-15 kcal mol^{-1} larger than CCSD(T) values. These inaccuracies of the MSINDO Hamiltonian were revealed in direct-dynamics calculations of the $H+CD_4$ reaction, which showed strong disagreement with experiments and more accurate simulations.[18, 19] Still, semiempirical Hamiltonians are so inexpensive for reactions of the size of $H+CH_4$, $H+C_2H_6$, and even larger, that investigation of ways to improve their accuracy is warranted. Development of a set of parameters specific for the reaction under consideration is an approach that has worked well for various systems,[19, 20, 22] and has in fact been used before for the $H+CD_4$ reaction.[18, 19]

In this work, we go beyond these earlier approaches by deriving an SRP-MSINDO Hamiltonian that is appropriate for not only the $H+CH_4 \rightarrow H_2+CH_3$ reaction but also for the $H+C_2H_6 \rightarrow H_2+C_2H_5$ reaction and possibly larger H+n-alkane reactions. A special characteristic of our approach is that we base our SRP development on a grid of *ab initio* points so that the accuracy of the SRP Hamiltonian can be calibrated in various regions of the global potential-energy surface. This approach marks a significant difference with the earlier development attempts of an SRP Hamiltonian for the $H+CD_4$ reaction, in which only information about geometry and energy of reagents, products, and transition state of the abstraction channel were used to obtain the specific reaction parameters.[18, 19]

The grid of *ab initio* points used to guide the SRP development consists of potential-energy surface relaxed scans of relevant coordinates of the various reaction channels described in Section 3.2. To map the potential-energy surface of the $H+CH_4 \rightarrow H_2+CH_3$ reaction, we scanned the H—H coordinate from the transition state value (0.88 Å at the MP2/aug-cc-pVDZ level) toward reagents at 0.05 Å steps until the H—H coordinate reached 3.88 Å. In each of the points of the scan, we enforced collinearity of the breaking and forming bonds but optimized the geometry of the inactive CH_3 moiety at the MP2/aug-cc-pVDZ level. A similar scan was carried out for the C—H bond that is breaking from its value at the transition state (1.43 Å) toward products at 0.05 Å steps until the C—H coordinate reached 4.42 Å. A minimum-energy reaction path for the H+CH_4 hydrogen-exchange channel was also included in the grid of *ab initio* points. Departing from the transition state (Figure 3.1(a)), we scanned the breaking C—H bond at 0.05 Å steps until it reached a value of 3.34 Å. The breaking and forming bonds were forced to be collinear, but the rest of the degrees of freedom were optimized. Note that the minimum-energy reaction path for this hydrogen-exchange channel is symmetric about the transition state; therefore, this scan captures the regions of the potential-energy surface going from the transition state to products and reagents. We carried out a third potential-energy surface scan for the H+CH_4 system that considered the angle between the forming and breaking bond of the abstraction reaction. Departing from the transition state, which possesses a 180° H—H'—C angle, we calculated the potential energy for H—H'—C angles down to 90.0° each 5.0° degrees. The rest of the coordinates were frozen at the MP2/aug-cc-pVDZ transition-state values. Accurately capturing this transition-state anisotropy curve is important for subsequent dynamics studies, as this region of the potential-energy surface controls critical dynamics properties, such as the angular distribution and the H_2 product rotational distribution.

Four additional potential-energy surface scans were carried out to map relevant regions of the H+C_2H_6 potential-energy surface, two each for abstraction and C-C breakage channels. In each channel, we started from the transition state and moved downhill toward reagents and products. For the abstraction channel, we scanned the H—H coordinate from its transition-state value (0.89 Å) to 3.89 Å at 0.05 Å steps, and the C—H coordinate from its transition-state value (1.40 Å) to 4.40 Å at 0.05 Å steps. The H—H'—C angle was held fixed at its transition-state value (176.2°). The C—C breakage minimum-energy reaction path was also mapped by scanning the H—C bond from the transition state to 4.37 Å at 0.05 Å steps and the C—C bond from the transition state to 4.86 Å at 0.05 Å steps. The rest of variables were optimized at the MP2/aug-cc-pVDZ level. Preliminary parameter optimization with these scans resulted in an SRP-MSINDO Hamiltonian that described poorly the H_2 bond. Therefore, we included in the fit 41 points belonging to the H_2 diatomic potential-energy curve from an internuclear distance of 0.55 Å to 0.95 Å at 0.01 Å steps.

Overall, the potential-energy surface scans just described provided over 300 *ab initio* points for both the H+CH_4 and H+C_2H_6 systems at the MP2/aug-cc-pVDZ level. However, since Tables I and II show that MP2 is not a very accurate method for H+alkane reactions, we recalculated the energies of all of the points of the scans at the CCSD(T)/aug-cc-pVDZ level. These points were then involved in the reoptimization of the parameters of MSINDO Hamiltonian.

The derivation of the parameters of the SRP-MSINDO Hamiltonian was based on a non-linear least-squares parameter optimization so that the differences of the SRP-MSINDO and CCSD(T)/aug-cc-pVDZ energies of the various potential-energy surface scans of both H+CH_4 and H+C_2H_6 reactions described before were minimized. Since most of the experimental reaction-dynamics information pertains to the abstraction channel, in the fitting process we emphasized that region of the potential-energy surface by increasing the weights of the corresponding points of the grid. After significant attempts, we determined that weighting the points corresponding to the H+CH_4 and H+C_2H_6 abstractions by factors of ~15 with respect to the points on the exchange and C-C breakage channel provided the minimum deviation between CCSD(T)/aug-cc-pVDZ and SRP-MSINDO energies. Therefore, the description of the abstraction channel in the SRP-Hamiltonian is substantially better than the exchange and C-C breakage channels.

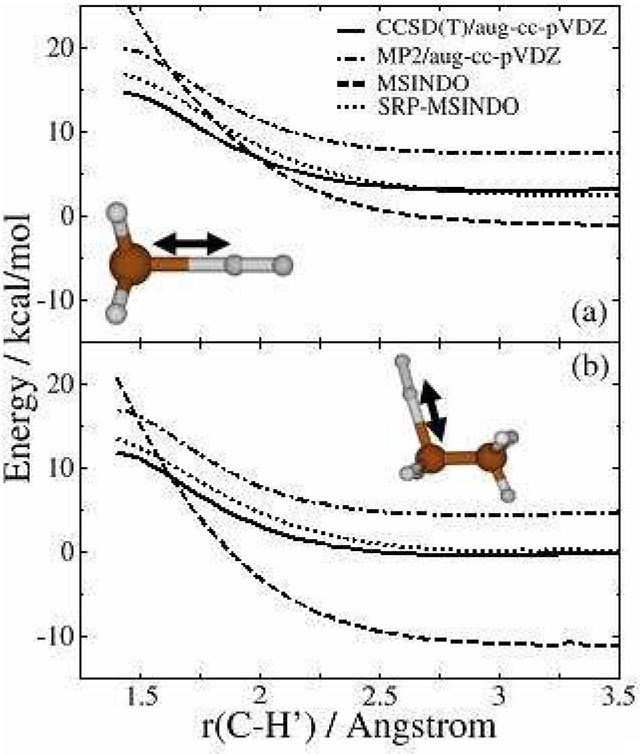

Figure 3.2: Potential-energy surface scans of the C-H' coordinate in the H+CH_4 → H_2+CH_3 (a) and H+C_2H_6 → H_2+C_2H_5 (b) reactions. The graphs show the reaction of the potential connecting the transition state to products. H' is the H atom that is undergoing abstraction.

The SRP-MSINDO parameters obtained after the optimization procedure are compared with the original set of parameters in Table 3.4. Typical relative differences between both sets of parameters usually less than 20%, and in no case the original and SRP parameters are different by more than a factor of 2. Figure 3.2 compares the estimates of the original MSINDO Hamiltonian with the CCSD(T)/aug-cc-pVDZ and SRP-MSINDO energies in representative potential-energy surface scans of the abstraction channel for both $H+CH_4$ and $H+C_2H_6$. The improvement in the description of the potential-energy surface by the SRP-MSINDO Hamiltonian is clearly evident, and this Hamiltonian reproduces quite accurately the CCSD(T)/aug-cc-pVDZ estimates. Tables I-III show the reaction energies, barriers, and transition state structures of the MSINDO and SRP-MSINDO Hamiltonians in comparison with distinctly more computationally expensive first-principles estimates. For the H+methane abstraction reaction, we see that while the original MSINDO Hamiltonian overestimates the experimental exothermicity by ~5 kcal mol^{-1}, the SRP Hamiltonian is within 1 kcal mol^{-1} of our most accurate calculation and

Table 3.4: Original and SRP MSINDO parameters involved in the H+alkane reactions.

Parameter	Original	SRP
ζ_s^U (H)	1.0060	0.8380
ζ_s (H)	1.1576	1.1280
I_s (H)	-0.5000	-0.4817
K_s (H)	0.1449	0.2374
$\alpha(1)$ (H)	0.3856	0.2526
$\alpha(2)$ (H)	0.50308	0.3669
ζ_s^U (C)	1.6266	1.0480
ζ_p^U (C)	1.5572	1.5206
ζ_s (C)	1.7874	1.8442
ζ_p (C)	1.6770	1.7480
I_s (C)	-0.8195	-0.9607
I_p (C)	-0.3824	-0.4211
ε_{1s} (C)	10.430	11.613
τ_{1s} (C)	5.0830	4.4681
K_s (C)	0.0867	0.1574
$\alpha(1)$ (C)	0.4936	0.5198
$\alpha(2)$ (C)	0.6776	0.5718

within 2 kcal mol^{-1} of the experiment. The performance of the SRP-MSINDO in the H+ethane abstraction reaction energy is slightly better, showing a deviation from experiment and our most accurate calculation smaller than 1 kcal mol^{-1}. Note also that the improvement with respect to the original Hamiltonian (>10 kcal mol^{-1}) is larger than in the H+methane reaction. The SRP-MSINDO abstraction reaction barriers show a deviation of about a 2 kcal mol^{-1} with respect to our most accurate calculations, while the original Hamiltonian overestimated the barriers by as much as 12 kcal mol^{-1}. The accuracy of the SRP-MSINDO Hamiltonian for the abstraction channel is even more remarkable if one compares it with the MP2 (Figure 3.2) and B3LYP results. Even though SRP-MSINDO electronic-structure calculations are orders of magnitude faster than MP2 and B3LYP calculations, they show more accuracy than these first-principle methods, whose errors are ~5 kcal mol^{-1} in the reaction barriers.

Another noticeable result of the reparametrization of the MSINDO Hamiltonian is the improvement in the description of the transition-state geometry for the abstraction channel. While the original Hamiltonian predicts a transition state with a much earlier character than first-principles estimates, the lengths of the breaking and forming bonds in the SRP-MSINDO transition states are in close geometric agreement with *ab initio* estimates (Table 3.2).

Regarding the description of the exchange channel, Table 3.3 shows that the SRP-MSINDO Hamiltonian also represents a notable improvement with respect to the original MSINDO results. Although the absolute difference between SRP-MSINDO and CCSD(T) data are larger than in abstraction channel, the relative differences are similar. In addition, SRP-MSINDO shows accuracy comparable to MP2/aug-cc-pVDZ and is slightly better than B3LYP/aug-cc-pVDZ. The SRP-MSINDO is however not superior to first-principles methods for the C-C breakage reaction channel, and shows notable differences with CCSD(T) data, particularly in the reaction barrier. Attempts to improve the performance of the SRP Hamiltonian in this region resulted in errors in the description of the other channels (abstraction and exchange). Since the C-C breakage channel has still not been studied in the experiment, we decided to carry out our dynamics calculations with the SRP-MSINDO Hamiltonian presented here, even if the dynamics of the C-C channel might not be as accurately captured as the rest of the channels.

In this section, we have shown a way to obtain a potentially-accurate electronic-structure method for H+alkane reactions by reoptimizing the parameters of a semiempirical Hamiltonian based on an extensive grid of *ab initio* data. The performance of the SRP Hamiltonian is superior to that of some mainstream first-principles methods for the lowest-energy reaction channel, even though the Hamiltonian is orders of magnitude faster. Next, we show the results of a direct-dynamics study of the $H+CH_4$ and $H+C_2H_6$ reaction using the SRP-MSINDO Hamiltonian derived in this work, which can be used to verify the global accuracy of this electronic-structure method.

3.4 Direct-Dynamics Study

We now present the results of a quasiclassical-trajectory (QCT) study of the H+methane and H+ethane reactions at high energies carried out with the SRP-MSINDO Hamiltonian described before. These results are compared with experiments and other calculations to calibrate the accuracy of the SRP-MSINDO semiempirical Hamiltonian in regions of the potential-energy surface removed from the minimum-energy reaction path. Batches of 50,000 trajectories per collision energy for $H+C_2H_6$ and 100,000 trajectories for $H+CH_4$ have been used in the calculations of the excitation function. 100,000 trajectories have been integrated at initial conditions where experimental data on product energy distributions are available also in $H+C_2H_6$. The trajectories have been started at an initial distance of 15.0 a.u. from the hydrogen radical to the center of mass of the reagent molecule and have been stopped after collision when distance between the centers of mass of the recoiling species reaches ~15 a.u. The maximum sampling impact parameters were 4.25 (4.50) a.u. for the $H+CD_4(CH_4)$ calculations, and 7.0 a.u. for the H+ethane calculations.

The initial coordinates and momenta of the reagent molecules have been selected using the VENUS program.[47] As it has been shown before,[20] the MSINDO Hamiltonian overestimates experimental vibrational frequencies by approximately 20%. Therefore, in selecting the initial conditions of the molecules involved in the calculations, we have assigned initial coordinates and momenta so that the molecules have vibrational energy corresponding to 80% of the SRP-MSINDO zero-point energy. This vibrational energy is within 1 kcal mol^{-1} of the experimental zero-point energy of the molecules examined in this work.

To further examine the performance of the SRP Hamiltonian developed in this work, we have also integrated trajectories with the ZBB3 potential-energy surface (PES) of Bowman and co-workers.[36] The details of these trajectory calculation are similar to those described above for the SRP-MSINDO Hamiltonian, including the fact that we have calculated 100,000 trajectories for each set of initial conditions. We note this is a factor for 5 more trajectories per set of initial conditions than calculated in earlier studies with the ZBB3 PES. [36]

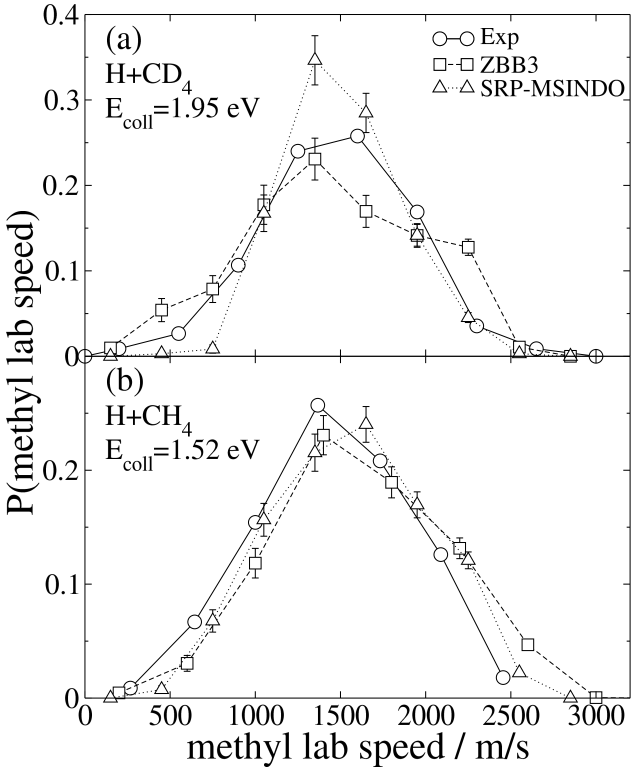

Figure 3.3: Measured and calculated laboratory speed distributions of the methyl fragment generated in the $H+CD_4 \rightarrow CD_3+HD$ reaction at 1.95 eV (a), and the $H+CH_4 \rightarrow CH_3+H_2$ reaction at 1.52 eV (b). The distributions are normalized to the height. The experimental data have been taken from Ref. [7] (a) and Ref. [8](b).

3.4.1 Product-energy distributions

Two sets of experiments have provided information about the amount of energy channeled to the various products degrees of freedom in the H+methane abstraction reaction. First, Camden et al. reported the laboratory speed distributions of the methyl product formed in the $H+CH_4$ and $H+CD_4$ hydrogen-abstraction reactions at high collision energies.[7, 8] Second, Germann et al. measured the rotational populations of the HD product arising from the $H+CD_4 \rightarrow HD+CD_3$ reaction at E_{coll}=1.5 eV.[5] Figure 3.3 shows the measured methyl laboratory speed distributions in the $H+CD_4 \rightarrow HD+CD_3$ reaction at E_{coll}=1.95 eV (Fig. 3.3(a)), and in the $H+CH_4 \rightarrow H_2+CH_3$ reaction at 1.52 eV (Fig. 3.3(b)) in comparison with the results from QCT calculations with the ZBB3 PES and SRP-MSINDO Hamiltonian. Both calculations agree well with each other and reproduce the measurements, lending confidence to the accuracy of the potential-energy surfaces. We note that the agreement with experiment of the SRP-MSINDO results shows a marked improvement over calculations performed with the original MSINDO Hamiltonian (not shown), which show distributions shifted by 750 m/s to higher speeds.

The comparison between the ZBB3 PES and SRP-MSINDO results in Figure 3.3 suggests that both surfaces provide similar energy partitioning into products' translation. Further analysis of the calculations indicates that these two surfaces actually predict very similar overall energy disposal in products. For the $H+CD_4 \rightarrow HD+CD_3$ reaction at E_{coll}=1.95 eV, the amounts of energy going into product translation, HD vibration, and HD rotation are 1.10 eV (1.14 eV), 0.65 eV (0.51 eV), and 0.50 eV (0.46 eV), respectively, for the ZBB3 PES (SRP-MSINDO). For the unsubstituted reaction at E_{coll}=1.52 eV, the energy released to translation, H_2 vibration, and H_2 rotation is 1.24 (1.19 eV), 0.41 eV (0.32 eV), 0.27 eV (0.30 eV), respectively. Although small, the most notable difference between both calculations is in the amount of energy going into vibration of the diatomic product, with SRP-MSINDO predicting slightly less H_2 or HD vibrational excitation than the ZBB3 PES.

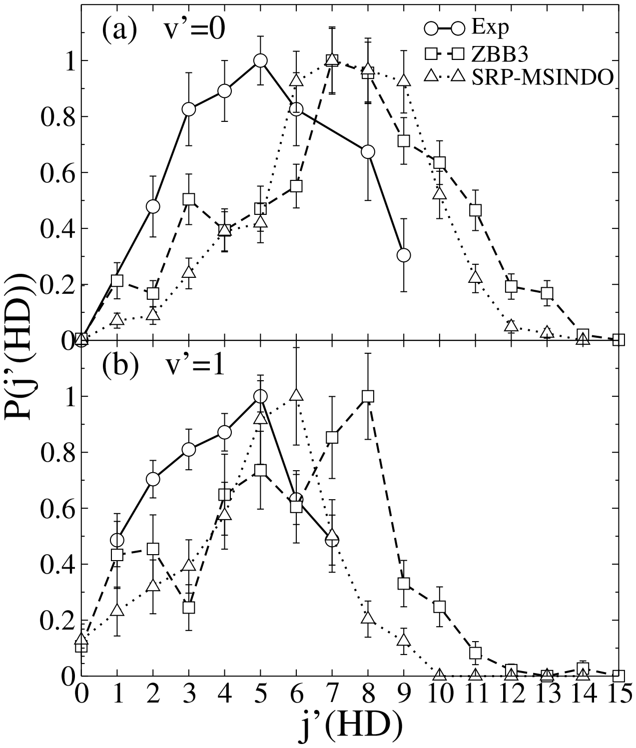

Figure 3.4: Measured and calculated HD rotational distributions generated in the $H+CD_4 \rightarrow HD(v',J')+CD_3$ reaction at E_{coll}=1.5 eV. The distributions are normalized to the height. The experimental data have been taken from Ref. [5].

The similar energy partitioning into diatomic product rotation provided by the ZBB3 PES and SRP-MSINDO Hamiltonian can be evidenced in Figure 3.4. The figure shows HD rotational distributions calculated at E_{coll}=1.5 eV in comparison with the experiments of Germann et al.[5] The calculations agree well with each other, but predict HD rotational distributions that are slightly more excited than the measured ones. For

HD(ν'=0) (Figure 3.4(a)), the calculated rotational distributions are shifted 2-3 quanta to higher J' states. This separation between theory and experiment has been discussed in detail before as possibly emerging from the details of the experiment.[23, 36] In effect, H atoms in the experiment were generated by HI photolysis at 266 nm, which generates two groups of H atoms. The collision energy of the fast group is 1.53 eV, and that of the slow group is 0.65 eV. Reactivity coming from the slow component would result in a slight decrease in average rotational excitation, shifting the measured distribution to smaller J' values. On the other hand, the contribution of the slow H atoms does not affect the rotational distribution in the HD(ν'=1) state because this state is not populated at low collision energies. Therefore, theory-experiment comparison of rotational distributions in the HD(ν'=1) vibrational state are less biased by possible experimental complications than in HD(ν'=0). Figure 3.4(b) shows the HD(ν'=1) rotational distributions. The agreement between the SRP-MSINDO results and experiment in this state is much better than in HD(ν'=0), suggesting accuracy in the potential-energy surface. The ZBB3 PES shows a slightly larger excitation than measured.

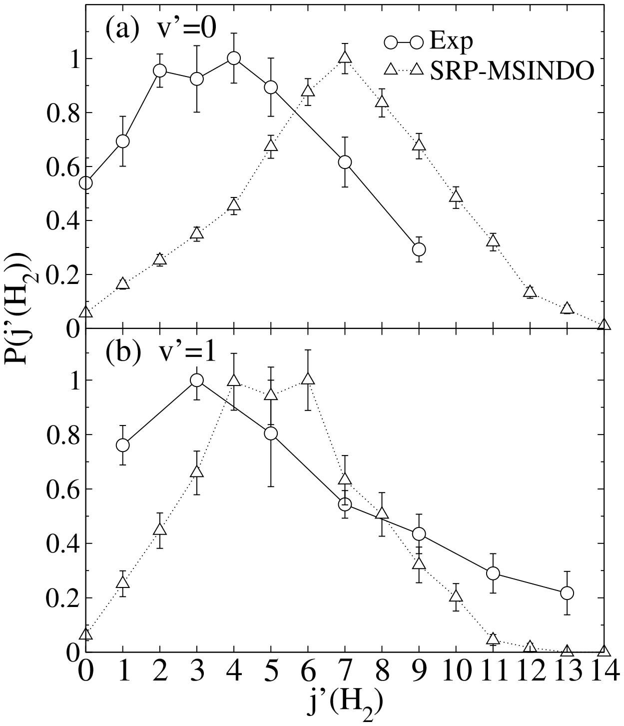

Figure 3.5: Measured and calculated HD rotational distributions generated in the $H+C_2D_6 \rightarrow H_2(\nu',J')+C_2H_5$ reaction at $E_{coll}=1.56$ eV. The distributions are normalized to the height. The experimental data have been taken from Ref. [6].

In a separate experiment, Germann et al. reported the rotational distributions of the H_2 product generated in the $H+C_2H_6 \rightarrow H_2+C_2H_5$ reaction at $E_{coll}=1.56$ eV.[6] Figure 3.5 presents a comparison between these experimental results and the SRP-MSINDO calculations. As with the $H+CD_4$ results, the calculated rotational distributions in the ground vibrational state (Fig. 3.5(a)) are shifted by approximately 3 J' states from the experiments. As in the case of $H+CD_4$, part of this disagreement is due to the slow component of the H atoms produced in HI photodissociation at 266 nm. The contribution of the slow component (E_{coll}=0.68 eV) might be even more important in H+ethane than in H+methane because the abstraction barrier in the larger system is smaller, and therefore the cross section at low energies is expected to be more significant. Fig. 3.5(b) exhibits the H_2(ν'=1) rotational distributions. The contribution of the slow H radicals should not play a role in the H_2(ν'=1) state, so theory-experiment comparison might be, in principle, more valid. Fig. 3.5(b) shows that the agreement between theory and experiment is indeed better than in H_2(ν'=0). However, a difference between SRP-MSINDO results and experiment that is not present in the H+CD_4 reaction but is appreciated here is the detection of a tail of high rotational excitation in the experiments. Germann et al. indicated that a difficulty of the H+C_2H_6 measurements is the contribution of the H_2 molecules coming from the reaction of the unphotodissociated HI and the H radicals. This reaction generates highly rovibrationally excited H_2 molecules, which are suspected to populate high J' states of the H_2(ν'=1) distribution.[6] Note that this problem was not present in the H+CD_4 distributions because the H_2 signal coming from the H+HI reaction does not overlap with the HD signal of the H+CD_4 reaction.

The experiments of Germann et al. on the H+CD_4[5] and H+C_2H_6[6] reactions at ~1.5 eV collision energy also provided some limited information about the vibrational distributions of the HD and H_2 products, respectively. In neither reaction were diatomic products in the ν'=2 state observed above the signal-to-noise ratio. Our calculations in the H+CD_4 reaction at 1.5 eV collision energy with both the ZBB3 PES and SRP-MSINDO agree with experiment. The ZBB3 PES (SRP-MSINDO Hamiltonian) predicts that 93% (99%) of the HD products are born in the ν'=0 and 1 states. The SRP-MSINDO Hamiltonian also agrees with the experimental information in the H+C_2H_6 reaction, with only 1% of H_2 products predicted to arise in ν'=2.

3.4.2 Excitation functions

The experiments by Camden et al. determined the relative excitation function of the $H+CD_4 \rightarrow HD+CD_3$ reaction in the 1.48-2.36 eV collision-energy range.[7] These experiments show a slight decrease in the integral cross section with increasing collision energy. Figure 3.6 displays the experimental relative cross sections in comparison with the QCT values obtained with the ZBB3 PES and SRP-MSINDO Hamiltonian. Both calculations describe the decrease in cross section with collision energy detected in the experiments, but the predictions of both potential-energy surfaces differ slightly. While the ZBB3 PES excitation function shows a more precipitous decrease in the cross section than experiment, the SRP-MSINDO cross-section decrease is not as sharp as seen in the experiment.

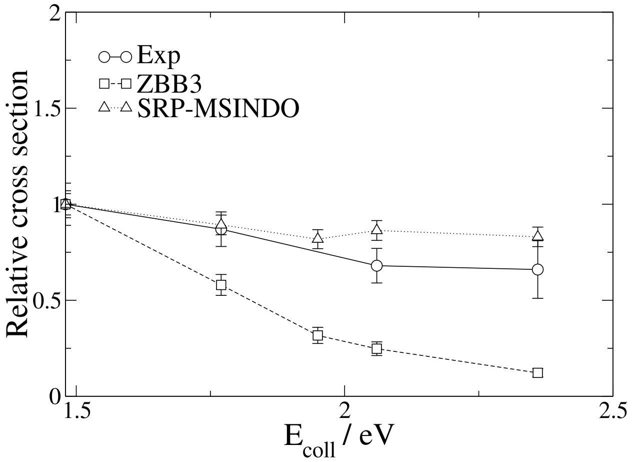

Figure 3.6: Measured and calculated relative excitation function for the H+CD$_4$ → HD+CD$_3$ reaction. The cross sections are normalized to the cross section value at 1.5 eV collision energy. The experimental data have been taken from Ref. [7].

While the excitation function presented in Figure 3.6 is based on *relative* cross sections, the early experiments of Germann et al.[5] reported the *absolute* cross section at 1.53 eV collision energy to be 0.50±0.11 a.u.. The results provided by the ZBB3 PES and SRP-MSINDO at E_{coll}=1.48 eV also predict very small absolute cross sections (0.30±0.02 and 0.36±0.03 a.u., respectively). The calculated cross sections are close to the experimental measurement, but just barely outside the lower limit of the experimental uncertainty. Notwithstanding, it should be noted that the values of the cross sections are very small, so the absolute difference in reactivity is minor. It should also be noted that both calculated cross sections are also close to one another. A point of significance is that the very small cross sections of this system pose an operational challenge in the calculation of dynamics properties with classical trajectories. For instance, typical reactive probabilities with the SRP MSINDO Hamiltonian are 5-6 reactive trajectories per each 1,000 calculated trajectories in the collision-energy range of Figure 3.6. This small reaction probability implies that an unusually large number of total trajectories need to be calculated, particularly if one wants to obtain state-to-state information with statistical significance.

Regarding the H+ethane reaction, Oldershaw and Gould measured the excitation function of the H+C$_2$D$_6$ → HD+C$_2$D$_5$ reaction in the 0.7-1.5 eV collision-energy range.[4] The measured cross sections show a monotonic increase in that range, and have been plotted in Figure 3.7 in comparison with the QCT values calculated with the SRP-MSINDO Hamiltonian. The calculated results agree well with the measurements, and this is particularly remarkable here because the experimental cross sections are not relative, but absolute. In the experimental work of Oldershaw and Gould, estimates of a simple line-of-centers model also captured the measured cross sections and predicted a decay in the cross section at energies above 1.5 eV. Figure 3.7 shows that the SRP-MSINDO calculations also exhibit a decrease in the cross section at high collision energies, in accord with the line-of-centers model. This behavior also matches what described earlier for the $H+CD_4 \rightarrow HD+CD_3$ reaction.

A second source of experimental absolute cross sections for the H+ethane reaction is the work of Germann et al.[6] These experiments were performed for the isotopically unsubstituted $H+C_2H_6 \rightarrow H_2+C_2H_5$ reaction, and determined that the absolute cross section at E_{coll}=1.56 eV was 5.4±1.8 a.u. The SRP-MSINDO cross section at that collision energy is 3.34±0.06 a.u., which, as in the $H+CD_4 \rightarrow HD+CD_3$ reaction, is just barely outside the lower limit of the experimental uncertainty.

In summary, the agreement of the trajectory results calculated with the SRP-MSINDO Hamiltonian and experiment is rather satisfactory in most of the dynamics properties explored. These include alkyl product speed distributions, rotational and vibrational state distributions of the diatomic product, and relative and absolute cross sections. The level of agreement between theory and experiment implies that the SRP-MSINDO Hamiltonian possesses accuracy for the H+methane and H+ethane abstraction reactions in regions far away from the minimum-energy reaction path. The comparison with experiment for the H+ethane reaction is even more significant because this is the first time that full-dimensional calculations based on a potential-energy surface derived from *ab initio* calculations have performed

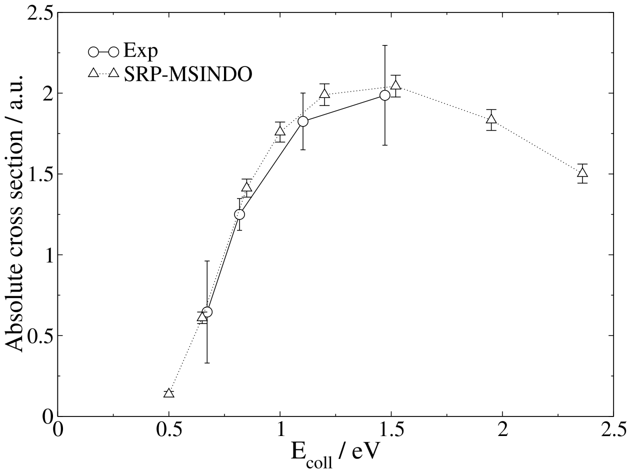

Figure 3.7: Measured and calculated excitation function for the $H+C_2D_6 \rightarrow HD+C_2D_5$ reaction. The experimental data have been taken from Ref. [4].

to reproduce the experiments. Finally, the performance of the SRP-MSINDO Hamiltonian for the $H+CH_4$ reaction is very similar to that of the state-of-the-art ZBB3 PES, even though there are slight differences in selected properties.

3.5 Concluding Remarks

We have studied the $H+CH_4$ and $H+C_2H_6$ reactions using electronic-structure theory and quasiclassical-trajectory calculations evolved with a specific-reaction-parameters semiempirical Hamiltonian.

The energetic profiles of the reactions have been calculated using high-level *ab initio* theory. These electronic-structure calculations focus not only on the low-energy reaction pathway—H abstraction to produce H_2+alkyl—but also on the H-atom exchange channel, and the C-C breakage channel in $H+C_2H_6$. We learn that the dependence of the reactions' energetics on the basis set is minor for all methods investigated in this work, and that a CCSD(T)//MP2 dual-level approximation is accurate in H+alkane systems studied. The reaction energy and barrier of $H+C_2H_6$ abstraction reaction are below the ones in $H+CH_4$, and the transition state is more reagents-like. These trends agree with the qualitative predictions of the Hammond's postulate. Regarding the high-energy channels, the barrier for H-atom exchange in $H+C_2H_6$ is slightly larger than in $H+CH_4$, likely due to steric impediments in the former reaction. We show that the $H+C_2H_6 \rightarrow CH_3+CH_4$ reaction has a barrier comparable to that of H-atom exchange. Both the H-exchange and C-C breakage channels show transition-state structures typical of SH_2 reactions. All of these high-energy reaction pathways are expected to be accessible in experiments that use heavy hydrogen halides as photoprecursors of H atoms.

Using a substantial grid of CCSD(T)/aug-cc-pVDZ single-point energies covering various regions of the $H+CH_4$ and $H+C_2H_6$ potential-energy surfaces, we have reoptimized the parameters of the MSINDO semiempirical Hamiltonian to obtain an SRP-MSINDO Hamiltonian suitable for H+alkane reactions. The reaction-energetics values of the abstraction channel provided by the SRP-MSINDO Hamiltonian are clearly superior to those of the standard MP2 and B3LYP methods with large basis sets, even though SRP-MSINDO is orders of magnitude faster than the first-principle methods.

Using the SRP-MSINDO Hamiltonian, we have conducted quasiclassical-trajectory studies of the $H+CH_4 \rightarrow H_2+CH_3$ and $H+C_2H_6 \rightarrow H_2+C_2H_5$ reactions and isotopomers at high collision energies. Various dynamics properties stemming from the calculations have been compared with experimental results on the hydrogen-abstraction channel and with the predictions of a very recent and state-of-the-art ZBB3 analytic potential-energy surface for H+CH_4. Calculated alkyl speed distributions are in very good agreement with experiment and the results of the ZBB3 PES. Calculated HD and H_2 rotational distributions are not in as great agreement with experiment, but some complications in the measurements impair a truly quantitative comparison. Regarding diatomic product vibration, the SRP-MSINDO calculations estimate less than 1% of the HD and H_2 products are born in ν'=2 in the H+CD_4 reaction at 1.5 eV and the H+C_2H_6 reaction at 1.56 eV, respectively. These results are in agreement with experiments, which did not detect ν'=2 products. The SRP-MSINDO also reproduces experimental measurements of cross sections in both the H+methane and H+ethane hydrogen-abstraction reactions.

The overall good performance of the SRP-MSINDO Hamiltonian for the two H+alkane reactions investigated in this work indicates the accuracy of this computationally-inexpensive electronic-structure method. The detailed comparison with the available experiments presented in this work is a particularly sensitive test of the global accuracy of the method because the calculations involve regions of the potential-energy surface well removed from the minimum-energy reaction path. Overall, the performance of the SRP-MSINDO method is very similar to that of the state-of-the-art ZBB3 PES for the H+CH_4 reaction. The advantage of the SRP-MSINDO method is that it was derived using approximately two orders of magnitude less *ab initio* points than the ZBB3 PES, and is suitable for the H+C_2H_6 reaction. However, the SRP-MSINDO Hamiltonian is not defect-free. For instance, the abstraction barriers exhibit errors of ~2 kcal mol^{-1}. Even though the magnitude of this inaccuracy is much smaller than that of MP2 or B3LYP methods, and does not appear to affect the dynamics at high energy, it will provide sizeable errors in calculations for which chemical accuracy is needed, such as rate-constant calculations. In addition, the C-C breakage barrier in the H+C_2H_6 is notably smaller than predicted by *ab initio* methods.

We will use the SRP-Hamiltonian developed in this chapter as the basis for a more full investigation of H+alkane reactions in Chapter 4. Additionally, while the

Hamiltonian developed here is not suitable for the study of other classes of reactions we will implement a similar methodology to study the reactions of fluorine atoms with alkanes and ultimately alkanethiolate self-assembled monolayers, in Chapters 5 and 6, respectively.

References

1. S. L. Mielke, K. A. Peterson, D. W. Schwenke, B. C. Garrett, D. G. Truhlar, J. V. Michael, M. C. Su and J. W. Sutherland, Physical Review Letters 91, 063201-063204 (2003).
2. D. H. Zhang, M. A. Collins and S. Y. Lee, Science 290, 961-963 (2000).
3. T. Wu, H.-J. Werner and U. Manthe, Science 306, 2227-2229 (2004).
4. G. A. Oldershaw and P. L. Gould, J. Chem. Soc. Faraday Trans. 2 81, 1507-1516 (1985).
5. G. J. Germann, Y.-D. Huh and J. J. Valentini, J. Chem. Phys. 96, 1957-1966 (1992).
6. G. J. Germann, Y.-D. Huh and J. J. Valentini, J. Chem. Phys. 96, 5746-5757 (1992).
7. J. P. Camden, W. Hu, H. A. Bechtel, D. J. A. Brown, M. R. Martin, R. N. Zare, G. Lendvay, D. Troya and G. C. Schatz, Journal of Physical Chemistry A 110, 677-686 (2006).
8. J. P. Camden, H. A. Bechtel, D. J. A. Brown and R. N. Zare, J. Chem. Phys. 123, 134301-134301/134309 (2005).
9. K. Bolton and W. L. Hase, in *Modern Methods for Multidimensional Dynamics Computations in Chemistry*, edited by D. L. Thompson (World Scientific, Singapore, 1998), pp. 143-189.
10. D. J. Garton, T. K. Minton, D. Troya, R. Pascual and G. C. Schatz, Journal of Physical Chemistry A 107 (23), 4583-4587 (2003).
11. D. Troya, R. Z. Pascual and G. C. Schatz, Journal of Physical Chemistry A 107 (49), 10497-10506 (2003).
12. D. Troya, R. Z. Pascual, D. J. Garton, T. K. Minton and G. C. Schatz, Journal of Physical Chemistry A 107 (37), 7161-7169 (2003).
13. D. Troya, G. C. Schatz, D. J. Garton, A. L. Brunsvold and T. K. Minton, Journal of Chemical Physics 120 (2), 731-739 (2004).
14. A. L. Brunsvold, D. J. Garton, T. K. Minton, D. Troya and G. C. Schatz, Journal of Chemical Physics 121 (23), 11702-11714 (2004).
15. D. Troya and G. C. Schatz, Journal of Chemical Physics 120 (16), 7696-7707 (2004).
16. A. Gonzalez-Lafont, T. N. Truong and D. G. Truhlar, Journal of Physical Chemistry 95 (12), 4618-4627 (1991).
17. G. Li, S. B. M. Bosio and W. L. Hase, Journal of Molecular Structure-THEOCHEM 556, 43-57 (2000).
18. T. Yan, C. Doubleday and W. L. Hase, Journal of Physical Chemistry A 108 (45), 9863-9875 (2004).
19. D. Troya and E. Garcia-Molina, Journal of Physical Chemistry A 109 (13), 3015-3023 (2005).
20. D. Troya and P. J. E. Weiss, Journal of Chemical Physics 124 (7), 074313/074311-074313/074312 (2006).
21. D. Troya, Journal of Physical Chemistry A 109 (26), 5814-5824 (2005).
22. D. Troya, Journal of Chemical Physics 123 (21), 214305/214301-214305/214311 (2006).

23. W. Hu, G. Lendvay, D. Troya, G. C. Schatz, J. P. Camden, H. A. Bechtel, D. J. A. Brown, M. R. Martin and R. N. Zare, J. Phys. Chem. A 110, 3017-3027 (2006).
24. A. Teslja and J. J. Valentini, J. Chem. Phys. 125, 132304 (2006).
25. J. J. Valentini, J. Phys. Chem. A 106, 5745-5759 (2002).
26. J. P. Camden, H. A. Bechtel, D. J. A. Brown and R. N. Zare, J. Chem. Phys. 124, 034311-034311/034317 (2006).
27. A. Chattopadhyay, S. Tasaki, R. Bersohn and M. Kawasaki, J. Chem. Phys. 95, 1033-1036 (1991).
28. T. V. Albu, J. Espinosa-Garcia and D. G. Truhlar, Chem. Rev. 107, 5101-5132 (2007).
29. J. Espinosa-Garcia, The Journal of Chemical Physics 116 (24), 10664-10673 (2002).
30. C. Rangel, J. Sanson, J. C. Corchado, J. Espinosa-Garcia and G. Nyman, J. Phys. Chem. A 110, 10715-10719 (2006).
31. C. Rangel, J. C. Garcia-Bernaldez and J. Espinosa-Garcia, Chem. Phys. Lett. 422, 581-585 (2006).
32. C. Rangel, J. C. Corchado and J. Espinosa-Garcia, J. Phys. Chem. A 110, 10375-10383 (2006).
33. J. Espinosa-Garcia, J. Phys. Chem. A 111, 5792-5799 (2007).
34. J. P. Camden, H. A. Bechtel, D. J. A. Brown, M. R. Martin, R. N. Zare, W. Hu, G. Lendvay, D. Troya and G. C. Schatz, Journal of American Chemical Society 127, 11898-11899 (2005).
35. X. Zhang, B. J. Braams and J. M. Bowman, J. Chem. Phys. 124, 021104-021101/021104 (2006).
36. Z. Xie, J. M. Bowman and X. Zhang, J. Chem. Phys. 125, 133120-133121/133128 (2006).
37. Z. Xie and J. M. Bowman, Chem. Phys. Lett. 429, 355-359 (2006).
38. X. Zhang, B. J. Braams and J. M. Bowman, J. Chem. Phys. 124, 021104-021101/021104 (2005).
39. B. Kerkeni and D. C. Clary, J. Chem. Phys. 123, 064305 (2005).
40. B. Kerkeni and D. C. Clary, Phys. Chem. Chem. Phys. 8, 917-925 (2006).
41. A. Chakraborty, Y. Zhao, H. Lin and D. G. Truhlar, J. Chem. Phys. 124, 044315 (2006).
42. M. J. Frisch, G. W. Trucks, H. B. Schlegel, G. E. Scuseria, M. A. Robb, J. R. Cheeseman, J. Montgomery, J. A. , T. Vreven, K. N. Kudin, J. C. Burant, J. M. Millam, S. S. Iyengar, J. Tomasi, V. Barone, B. Mennucci, M. Cossi, G. Scalmani, N. Rega, G. A. Petersson, H. Nakatsuji, M. Hada, M. Ehara, K. Toyota, R. Fukuda, J. Hasegawa, M. Ishida, T. Nakajima, Y. Honda, O. Kitao, H. Nakai, M. Klene, X. Li, J. E. Knox, H. P. Hratchian, J. B. Cross, V. Bakken, C. Adamo, J. Jaramillo, R. Gomperts, R. E. Stratmann, O. Yazyev, A. J. Austin, R. Cammi, C. Pomelli, J. W. Ochterski, P. Y. Ayala, K. Morokuma, G. A. Voth, P. Salvador, J. J. Dannenberg, V. G. Zakrzewski, S. Dapprich, A. D. Daniels, M. C. Strain, O. Farkas, D. K. Malick, A. D. Rabuck, K. Raghavachari, J. B. Foresman, J. V. Ortiz, Q. Cui, A. G. Baboul, S. Clifford, J. Cioslowski, B. B. Stefanov, G. Liu, A. Liashenko, P. Piskorz, I. Komaromi, R. L. Martin, D. J. Fox, T. Keith, M. A. Al-Laham, C. Y. Peng, A. Nanayakkara, M. Challacombe, P. M. W. Gill, B. Johnson,

W. Chen, M. W. Wong, C. Gonzalez and J. A. Pople, (Gaussian Inc., Wallingford, CT, 2004).

43. J. P. Layfield, M. D. Owens and D. Troya, The Journal of Chemical Physics 128 (19), 194302-194312 (2008).
44. D. Troya, J. Phys. Chem. A 111, 10745-10753 (2007).
45. A. S. Hammond, J. Am. Chem. Soc. 77, 334-338 (1955).
46. B. Ahlswede and K. Jug, J. Comput. Chem. 20 (6), 563-571 (1999).
47. W. L. Hase, R. J. Duchovic, X. Hu and e. al., QCPE 16, 671 (1996).

Chapter 4
Theoretical study of the dynamics of H+alkane reactions

Reprinted from Chemical Physics Letters, **467**, J. P. Layfield and D. Troya,, Theoretical study of the dynamics of H + alkane reactions, 243-248,Copyright (2008), with permission from Elsevier.

4.1 Introduction

There is a growing interest in the field of reaction dynamics to study polyatomic reactions.[1] While experimental and theoretical investigations of low-dimensionality (e.g. triatomic) reactions continue to provide new reaction-dynamics paradigms,[2] recent efforts are attempting to study reactions of increasing dimensionality and complexity. The reactions in the H+alkane family are an interesting class of reactions helping to bridge the gap between triatomic and polyatomic reactions as they are among the simplest radical+polyatomic-molecule systems.[3] The smallest reaction in the family, $H+CH_4$, actually represents the simplest reaction that can occur at a tetrahedral center and has been studied extensively by experimental [3-11] and theoretical[9, 10, 12-22] efforts. In addition, the H+alkane systems also carry the physical importance of being major propagation carriers for combustion reactions.[23]

Early studies of the $H+CD_4$ reaction initially proposed that a "rebound" mechanism in which the H_2 product scatters backwards with respect to the atom's initial direction dominated the reaction.[24] This mechanism is similar to the one described for the simpler $H+D_2$ reaction.[25] However, recent joint experimental and theoretical efforts have shown that as collision energy increases, a stripping type mechanism that occurs at large impact parameters competes with the rebound mechanism.[3]

In contrast to the wealth of information available for the $H+CH_4$ reaction, there has been significantly less theoretical and experimental study of the next reaction of the H+alkane family, $H+C_2H_6$. Valentini and co-workers measured absolute cross sections and H_2 rotational state distributions for the $H+C_2H_6$ reaction at 1.5eV collision energy,(26) and Gould and Oldershaw obtained an excitation function for the $H+C_2D_6$ reaction.[26] In what regards to theory, no calculations on the $H+C_2H_6$ reaction dynamics that establish direct comparison with those experimental measurements have been conducted until very recently due to the absence of a reliable global potential-energy surface.

By propagating classical trajectories on the fly with an inexpensive semiempirical Hamiltonian, our group was recently able to perform a detailed study of both the $H+CH_4$ and $H+C_2H_6$ reactions.[27] A salient feature of that work is that the semiempirical Hamiltonian was optimized specifically for H+alkane reactions so that it describes the potential-energy surface with accuracy comparable to high-level *ab initio* predictions. Indeed, an extensive calibration of the semiempirical Hamiltonian indicated that its accuracy was superior to standard electronic-structure methods, such as MP2 and B3LYP, when compared with CCSD(T) predictions. However, the Hamiltonian is orders of magnitude faster than any of these first-principles methods and enables timely direct-dynamics studies. The Hamiltonian showed considerable accuracy when tested by the comparison of results obtained from quasiclassical trajectories integrated with the semiempirical Hamiltonian with experiment for both the $H+CH_4$ and $H+C_2H_6$ reactions. The calculations reproduce the experiments in both $H+CH_4 \rightarrow H_2+CH_3$ and $H+C_2H_6 \rightarrow H_2+C_2H_5$ reactions, including excitation functions and product-energy distributions. The results for the $H+CH_4$ reaction were also in good agreement with those obtained using the highly accurate ZBB3 PES of Bowman and co-workers.[28]

The availability of a computationally inexpensive but accurate electronic-structure method for H+alkane reactions provides an excellent opportunity to make progress in our understanding of the dynamics of polyatomic chemical reactions. Therefore, in this work we perform a comparative study of the dynamics of the $H+CH_4$, $H+C_2H_6$, and $H+C_3H_8$ reactions with the goal of learning the effect of the length of the alkane molecule on the dynamics of the hydrogen-abstraction reactions by H atoms.

This type of comparative study has been done before on the cousin Cl+alkane reactions using experimental methods. The Zare group has studied the dynamics of Cl+methane[29, 30] and Cl+ethane reactions,[31] and the Dagdigian group investigated the dynamics of the Cl+propane[32] and isobutane[33] reactions. A difference between those studies and the one presented here is that the collision energies in this study are about one order of magnitude larger than in the Cl+alkane work, so the usefulness of a comparison between both bodies of work is limited.

4.2 Theoretical Details

We have studied the dynamics of the H+CH_4, C_2H_6, and C_3H_8 using direct quasiclassical trajectories. The forces needed to propagate the trajectories were calculated on the fly using a specific-reaction-parameter version of the semiempirical MSINDO Hamiltonian (SRP-MSINDO).[34] The SRP-MSINDO Hamiltonian was obtained based on high-quality CCSD(T) *ab initio* energies of the global potential-energy surface, and exhibits better accuracy than MP2 and B3LYP calculations with large basis sets for the title reactions. Table 4.1 shows a comparison between *ab initio* and semiempirical reaction energies and barriers for the H+RH→R+H_2 (R=CH_3, C_2H_5, C_3H_7) reactions. The data show that the improved MSINDO Hamiltonian reproduces the high-level

Table 4.1: Calculated reaction energies and barriers (kcal mol^{-1}) for H+alkane → H_2+alkyl reactions.[a]

	Barrier			Reaction energy		
	CCSD(T)[b]	MP2[c]	SRP-MSINDO[d]	CCSD(T)[b]	MP2[c]	SRP-MSINDO[d]
H+CH_4	13.47 (14.77)	18.54 (19.84)	15.80 (16.82)	0.59 (3.51)	4.98 (7.89)	-1.08 (2.37)
H+C_2H_6	10.36 (11.95)	15.37 (16.97)	11.90 (13.53)	-2.51 (0.60)	2.21 (5.32)	-3.89 (-0.25)
H+C_3H_8 (1')[e]	10.28 (11.82)	15.37 (16.91)	12.03 (13.48)	-2.12 (0.86)	2.72 (5.69)	-4.89 (-1.69)
H+C_3H_8 (2')[f]	7.83 (9.51)	12.70 (14.38)	10.27 (12.03)	-4.55 (-1.47)	0.47 (3.54)	-5.46 (-2.32)

[a] Values between parentheses correspond to classical (i.e., not zero-point corrected) reaction energies and barriers.

[b] CCSD(T) calculations with the aug-cc-pVDZ basis set employing geometries and frequencies calculated at the MP2/aug-cc-pVDZ level

[c] MP2 calculations with the aug-cc-pVDZ basis set.

[d] Specific reaction parameters MSINDO Hamiltonian

[e] Energies corresponding to hydrogen abstraction at the out-of-plane primary site of C_3H_8

[f] Energies corresponding to hydrogen abstraction at the secondary site of C_3H_8

CCSD(T)/aug-cc-pVDZ results with an accuracy clearly superior to MP2/aug-cc-pVDZ. On average, the SRP-MSINDO method overestimates the CCSD(T)/aug-cc-pVDZ barriers by ~2 kcal mol^{-1}. In contrast, the MP2/aug-cc-pVDZ barriers are on average ~5 kcal mol^{-1} larger than CCSD(T)/aug-cc-pVDZ data. The same behavior is visible for the reaction energies, but the average deviation of MSINDO from CCSD(T) decreases to ~1 kcal mol^{-1}, and the MP2 one to ~4.5 kcal mol^{-1}. It should be noted that the accuracy of the SRP-MSINDO Hamiltonian does not only apply to the properties of the minimum-energy reaction path highlighted in Table 4.1, but also to high-energy regions of the potential-energy surface. For instance, the root-mean-square deviation between CCSD(T)/aug-cc-pVDZ and SRP-MSINDO calculations of the H-H'-C transition-state bending angle in the H+CH_4 reaction is 2.4 kcal mol^{-1} in the 180-90^{o} range, for which the electronic energy increases by about 30 kcal mol^{-1}. In addition, other high-energy regions of the potential-energy surface, such as those leading to hydrogen-atom exchange and C-C breakage reactions, are also well captured, as described in detail in our earlier work with this semiempirical Hamiltonian.[27]

Since the goal of this paper is to establish a comparison of the dynamics first few members of the H+alkane abstraction-reaction family, it is important to verify if the changes in the reaction energetics along the family are captured by the SRP-MSINDO Hamiltonian. CCSD(T) results indicate that the reaction energy and barrier decrease notably when going from methane to ethane, and the SRP-MSINDO method reproduces this result (see Table 4.1). In addition, the H+propane abstraction reaction has two distinct channels: hydrogen abstraction at the primary site to produce the H_2 + n-C_3H_7 species (1' channel), and abstraction at secondary sites yielding H_2 + i-C_3H_7 (2' channel). CCSD(T) data show that hydrogen abstraction at the secondary site has a smaller barrier and is more exothermic than at the primary sites, and the SRP-MSINDO Hamiltonian also reproduces this result.

These comparisons between SRP-MSINDO and CCSD(T)/aug-cc-pVDZ reaction energies and barriers demonstrate that the semiempirical method captures with accuracy the energetics of H+alkane reactions. Therefore, we have used the SRP-MSINDO Hamiltonian to propagate classical trajectories for the H+methane, ethane, and propane reactions with confidence that the major trends in the dynamics will be satisfactorily borne out by this low-cost electronic-structure method.

To investigate the dynamics of the title reactions, we have calculated batches of 50,000 trajectories at collision energies from the threshold to ~2.5 eV for the H+CH_4, H+C_2H_6, and H+C_3H_8 systems. The trajectories were started at an initial distance of 15 a.u. from the hydrogen atom to the center of mass of the target molecule and were stopped when the centers of mass of the recoiling species were ~15 a.u. apart after collision. The maximum sampling impact parameters were 4.5 a.u. for H+CH_4, 7.0 a.u. for H+C_2H_6, and 10.0 a.u. for H+C_3H_8. The initial conditions for the hydrocarbon molecules were selected using the VENUS program [35] and consider zero-point vibrational motion and no rotation. The assignment of zero-point energy is as follows. From the fixed energies of the ground vibrational states of each of the normal modes of the molecules, the amplitudes of the normal modes are calculated. With these amplitudes, normal mode-coordinates and velocities are calculated with random phase, and transformed into Cartesian coordinates and momenta. The spurious angular momentum that emerges from this procedure is removed by scaling the molecule coordinates and momenta so that the total internal energy of the molecule corresponds to the zero-point energy.

4.3 Results

To establish a thorough comparison between the dynamics of three simplest H-abstraction reactions of the H+alkane family, we present calculated excitation functions, opacity functions, angular distributions, and partitioning of available energy into the various products' degrees of freedom. Particular attention is given to the comparison between the dynamics of abstraction at primary and secondary sites in the H+propane reaction.

4.3.1 Excitation Functions

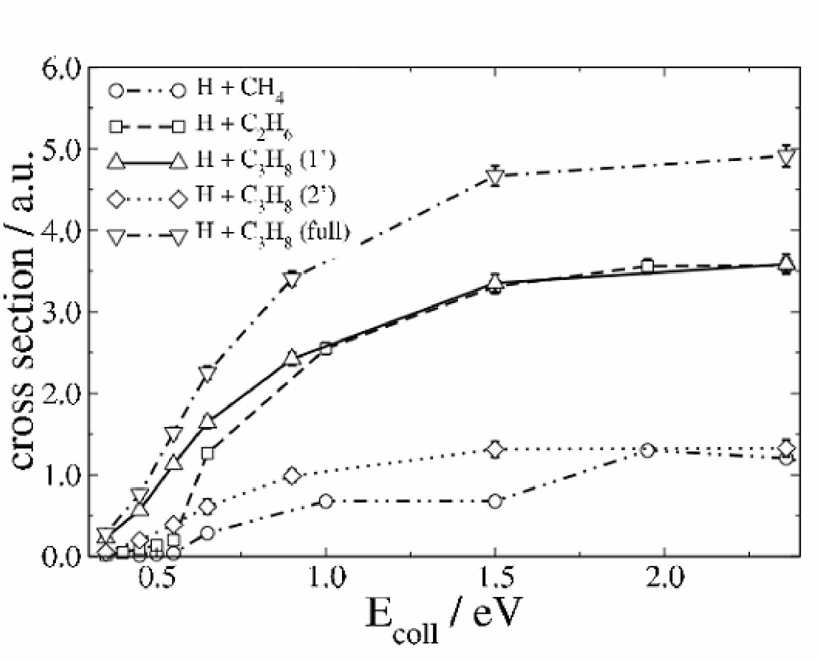

Figure 4.1: Excitation functions (reactive cross section *vs*. collision energy) for the indicated H+alkane → H$_2$+alkyl reactions. H+C$_3$H$_8$ (1'), and H+C$_3$H$_8$ (2') are the excitation functions for abstraction at the primary and secondary sites of propane, respectively, and H+C$_3$H$_8$ (full) represents all hydrogen abstractions from propane.

Figure 4.1 shows the excitation functions for all of the reactions studied. All the excitation functions have similar shapes, with an initial rise in the reactive cross section after threshold and a cross-section plateau at high collision energies. Comparison of the excitation function of the various systems reveals that cross sections increase with the size of the target molecule. Neglecting the changes in the barrier heights for the various systems, this result is expected simply based on the fact that the number of hydrogen atoms available for abstraction increases with the length of the hydrocarbon. To verify if this statistical consideration is solely responsible for the differences in the cross section between the various systems, one can compare the ratios of the calculated cross sections to the ratio of hydrogen atoms per hydrocarbon (4 : 6 : 8 for methane, ethane, and propane, respectively). At E_{coll}=2.36 eV, the calculated cross-section ratio is 4.0 : 11.6 : 32.7, a significant deviation from the statistical ratio. These ratios indicate that the longer hydrocarbons are more reactive than would be expected from statistical considerations. This result can be well understood from the fact that the longer hydrocarbons undergo reaction with substantially larger impact parameters, leading to an enhanced reactivity beyond the expected statistical considerations. Evidence for the increased reactivity at larger impact parameters with the size of the alkane molecules at E_{coll}=2.36 eV is provided by the maximum reactive impact parameters under those conditions, which are 4.4, 5.9, and 6.6 a.u. for the H+methane, ethane, and propane reaction, respectively.

Figure 4.1 also shows the separate contribution of the cross section for abstraction at the primary (1' channel) and secondary (2' channel) sites to the total cross section in the H+propane reaction. At the highest collision energy examined (2.36 eV), the primary : secondary cross-section ratio is 2.7 : 1.0. This ratio is very close to the statistical ratio of hydrogen atoms at each site (3 : 1). Examination of the maximum impact parameter leading to reaction for each channel (6.6 and 5.2 a.u. for primary and secondary channels, respectively), reveals the expected result that abstraction of hydrogen atoms primary sites can occur at longer impact parameters due to the larger separation of these hydrogen atoms from the center of mass of the propane molecule.

An interesting result in Figure 4.1 is that at the larger collision energies investigated in this work, the cross section for abstraction at the primary sites of propane overlaps with that of ethane. In classical trajectories, the reactive cross section, σ, can be approximated by the equation $\sigma = \pi\, b_{max}^2\ (N_{reactive}/N_{total})$, where b_{max} is the maximum parameter leading to reaction, and $N_{reactive}/N_{total}$ is the reaction probability (ratio of reactive to total trajectories calculated). As mentioned before, b_{max} for the reaction at primary sites of propane (6.6 a.u. at E_{coll}=2.36 eV) is slightly larger than that for ethane (5.9 a.u. at the same collision energy). Therefore, a larger cross section could be expected for reaction at primary sites in propane. The result that the cross sections for primary sites in propane and ethane is essentially identical, implies that the reaction probability for abstraction at primary sites in propane is slightly smaller than that for ethane. A plausible reason for the decrease in reactivity of the primary sites of propane with respect to ethane is the presence of reactive secondary sites in propane, which compete with the primary sites in the dynamics studies.

4.3.2 Opacity Functions

Further insight into the reactivity of H+alkane reactions can be gained by examination of the opacity function (probability of reaction as a function of the impact parameter). Figure 4.2 presents a comparison of the opacity functions for the H+alkane reactions studied here. Note that the opacity function for the H+propane reaction (Fig. 4.2(c)) corresponds to abstraction at the primary sites only ($H+C_3H_8 \rightarrow H_2+n\text{-}C_3H_7$). The first major trend revealed by the figure is that reactions occur at much longer impact parameters as the size of the target molecule increases. This expected trend was anticipated by the values of the maximum impact parameters leading to reaction discussed before. Additional examination of the opacity functions for each system at the three collision energies included in the figure indicates that as the collision energy increases, hydrogen abstraction can occur at longer impact parameters. This result implies a widening of the cone of acceptance for reaction with collision energy. While this increase in the reactive impact parameter is rather large when going from E_{coll}=0.65 eV to 1.50 eV, it is very moderate when going from E_{coll}=1.50 eV to 2.36 eV. This result suggests that the reactions' cone of acceptance has an effective maximum value that is reached at the collision energies explored here, and is consistent with the plateau shape of the excitation functions seen in Figure 4.1.

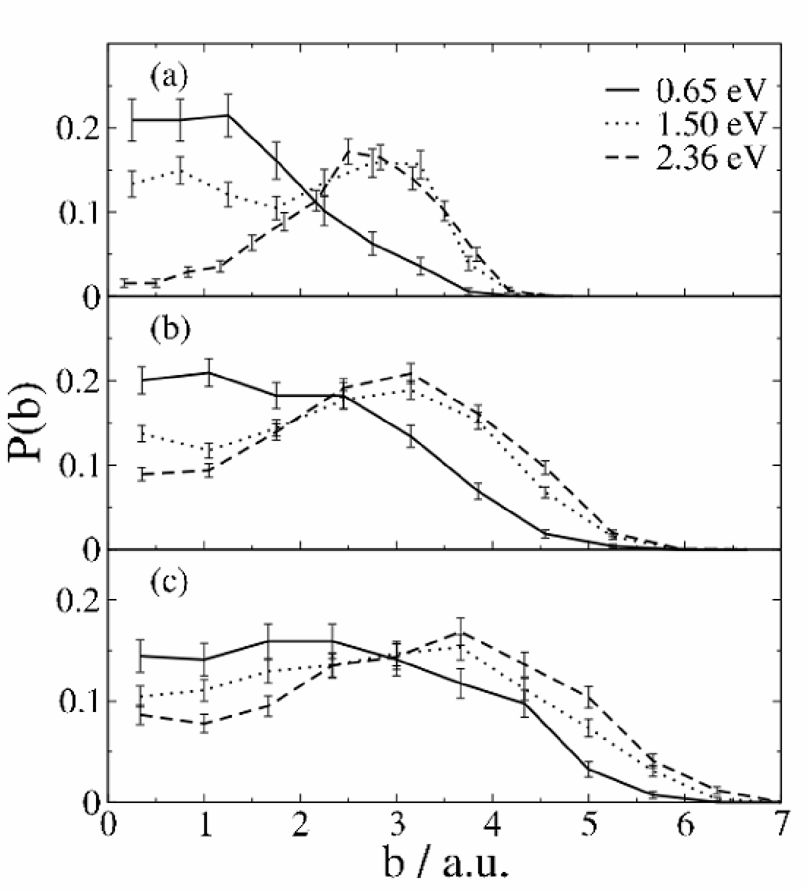

Figure 4.2: Opacity functions (probability of reaction at impact parameter b *vs.* impact parameter) for the $H+CH_4 \rightarrow H_2+CH_3$ (a), $H+C_2H_6 \rightarrow H_2+C_2H_5$ (b), and $H+C_3H_8 \rightarrow H_2+C_3H_7$ (1') (c) reactions at the indicated collision energies.

Another key insight that can be gained by examining the evolution of the opacity functions with collision energy for each system is the sizeable decrease in reactivity at smaller impact parameters as the collision energy increases. At the lowest collision energy examined (0.65 eV), the opacity function shows a plateau at low impact parameters and then a decrease at high impact parameters for all systems. As the collision energy increases, we see a decrease in the value of the opacity function at very low impact parameters. The opacity function then increases to reach a peak at intermediate values of the impact parameter before falling off to zero at the maximum reactive impact parameter. The reason for the decrease of reactivity at low impact parameters with increasing collision energy can be tied to the regions of the potential-energy surface explored at the various collision energies. Low-impact-parameter collisions involve a hard hit between reagents, in which direct interaction between the incoming H atom and a C atom in the alkane molecules can take place. At low collision energies, trajectories started with a small impact parameter may explore near collinear H—H—C arrangements, which are required for the abstraction reaction. As the collision energy increases, the large velocity of the incoming H atom makes is possible for the system to fly past the collinear transition state, leading to highly repulsive non-reactive H—H—C arrangements in which both H—H and C—H bonds are compressed beyond their equilibrium values at the transition state, which diminishes reactivity. A second possible scenario at low impact parameters occurs when the system does not explore collinear H—H—C arrangements. These trajectories hence involve a more direct interaction between the incoming hydrogen atom and a carbon atom. At high collision energies, such trajectories may lead to high-energy reaction channels, such as H-exchange, and C-C breakage (for H+ethane and H+propane), which are accessible at collision energies above ~1.5 eV. Both the exploration of repulsive regions of the potential-energy surface and the presence of competing high-energy reaction channels therefore decrease the reactivity of the abstraction reaction at low impact parameters and high collision energies.

We have also analyzed the opacity functions of the hydrogen abstraction reactions at primary and secondary sites for H+propane collisions (not shown). As mentioned above, reaction at primary sites can occur with longer impact parameters. Therefore, the opacity functions of primary abstraction extend to larger b values than those of secondary abstraction at all collision energies. At low impact parameters, the value of the opacity function for secondary abstraction is slightly larger than that for primary abstraction. This result bodes well with the idea that since secondary hydrogen atoms are bound to the central carbon atom of propane, these sites are statistically sampled more frequently at low impact parameters than primary sites.

4.3.3 Angular Distributions

Another key metric for the understanding of the dynamics behavior of a reactive system is the angular distribution. Figure 4.3 shows the **kk’** angular distribution for all three systems studied at collision energies ranging from 0.65 to 2.36 eV. In this work, **k** is the initial relative velocity vector pointing from the H atom to the molecule center of mass, and **k’** is the final relative velocity vector pointing from the center of mass of the alkyl product to the H_2 molecule. Figure 4.3(a) shows the result for the $H+CH_4 \rightarrow H_2+CH_3$ reaction, where a clear evolution from strongly backward to increasingly sideways and forward scattering can be appreciated as collision energy increases. The explanation for this behavior can be traced to the accessible regions of the global potential-energy surface at the various collision energies. At low collision energies, the system is restricted to regions of the potential-energy surface in the vicinity of the minimum-energy reaction path. For the $H+CH_4 \rightarrow H_2+CH_3$ reaction, electronic-structure calculations show that the minimum-energy path is characterized by a collinear approach of the H atom to one of the C-H

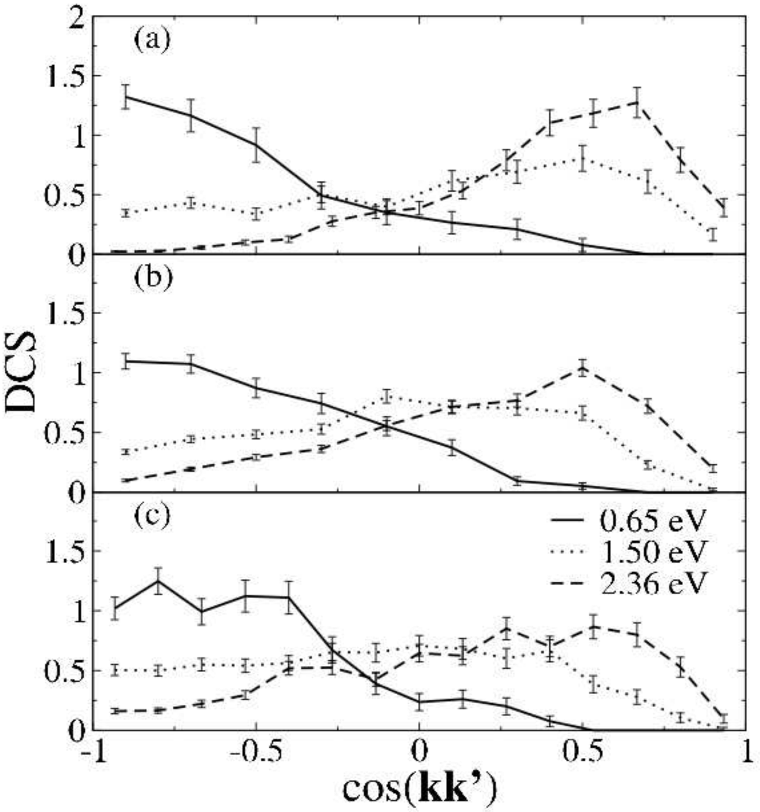

Figure 4.3: Angular distributions expressed in terms of normalized differential cross sections (DCS, (2π/σ)(dσ/dΩ’), where Ω’ is the solid angle) for the $H+CH_4 \rightarrow H_2+CH_3$ (a), $H+C_2H_6 \rightarrow H_2+C_2H_5$ (b), and $H+C_3H_8 \rightarrow H_2+C_3H_7$ (1’) (c) reactions at the indicated collision energies.

bonds in methane, followed by a collinear separation in which H_2 recoils from CH_3 product in a direction exactly opposite to that of the incoming H radical. This mechanism is often termed as 'rebound dynamics' and leads to strongly backward **kk'** angular distributions (cos(**kk'**) → -1), as can be seen for E_{coll}=0.65 eV in Figure 4.3(a). Preferential reactivity at low impact parameters is also a rubric of rebound dynamics, and our results for H+CH_4 at 0.65 eV in Figure 4.2(a) corroborate this feature of the reaction mechanism.

An increase in the initial collision energy lifts the restriction of the system to traverse the area of the potential-energy surface near the minimum-energy reaction path and opens up other reaction pathways. Reactions can take place at longer impact parameters, which can be observed in the opacity functions of Figure 4.2 at high energies. Reaction at large impact parameters opens the possibility for 'stripping dynamics'. This mechanism is characteristic of peripheral reactions, in which the incoming radical largely does not change its initial momentum as it flies past the molecule and strips an atom. The **kk'** angular distributions of reactions following stripping dynamics are subsequently markedly forward (cos(**kk'**)→1). Mechanisms intermediate between rebound (low impact parameters, backward angular distributions) and stripping dynamics (large impact parameters, forward angular distributions) lead to sideways scattering (cos(**kk'**)~0). With these arguments in mind, the evolution from mostly backward to increasingly sideways/forward scattering at higher collision energies seen in Fig. 4.3 corresponds well with a change in the scattering mechanism from rebound to an increasingly stripping type.

The results presented here for the $H+CH_4 \rightarrow H_2+CH_3$ reaction have been discussed at length by the Zare group [3] in light of recent experiments and complementary theoretical work. The novelty of the results presented in Figure 4.3 is that the mechanistic insight drawn from the studies of the $H+CH_4 \rightarrow H_2+CH_3$ reaction seems to apply perfectly to reactions of H radicals with longer-chain alkane molecules. For both the $H+C_2H_6$ and $H+C_3H_8$ hydrogen-abstraction reactions, the angular distributions at low collision energy (0.65 eV) are dominated by backward scattering (Figs. 4.3(b) and 4.3(c), respectively). A shift toward increasingly sideways and forward distributions is evident as the collision energy increases. This evolution in the angular distributions is tied to the trends in the opacity functions, which show a preference for larger impact parameters as the collision energy increases (Figs. 4.2(b), and 4.2(c), respectively).

Even though the major trends in the angular distributions of the H+C_2H_6, and H+C_3H_8 reactions agree with those of the H+CH_4 reaction, there is an appreciable "flattening" of the angular distributions at E_{coll}=2.36 eV as the size of the target molecule increases. For instance, while for the H+CH_4 reaction there is no backward scattering at E_{coll}=2.36 eV, backward scattering is not negligible at that energy for the H+C_2H_6 and H+C_3H_8 reactions. This transition to an increasingly isotropic angular distribution with alkane size is likely a result of the non-spherical shape of the larger alkane molecules, which slightly impairs the direct connection between impact parameter and scattering angle that is evident in the H+CH_4 reaction.

The angular distributions for the H+C_3H_8 reaction presented in Fig. 4.3(c) correspond exclusively to the reaction at the primary sites of propane. Comparison of the angular distributions for abstraction at the primary and secondary does not reveal sharp differences at any of the collision energies investigated in this work. For instance, the average **kk'** angles for the reactions at primary (secondary) sites are: 131.3° (137.5°) at E_{coll}=0.65 eV, and 93.7° (99.9°) at E_{coll}=2.36 eV. Therefore, the reaction mechanism described above for primary sites appears to apply broadly also to secondary sites in propane.

4.3.4 Energy Partitioning in Products

To gather further insight into the dynamics of H+alkane abstraction reactions, we now discuss the partitioning of available energy into the various product degrees of freedom, including relative product translation, H_2 rotation and vibration, and alkyl internal energy.

Figure 4.4 shows the trends in energy disposal as a function of collision energy in terms of average fractions of available energy, $<f'_i>$. The total available energy in products is defined as the sum of products relative translational energy, H_2 rotational energy, and H_2 vibrational energy and alkyl internal energy above their corresponding zero-point energies. If the energy into H_2 vibration or alkyl energy is below their zero point, the fractions of energy in these modes are defined to be zero, and the available energy is recomputed by adding the rest of product energies.

Most of the energy is channeled into products relative translation for all of the reactions studied in the entire range of collision energies (Fig. 4.4(a)). The average fractions of product relative translation decrease with collision energy, indicating that product internal excitation is favored at high collision energies. An interesting result is that the structure of the reagent alkane molecule influences the amount of energy going into translation. Larger alkanes seem to promote energy release into products internal excitation, suggesting that the molecular degrees of freedom not directly involved in the process of bond making/breaking are not entirely orthogonal to the reaction coordinate, particularly at high energies. Also interesting is the fact that reaction at secondary sites in $H+C_3H_8$ results in less release into products translation than reaction at primary sites.

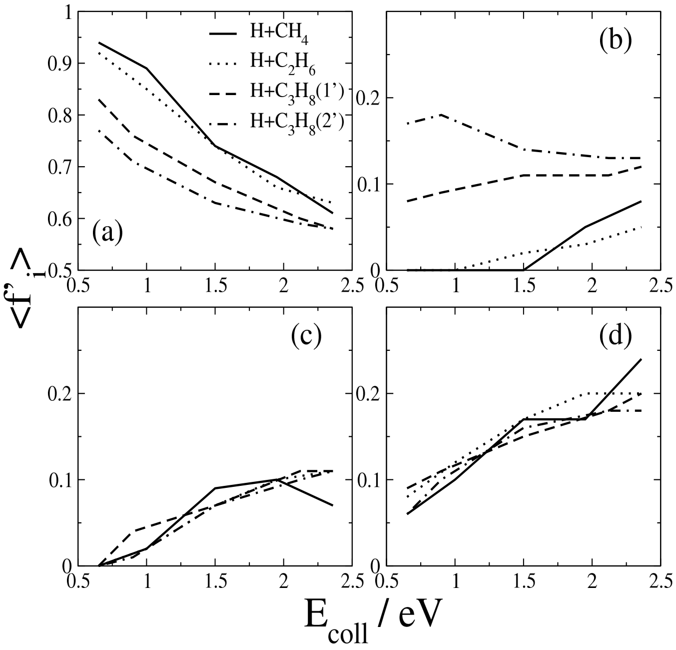

Figure 4.4: Average fractions of energy in various products degrees of freedom for the indicated H+alkane→H_2+alkyl reactions as a function of collision energy. (a) Average fractions of products translation; (b) average fractions of alkyl internal energy; (c) average fractions of H_2 vibration; (d) average fractions of H_2 rotation.

Figures 4.4(c) and (d) exhibit the fractions of available energy going into H_2 vibration and rotation, respectively. An increase in collision energy favors energy deposition into these modes for all reactions studied. Remarkably, the fractions of H_2 energy are rather insensitive to the reaction under study, which implies that energy disposal to the newly-formed H_2 is not markedly influenced by the structure of the alkane molecule from which abstraction is produced. This result is consistent with measurements of Varley and Dagdigian in the Cl+isobutane and propane reactions at energies much smaller than those studied here, in which the energy channeled into rotation of the newly formed diatomic molecules did not depend strongly on the abstraction site.[32, 33]

The average fractions of alkyl energy are displayed in Figure 4.4(b). The first apparent trend in the figure is that the fraction of available energy going into the alkyl fragment is more insensitive to collision energy than the other products degrees of freedom examined. Interestingly, there is a notable difference between the various reactions, with larger alkyl fragments receiving a larger fraction of available energy. In addition, energy released to the i-propyl product in the H+propane abstraction reaction at secondary sites abstraction is larger than to the n-propyl product in the primary-site reaction, and the difference between the two is more accentuated at low collision energies. Comparison of Figures 4.4(a) and (b) shows that the trend of increasing energy partitioning to the alkyl product with molecular size occurs at the expense of product translation.

In summary, the emerging picture of energy partitioning in products of the H+alkane → H_2+alkyl reactions is as follows. Most of the available energy goes into product translation, but this propensity decreases with collision energy. As the collision energy increases, internal excitation of the H_2 product becomes important. Reactions with larger alkanes deposit less energy into product translation because larger alkyl fragments absorb more energy released from the reaction, particularly at low collision energies.

4.4 Concluding remarks

Quasiclassical trajectories have been calculated for the H + methane, ethane, and propane reactions using a specific-reaction-parameters semiempirical Hamiltonian to describe the potential-energy surface. Cross sections, opacity functions, angular distributions, and energy partitioning in products are examined to obtain thorough insight into the dynamics of H+alkane reactions. A change in mechanism is seen from predominantly rebound to increasingly stripping dynamics as collision energy increases. While this shift in the mechanism was described for the H+CH_4 reaction in prior work, our results indicate that it seems general to H+alkane reactions. Subtle differences in the dynamics of the H+alkane reactions are found throughout the properties examined, but the most noteworthy is the increased channeling of available energy to the alkyl product with alkane size at the expense of product translation.

This work presented in this chapter completes our studies of the H+alkane family of reactions. We have shown that using *ab initio* data from the relevant regions of the

PES for the $H+CH_4$ and $H+C_2H_6$ chemical systems we can build an SRP-Hamiltonian which can be used in a direct-dynamics theoretical study for the first few reactions in the H+alkane family of reactions. The methodology used to implement this study and the work in Chapter 3 will be used in Chapter 5 to study the reactions in the F+alkane family and extended with a QM/MM technique in Chapter 6 to study the reactions of fluorine atoms and alkanethiolate self-assembled monolayers.

References

1. S. J. Greaves, J. Kim, A. J. Orr-Ewing and D. Troya, Chemical Physics Letters **441** (4-6), 171-175 (2007).
2. M. H. Alexander, G. Capecchi and H.-J. Werner, Science **296** (5568), 715 (2002).
3. J. P. Camden, H. A. Bechtel, D. J. A. Brown, M. R. Martin, R. N. Zare, W. Hu, G. Lendvay, D. Troya and G. C. Schatz, J. Am. Chem. Soc. **127** (34), 11898-11899 (2005).
4. J. J. Valentini, J. Phys. Chem. A **106** (24), 5745-5759 (2002).
5. A. Teslja and J. J. Valentini, The Journal of Chemical Physics **125** (13), 132304-132322 (2006).
6. G. J. Germann, Y.-D. Huh and J. J. Valentini, The Journal of Chemical Physics **96** (3), 1957-1966 (1992).
7. G. J. Germann, Y.-D. Huh and J. J. Valentini, Chemical Physics Letters **183** (5), 353-356 (1991).
8. J. P. Camden, H. A. Bechtel and R. N. Zare, Angewandte Chemie International Edition **42** (42), 5227-5230 (2003).
9. W. Hu, G. Lendvay, D. Troya, G. C. Schatz, J. P. Camden, H. A. Bechtel, D. J. A. Brown, M. R. Martin and R. N. Zare, J. Phys. Chem. A **110** (9), 3017-3027 (2006).
10. J. P. Camden, W. Hu, H. A. Bechtel, D. J. A. Brown, M. R. Martin, R. N. Zare, G. Lendvay, D. Troya and G. C. Schatz, J. Phys. Chem. A **110** (2), 677-686 (2006).
11. J. P. Camden, H. A. Bechtel, D. J. A. Brown and R. N. Zare, The Journal of Chemical Physics **123** (13), 134301-134309 (2005).
12. J. Espinosa-Garcia, J. Phys. Chem. A **111** (26), 5792-5799 (2007).
13. J. Espinosa-Garcia, The Journal of Chemical Physics **116** (24), 10664-10673 (2002).
14. C. Rangel, J. Sanson, J.C. Corchado and J. Espinosa-Garcia, J. Phys. Chem. A **110**, 10715-10719 (2006).
15. T. Wu, H.-J. Werner and U. Manthe, The Journal of Chemical Physics **124** (16), 164307-164312 (2006).
16. R. van Harrevelt, G. Nyman and U. Manthe, The Journal of Chemical Physics **126** (8), 084303-084306 (2007).
17. J. Palma, J. Echave and D. C. Clary, J. Phys. Chem. A **106** (36), 8256-8260 (2002).
18. F. Huarte-Larranaga and U. Manthe, The Journal of Chemical Physics **116** (7), 2863-2869 (2002).
19. F. Huarte-Larranaga and U. Manthe, The Journal of Chemical Physics **113** (13), 5115-5118 (2000).
20. J. M. Bowman, D. Wang, X. Huang, F. Huarte-Larranaga and U. Manthe, The Journal of Chemical Physics **114** (21), 9683-9684 (2001).
21. M. J. T. Jordan and R. G. Gilbert, The Journal of Chemical Physics **102** (14), 5669-5682 (1995).
22. X. Zhang, B. J. Braams and J. M. Bowman, The Journal of Chemical Physics **124** (2), 021104-021104 (2006).

23. J. Warnatz, in *Combustion Chemistry*, edited by J. W. C. Gardiner (Springer-Verlag, New York, 1984), pp. 197.
24. L. M. Raff, The Journal of Chemical Physics **60** (6), 2220-2244 (1974).
25. S. C. Althorpe, F. Fernandez-Alonso, B. D. Bean, J. D. Ayers, A. E. Pomerantz, R. N. Zare and E. Wrede, Nature **416** (6876), 67-70 (2002).
26. G. A. Oldershaw and P. L. Gould, J. Chem. Soc., Faraday Trans. 2 **81** (81), 1507-1516 (1985).
27. J. P. Layfield, M. D. Owens and D. Troya, The Journal of Chemical Physics **128** (19), 194302-194312 (2008).
28. Z. Xie, J. M. Bowman and X. Zhang, The Journal of Chemical Physics **125** (13), 133120-133128 (2006).
29. W. R. Simpson, T. P. Rakitzis, S. A. Kandel, T. Lev-On and R. N. Zare, J. Phys. Chem. **100** (19), 7938-7947 (1996).
30. W. R. Simpson, T. P. Rakitzis, S. A. Kandel, A. J. Orr-Ewing and R. N. Zare, Journal of Chemical Physics **103** (17), 7313 (1995).
31. S. A. Kandel, T. P. Rakitzis, T. Lev-On and R. N. Zare, Journal of Chemical Physics **105** (17), 7550 (1996).
32. D. F. Varley and P. J. Dagdigian, Chemical Physics Letters **255** (4-6), 393-400 (1996).
33. D. F. Varley and P. J. Dagdigian, J. Phys. Chem. **100** (11), 4365-4374 (1996).
34. B. Ahlswede and K. Jug, Journal of Computational Chemistry **20** (6), 563-571 (1999).
35. W. L. Hase, R. J. Duchovic, X. Hu, A. Komornicki, K. Lim, D. Lu, G. H. Peslherbe, K. N. Swamy, S. R. Vande Linde, A. J. C. Varandas, H. Wang and R. J. Wolf, (1996), pp. 55.

Chapter 5
Direct-dynamics study of the F+CH_4, C_2H_6, C_3H_8, and i-C_4H_{10} reactions

Reproduced in part with permission from J. P. Layfield, A. F. Sweeney and D. Troya, *J. Phys. Chem. A* 113 (16), 4294 (2009).

5.1 Introduction

Recent measurements of the dynamics of atomic-radical+alkane reactions are continuing to instigate the development of theoretical reaction-dynamics studies that complement the descriptions that experiment can provide.[1-7] Use of full-dimensional quantum-dynamics techniques coupled with highly accurate analytic potential-energy surfaces has enabled impressive agreement between experimental results and theoretical predictions for various triatomic systems,[8, 9] but progress to larger reactions has been slow. The ability to move from triatomic reactions to higher-dimensionality systems, such as radical+alkane reactions, is difficult due to two main limiting factors. First, a full quantum-dynamics treatment of multidimensional chemical reactions is currently unwieldy. Second, despite promising advances,[10,11] approaches to obtain analytical potential-energy surfaces for polyatomic reactions in a timely manner are still scarce.

Accurate potential-energy surfaces are required to enable quantitative description of the dynamics of chemical reactions by theoretical means. Construction of these potential-energy surfaces has traditionally been carried out by fitting analytic functions to high-quality *ab initio* data. However, physically-reasonable behavior in regions of the global potential-energy surface not covered by the *ab initio* data cannot always be guaranteed in this approach, and this becomes an issue for systems having many degrees of freedom, such as radical+alkane reactions. A way to circumvent the need for an explicit potential-energy surface is the use of direct dynamics.[10] Direct-dynamics studies calculate the necessary information about the potential-energy surface using electronic-structure methods whenever they are required in the dynamics simulation. A disadvantage of this method is that a typical reaction-dynamics study using classical trajectories can require an excess of 10^7 energy and gradient calculations, which dramatically confines the types of electronic-structure methods that can be used in all but the simplest reactions. This limitation restricts the overall accuracy of the studies and represents a major hurdle for the use of direct dynamics.

Semiempirical Hamiltonians have emerged as a promising class of electronic-structure methods for timely computation of the myriad potential energies and gradients involved in a direct-dynamics study. These computationally-inexpensive methods are a simplification of the Hartree-Fock theory based on neglect of three- and four-centered integrals, parameterization of additional lower-order integrals, and use of pseudo-minimal basis sets, among other approximations.[11] These approximations drastically reduce the computational expense associated with *ab initio* and even density-functional theories, making semiempirical Hamiltonians attractive candidates for use in large-scale reaction-dynamics studies. The deficiencies in accuracy resulting from these major simplifications to Hartree-Fock theory are partially compensated by including into the Hamiltonian empirical parameters, which are adjusted using information obtained at a more sophisticated level of theory or from experiment. While the resulting semiempirical Hamiltonians possess impressive accuracy/computational-expense ratios for the systems included in the derivation of the empirical parameters, accuracy outside the calibration set is commonly lacking. This is particularly true in the description of the global potential-energy surfaces of chemical reactions, as situations in which bonds are forming or breaking are typically not included in the calibration sets of popular semiempirical Hamiltonians.

Building a specific-reaction-parameter (SRP) semiempirical Hamiltonian has proven to be a convenient method to overcome the often-large inaccuracies of standard semiempirical methods in describing global potential-energy surfaces of relatively simple chemical reactions.[12-19] SRP Hamiltonians are created by deriving a new set of parameters so that the Hamiltonians describe *ab initio* or experimental information on the potential-energy surface of only a single reaction as accurately as possible. The improved semiempirical Hamiltonians are then used in direct-dynamics calculations of the single reaction under consideration, and their accuracy can be further tested by the comparison of computed dynamics properties with available experimental results. While this approach has shown to work reasonably well in a variety of reaction-dynamics studies, one of its limitations is that a SRP Hamiltonian needs to be derived for each specific reaction under study. Very recent efforts have investigated the possibility of deriving SRP Hamiltonians specific to a homologous *family* of reactions, in contradistinction with a *single* reaction. Specifically, our group has recently derived a SRP Hamiltonian to study the H+alkane class of reactions by including *ab initio* information of the potential-energy surface of the first few members of the family in the derivation of the SRP set of parameters.[20] The resulting Hamiltonian generally reproduces experimental information, including relative excitation functions, alkyl product speed distributions, and angular distributions for the H+methane → H_2+methyl reaction, and the absolute excitation function of the $H+C_2D_6 \rightarrow H_2+C_2D_5$ reaction. The encouraging results of the SRP Hamiltonian for these two reactions have elicited a study of its applicability to larger reactions in the family. [21]

In this paper, we develop a SRP Hamiltonian for the F+alkane class of reactions and carefully calibrate its accuracy by comparison of calculated dynamics properties in the $F+CH_4 \rightarrow HF+CH_3$, $F+CD_4 \rightarrow DF+CD_3$, and $F+C_2H_6 \rightarrow HF+C_2H_5$ reactions with available experiments. Once the accuracy of the Hamiltonian is determined, we investigate the F+methane, ethane, propane, and i-butane reactions with the goal of learning the effect that the abstraction site in the alkane molecule (i.e., primary *vs.* secondary *vs.* tertiary) and alkyl fragment size have on the reaction dynamics. Motivation for these studies is provided in part by the intense activity that has been recently focused on the F+alkane → HF+alkyl family of reactions. The dynamics of the $F+CH_4 \rightarrow HF+CH_3$ reaction has been extensively studied due to its significant potential as a chemical laser[22] and for fundamental reasons. Experimental studies have provided CH_3 product energy distributions,[23] HF rovibrational state distributions,[4] relative excitation functions,[24] and angular distributions.[25] Isotopically substituted analogues of the $F+CH_4$ reaction have also been extensively studied.[1, 26, 27] Several theoretical reaction-dynamics studies of the $F+CH_4$ system based on analytical surfaces,[28, 29] interpolated surfaces,[30] and a SRP Hamiltonian[18] have emerged recently, providing different levels of agreement with experiment. In stark contrast with the vigorous theoretical studies of the $F+CH_4 \rightarrow HF+CH_3$ reaction, analogous studies for the next member of the F+alkane family, $F+C_2H_6 \rightarrow HF+C_2H_5$, are lacking, which is likely due to the difficulty in deriving analytic potential-energy surfaces mentioned before. In fact, no direct comparison between calculated vibrational distributions of the HF product arising from a full-dynamics study and those measured by Nesbitt and co-workers[5] has been reported yet, and this provides additional motivation for the present study.

The remainder of this paper is as follows. First, we show *ab initio* calculations performed to capture the main aspects of the F+alkane potential-energy surfaces. Then we use this information to reparameterize a semiempirical Hamiltonian. We then present a direct-dynamics study where this Hamiltonian is used to propagate trajectories for the F+CH_4, C_2H_6, C_3H_8, and i-C_4H_{10} reactions with a focus on computing experimentally-determined properties to test the accuracy of the Hamiltonian and investigate the differences in the dynamics of F+alkane reactions as a function of the reagent alkane molecule.

5.2 Electronic-Structure Calculations

5.2.1 *Ab initio* Study

We have characterized the main stationary points of the F+CH_4, C_2H_6, C_3H_8, and i-C_4H_{10} reactions using both *ab initio* and semiempirical methods. *Ab initio* geometry optimizations and frequency calculations have been performed for all reactions using second-order Moller-Plesset perturbation theory (MP2) in combination with Dunning's correlation-consistent double-zeta basis set augmented with diffuse functions (aug-cc-pVDZ). Single-point coupled-cluster calculations with single, double, and pertubative triple excitations [CCSD(T)] with the same basis set have been carried out with the MP2 geometries to obtain a higher-accuracy estimate of the energies. The validity of these CCSD(T)//MP2 dual-level calculations in determining reaction energies has been shown before for the F+CH_4 reaction, where 'pure' CCSD(T)/aug-cc-pVDZ results agree with CCSD(T)/aug-cc-pVDZ//MP2/aug-cc-pVDZ energies within 0.01 kcal mol^{-1}.[18] All of the *ab initio* calculations have been performed using the GAUSSIAN03 package of programs.[31] Even though non-adiabatic crossings between the three potential-energy surfaces that correlate with the $^2P_{3/2}$ and $^2P_{1/2}$ states of F are expected, experiments on the effect of non-adiabatic dynamics are still lacking. Therefore, our calculations refer only to the ground-state potential-energy surface.

Table 5.1 shows the calculated energies of the F+alkane reactions studied in this work in comparison with experiment.[32, 33] The F+C_3H_8 and F+i-C_4H_{10} reaction each have two possible channels, corresponding to the two possible sites of hydrogen abstraction in each alkane molecule (primary and secondary in C_3H_8 and primary and tertiary in i-C_4H_{10}). Moreover, there are two symmetry-inequivalent primary sites for each of these two reactions at 0 K (see Figs. 1 and 2 of Ref. [34]), but the differences in the potential-energy surfaces of these two approaches is so small that we will not distinguish them here. Instead, we report here the lowest-energy channel for primary abstraction, which for both C_3H_8 and i-C_4H_{10} correspond to sites that produce $CH_2CH_2CH_3$ and $CH_2CH(CH_3)_2$ radicals of C_1 symmetry.

The CCSD(T)/aug-cc-pVDZ results shown in Table 5.1 uniformly underestimate the experimental reaction exothermicity beyond the limit of chemical accuracy (~1 kcal mol^{-1}) for all of the reactions studied. This inability of CCSD(T)/aug-cc-pVDZ calculations to capture the reaction energies with chemical accuracy is mainly due to the use of an insufficiently large basis set. In effect, complete-basis-set extrapolations from CCSD(T)/aug-cc-pVTZ and –pVQZ calculations for the $F+CH_4 \rightarrow HF+CH_3$ (Δ_rH=-33.18 kcal mol^{-1}) and $F+C_2H_6 \rightarrow HF+C_2H_5$ reaction (Δ_rH=-36.78 kcal mol^{-1}) provide the level of agreement with experiment expected from CCSD(T) calculations. In contrast to the uniform underestimation of the reaction exothermicities by CCSD(T)/aug-cc-pVDZ calculations, MP2/aug-cc-pVDZ reaction energies are usually more exothermic than experiment for the smaller members of the family, but coincidentally agree with experiment quite well for the F+i-C_4H_{10} reactions.

Table 5.1 also contains results obtained with the standard MSINDO semiempirical Hamiltonian.[35, 36] Remarkably, the reproduction of the reaction energy of the $F+CH_4 \rightarrow HF+CH_3$ is comparable to that of MP2/aug-cc-pVDZ calculations, even though the *ab initio* calculations are orders of magnitude more computationally demanding. However, the ability of MSINDO to be within 3 kcal mol^{-1} of the experimental reaction energy in $F+CH_4$ quickly disappears when one examines the results for larger F+alkane reactions.

For $F+C_2H_6$, the errors in the MSINDO predictions rise to 10 kcal mol^{-1}, and they continue to escalate for the reaction energies involving secondary and tertiary sites. In fact, the poorest description of the experiment occurs for the abstraction at the tertiary site in the F+i-C_4H_{10} reaction, for which the MSINDO reaction energy is almost 20 kcal mol^{-1} more negative than experiment.

Table 5.1. Reaction energies for F+alkane→HF+alkyl reactions.[a]

Reaction	CCSD(T)[b]	MP2[c]	MSINDO	SRP-MSINDO	Exp.[h,i]
F+CH_4	-30.09 (-26.63)	-35.24 (-31.78)	-36.59 (-32.70)	-32.10 (-28.21)	-31.4, -31.6
F+C_2H_6	-33.20 (-29.54)	-38.08 (-34.35)	-46.50 (-42.80)	-35.40 (-31.63)	-35.3, -35.8
F+C_3H_8 (1)[d]	-32.81 (-29.28)	-37.50 (-33.99)	-45.88 (-42.68)	-35.95 (-32.25)	-35.2, -35.4
F+C_3H_8 (2)[e]	-35.24 (-31.62)	-39.75 (-36.13)	-53.95 (-50.69)	-38.59 (-34.99)	-38.6, -37.8
F+i-C_4H_{10} (1)[f]	-32.13 (-28.70)	-36.65 (-33.23)	-46.62 (-43.36)	-36.25 (-32.75)	-35.7
F+i-C_4H_{10} (3)[g]	-36.43 (-33.16)	-40.67 (-37.40)	-60.17 (-56.90)	-40.85 (-37.25)	-40.7

[a] Energies are reported in kcal mol^{-1}. Values in parentheses correspond to classical energies, i.e., not corrected by zero-point energies.
[b] CCSD(T)/aug-cc-pVDZ//MP2/aug-cc-pVDZ energies.
[c] MP2/aug-cc-pVDZ energies.
[d] $F+C_3H_8 \rightarrow HF+CH_2CH_2CH_3$
[e] $F+C_3H_8 \rightarrow HF+CH_3CHCH_3$
[f] $F+i\text{-}C_4H_{10} \rightarrow HF+CH_2CH(CH_3)_2$
[g] $F+i\text{-}C_4H_{10} \rightarrow HF+C(CH_3)_3$
[h] Experimental Data from Ref. [37]
[i] Experiemental Data from Ref. [38]

Notwithstanding, the expected trend[39] that the reactions become more exothermic in the primary → secondary → tertiary sequence is borne out by all electronic-structure methods, including MSINDO.

Table 5.2 shows the calculated barriers for the F+alkane reactions studied here and the essential geometric parameters of the corresponding transition states, including the lengths of the forming (F-H) and breaking (C-H) bonds and the angle formed by

Table 5.2. Calculated transition-state geometric properties and reaction barriers for F+alkane→HF+alkyl reactions.[a]

	R(F-H) / Å	R(C-H) / Å	∠ F-H-C / °	Energy[b] / kcal mol^{-1}
MP2/aug-cc-pVDZ				
$F+CH_4$	1.466	1.137	180.0	1.45 (3.44)
$F+C_2H_6$	1.545	1.130	161.3	0.15 (1.65)
$F+C_3H_8$ (1)[c]	1.552	1.131	156.6	-0.02 (1.36)
$F+C_3H_8$ (2)[d]	1.621	1.125	149.4	-0.58 (0.38)
$F+i\text{-}C_4H_{10}$ (1)[e]	1.549	1.130	157.8	-0.08 (1.33)
$F+i\text{-}C_4H_{10}$ (3)[f]	1.691	1.122	148.7	-1.00 (-0.39)
MSINDO				
$F+CH_4$	1.284	1.131	180.0	2.53 (3.85)
$F+C_2H_6$	1.400	1.128	165.7	0.97 (1.91)
SRP-MSINDO				
$F+CH_4$	1.546	1.117	180.0	0.85 (1.16)

[a] Reactions missing from the table indicate that a transition state could not be located with that particular method.

[b] Values in parentheses correspond to classical energies, i.e., not corrected by zero-point energies.

[c] $F+C_3H_8 \rightarrow HF+CH_2CH_2CH_3$

[d] $F+C_3H_8 \rightarrow HF+CH_3CHCH_3$

[e] $F+i\text{-}C_4H_{10} \rightarrow HF+CH_2CH(CH_3)_2$

[f] $F+i\text{-}C_4H_{10} \rightarrow HF+C(CH_3)_3$

them. (The absence of values for some of the reactions under the MSINDO calculations means that no first-order transition state was found for those reactions.) The properties of the transition state of the $F+CH_4 \rightarrow HF+CH_4$ reaction have been discussed at length in the literature.[18] Briefly, the transition state located at the MP2/aug-cc-pVDZ level has a much earlier character than the predictions of CCSD(T)/aug-cc-pVDZ (R(F-H)=1.643 Å, R(C-H)=1.124 Å, ∠ F-H-C = 153.4°, reaction barrier=-0.43(0.32) kcal mol^{-1} [18]). This result limits the usefulness of dual-level CCSD(T)/aug-cc-pVDZ//MP2/aug-cc-pVDZ calculations of the reactions barriers, and therefore such calculations are not shown in Table 5.2. Two points are worth noting about the transition state of the $F+CH_4 \rightarrow HF+CH_3$ reaction predicted by the standard MSINDO semiempirical Hamiltonian. First, it has a much earlier character than MP2. Second, the reaction barrier (3.85 kcal mol^{-1} without inclusion of zero-point energy) is higher than MP2/aug-cc-pVDZ. This result is significant because in the experiments carried out by the Nesbitt group on this reaction, the collision energy is only 1.8 kcal mol^{-1}, which is below the MSINDO classical barrier. Therefore, even though the absolute difference between the MSINDO barrier and more accurate estimates is relatively small, quasiclassical-trajectory studies at the collision energy of the Nesbitt experiment would result in no reactivity unless zero-point energy leakage from the CH_4 molecule to the reaction coordinate occurs. To further investigate the ability of the original MSINDO Hamiltonian to simulate experiment, we integrated 10,000 trajectories at 1.8 kcal mol^{-1} collision energy and found only 4 reactive ones, which emerge from zero-point energy violations along the trajectories. Therefore, even though the deviations between the predictions of the standard MSINDO Hamiltonian and *ab initio* methods are not dramatic for the $F+CH_4$ reaction, this method clearly does not provide reliable physical insight into the reaction under experimental conditions.

Examination of the MP2 saddle-point geometries for the various F+alkane reactions in Table 5.2 shows that the transition state becomes increasingly earlier along the primary → secondary → tertiary sequence. This shift in the geometry of the transition state towards reagents is accompanied by a decrease in the barrier height and an increase in the reaction exothermicity (Table 5.1). All these results are rubrics of the well-known Hammond postulate,[40] and nicely agree with similar recent work on O+alkane reactions.[34]

CCSD(T)/aug-cc-pVDZ geometry optimizations failed to locate a transition state for the $F+C_2H_6 \rightarrow HF+C_2H_5$ reaction. To verify whether this reaction possesses a first-order saddle point at the CCSD(T)/aug-cc-pVDZ level, we show in Figure 5.1 contour plots of the relevant region of the potential energy surface calculated at that level of theory. The two dimensional grid of points has been obtained by scanning the breaking and forming bonds in a collinear geometry while holding the rest of the coordinates of the system fixed at their values in reagents. The fact that the F-H and C-H bonds are collinear and the ethyl moiety is not allowed to relax during the scans will result in an increase in the potential energy with respect to the true minimum-energy reaction path. Figure 5.1 shows that even though the calculated scans do not truly represent the minimum-energy reaction path, the pathway from reagents to products is continuously downhill at the CCSD(T)/aug-cc-pVDZ level, confirming the absence of a first-order transition state. Based on Hammond's postulate, we do not anticipate that the larger reactions will exhibit transition states at the CCSD(T)/aug-cc-pVDZ level, particularly for the more exothermic secondary and tertiary reaction channels.

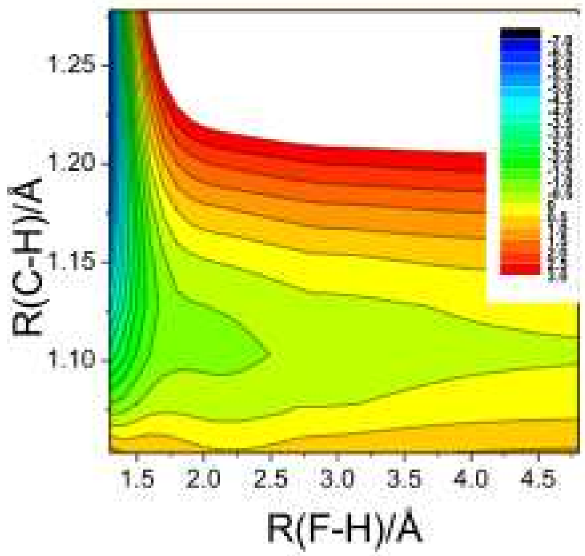

Figure 5.1: Contour plot of the potential-energy surface of the F+C_2H_6→HF+C_2H_5 reaction at the CCSD(T)/aug-cc-pVDZ level. F-H is the forming bond and C-H is the breaking bond. These bonds are held collinear in the scans and the rest of the variables are fixed at their values in reagents. Units of the z-axis scale are kcal mol^{-1}.

5.2.2 SRP-MSINDO Hamiltonian

As stated earlier, a computationally inexpensive method to calculate the potential energy and energy gradients of the system is essential for extensive direct-dynamics studies of all but the smallest chemical reactions. Semiempirical methods offer this attractive feature, but as shown in the prior section, do not generally provide sufficient accuracy to achieve meaningful results. For instance, the MSINDO Hamiltonian overestimates the exothermicity of the F+alkane reactions other than F+CH_4 by at least 10 kcal mol^{-1}. Additionally, the errors in the difference in reaction energies between primary and secondary sites in propane (~8 kcal mol^{-1} for MSINDO and ~3 kcal mol^{-1} experimentally) and primary and tertiary sites for F+i-C_4H_{10} (~15 kcal mol^{-1} for MSINDO and ~5 kcal mol^{-1} experimentally) would likely result in inaccurate conclusions when comparing the dynamics of the reactions at the various sites.

With the goal of obtaining more meaningful results in direct-dynamics studies of F+alkane reactions, we have derived a SRP-MSINDO Hamiltonian specific to that family of reactions that possesses higher accuracy than the standard Hamiltonian. The parameter set for this Hamiltonian has been derived using *ab initio* information of the energetically accessible regions of the F+CH_4 and F+C_2H_6 potential-energy surfaces at the conditions of extant experiments, in addition to the reaction energies of all of the reactions studied here. The *ab initio* characterization of the potential-energy surface of the $F+CH_4 \rightarrow HF+CH_3$ reaction was carried out via scans of the breaking and forming bonds in a collinear geometry. The forming H-F bond distance was scanned from its value at the MP2/aug-cc-pVDZ transition state (1.46 Å) to 3.96 Å at 0.05 Å steps. During this scan, the F-H-C atoms are forced to be collinear, but the remaining degrees of freedom are optimized at the MP2/aug-cc-pVDZ level. A similar scan of the potential-energy surface was performed for the breaking C-H bond from its distance at the transition state obtained with the same electronic-structure level (1.14 Å) to 3.64 Å at 0.05 Å steps. To obtain a better coverage of regions of the potential removed from the collinear approach and incorporate important points of relatively high energy, we scanned the angle between the forming H-F and breaking C-H bonds from 180° (value of the angle at the transition state in MP2/aug-cc-pVDZ calculations) to 90.0° with steps of 1.0°. In this scan, the H-F and C-H coordinates were held fixed at their transition-state values, but the rest of the coordinates were relaxed at the MP2/aug-cc-pVDZ level. A similar *ab initio* characterization of the potential-energy surface of the $F+C_2H_6 \rightarrow HF+C_2H_5$ reaction was performed, including a scan of the H-F bond from the transition state (1.54 Å) to 5.24 Å at 0.05 Å steps and a scan of the C-H bond from the transition state (1.13 Å) to 4.83 Å with the same step size. In all of the F+C_2H_6 potential-energy scans, the forming and breaking bonds were constrained to the corresponding angle at the transition state (161.3°), but the C_2H_5 moiety was relaxed at the MP2/aug-cc-pVDZ level. Since the MP2/aug-cc-pVDZ level of theory does not provide a highly-accurate description of the

F+alkane reaction energetics, we have recalculated the energy of each of the points of the MP2/aug-cc-pVDZ scans at the CCSD(T)/aug-cc-pVDZ level.

Preliminary reparameterization efforts using the CCSD(T)/aug-cc-pVDZ energies of the 5 scans described before resulted in rather inaccurate H-F and C-C equilibrium bond distances. To avoid those deficiencies, we subsequently included in the *ab initio* grid a scan of the HF molecule internuclear distance from 0.735 Å to 1.275 Å and a scan of the C-C bond in ethane from 1.430 Å to 1.620 Å. Both scans used a 0.010 Å step size. The grid of *ab initio* information used for the reparameterization of the MSINDO Hamiltonian also contained the reaction energies of all of the reactions in Table 5.1. Starting with the parameters of the F, H, and C atoms in the standard MSINDO Hamiltonian, we used a non-linear least-squares procedure to obtain a new set of parameters for which the differences between the CCSD(T)/aug-cc-pVDZ energies of the points in the grid described before and semiempirical energies were minimum. The parameters were not constrained at any point during the procedure. After several initial attempts, it was determined that attributing different weights to various points of the *ab initio* grid resulted in an overall better fit. Thus, the final set of SRP parameters was obtained by weighting the points of the entrance channel of the F+CH_4 reaction and the exit channel of the F+C_2H_6 reaction 10 times more heavily than the rest of the points. The SRP parameters obtained in this way are shown in comparison with the original MSINDO parameters in Table 5.3. The relative differences between the original parameters and the new SRP-MSINDO parameters are on average 14%, with only one of the 28 parameters varying by more than a factor of two.

The improvement in the accuracy of the MSINDO Hamiltonian when using the set of parameters derived here for the F+alkane reactions can be clearly seen in Tables 5.1 and 5.2. Table 5.1 shows that while the original MSINDO Hamiltonian grossly overestimates the CCSD(T)/aug-cc-pVDZ energy of many of the F+alkane reactions studied here, the SRP Hamiltonian is in substantially better agreement, exhibiting an accuracy comparable to MP2/aug-cc-pVDZ. Remarkably, the large errors in the differences between the reaction energies of primary and secondary, and primary and tertiary sites obtained with the MSINDO Hamiltonian are nicely corrected in the SRP-MSINDO Hamiltonian. Regarding the transition state locations and energies, SRP-

MSINDO also exhibits better agreement with the CCSD(T)/aug-cc-pVDZ results than the original MSINDO Hamiltonian or even MP2/aug-cc-pVDZ results. Notably, the SRP-MSINDO F-H bond distance is 6% shorter than the CCSD(T)/aug-cc-pVDZ result, which is roughly half the deviation of the MP2/aug-cc-pVDZ result. Moreover, the SRP-MSINDO Hamiltonian does not exhibit a barrier for the F+C_2H_6 reaction, which is in agreement with the CCSD(T)/aug-cc-pVDZ predictions (Fig. 5.1). This can be verified in Fig. 5.2a, where we show a contour plot of SRP-MSINDO energies for the same region of the potential-energy surface of the F+C_2H_6 reaction as that displayed in Fig. 5.1 with CCSD(T)/aug-cc-pVDZ energies. In contrast with the absence of an appreciable barrier on the classical potential-energy surface predicted by both CCSD(T)/aug-cc-pVDZ and SRP-MSINDO, the contour plot for MP2/aug-cc-pVDZ (Fig. 5.2b) clearly shows a transition state for this collinear approach in which the geometry of the inactive C_2H_5 moiety is fixed to its geometry in reagents.

Table 5.3. List of MSINDO and SRP-MSINDO parameters that were involved in the SRP development.[a]

Parameter	MSINDO	SRP-MSINDO
ζ_s^U (H)	1.006	1.11357
ζ_s (H)	1.1576	1.0749
K_s (H)	0.1449	0.1713
I_s (H)	-0.5000	-0.4841
ζ_s^U (C)	1.6266	1.2780
ζ_p^U (C)	1.5572	1.6829
ζ_s (C)	1.7874	2.2545
ζ_p (C)	1.677	1.6671
K_s (C)	0.0867	.09632
τ_{1s} (C)	5.083	5.1193
ε_{1s} (C)	10.43	10.6686
I_s (C)	-0.8195	-0.7793
I_p (C)	-0.3824	-0.3872
ζ_s^U (F)	2.3408	2.1754
ζ_p^U (F)	2.2465	2.2079
ζ_s (F)	2.4974	2.8586
ζ_p (F)	2.351	2.4626
K_s (F)	0.1769	0.1602
τ_{1s} (F)	8.6043	8.6438
ε_{1s} (F)	25.19	28.2496
I_s (F)	-2.0238	-2.4281
I_p (F)	-0.6868	-0.7015
$\alpha(1)$ (H)	0.3856	0.3811
$\alpha(2)$ (H)	0.5038	0.3432
$\alpha(1)$ (C)	0.4936	0.5465
$\alpha(2)$ (C)	0.6776	0.3410
$\alpha(1)$ (F)	0.1521	0.1489
$\alpha(2)$ (F)	0.1059	0.0031

[a] For a definition of parameters, please see Ref. [35].

A more complete calibration of the accuracy of the SRP-MSINDO Hamiltonian with respect to the CCSD(T)/aug-cc-pVDZ results that we have used as a benchmark is presented in Figures 5.3 and 5.4. Figure 5.3 displays the F-H and C-H scans for the $F+CH_4 \rightarrow HF+CH_3$ reaction that have been used in the reoptimization of the MSINDO Hamiltonian parameters as described before. Figure 5.3a shows the region of the potential-energy surface connecting the transition state with reagents. The SRP-MSINDO results deviate from the more accurate CCSD(T)/aug-cc-pVDZ values uniformly by about 0.5 kcal mol^{-1}, and they considerably improve upon the MP2/aug-cc-pVDZ energies. A deficiency of the SRP-MSINDO Hamiltonian is that it is unable to describe the van der Waals' well in the reagents valley predicted by the CCSD(T)/aug-cc-pVDZ method. This well is caused by dispersion interactions between the approaching reagent species, which are known to be difficult to model by all but the most sophisticated treatments of electron correlation. Even though SRP-MSINDO does not capture the well region with excellent accuracy, it represents a great improvement over an earlier SRP-PM3 Hamiltonian published before.[18] That Hamiltonian exhibited a sharp, deep well in the region of the potential-energy surface preceding the transition state. This well did not appear to affect classical-trajectory calculations at low energies, however, the appearance

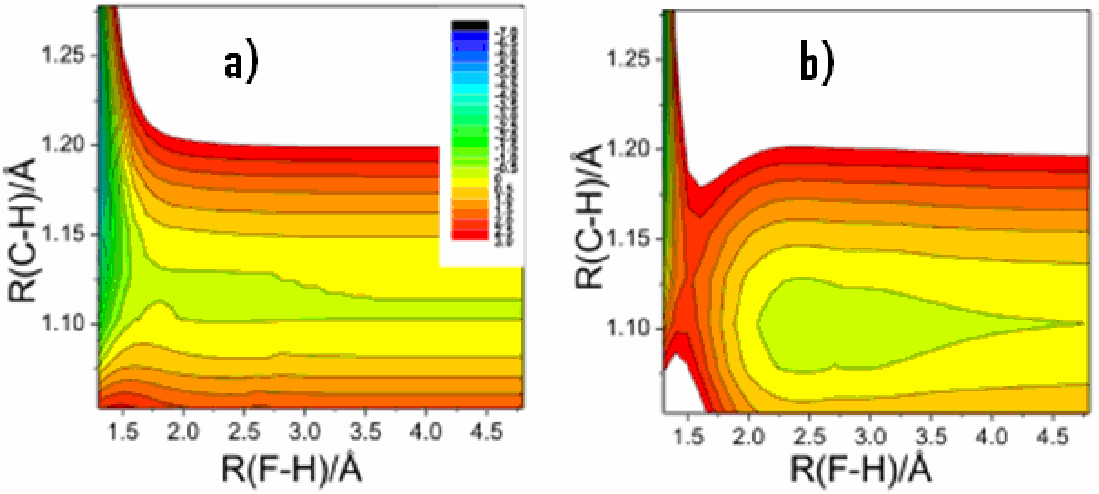

Figure 5.2: Contour plot of the potential-energy surface of the $F+C_2H_6 \rightarrow HF+C_2H_5$ reaction at the SRP-MSINDO (a) and MP2/aug-cc-pVDZ (b) levels. F-H is the forming bond and C-H is the breaking bond. These bonds are held collinear in the scans and the rest of the variables are fixed at their values in reagents. The scale of the z-axis (potential energy) is the same as in Fig. 1.

of that spurious well in the SRP-PM3 Hamiltonian points out the necessity of providing a dense coverage of *ab initio* information when deriving SRP Hamiltonians.

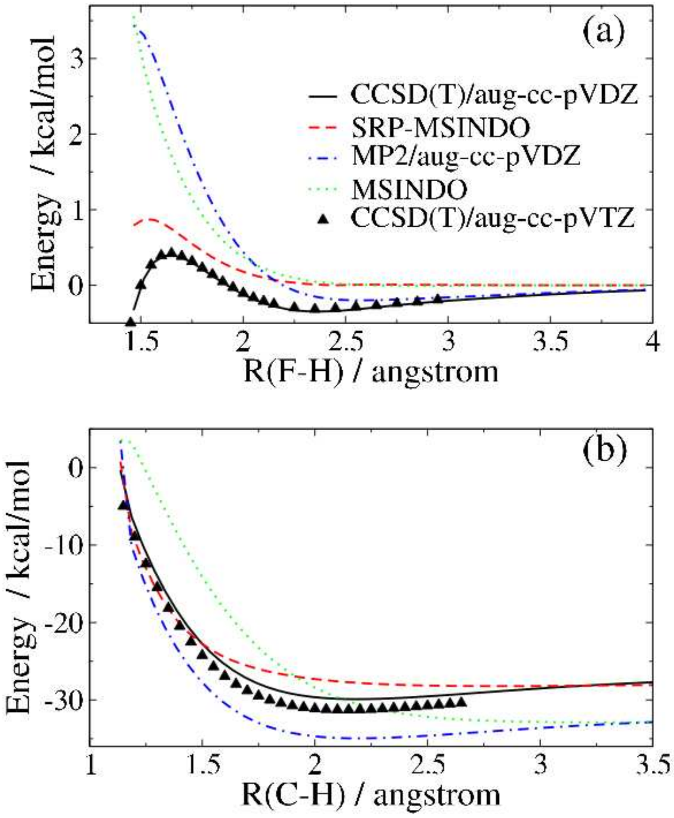

Figure 5.3: Potential-energy surface profiles of the $F+CH_4 \rightarrow HF+CH_3$ reaction calculated at various levels of theory. (a) Represents the region of the potential-energy surface connecting the transition state with reagents and (b) is for the region connecting the transition state with products.

Figure 5.3b shows the region of the $F+CH_4 \rightarrow HF+CH_3$ potential-energy surface (PES) connecting the transition state with products. All of the methods predict a precipitous fall in the potential energy with small increases in the C-H coordinate right after the transition state. Much as in the reagents region, while SRP-MSINDO is quite close to the CCSD(T)/aug-cc-pVDZ energies, the agreement is not quantitative. Notably, SRP-MSINDO is unable to describe the well caused by dipole/quadrupole electronic interactions between the separating HF and CH_3 species in the products valley.

Comparisons between similar potential-energy profiles predicted by various electronic-structure methods for the F+C_2H_6 → HF+C_2H_5 reaction are shown in Fig. 5.4. The overall conclusions about the accuracy of the SRP-MSINDO Hamiltonian stemming from the figure are analogous to those mentioned above for the F+CH_4 → HF+CH_3 reaction. SRP-MSINDO reproduces CCSD(T)/aug-cc-pVDZ energies with better accuracy than MP2/aug-cc-pVDZ, except for the shallow potential-energy wells in the reagents and products valleys. Figures 5.3 and 5.4 also include CCSD(T) points calculated with the larger aug-cc-pVTZ basis set in an attempt to calibrate the error of the SRP Hamiltonian emerging from having used the relatively small aug-cc-pVDZ basis set in the CCSD(T) calculations used in the fit. Interestingly, use of the aug-cc-pVTZ basis set does not have a dramatic impact on the CCSD(T) energies in reagents, as shown in Figures 5.3(a) and 5.4(a). In products, use of the larger basis set results in a slightly more exothermic energy profile. For instance the F+CH_4→HF+CH_3 reaction is predicted by CCSD(T)/aug-cc-pVTZ calculations to be 1.3 kcal mol^{-1} more exothermic than by CCSD(T)/aug-cc-pVDZ. For the F+C_2H_6→HF+C_2H_5 reaction, the difference between the aug-cc-pVDZ and –TZ exothermicities increases to 1.7 kcal mol^{-1}. These basis-set studies give a measure of the limits of the accuracy of the SRP MSINDO

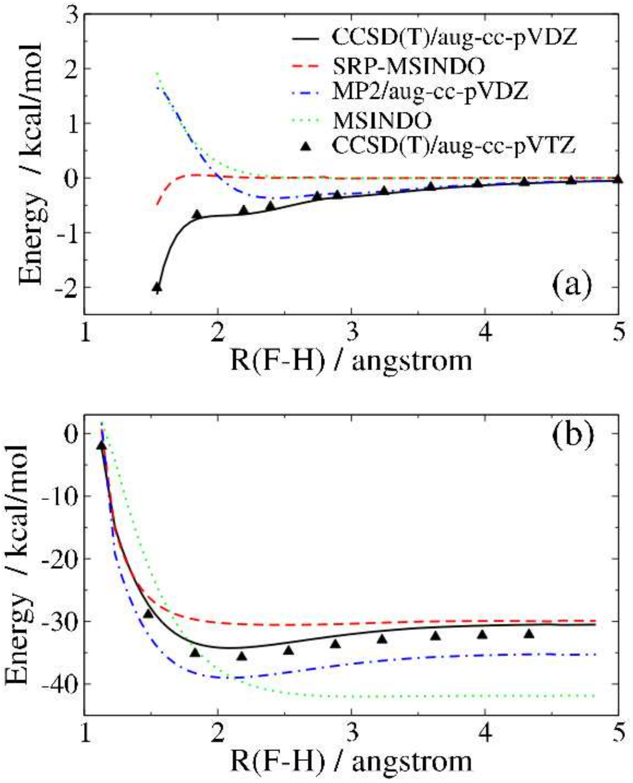

Figure 5.4: Potential-energy surface profiles of the F+C_2H_6→HF+C_2H_6 reaction calculated at various levels of theory. (a) Represents the region of the potential-energy surface connecting the transition state with reagents and (b) is for the region connecting the transition state with products.

Hamiltonian stemming from the limited accuracy of the CCSD(T)/aug-cc-pVDZ calibration data points.

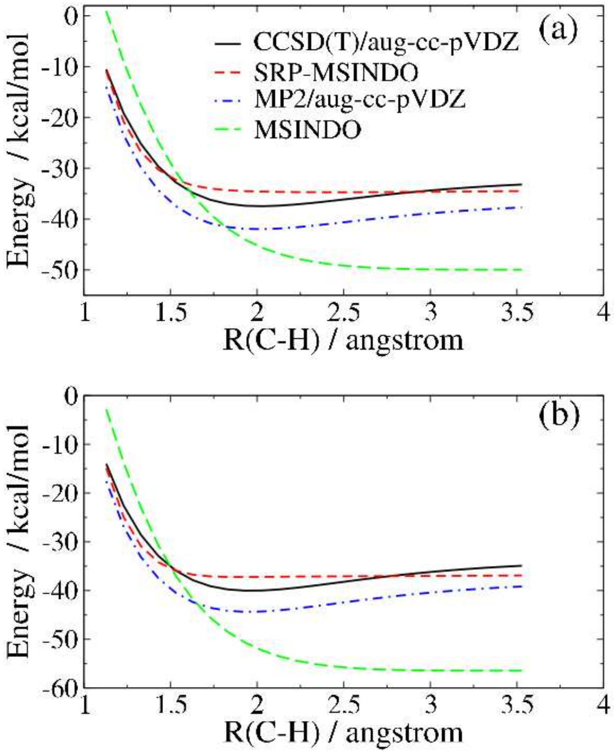

Figure 5.5: Profiles of the region of the potential-energy surface connecting the transition state with products for the $F+C_3H_8 \rightarrow HF+CH_3CHCH_3$ (a) and $F+i\text{-}C_4H_{10} \rightarrow HF+t\text{-}C_4H_9$ (b) reactions calculated at various levels of theory.

Figures 5.3 and 5.4 show the performance of the SRP-MSINDO Hamiltonian in the chemical reactions for which *ab initio* information was explicitly included in the reparameterization. A test of the idea that SRP Hamiltonians can be derived for families of reactions without the need to include *ab initio* information for all the members of the family can therefore be provided by examining a comparison between CCSD(T)/aug-cc-pVDZ scans for the $F+C_3H_8$ and $F+i\text{-}C_4H_{10}$ reactions and the corresponding SRP-MSINDO energies. This is what we show in Figure 5.5 for the regions of potential-energy surface connecting the transition state with products for the $F+C_3H_8 \rightarrow HF+CH_3CHCH_3$ (Fig. 5.5a) and $F+i\text{-}C_4H_{10} \rightarrow HF+C(CH_3)_3$ (Fig. 5.5b). We choose to show the profiles of the abstractions at the secondary and tertiary sites in these larger reactions because explicit information about these abstraction channels other than the reaction energies was not included in the SRP optimization, and this therefore poses a more demanding test than the primary channels. The conclusion from Fig. 5.5 is that the SRP Hamiltonian for F+alkane reactions derived in this work using detailed *ab initio* information of only the first two members of the family appears to capture larger reactions of the family with comparable accuracy. This conclusion is particularly important, as it offers a practical way to derive improved semiempirical Hamiltonians for a variety of large-dimensionality chemical reactions with minimal high-level *ab initio* characterization of their PES.

5.3 Direct-dynamics Study

Using the SRP-MSINDO Hamiltonian derived in this work, we have integrated direct quasiclassical trajectories of the F+CH_4, C_2H_6, C_3H_8, and i-C_4H_{10} reactions. Batches of 20,000 trajectories calculated for each system and set of initial conditions except for systems and conditions where experimental information exists, for which we raised the number of trajectories to 50,000. The trajectories have been started with the F atom at a distance of 15 a.u. from the center of mass of the hydrocarbon molecule and stopped when the products are ~15 a.u. apart. The maximum sampling impact parameters are 7.0 a.u., for F+CH_4, and 10 a.u. for F+C_2H_6, F+C_3H_8, and F+i-C_4H_{10} reactions. Initial conditions for the hydrocarbon reagent molecules consider initial zero-point energy and no rotation, and were selected using the VENUS program.[41] The MSINDO Hamiltonian is known to overestimate vibrational frequencies by ~20%,[16, 20] so we have used VENUS to select initial coordinates and momenta that correspond to 80% of the MSINDO zero-point energy in each of the normal modes. This procedure gives the alkane molecules zero-point energy that corresponds to the experimental values.

From analysis of the atomic initial and final coordinates and momenta, we have calculated a variety of dynamics properties, including partitioning of energy in products, angular distributions, and opacity functions. We first show comparisons with experiment with the goal of calibrating the accuracy of the SRP-MSINDO method for dynamics calculations and subsequently present the results of a comparative study of the dynamics of the various F+alkane reactions studied in this work.

5.3.1 Comparison with experiments

Figure 5.6 shows the HF vibrational distributions arising in the $F+CH_4 \rightarrow HF+CH_3$ (Fig. 5.6a) and $F+C_2H_6 \rightarrow HF+C_2H_5$ (Fig. 5.6b) reactions at 1.8 and 3.2 kcal mol^{-1} collision energy (E_{coll}), respectively. The HF vibrational distributions of the F+CH_4 reaction show agreement between SRP-MSINDO and the experimental results of Nesbitt and co-workers,[4] with both distributions being clearly inverted and peaking at $\nu'=2$. Quantitatively, the average HF vibrational energy (including zero-point energy) in the SRP-MSINDO energy is 26.7±0.2 kcal mol^{-1}, while the experiment is 27.4 kcal mol^{-1}.

The figure also shows the results calculated using quasiclassical trajectories the original MSINDO Hamiltonian at 3.2 kcal mol^{-1}. This collision energy is slightly larger than the one used in the experiment and SRP-MSINDO calculations because, as previously stated, MSINDO calculations at 1.8 kcal mol^{-1} do not provide significant reactive due to the high reactive barrier of this method. 3.2 kcal mol^{-1} represents a collision energy above the barrier in the MSINDO calculations similar to that in experiment. MSINDO clearly underestimates the level of vibrational excitation going into HF vibration, with the peak of the distributions being at ν'=1. Figure 5.3b shows that the origin of this discrepancy with experiment is due to the incorrect shape of the MSINDO potential-energy surface, and not the reaction exothermicity.

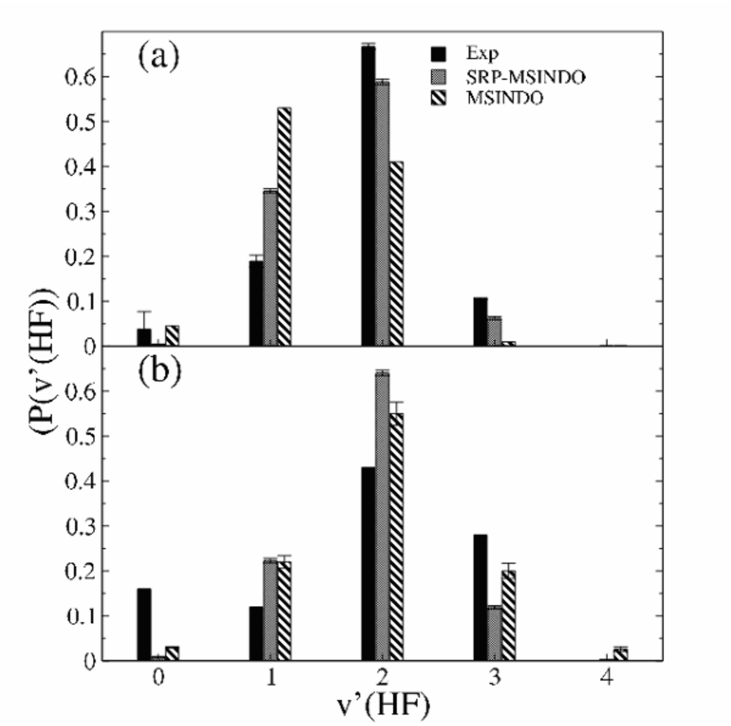

Figure 5.6: HF vibrational state distribution for the $F+CH_4 \rightarrow HF+CH_3$ reaction at E_{coll}=1.8 kcal mol^{-1} (a), and the $F+C_2H_6 \rightarrow HF+C_2H_5$ reaction at E_{coll}=3.2 kcal mol^{-1}. The experimental results in (a) are taken from Ref. [4] and in (b) from Ref. [5]. The collision energy in (a) for the MSINDO results is 3.2 kcal mol^{-1} (see text).

Figure 5.6b shows the SRP-MSINDO HF vibrational distribution arising from the $F+C_2H_6$ reaction at E_{coll}=3.2 kcal mol^{-1} in comparison to the experiments by the Nesbitt group.[5] To our knowledge, this is the first time that full dynamics calculations are used to simulate those experiments. While the vibrational distributions do not agree quantitatively, the peak of both distributions still occurs at ν'=2, neither shows significant population in ν'=4, and the average HF vibrational energies are in reasonable agreement with each other (28.7±0.2 kcal mol^{-1} for SRP-MSINDO and 25.7 kcal mol^{-1} in the experiment, including zero-point energy). The main source of discrepancy between theory and experiment occurs for ν'=0, where the experiments report 16% of the population, but our calculations only yield 1%. An intriguing aspect of the experiment is the bimodal nature of the vibrational distributions, with ν'=1 showing less population than ν'=0 and ν'=2. In the experiments, it was discussed that the presence of a larger alkyl fragment than in the case of the F+CH_4 reaction might elicit a second mechanism, in addition to a direct, impulsive release of energy in the onset of product separation, that would channel energy from the 'active' F-H-C moiety into the alkyl fragment via intramolecular vibrational redistribution (IVR). This second mechanism would act to exclusively populate the HF(ν'=0) state. Even though classical trajectories are known to accelerate the rate of IVR, the presence of the speculated mechanism is not seen in the present calculations, so the intriguing bimodality of the experimental distributions must emerge from errors in the SRP-MSINDO Hamiltonian or in our classical treatment of the nuclear dynamics. To verify that the absence of significant population in HF(ν'=0) is not associated with zero-point energy leakage from the C_2H_6 molecule into the newly-formed HF bond, we have integrated trajectories in which C_2H_6 is started with only half or a quarter of the zero-point energy. None of these calculations yields significant population in HF(ν'=0), suggesting that the inability of the calculations to reproduce the subtle bimodality seen in the experiment might be tied to inaccuracies in the SRP-MSINDO Hamiltonian or quantum effects.

Figure 5.6b also shows the results for the MSINDO Hamiltonian. Even though the MSINDO calculations seem to be in good agreement with experiment, analysis of the average energy deposited into HF vibration (33.4 kcal mol^{-1}) shows a relatively large (~7.5 kcal mol^{-1}) overestimation of the experiment (25.7 kcal mol^{-1}). An interesting result is that the HF vibrational distributions obtained with the original MSINDO Hamiltonian in the F+C_2H_6 reaction (Fig. 5.6a) appear to be in better agreement with experiment than in the F+CH_4 reaction (Fig. 5.6b). However, a detailed analysis suggests that the improvement in the agreement with experiment for the F+C_2H_6 reaction is largely fortuitous. As shown in Fig. 5.6a, MSINDO underestimates the amount of vibrational excitation going into HF. This underestimation is fortunately balanced out by the ~10 kcal mol^{-1} overestimation of the reaction exothermicity in the F+C_2H_6 reaction by this method (Table 5.1) so that the amount of energy going into HF seems to agree better with experiment than in the F+CH_4 reaction.

The Liu group has measured additional information about the release of energy into products for the F+CD_4→DF+CD_3, including partition of energy into translation, DF vibration, and DF rotation at various collision energies.[1, 42] A particularity of those measurements is that they correspond to specific internal states of the CD_3 product. This detail challenges a quantitative comparison with our quasiclassical-trajectory results, since no exact technique to map coordinates and momenta of polyatomic molecules into vibrational states currently exists. In addition, classical-dynamics calculations suffer from rapid IVR, which further complicates the determination of the exact final quantum state of a polyatomic vibration via projection of final coordinates and momenta into harmonic normal modes.[30] Even though establishing comparisons between quasiclassical-trajectory calculations and the CD_3 state-selected experiments is not possible at a quantitative level, a comparison of the trends can provide further insight into the accuracy of the calculations. The Liu group have provided insight into the dependence of energy partitioning in products with collision energy for the F+CD_4→DF+CD_3(0000,N~4) reaction.[42] These state-specific results indicate that the amounts of HF rotational energy and products relative translational energy increase with increasing collision energy. On the other hand, HF vibrational excitation decreases with collision energy.

Table 5.4 presents the calculated results of energy partitioning in products at the same collision energies measured in the experiments. The results include averages over all of the trajectories, and of the trajectories in which CD_3 emerges with less energy than its nominal zero-point energy (values between parentheses). The restriction of the analysis to trajectories with low CD_3 is a rough attempt to represent ground-state CD_3, as measured in the experiment. Regardless of the analysis method, the calculated trends agree with experiment: while DF rotational and relative translational energies increase with collision energy, DF vibrational energy decreases with increasing collision energy. Even though the calculations reproduce the experimental trends, limitations in the accuracy of the calculated energy partitioning to DF rotation and relative translation are evident. In the experiment, the largest amount of DF rotational excitation measured was 1.4 kcal mol^{-1} (at E_{coll}=8.37 kcal mol^{-1}), which is notably smaller than the calculated results irrespective of the way trajectories are analyzed. In addition, the largest average final relative translational energy measured was 9.8 kcal mol^{-1} (at E_{coll}=8.37 kcal mol^{-1}),

Table 5.4. Calculated average energies in products in the F+CD$_4$ → DF+CD$_3$ reaction.[a,b]

E_{coll} / kcal mol^{-1}	$< E'_{V(DF)}>^c$	$< E'_{R(DF)}>$	$< E'_T>$	$< E'_{CD3}>$
1.48	25.6(28.0)	2.7(3.1)	7.7(7.6)	13.1(10.5)
2.77	24.7(27.5)	3.3(3.5)	9.0(8.9)	13.4(10.5)
5.37	23.1(26.2)	4.1(4.2)	12.0(11.8)	13.5(10.5)
8.36	21.9(25.7)	4.9(4.9)	15.1(14.6)	14.1(10.6)

[a] All energies in kcal mol^{-1}

[b] Values between parentheses correspond to trajectories in which CD$_3$ arises with less energy that its nominal zero point energy.

[c] Calculated from the bottom of the potential well of DF.

also smaller than the calculated results. These results clearly point out inaccuracies in the calculations, which originate from the potential-energy surface, the quasiclassical-trajectory method, or more likely a combination of both. Part of the errors in the quasiclassical trajectories might emerge from excessive leakage of the energy of reagent normal modes that should largely be adiabatic into the reaction coordinate. In an attempt to quantify the possible errors introduced by excessive zero-point-energy leakage, we have performed trajectory calculations at E_{coll}=5.37 kcal mol^{-1} with varying degrees of initial vibrational excitation in CD$_4$. Calculations with one half or one quarter of the initial CD$_4$ vibrational energy used in the calculations of Table 5.4 indicate a correlation between initial CD$_4$ vibration and final DF and CD$_3$ internal energy. However, the amount of energy released

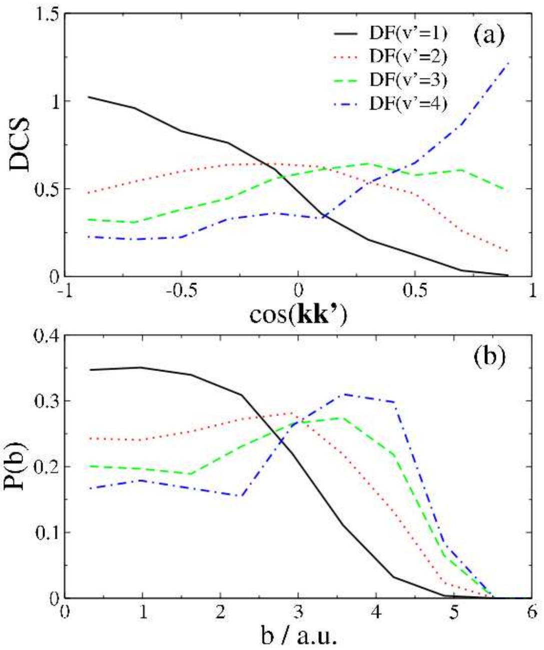

Figure 5.7: Calculated DF vibrational state-specific angular distributions in terms of differential cross sections (a), and opacity functions (b) for the F+CD$_4$ → DF+CD$_3$ reaction at E_{coll}=5.37 kcal mol^{-1}. The distributions are normalized for area. Absolute cross sections for the DF(ν')=1, 2, 3, and 4 states are (a.u.) 10.4, 21.4, 14.3, and 1.6, respectively.

into product relative translation is unaffected by the amount of initial vibrational energy in CD_4, suggesting that the overestimation of experiments by our calculations in this property discussed before is likely a weakness of the SRP-MSINDO Hamiltonian derived in this work.

In addition to energy partitioning in products, the CD_3(0000, N~4) state-specific measurements provided information about the angular distributions. In particular, DF vibrational state-resolved angular distributions clearly showed an evolution from backward scattering to sideways and forward scattering with increasing vibrational excitation in DF.[1] In Fig. 5.7a, we show DF vibrational-specific angular distributions obtained in the $F+CD_4 \rightarrow DF+CD_3$ reaction at E_{coll}=5.37 kcal mol^{-1}. The calculations replicate the trend that highly vibrationally excited DF has a larger propensity than vibrationally colder DF to scatter in the forward direction. This is an important result, as the experiments speculated that forward scattering for DF(ν'=4) might herald the appearance of a reactive resonance. The presence of a backward → forward trend with increasing DF excitation in our classical calculations indicates that a reactive resonance does not seem necessary to obtain this trend. Instead, the DF vibrational state-specific opacity functions in Fig. 5.7b show that the trend can be partially explained by the preference of collisions at longer impact parameters to form vibrationally excited DF. These reactions at long impact parameters also provide more forward scattering, as F+alkane reactions are dominated by a direct reaction mechanism.

In summary, comparisons between the predictions of the SRP-MSINDO Hamiltonian derived in the work and experimental results on the $F+CH_4$, $F+CD_4$ and $F+C_2H_6$ reactions reveal that the Hamiltonian captures the broader aspects of the dynamics, including the amount of vibrational energy partitioned into the newly-formed bond and angular distributions. Even though the agreement with experiment is not quantitative in some properties, all of the experimental trends are satisfactorily reproduced by the calculations. In the following, we present a comparative study between the dynamics of the $F+CH_4$, $F+C_2H_6$, $F+C_3H_8$, and F+i-C_4H_{10} reaction with the goal of identifying how the length of the alkane molecule and the site of abstraction influence the reaction dynamics**.**

5.3.2 Comparative dynamics of F+alkane reactions

Figure 5.8a shows the HF vibrational distributions of all the channels of all 4 chemical reactions investigated in this work at E_{coll}=3.2 kcal mol^{-1}. Leaving the F+CH_4 reaction aside, the trend for rest of the reactions at primary abstraction sites is that HF vibrational excitation decreases with increasing size of the reagent alkane molecule. Since the exothermicity of the primary abstraction reaction is very similar for all F+alkane reactions studied here except F+CH_4, the conclusion offered by these results is that the size of the alkane molecule helps channel energy in modes other than HF vibration. Comparing the HF vibrational distributions for abstraction at primary *vs.* secondary and tertiary sites reveals that energy release to HF vibration increases along the primary→secondary→tertiary sequence. This result bodes well with the corresponding exothermicities.

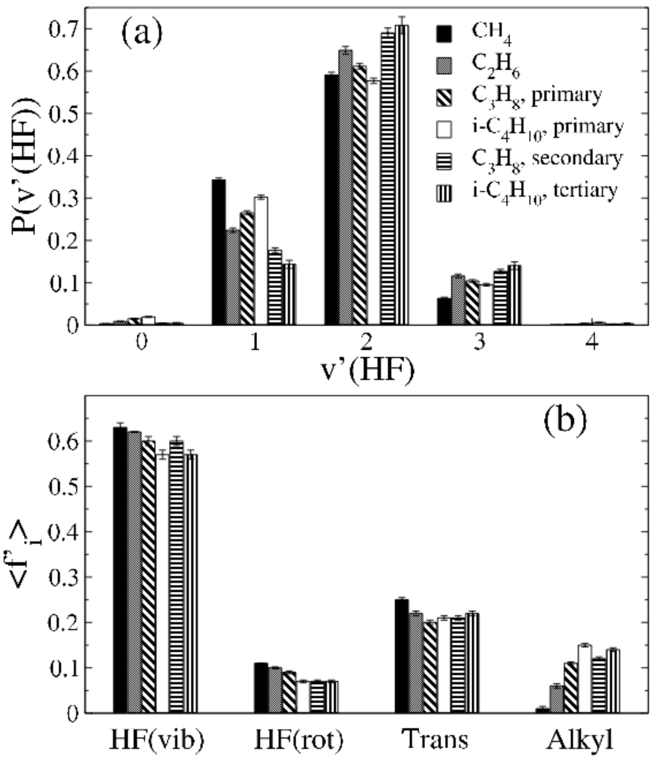

Figure 5.8: Calculated HF vibrational state distributions (a), and average fractions of available energy in products (b) for various F+alkane reactions at E_{coll}=3.2 kcal mol^{-1}. The average fractions of alkyl internal energy and HF vibrational energy in (b) are calculated from the corresponding zero-point energy levels.

To gain further insight into these trends, we show in Fig. 5.8b fractions of available energy into various products degrees of freedom for all of the channels in all of the reactions studied at E_{coll}=3.2 kcal mol^{-1}. The figure shows that HF vibration is the preferred mode for energy deposition in products, followed by relative translation. In comparison, partitioning to HF rotation and internal alkyl energy is relatively small. Examination of the average fractions of energy in products for the primary channels of all reactions indicates a general trend to decrease the fraction of energy going into HF vibration, rotation, and translation with the size of the reagent alkane molecule. Consequently, the fractions of energy going into the alkyl fragment rise rapidly for larger alkane molecules. This result suggests that the modes of the alkyl moiety that do not participate directly in the bond breakage/formation process governing F+alkane reactivity are not entirely orthogonal to the reaction coordinate. The origin of the fact that energy partitioning into the alkyl degrees of freedom is enhanced for reactions involving larger alkanes is likely the rapid growth of low-energy normal modes. These large-amplitude vibrational modes of the forming alkyl moiety can effectively couple to the reaction coordinate and absorb energy released in the reactive process. Comparison of energy partitioning into the alkyl product between primary and secondary sites in the F+C_3H_8 reaction and primary and tertiary sites in the F+i-C_4H_{10} reaction shows a relative insensitivity of the fractions to the abstraction site. Therefore, the fact that the HF vibrational distributions exhibited in Fig. 5.8a are more excited for secondary and tertiary sites than for primary sites is primarily driven by the larger exothermicity of the former sites.

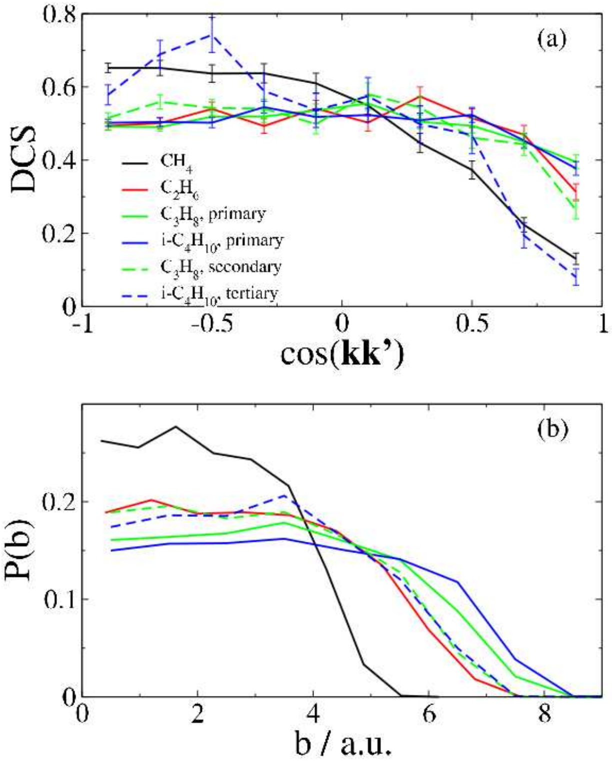

Figure 5.9: Calculated angular distributions expressed in terms of differential cross sections (a) and opacity functions (b) for various F+alkane reactions at E_{coll}=3.2 kcal mol^{-1}. The distributions are normalized for area. Absolute cross sections for the F+CH_4, C_2H_6, C_3H_8, and i-C_4H_{10} reactions are (a.u.) 50.9, 96.2, 120.7, and 142.0, respectively.

Finally, we present the angular distributions of the various reactions and channels at E_{coll}=3.2 kcal mol^{-1} in Fig. 5.9a, and the corresponding opacity functions in Fig. 5.9b. The angular distributions show a larger flux in the backward hemisphere than in the forward hemisphere. This result, in combination with the large reaction-probabilities at low impact parameters in Figure 5.9b, suggests that a direct rebound-like mechanism in which the HF product travels in a direction opposite to that followed by the F atom is more probable than a mechanism in which the F atom abstracts a hydrogen atom as it flies past the molecules without significantly changing its direction of travel. Leaving the results of the F+methane reaction aside, we see that the angular distributions for all of the reactions at primary sites essentially overlap. This result suggests that the reaction mechanism is largely the same for all of these abstraction reactions. A more interesting result emerges when comparing the angular distributions of the primary and secondary channels in the $F+C_3H_8$ reaction; reaction at secondary sites result in slightly more backward angular distributions than at primary sites. This trend is exaggerated when comparing primary and tertiary sites in the F+i-C_4H_{10} reaction, where the angular distribution for tertiary sites is clearly more backward than that of the primary sites. The origin of such a result seems to be tied to the location of the secondary and tertiary sites of the propane and i-butane molecules with respect to primary sites. Primary sites are more removed from the center of mass than secondary or tertiary sites, thereby enabling reactions at longer impact parameters. In these more peripheral reactions on primary sites, the fluorine atom can abstract a primary hydrogen atom without largely changing its momentum, which enhances forward scattering. This mechanism is popularly known as stripping dynamics. The presence of enhanced stripping dynamics in abstractions at primary sites due to a more peripheral reaction is reinforced by the opacity functions in Fig. 5.9b. In that figure, one can see that reactions at primary sites in $F+C_3H_8$ and F+i-C_4H_{10} collisions do indeed take place at longer impact parameters than in the corresponding secondary and tertiary sites. The figure can also be used to provide an estimate of the effective size of the alkane molecules used in this work. In effect, comparison of the maximum impact parameters leading to reaction for all the primary abstraction sites shows the expected trend that the effective molecular size increases in the methane → ethane → propane → i-butane sequence.

5.4 Concluding remarks

We have used *ab initio* calculations to map the potential-energy surface of the $F+CH_4$ and $F+C_2H_6$ reactions in areas predominantly around the minimum-energy reaction path, but also exploring other areas of the PES that are energetically accessible in previously reported experimental studies. Using this *ab initio* information, we have reparameterized the MSINDO semiempirical Hamiltonian to correct the largest errors of this electronic-structure method in its description of the F+alkane reactions, particularly the sharp overestimation of the exothermicities of the reactions. The empirical parameter set specific to the F+alkane hydrogen abstraction reactions endows the MSINDO Hamiltonian with a good degree of accuracy in comparison with CCSD(T)/aug-cc-pVDZ energies. Except for the shallow intermolecular wells in the reagents and products valleys, the SRP-MSINDO Hamiltonian is shown to outperform the predictions of MP2/aug-cc-pVDZ calculations for the regions of the potential-energy surface covered in our study.

Using this computationally-inexpensive SRP-MSINDO Hamiltonian, we have carried out an extensive direct-dynamics quasiclassical trajectory study of the F+methane, ethane, propane and i-butane reactions. To test the accuracy of the Hamiltonian in dynamics calculations, we have compared a variety of calculated dynamics properties with available experiments, including HF vibrational distributions, energy partitioning in products and vibrational state-specific angular distributions. The SRP-MSINDO Hamiltonian is seen to reproduce all of the trends found in the experiment, but the agreement with experiment is not always quantitative, particularly in regards to the amount of energy released to HF rotation and relative translation.

Comparison of the dynamics of the hydrogen-abstraction F+alkane reactions studied in this work reveals a number of interesting results. First, HF vibrational distributions of reactions at primary sites become increasingly colder as the size of the reagent alkane molecule increases. This result seems to be tied to the increase in the number of energy modes that larger alkyl molecules can couple to the reaction coordinate, which effectively absorb some of the energy released during reaction. On the other hand, the HF vibrational distributions become increasingly hotter for reactions along the primary → secondary → tertiary abstraction-site sequence. This is a consequence of the increase in exothermicity along that sequence, and not to a difference in the relative energy partitioning in products for the various sites. Analysis of angular distributions and opacity functions helps elucidate the broader aspects of the reaction mechanisms. Reactions at primary sites are more peripheral than at secondary and tertiary sites, and therefore exhibit less backward scattering than the more central reactions.

A major conclusion of this work is that reparameterization of a semiempirical Hamiltonian is an attractive strategy to enable dynamics studies of relatively large chemical reactions. Our study shows that by using extensive *ab initio* information of only the smallest members of a family of chemical reactions, one can generate electronic-structure methods that are reasonably accurate for homologous reactions in the family. While the semiempirical Hamiltonians are not appropriate for extremely precise studies in which subchemical accuracy is required in the potential-energy surface, this paper contains evidence that they can capture most of the reaction-dynamics trends.

The work presented in this chapter concludes our investigation of gas-phase reaction dynamics. However in Chapter 6 we use a very similar SRP-MSINDO Hamiltonian to the one that has been developed here to serve as the quantum mechanical method in a QM/MM study of the reactions between impinging fluorine atoms and alkanethiolate self-assembled monolayers.

References

1. J. J. Lin, J. Zhou, W. Shiu and K. Liu, Science **300** (5621), 966 (2003).
2. J. P. Camden, H. A. Bechtel, D. J. Ankeny Brown, M. R. Martin, R. N. Zare, W. Hu, G. Lendvay, D. Troya and G. C. Schatz, J. Am. Chem. Soc. **127** (34), 11898-11899 (2005).
3. W. R. Simpson, T. P. Rakitzis, S. A. Kandel, A. J. Orr-Ewing and R. N. Zare, J. Chem. Phys. **103** (17), 7313 (1995).
4. W. W. Harper, S. A. Nizkorodov and D. J. Nesbitt, J. Chem. Phys. **113** (9), 3670-3680 (2000).
5. E. S. Whitney, A. M. Zolot, A. B. McCoy, J. S. Francisco and D. J. Nesbitt, J. Chem. Phys. **122** (12), 124310-124310 (2005).
6. L. Wen, H. Cunshun, M. Patel, D. Wilson and A. Suits, J. Chem. Phys. **124** (1), 11102 (2006).
7. D. F. Varley and P. J. Dagdigian, J. Phys. Chem. **100** (11), 4365-4374 (1996).
8. S. L. Mielke, K. A. Peterson, D. W. Schwenke, B. C. Garrett, D. G. Truhlar, J. V. Michael, M.-C. Su and J. W. Sutherland, Phys. Rev. Lett. **91** (6), 063201 (2003).
9. X. Wang, W. Dong, X. Chunlei, L. Che, X. Wang, P. Casavecchia, X. Yang, B. Jiang, D. Xie, S.-Y. Lee, D. H. Zhang, J.-H. Werner and M. H. Alexander, Science **322** (5901), 573 (2008).
10. K. Bolton and H. L. Hase, in *Modern Methods for Multidimensional Dynamics Computations in Chemistry*, edited by D. L. Thompson (World Scientific, Singapore, 1998), pp. 143.
11. T. Bredow and K. Jug, Theor. Chem. Acc. **113** (1), 1-14 (2005).
12. A. Gonzalez-Lafont, T. N. Truong and D. G. Truhlar, J. Phys. Chem. **95** (12), 4618-4627 (1991).
13. W. Hu, G. Lendvay, D. Troya, G. C. Schatz, J. P. Camden, H. A. Bechtel, D. J. A. Brown, M. R. Martin and R. N. Zare, J. Phys. Chem. A **110** (9), 3017-3027 (2006).
14. G. H. Peslherbe and W. L. Hase, J. Chem. Phys. **104** (20), 7882 (1996).
15. T. Yan, C. Doubleday and W. L. Hase, J. Phys. Chem. A **108** (45), 9863-9875 (2004).
16. D. Troya and E. Garcia-Molina, J. Phys. Chem. A **109** (13), 3015-3023 (2005).
17. D. Troya, J. Phys. Chem. A **109** (26), 5814-5824 (2005).
18. J. P. Camden, H. A. Bechtel, D. J. A. Brown, M. R. Martin, R. N. Zare, W. Hu, G. Lendvay, D. Troya and G. C. Schatz, J. Am. Chem. Soc. **127** (34), 11898-11899 (2005).
19. D. Troya and P. J. E. Weiss, J. Chem. Phys. **124** (7), 74313 (2006).
20. J. P. Layfield, M. D. Owens and D. Troya, J. Chem. Phys. **128** (19), 194302-194312 (2008).
21. J. P. Layfield and D. Troya, Chem. Phys. Lett. **In press** (2008).
22. J. H. Parker and G. C. Pimentel, J. Chem. Phys. **51** (1), 91-96 (1969).
23. K.-i. Sugawara, F. Ito, T. Nakanaga, H. Takeo and C. Matsumura, J. Chem. Phys. **92** (9), 5328-5337 (1990).
24. W. Shiu, J. J. Lin, K. Liu, M. Wu and D. H. Parker, The Journal of Chemical Physics **120** (1), 117-122 (2004).

25. W. W. Harper, S. A. Nizkorodov and D. J. Nesbitt, Chem. Phys. Lett. **335** (5-6), 381-387 (2001).
26. J. Zhou, J. J. Lin, W. Shiu, S.-C. Pu and K. Liu, J. Chem. Phys. **119** (5), 2538-2544 (2003).
27. W. Shiu, J. J. Lin, K. Liu, M. Wu and D. H. Parker, J. Chem. Phys. **120** (1), 117-122 (2004).
28. J. Espinosa-Garcia, J. Phys. Chem. A **111** (18), 3497-3501 (2007).
29. D. Troya, J. Millan, I. Banos and M. Gonzalez, J. Chem. Phys. **120** (11), 5181-5191 (2004).
30. J. F. Castillo, F. J. Aoiz, L. Banares, E. Martinez-Nunez, A. Fernandez-Ramos and S. Vazquez, J. Phys. Chem. A **109** (38), 8459-8470 (2005).
31. M. J. Frisch, G. W. Trucks, H. B. Schlegel, G. E. Scuseria, M. A. Robb, J. R. Cheeseman, J. Montgomery, J. A.;, T. Vreven, K. N. Kudin, J. C. Burant, J. M. Millam, S. S. Iyengar, J. Tomasi, V. Barone, B. Mennucci, M. Cossi, G. Scalmani, N. Rega, G. A. Petersson, H. Nakatsuji, M. Hada, M. Ehara, K. Toyota, R. Fukuda, J. Hasegawa, M. Ishida, T. Nakajima, Y. Honda, O. Kitao, H. Nakai, M. Klene, X. Li, J. E. Knox, H. P. Hratchian, J. B. Cross, V. Bakken, C. Adamo, J. Jaramillo, R. Gomperts, R. E. Stratmann, O. Yazyev, A. J. Austin, R. Cammi, C. Pomelli, J. W. Ochterski, P. Y. Ayala, K. Morokuma, G. A. Voth, P. Salvador, J. J. Dannenberg, V. G. Zakrzewski, S. Dapprich, A. D. Daniels, M. C. Strain, O. Farkas, D. K. Malick, A. D. Rabuck, K. Raghavachari, J. B. Foresman, J. V. Ortiz, Q. Cui, A. G. Baboul, S. Clifford, J. Cioslowski, B. B. Stefanov, G. Liu, A. Liashenko, P. Piskorz, I. Komaromi, R. L. Martin, D. J. Fox, T. Keith, M. A. Al-Laham, C. Y. Peng, A. Nanayakkara, M. Challacombe, P. M. W. Gill, B. Johnson, W. Chen, M. W. Wong, C. Gonzalez and J. A. Pople, (Gaussian, Inc., Wallingford, CT, 2004).
32. C. Møller and M. S. Plesset, Physical Review **46** (7), 618 (1934).
33. R. J. Bartlett, Annual Review of Physical Chemistry **32**, 359-401 (1981).
34. D. Troya, J. Phys. Chem. A **111** (42), 10745 (2007).
35. B. Ahlswede and K. Jug, J. Comp. Chem. **20** (6), 572-578 (1999).
36. B. Ahlswede and K. Jug, J. Comp. Chem. **20** (6), 563-571 (1999).
37. Reaction energies calculated from teh experimental heats of formation at 298 K reported in http://www.iupac-kinetic.ch.cam.ac.uk.
38. Reaction energies calculated from teh experimental heats of formation at 298 K reported in http://www.webbook.nist.gov/chemistry.
39. P. Andresen and A. C. Luntz, J. Chem. Phys. **72** (11), 5842-5850 (1980).
40. G. S. Hammond, J. Am. Chem. Soc. **77** (2), 334-338 (1955).
41. W. L. Hase, R. J. Duchovic, X. Hu, A. Komornicki, K. Lim, D. Lu, G. H. Peslherbe, K. N. Swamy, S. R. Vande Linde, A. J. C. Varandas, H. Wang and R. J. Wolf, (1996), pp. 55.
42. J. Zhou, J. J. Lin, W. Shiu and K. Liu, J. Chem. Phys. **119** (10), 4997-5000 (2003).

Chapter 6
Theoretical Study of the Dynamics of F+Alkanethiol Self-Assembled Monolayer Hydrogen-Abstraction Reactions

Reprinted with permission from J. P. Layfield and D. Troya, The Journal of Chemical Physics **132** (13), 134307 (2010). Copyright (2010), American Institute of Physics.

6.1 Introduction

There is a growing interest in the field of reaction dynamics to understand chemical reactions involving an increasing number of degrees of freedom. In particular, the reactions between atomic radicals and gas-phase alkanes have been heavily studied with both theoretical and experimental techniques in recent time.[3-5] This interest in characterizing the dynamics of radical+alkane reactions has progressed to the gas/surface reaction-dynamics field, where a variety of experiments have probed detailed aspects of the dynamics of radical/condensed-phase alkane reactions.[2, 6-15]

Examples of experimental gas/organic-surface reaction-dynamics studies are provided by the ample work by the Minton[6-8] and McKendrick[9-13] groups on the reactions of ground-state oxygen atoms with squalane ($C_{30}H_{62}$, a low-vapor-pressure liquid alkane at room temperature). Using a hyperthermal (up to ~115 kcal mol^{-1} collision energy) beam of atomic oxygen and time-of-flight detection of the product species, the Minton group has investigated a variety of dynamics properties in O+squalane collisions, including energy transfer in inelastic encounters, and product translational-energy and angular distributions.[6-8] McKendrick and co-workers have also studied O+squalane reactions, but using a different experimental set-up.[9-13] In these experiments, low-energy (~3.4 kcal mol^{-1} average collision energy) O(^{3}P) atoms are produced via photodissociation of NO_2 at 355 nm, and laser-induced fluorescence is used to determine the internal-state distributions of the nascent OH product, which complement the product translational and angular information provided by the Minton experiments. Alkane liquids other than squalane have also been investigated by the McKendrick group to understand the role of surface composition and organization on interfacial reaction dynamics.[13]

While squalane has been a benchmark liquid alkane surface in many experimental studies, recent work has investigated the dynamics of O(^{3}P) collisions with an alkanethiol self-assembled monolayer (SAM), which exemplifies semicrystalline organic surfaces.[14] A key finding in this experimental study is that the relatively smooth and highly-ordered SAM surfaces are not as effective as the rougher squalane surface in thermalizing the nascent OH product under identical initial conditions. The study suggests that product species generated in reactions with the rough liquid have a larger probability to experience subsequent collisions with the surface that lead to thermal accommodation of the gas species. These secondary collisions are not as likely in the atomically-smooth SAMs, and the corresponding product-energy distributions do not show as much thermalization as in collisions with squalane. Kandel *et al.* have provided additional understanding of radical reactions on SAMs by following the degradation of octanethiol SAMs by hydrogen-atom bombardment using scanning tunneling microscopy.[18, 19]

Of direct interest to the work presented in this paper are the measurements by Nesbitt and co-workers on the reactions of fluorine radicals with liquid squalane.[2, 15] High-resolution infrared absorption measurements of the nascent HF product have revealed detailed rovibrational-state distributions and partial translational-energy information. Comparison between the product properties in F+squalane reactions and those in the counterpart O+squalane system described before shows dramatic differences between the two systems. For instance, even though the collision energy in the F+squalane experiments (0.7±0.3 kcal mol^{-1}) is substantially smaller than in the O+squalane experiments, the product HF vibrational distributions are notably hotter than the OH distributions. In effect, while experiments report an inverted vibrational distribution of HF,[18,19] less than 10% population in OH($\nu'=1$) is observed in squalane reactions with oxygen at low energies.[20] This difference in product internal excitation seems to be tied to the significant differences in the potential-energy surfaces of both reactions. For instance, while O+alkane hydrogen-abstraction reactions are only slightly exothermic ($\Delta_r H$ = ~ 0 – -5 kcal mol^{-1}),[21] F+alkane reactions are markedly exothermic ($\Delta_r H$ = ~ -35 – -40 kcal mol^{-1}),[22] thus making available more energy in products. In addition, the barriers for hydrogen abstraction by ground-state atomic oxygen from primary, secondary, and tertiary alkane sites are between 3 and 10 kcal mol^{-1},[21] but the analogous reactions involving fluorine atoms show little or no barrier even for primary sites.[22] Another interesting result in the F+squalane experiments is the presence of a strong positive correlation between HF rotational and translational excitation across all accessible HF vibrational states.[2, 15] This correlation points to the role of secondary collisions in the microscopically-rough squalane surface in cooling the rotational and translational HF degrees of freedom for products that do not impulsively recoil from the surface immediately after reaction.

In contrast with the wealth of experimental studies on the dynamics of radical/organic-surface collisions, analogous theoretical studies have been so far sparse. This paucity of theoretical work is mostly due to the difficulty in propagating classical trajectories for gas/organic-surface systems, which in their most simplistic model representations are comprised of literally hundreds of atoms. Driven by the fact that accurate analytic potential-energy functions for such large systems are difficult to obtain, and direct-dynamics studies employing high-level electronic-structure methods are prohibitive, hybrid quantum-mechanics/molecular-mechanics (QM/MM) schemes have emerged as a promising approach to represent the potential-energy surface of gas/surface systems. In these QM/MM approaches to gas/surface scattering, the system is divided into an active region, where the radical reactions with the surface take place, and an inactive surface region, which provides structural integrity to the active region.[23] The potential-energy surface of the bond formation/breakage processes occurring in the active region is described using QM methods (commonly semiempirical Hamiltonians), while the inactive region is represented with computationally-inexpensive MM force fields. Using this approach, Hase[24] and Schatz[25, 26] studied the reactions of oxygen atoms with SAMs and squalane to make contact with the experiments mentioned before.

More recently, Radak *et al.*[17] have continued to use this approach to investigate the reactions of fluorine atoms with squalane in an attempt to complement the available measurements on that reaction.[2, 15] The large computational expenditure associated with the calculations forced the authors to propagate trajectories at much higher collision energies (11.53 and 23.06 kcal mol^{-1}) than experiment (0.7±0.3 kcal mol^{-1}), making it difficult to establish quantitative comparisons between theory and experiment. Notwithstanding, the calculations captured the major experimental trends, including an inverted HF vibrational distribution, and the quenching of HF rotational excitation as a function of its residence time on the surface prior to desorption. Another difficulty in those F+squalane computational studies is the inaccuracies of the MSINDO Hamiltonian,[27, 28] which was used to treat the QM portion of the potential-energy surface. An example of these inaccuracies is seen in the description of the reaction barrier. For instance, while highly-accurate CCSD(T) calculations indicate the absence of a barrier for the $F+C_2H_6 \rightarrow HF+C_2H_5$ reaction,[22] the MSINDO Hamiltonian exhibits a first-order transition state of significant energy above reagents (1.9 kcal mol^{-1}). More importantly, the Hamiltonian predicts reaction energies that are notably more exothermic than experiments (~15 kcal mol^{-1} overestimation of the reaction energy for abstraction at secondary sites and ~20 kcal mol^{-1} at tertiary sites).

In this paper, we aim to augment our theoretical understanding of the dynamics of gas/organic-surface reactions by investigating the reaction of fluorine atoms with an alkanethiol self-assembled monolayer. While the QM/MM theoretical framework that we employ in this paper is essentially identical in nature to that of the work described before, a key improvement in this work is the use of a specific-reaction-parameters (SRP) semiempirical Hamiltonian to describe the QM region, as opposed to a standard Hamiltonian. SRP Hamiltonians are based on the reoptimization of the empirical parameters contained in the Hamiltonian for a particular chemical reaction so that the Hamiltonian is accurate for that specific reaction.[29] This approach has recently proved useful in improving the general lack of accuracy found in common semiempirical methods in reaction-dynamics studies, while maintaining an affordable computational expenditure.[22, 30-33] A low computational expense is supremely necessary when a large number (>10^6) of energy gradients need to be calculated, as is the case in classical-trajectory reaction-dynamics studies. While the SRP method has been shown to be quite effective at reproducing the PES and dynamics of a number of reaction classes, there are limitations to the size and type of systems that can be studied with this technique. For instance, Hase and co-workers have shown that for highly-correlated systems, where large basis sets are necessary, semiempirical methods might not be flexible enough to capture the entire potential-energy surface with high accuracy.[34]

The SRP Hamiltonian used here to describe hydrogen abstraction from an alkane surface by fluorine atoms is based on recent work on model gas-phase F+alkane reactions.[22] In this work, a modified version of this SRP Hamiltonian is used to propagate trajectories of F+SAM collisions at energies comparable to those of the experiments on F+squalane. Analysis of the trajectories provides HF product-energy distributions and mechanistic information about the hydrogen-abstraction reactions. Particular emphasis is given to the elucidation of the role of post-reaction HF/surface collisions in cooling the HF product rotational, translational, and vibrational degrees of freedom.

The remainder of this paper is organized as follows. First, we present the details of the computational methods used in this study, including the reparameterization of the semiempirical MSINDO Hamiltonian, the QM/MM hybrid method used to describe the potential-energy surface, and the specifics of the trajectory calculations. We then show the results of our direct-dynamics QM/MM study of F+SAM collisions, including comparison with both experimental and prior theoretical results on the F+squalane reaction. Finally, we offer concluding remarks.

6.2 Computational Details

In this section, we describe the development of a specific-reaction-parameters semiempirical Hamiltonian that accurately reproduces *ab initio* data on the potential-energy surface of elementary F+alkane reactions. We then explain the incorporation of this SRP Hamiltonian into a hybrid QM/MM scheme that is used to describe the potential-energy surface for the entire F+SAM system investigated in this work, and the details of the gas/surface trajectory calculations.

6.2.1 Specific-Reaction-Parameters Hamiltonian

To describe the potential-energy surface of the interaction of fluorine atoms with alkanes, we have optimized the parameters of the MSINDO Hamiltonian so that it captures with accuracy the energetics of benchmark F+alkane reactions. This effort is heavily based on recent work by our group on the dynamics F+methane, ethane, propane, and isobutane reactions,[22] so we refer the reader to that paper for full details of the semiempirical-Hamiltonian optimization. Briefly, the SRP-MSINDO Hamiltonian in this work was obtained using a grid of high-quality *ab initio* points of the potential-energy surface of model gas-phase F+alkane reactions as a reference. The *ab initio* map primarily included information on the $F+CH_4 \rightarrow HF+CH_3$ and $F+C_2H_6 \rightarrow HF+C_2H_5$ reactions around the minimum-energy-reaction path, but also probed other regions, including the cone of acceptance for the $F+CH_4 \rightarrow HF+CH_3$ reaction. All of the *ab initio* calculations were computed using unrestricted coupled-cluster theory with single, double, and perturbative triple excitations[35] [CCSD(T)] in combination with Dunning's correlation consistent double-ζ basis set augmented with diffuse functions (aug-cc-pVDZ).[36] Sample calculations using the aug-cc-pVTZ basis set were also conducted to investigate the effect of the size of the basis set on the *ab initio* calculations, which was found to be minor. Using this grid of high-level *ab initio* information, the parameters of the F, H, and C atoms in the MSNDO Hamiltonian were optimized using a non-linear least-squares method so that the differences between the semiempirical and *ab initio* energies were minimal. The SRP-MSINDO Hamiltonian derived in this way closely reproduces CCSD(T)/aug-cc-pVDZ energies for the first members of the F+alkane reactions (including F+methane, ethane, propane, and isobutane), and is superior to other more computationally demanding electronic-structure methods, including Möller-Plesset second-order perturbation theory (MP2) with the aug-cc-pVDZ basis set.

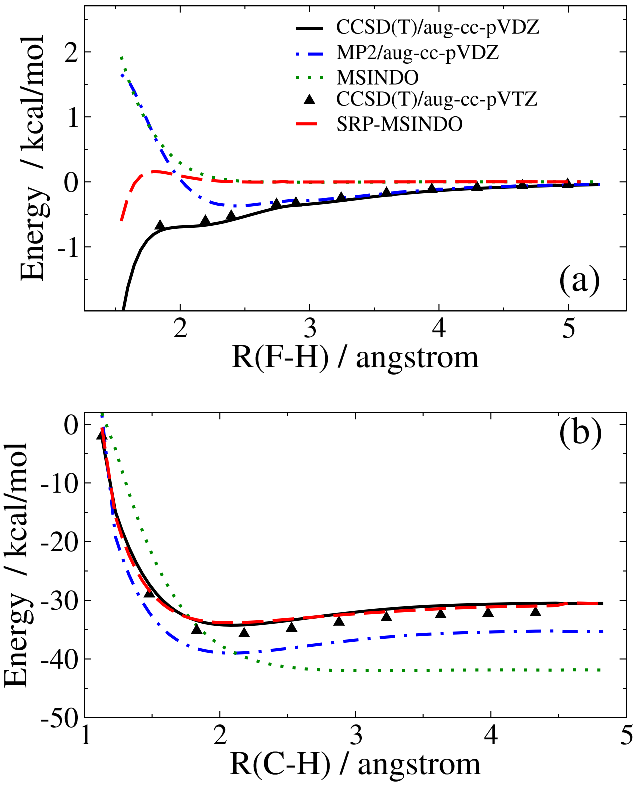

Figure 6.1: Potential-energy-surface profiles of the $F+C_2H_6 \rightarrow HF+C_2H_6$ reaction calculated at various levels of theory. (a) Represents the region of the potential-energy surface connecting the transition state with reagents and (b) is for the region connecting the transition state with products (see text). CCSD(T) calculations are based on geometries obtained at the MP2/aug-cc-pVDZ level.

Figure 6.1 illustrates the accuracy of the SRP-MSINDO Hamiltonian derived in this way in comparison with *ab initio* calculations for the $F+C_2H_6 \rightarrow HF+C_2H_5$ reaction. The figure shows relaxed scans of the region of the potential-energy surface connecting the reagents (a) and products (b) asymptotes with the strong-interaction region. Figure 6.1a shows a scan of the F-H forming bond from 1.54 Å to 5.24 Å at 0.05 Å steps and Figure 6.1b represents a scan of the C-H breaking bond from 1.13 Å to 4.83 Å with a step size of 0.1 Å. The figure clearly indicates the improvement in accuracy of the SRP-MSINDO Hamiltonian with respect to the original MSINDO Hamiltonian. For instance, the SRP-MSINDO Hamiltonian does not show an appreciable barrier for reaction, in agreement with CCSD(T)/aug-cc-pVDZ and –pVTZ energies. On the other hand, the original Hamiltonian and the MP2/aug-cc-pVDZ results predict a sizeable barrier (Fig.6.1a). The reaction energy is also satisfactorily reproduced by the SRP-MSINDO calculations, which also improve upon MSINDO and MP2/aug-cc-pVDZ results. The major difference between the SRP-MSINDO Hamiltonian derived in this work and that of Ref. 22 is in the description of the attractive well in the products' valley, which can be seen in Fig. 6.1b. This well in the potential-energy surface is caused by stabilizing intermolecular dipole-quadrupole interactions between the nascent HF product and the alkyl radical. While the original version of the MSINDO Hamiltonian and the previously-derived SRP-MSINDO Hamiltonian[22] do not capture this subtlety of the potential-energy surface, the SRP-MSINDO Hamiltonian derived in this work satisfactorily reproduces the high-level CCSD(T) data. This improvement indicates that even though semiempirical Hamiltonians are based on drastic approximations to the Hartree-Fock solution of the electronic Schrödinger equation, relatively weak intermolecular interactions can be accounted for via reparameterization of the Hamiltonian. The parameters of the SRP-MSINDO Hamiltonian derived in this work are collected in Table 6.1 of the supporting information.

The level of agreement between the SRP-MSINDO Hamiltonian derived in this work and CCSD(T) energies showcased in Figure 6.1 for the $F+C_2H_6 \rightarrow HF+C_2H_5$ reaction extends to other members of the F+alkane → HF+alkyl family of reactions. Table 6.2 of the supporting information contains quantitative comparisons between the SRP-MSINDO Hamiltonian and CCSD(T) data for some of the simplest F+alkane gas-phase reactions, and suggests that the accuracy of the SRP-MSINDO Hamiltonian is general to the F+alkane family of reactions. These results lend confidence to the use of this improved Hamiltonian to describe the reactive region of the potential-energy surface in F+alkanethiol SAM reaction-dynamics studies as described below.

Table 6.1: List of MSINDO and SRP-MSINDO parameters that were involved in the SRP development.[a]

Parameter	MSINDO	SRP-MSINDO
ζ_s^U (H)	1.006	1.365
ζ_s (H)	1.1576	1.2736
K_s (H)	0.1449	0.1979
I_s (H)	-0.5000	-0.3708
ζ_s^U (C)	1.6266	0.9938
ζ_p^U (C)	1.5572	1.8790
ζ_s (C)	1.7874	1.6282
ζ_p (C)	1.677	1.622
K_s (C)	0.0867	0.1257
K_p (C)	0.0478	0.0428
τ_{1s} (C)	5.083	5.663
ε_{1s} (C)	10.43	12.12
I_s (C)	-0.8195	-0.9952
I_p (C)	-0.3824	-0.4373
ζ_s^U (F)	2.3408	2.3034
ζ_p^U (F)	2.2465	2.7611
ζ_s (F)	2.4974	2.4018
ζ_p (F)	2.351	2.377
K_s (F)	0.1769	0.1019
K_p (F)	0.0127	0.0101
τ_{1s} (F)	8.6043	9.0039
ε_{1s} (F)	25.19	27.35
I_s (F)	-2.0238	-2.2337
I_p (F)	-0.6868	-0.7873
$\alpha(1)$ (H)	0.3856	0.3924
$\alpha(2)$ (H)	0.5038	0.2306
$\alpha(1)$ (C)	0.4936	0.4926
$\alpha(2)$ (C)	0.6776	0.6935
$\alpha(1)$ (F)	0.1521	0.1654
$\alpha(2)$ (F)	0.1059	0.0593

[a] For a definition of parameters, please see Ref. [37].

Table 6.2: Reaction energies for F+alkane→HF+alkyl reactions.[a]

Reaction	CCSD(T)[b]	MP2[c]	MSINDO	SRP-MSINDO	Exp. [d,e]
F+CH_4	-30.09 (-26.63)	-35.24 (-31.78)	-36.59 (-32.70)	-31.03 (-26.83)	-31.4, -31.6
F+C_2H_6	-33.20 (-29.54)	-38.08 (-34.35)	-46.50 (-42.80)	-33.19 (-30.85)	-35.3, -35.8
F+C_3H_8 (1)[f]	-32.81 (-29.28)	-37.50 (-33.99)	-45.88 (-42.68)	-34.5 (-30.93)	-35.2, -35.4
F+C_3H_8 (2)[g]	-35.24 (-31.62)	-39.75 (-36.13)	-53.95 (-50.69)	-37.00 (-35.95)	-38.6, -37.8
F+i-C_4H_{10} (1)[h]	-32.13 (-28.70)	-36.65 (-33.23)	-46.62 (-43.36)	-35.49 (-31.85)	-35.7
F+i-C_4H_{10} (3)[i]	-36.43 (-33.16)	-40.67 (-37.40)	-60.17 (-56.90)	-44.48 (-40.91)	-40.7

[a] Energies are reported in kcal mol^{-1}. Values in parentheses correspond to classical energies, i.e., not corrected by zero-point energies.

[b] CCSD(T)/aug-cc-pVDZ//MP2/aug-cc-pVDZ energies.

[c] MP2/aug-cc-pVDZ energies.

[d] Ref. 38

[e] Ref. 39

[f] $F+C_3H_8 \rightarrow HF+CH_2CH_2CH_3$

[g] $F+C_3H_8 \rightarrow HF+CH_3CHCH_3$

[h] $F+i\text{-}C_4H_{10} \rightarrow HF+CH_2CH(CH_3)_2$

[i] $F+i\text{-}C_4H_{10} \rightarrow HF+C(CH_3)_3$

6.2.2 QM/MM scheme

The F+SAM system simulation unit cell is comprised of the fluorine atom and 25 octanethiol chains arranged according to their positions on an Au(111) surface.[40] Periodic boundary conditions are used to replicate infinitely this unit cell in the two surface directions. Drawing inspiration from earlier work,[24, 25] the potential-energy surface of this F+SAM system has been represented using a QM/MM scheme. The active (QM) region is comprised of the ethyl termini of 7 chains of the octanethiol SAM surface and the fluorine atom. These 7 ethyl moieties are arranged so that one central chain is surrounded by its six nearest neighbors. The remainder of the SAM surface constitutes the inactive (MM) region. A schematic of this QM/MM separation is shown in Figure 6.2. The QM/MM boundary in the seven central octanethiol chains occurs at the third C-C bond from the gas/surface interface. Hydrogen link atoms are used to cap the carbon radicals generated in the QM/MM separation and saturate the carbon valence shell for the electronic-structure calculations of the active site. Once the active and inactive regions are defined, the potential energy of the system is computed using the popular mechanical-embedding procedure:[41]

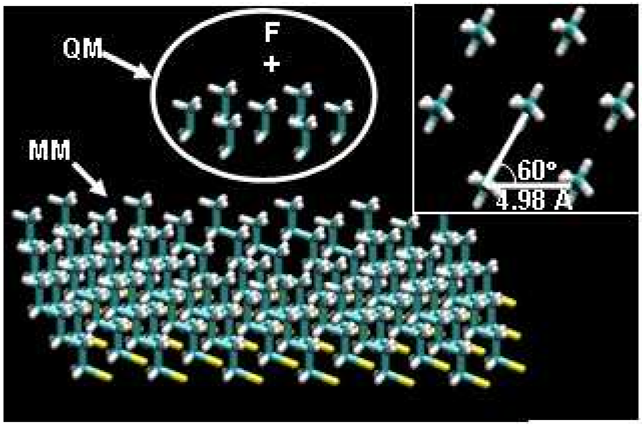

Figure 6.2: Schematic of the QM/MM procedure showing the delineation between the structural MM region and the reactive QM region. The inset shows a top view of the region of the SAM surface included in the QM region.

$$E_{QM/MM} = E_{(active+inactive)}(MM) - E_{(active)}(MM) + E_{(active)}(QM) \quad \textbf{(6.1)}$$

According to Eqn. 6.1, obtaining the potential energy of the system requires three calculations. First, the energy of the entire F+SAM system is computed at the MM level. Second, the energy of the active region is computed also at the MM level and subtracted from the overall system energy. Finally, the energy of the active region is computed at the QM level and added back in to yield the QM/MM energy. A similar recipe is applied to compute the forces on each atom (energy gradients) required to propagate classical trajectories. In this work, the QM calculations of the active region are carried out using the SRP Hamiltonian described before, and the MM calculations are conducted using the all-atom OPLS force field,[42, 43] as implemented in the TINKER package of programs.[44] Of the three calculations, the QM evaluation of energy (and gradients) of the active region using the SRP-MSINDO calculation is clearly the most time-consuming step. Even though calculation of the millions of energy gradients required in routine classical-trajectory studies of reaction dynamics is relatively inexpensive for small gas-phase systems such as F+CH_4 or F+C_2H_6 using semiempirical Hamiltonians, the QM calculations in this work involve electronic-structure calculations of a system of over 100 valence electrons using an unrestricted reference. Even using semiempirical Hamiltonians, calculation of millions of energy gradients for such a large system is still challenging, and virtually leaves these approximate methods as the only reasonable electronic-structure technique for such large-scale calculations. In this context, the development SRP Hamiltonians that can capture the potential-energy surface of reactive systems with reasonable accuracy appears to be a particularly useful strategy.

6.2.3 Dynamics calculations

Two sets of reaction-dynamics calculations have been conducted in this work. First, we have propagated quasiclassical trajectories of the F+CH_4 and F+C_2H_6 reactions to calibrate the accuracy of the SRP-MSINDO Hamiltonian derived in this work via comparison with available experiments. Batches of 50,000 trajectories have been calculated for each system and set of initial conditions. The trajectories have been started with the F atom at a distance of 15 a.u. from the center of mass of the hydrocarbon molecule and stopped when the recoiling products are ~15 a.u. apart. The maximum sampling impact parameters are 7.0 a.u. for F+CH_4, and 10 a.u. for F+C_2H_6. Initial conditions for the hydrocarbon reagent molecules consider zero-point energy and no rotational energy and have been generated using the VENUS program.[45] The MSINDO Hamiltonian is known to overestimate vibrational frequencies by ~20%,[22, 32] and therefore we have selected initial coordinates and momenta that correspond to 80% of the MSINDO zero-point energy in each of the normal vibrational modes. This procedure gives the alkane molecules an amount of vibrational energy that corresponds to the experimental zero point.

Second, the body of this work is comprised of F+SAM gas/surface trajectory calculations. Initial conditions for the seven ethane moieties of the active region of the QM/MM potential-energy surface were selected using VENUS with coordinates and momenta that also correspond to 80% of the MSINDO zero-point energy in each of the normal modes. The rest of atoms in the surface, which belong to the inactive region, start the trajectories with coordinates and momenta taken from a 1 ns canonical (constant temperature (300 K) and pressure (1 atm)) simulation. The impinging fluorine atom is initially located at least 10 a.u. above the surface of the SAM, a distance long enough that the interaction between the fluorine atom and the surface is negligible. The initial velocity components of the F atom are selected according to the collision energy, angle of incidence, and azimuthal angle. The collision energy was varied over the 0.80-11.53 kcal mol^{-1} range, and the incidence angle (θ_{inc}), defined as the angle between the fluorine initial velocity vector and the surface normal is varied from 0° to 60°. The azimuthal angle, which is formed between the projection of the initial fluorine velocity vector into a plane parallel to the surface and the projection of the alkanethiol chains into the same plane, is selected randomly between 0° and 360°. The fluorine atoms are aimed at a circular 21.5 $Å^2$ area surrounding the tip of the central QM chain, which constitutes the reactive unit cell of the SAM and is uniformly sampled by the trajectories of the fluorine atom. Since the lateral separation distance between the chains is ~4.98Å and they are arranged in a hexagonal pattern, the target area samples completely the entire SAM unit cell, and therefore the entire SAM surface. With those initial conditions, batches of 1000 classical trajectories are integrated until the fluorine atom has reached a height of 30 a.u. above the sulfur level or ~20 a.u. above the exposed terminus of the SAM surface. Occasionally, trajectories where the fluorine atom is trapped on the surface, either as an unreacted fluorine atom or after an abstraction reaction as HF, for more than 7.5 ps occur. Less than 2% of the total trajectories undergo this trapping process at all initial conditions, and are discarded from the analysis. From the initial and final atomic coordinates and momenta, HF vibrational, rotational, and translational-energy distributions are calculated and compared with experiment where available.

6.3 Results

6.3.1 Gas-phase calculations

To calibrate the accuracy of the SRP-MSINDO Hamiltonian used in this work for the F+alkane family of reactions, we have propagated trajectories for the F+CH_4 and F+C_2H_6 reactions under conditions where experimental information exists.[1, 16, 46] Analysis of trajectories for the F+CH_4 → HF+CH_3 reaction at E_{coll}= 1.8 kcal mol^{-1} shows an inverted HF product vibrational distribution in good agreement with experiment. Quantitatively, the average energy going to HF vibration in the calculations (28.3±0.2 kcal mol^{-1}) matches quite well experiment (27.4 kcal mol^{-1}).[16] Similar results are obtained in the analysis of the F+C_2H_6 → HF+C_2H_5 reaction at E_{coll}=3.2 kcal mol^{-1}, but the calculations slightly overestimate the experiments ($<E_{vib,HF}>$=31.2±0.2 kcal mol^{-1} *vs.* 25.7 kcal mol^{-1}, respectively). In this reaction, both theory and experiment show qualitatively similar HF vibrational distributions with peaks in ν'=2 and a larger population in ν'=3 than ν'=1. However, the largest discrepancy between theory an experiment is that the calculations do not show significant population in the HF(ν'=0) state, but the measurements show 15±4% population. The lack of quantitative agreement between theory and experiment might be rooted in weaknesses in the SRP Hamiltonian derived in this work. Calculations using preliminary SRP MSINDO Hamiltonians, and other semiempirical Hamiltonians (PM3) all fail to provide substantial population in HF(ν'=0). Direct-dynamics calculations employing high-quality *ab initio* methods, seem therefore necessary to clarify whether the absence of population in

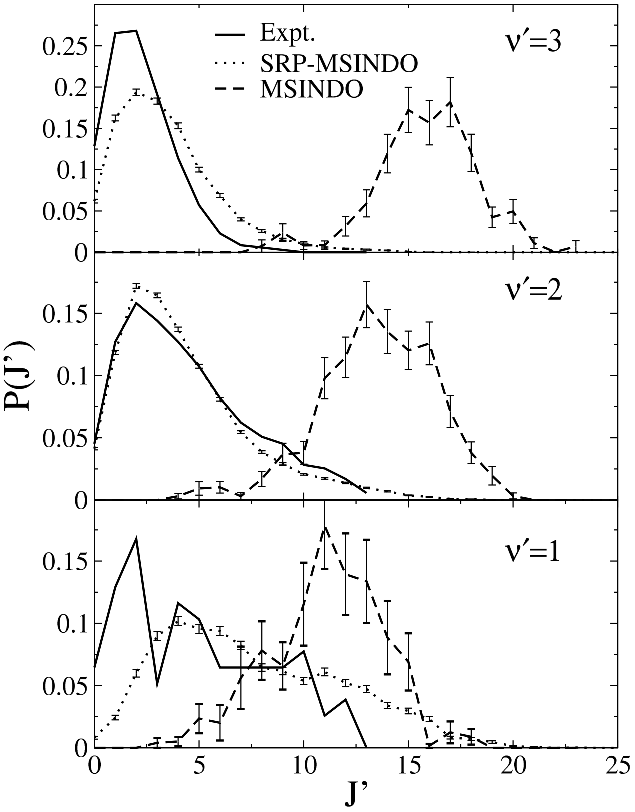

Figure 6.3: HF rotational state distributions for the F+CH_4 → HF+CH_3 reaction at E_{coll}=1.8 kcal mol^{-1}. The experiments are taken from Ref. [16]

HF(ν'=0) is tied to inaccuracies in the SRP potential-energy surfaces. Recent calculations by Sun and Hase have shown that even MP2/6-31G* direct-dynamics calculations in the related $C_2H_5F \rightarrow HF+C_2H_4$ reactions are not accurate enough to provide quantitative HF vibrational distributions,[47] so large basis sets might be needed in the calculations.

Figure 6.3 shows calculated HF rotational distribution for the $F+CH_4 \rightarrow HF(\nu',J')+CH_3$ reaction at E_{coll}=1.8 kcal mol^{-1} in comparison with experiment.[16] The experimental distributions show the expected trend of rotational cooling with increasing vibrational excitation, which is illustrative of the competition between HF vibration and rotation. These trends are correctly reproduced by the calculations using the SRP-MSINDO Hamiltonian. Quantitatively, the average energy in HF rotation over all vibrational states is 1.5 kcal mol^{-1} for SRP-MSINDO compared to 1.4 kcal mol^{-1} in the experiment. Figure 6.4 shows an analogous theory-experiment comparison of HF rotational distributions but for the $F+C_2H_6 \rightarrow HF+C_2H_5$ reaction at E_{coll}=3.2 kcal mol^{-1}. Also included in the figure are the results obtained with the original MSINDO Hamiltonian under identical initial conditions. Clearly, the SRP-MSINDO Hamiltonian represents a vast improvement over the original Hamiltonian and agrees reasonably well with experiment.

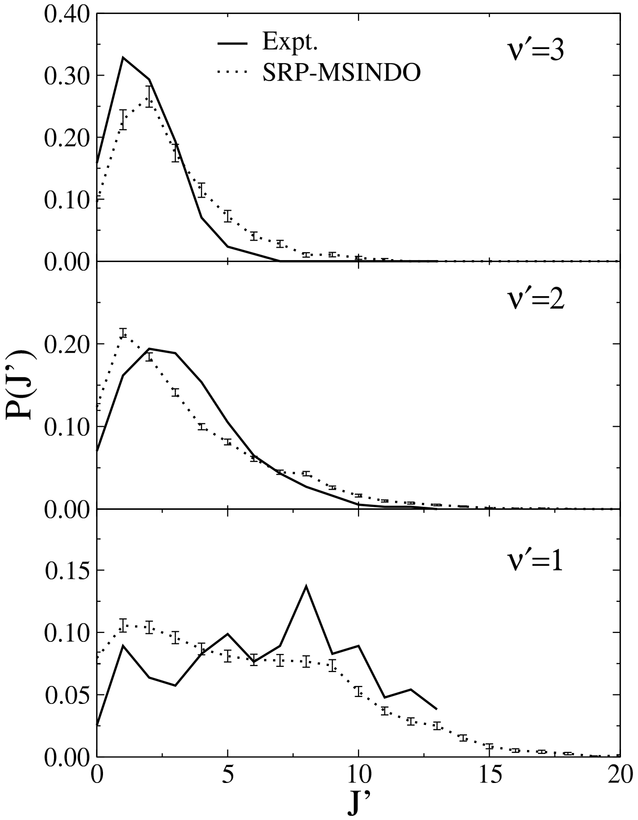

Figure 6.4: HF rotational state distributions for the $F+C_2H_6 \rightarrow HF+C_2H_5$ reaction at E_{coll}=3.2 kcal mol^{-1}. The experiments are taken from Ref. [1]

A note of interest is the colder HF rotational distributions found in both theory and experiment in the $F+C_2H_6$ reaction compared to the $F+CH_4$ reaction. This is somewhat unexpected because the available energy in products in the $F+C_2H_6$ reaction is 5.3 kcal mol^{-1} larger than in $F+CH_4$ due to the combined effect of the larger exothermicity (–35.3 in $F+C_2H_6 \rightarrow HF+C_2H_5$ *vs.* –31.4 kcal mol^{-1} in $F+CH_4$

→ $HF+CH_3$)[48] and the larger collision energy used in the experiments (3.2 *vs.* 1.8 kcal mol^{-1}) in the larger reaction. Two effects might contribute to the apparent cooling of the HF rotational distributions in the $F+C_2H_6$ reaction compared to the $F+CH_4$ reaction. First, the presence of a larger alkyl moiety can enhance the amount of energy being channeled into that product, thus limiting the overall available energy. Second, the attractive alkyl·····HF well in the products' valley is deeper for the $F+C_2H_6$ reaction than for the $F+CH_4$ reaction (4.6 *vs.* 3.3 kcal mol^{-1} below the products' asymptote, respectively, calculated at the CCSD(T)/aug-cc-pVTZ//MP2/aug-cc-pVDZ level) and is therefore expected to have a larger cooling effect in the $F+C_2H_6$ reaction. The effect of this well on the rotational distributions is induced by its collinear C····H-F geometry, which arrests the torque on the recoiling HF product and thus reduces the amount of rotational excitation. Orr-Ewing and co-workers have shown that post-transition state dynamics in Cl+alkane → HCl+alkyl reactions, which possess a similar well in the products' valley, govern the amount of rotational energy partitioned to the HCl product.[49] Thus, the increased $HF\cdots C_2H_5$ attraction should serve to cool the HF rotations more effectively than the weaker $HF\cdots CH_3$ interaction.

The reasonable level of agreement between experiment and calculations on these model gas-phase F+alkane systems serves to calibrate the accuracy of the SRP-MSINDO Hamiltonian, which we have subsequently used to describe the reactive potential in the F+SAM calculations described below.

6.3.2 Gas/surface calculations

In the following, we focus on characterizing the dynamics of F+SAM hydrogen-abstraction reactions, including reaction probabilities and HF internal-state distributions, and on providing insight into the reaction mechanism. Comparisons between the results provided by the SRP and original MSINDO Hamiltonian are made throughout in an effort to characterize the importance of differing potential-energy surfaces on the dynamics of F+SAM collisions.

6.3.2.1 Reactive Probabilities

As mentioned before, the QM/MM boundary in this work is drawn between the second and third topmost carbon atoms of the SAM. Such separation assumes that all reactivity comes from the $–CH_2–CH_3$ tip of the SAM chains, or in other words, that fluorine atoms do not penetrate the surface beyond the boundary. To verify this approximation, Table 6.3 shows reactive probabilities for hydrogen abstraction in F+SAM collisions for the terminal (–CH_3) and subterminal (–CH_2–CH_3) sites of the active region of the SAM. The results correspond to calculations conducted at normal incidence, which promotes penetration, and various collision energies. The table indicates that the majority of reactions occur at the methyl terminus, with less than 5% of the reactive trajectories leading to abstraction in the subterminal moiety in the SRP-MSINDO Hamiltonian. These results justify the placement of the QM/MM boundary between the second and third terminal carbon atoms of the octanethiol chains.

At low collision energies, the SAM surface is quite reactive, with ~75% of all trajectories resulting in abstraction from the terminal carbon atoms. Comparison between the reaction probabilities of the SRP and original Hamiltonian reveals some of the effects of reparameterization of the SRP-MSINDO Hamiltonian based on *ab initio* data. First, the reactivity of the original Hamiltonian is much lower than that of the SRP Hamiltonian. This result is a direct reflection of the elimination of the barrier to reaction present in the original Hamiltonian (1.9 kcal mol^{-1} in the $F+C_2H_6 \rightarrow HF+C_2H_5$ reaction, Fig. 6.1). The absence of a barrier in the SRP-MSINDO Hamiltonian implies that hydrogen abstraction is highly likely when fluorine radicals are in the vicinity of an alkane C—H bond. In fact, the calculations reveal that if an incoming fluorine radical comes within ~1.3 Å (2.5 bohr) of a hydrogen atom, abstraction will be produced. Since the terminal –CH_3 group is the moiety first encountered when F approaches the surface, most of the reactivity occurs in that unit, and few F atoms are able to make it to the subterminal –CH_2– group. The presence of a barrier in the original Hamiltonian implies that the interaction between the incoming F atoms and the terminal –CH_3 group is not as reactive as in the barrierless SRP-MSINDO Hamiltonian. Thus, F atoms are more likely to penetrate the SAM and abstract hydrogen atoms at the subterminal –CH_2– unit with the original Hamiltonian.

Since the ability to penetrate the SAM surface depends on the initial collision energy, one would expect an increase in the probability of hydrogen abstraction in the reactivity in the subterminal –CH_2– unit with increasing collision energy. This expectation is nicely corroborated by the data for the original MSINDO Hamiltonian, which shows an increase in the reaction probability in the subterminal position from 4% to 14% with an increase in the collision energy from 3.20 to 11.53 kcal mol^{-1}. On the other hand, the large reactivity of the terminal –CH$_3$ group in the SRP-MSINDO Hamiltonian precludes substantial penetration, regardless of the initial collision energy. Another interesting trend offered by the results in Table 6.3 is the different increase in reactivity with collision energy for the original and SRP Hamiltonians. While reactivity doubles from E$_{coll}$=3.20 to 11.53 kcal mol^{-1} in the original Hamiltonian, it increases by less than 10% in the SRP-MSINDO calculations. The large increase in reactivity with increasing collision energy is a signature of an activated process in the original MSINDO Hamiltonian, consistent with the presence of a barrier in

Table 6.3: Reactive probabilities for F+SAM collisions at normal incidence and various collision energies. [a]

E$_{coll}$ (kcal mol^{-1})	Inelastic	Abstraction (1’)	Abstraction (2’)	Trapped
Original MSINDO				
3.2	0.67	0.29	0.04	0.00
11.53	0.35	0.50	0.14	0.00
SRP-MSINDO				
0.8	0.25	0.73	0.01	0.01
3.2	0.21	0.78	0.01	0.00
11.53	0.13	0.85	0.01	0.01

[a] Reaction at 1’ sites correspond to abstraction of hydrogen atoms of the terminal –CH$_3$ group, and 2’ sites are for the subterminal –CH$_2$– group.

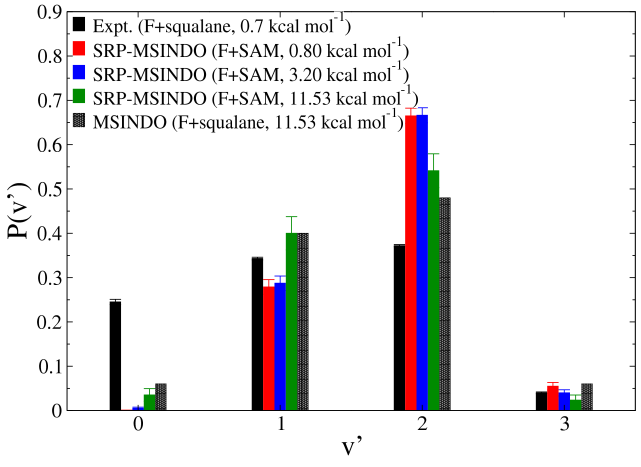

Figure 6.5: HF vibrational state distributions in F collisions with a SAM at various initial collision energies and normal incidence. Also shown are the experimental results of the F+squalane reaction (Ref. [2]) and theoretical results from Ref. [17]

this Hamiltonian. This trend is not so strong on the SRP-MSINDO Hamiltonian, which in agreement with high-level *ab initio* calculations, does not present a barrier to reaction.

6.3.2.2 HF Vibrational Distributions

Figure 6.5 shows the vibrational-state distributions of the HF product in F+SAM hydrogen-abstraction reactions. Included in the figure are the results calculated in this work at various collision energies when F approaches normal to the surface (θ_{inc}=0°). As has been seen in gas-phase,[1, 16, 22] and in gas/surface studies,[2, 15] the HF vibrational distributions emerging in F+alkane reactions are inverted, with the peak typically being at ν'=2, and this is true also in the current F+SAM calculations. An interesting result of the present F+SAM calculations is that the vibrational distributions become cooler with increasing collision energy. For instance, while at the lowest collision energy examined in this work (0.8 kcal mol^{-1}) the population in the ν'=2 state is more than twice larger than that in ν'=1, at E_{coll}=11.53 kcal mol^{-1}, the populations of the ν'=1 and ν'=2 states become more comparable. Quantitative data of the average vibrational energy in HF as a function of collision energy can be seen in Table 6.4. The trend of HF vibrational excitation being inversely correlated with collision energy has been witnessed before in gas-[22, 50] and condensed-phase[17] reactions of the F+alkane family. There are two main reasons for the cooling of HF vibration with increased collision energy in gas/surface reactions. First, as collision energy increases, the system can explore regions of the potential-energy surface beyond the minimum-energy reaction path. F+alkane reactions all have a very early transition state, with relatively long F—H distances that enable a large storage of energy in product HF vibration as the reaction proceeds. At high collision energies, reaction can occur at other geometries that do not favor so much energy disposal in HF vibration. Second, HF formed in F+SAM encounters at high collision energy might experience a more violent impact with the surface immediately after being formed than at low collision energies. Since F+alkane reactions are peripheral, it is possible that some of the F atoms approaching in a direction normal to the surface abstract hydrogen atoms prior to reversing its linear momentum in the surface direction. This implies that, momentarily, the forming HF product travels towards the surface prior to reaching its turning point. The subsequent strong interaction with the surface might facilitate energy transfer to the SAM chains, thus removing part of the energy initially partitioned to HF vibration.

The F+SAM results obtained in this work are compared in Figure 6.5 with the experiments in the cousin F+squalane reaction,[2, 15] which were carried out at E_{coll}=0.7±0.3 kcal mol^{-1} and normal incidence, and with the F+squalane calculations of Radak *et al.* at E_{coll}=11.53 kcal mol^{-1} (Ref. [17]). Since the F+squalane calculations did not consider normal incidence, the results in Figure 6.5 represent an average of three different incident angles probed in that work (30°, 45°, and 60°). There are two noteworthy conclusions stemming from the comparison of F+SAM and F+squalane HF vibrational distributions. First, the F+squalane calculations at 11.53 kcal mol^{-1} provide HF distributions remarkably similar to the F+SAM results at the same collision energy. Even though the F+squalane calculations were performed with the original MSINDO Hamiltonian, it seems that the relatively large collision energy of the calculations washes out the differences in the potential-energy surfaces and between the SAM and the squalane surfaces. Lower-energy collisions that sample regions of the energy surface closer to the minimum-energy reaction path might be more indicative of the effect of the alkane surface structure and the potential-energy surface in the calculations. Second, the experiments report HF distributions that are colder than all of the calculations. Of

Table 6.4: Average energies and scattering angle (θ_f) in the HF product generated in the F+SAM reaction at various collision energies and incident angles.[a,b]

E_{coll}	θ_{inc}	$< E'_T>$	$< E'_{VIB}>$	$< E'_{ROT}>$	$< \theta_f >$
0.80	0°	3.2	23.2	0.9	33.9
3.20	0°	4.0 (6.6)	22.5 (22.0)	0.9(7.1)	31.1(33.7)
11.53	0°	4.7 (6.9)	20.9 (18.8)	1.0(5.6)	31.2(25.0)
3.20	30°	4.0	23.1	0.9	33.2
3.20	60°	3.6	23.6	0.9	34.2

[a] All energies are in kcal mol^{-1} and angle in degrees. Errors bars are approximately 10%
[b] Values between parentheses correspond to calculations with the original MSINDO Hamiltonian.

particular significance is the inability of the calculations to reproduce the relatively large population in the HF(ν'=0) state. The measurements by the Nesbitt group in the gas/surface reaction also show HF vibrational distributions significantly colder than in the F+CH_4 or F+C_2H_6 experiments of the same group,[1, 16] which led the authors to propose that secondary collisions on the squalane surface might be involved in the cooling of the HF vibrational distributions. Post-reaction HF collisions on the squalane surface that quench the vibrational excitation of the diatomic species require relatively long residence times on the surface (several tens of picoseconds). This trapping is facilitated by the roughness of the surface of liquid squalane, which makes it possible for HF to be attracted to various alkane strands of the liquid simultaneously. The F+squalane calculations at E_{coll}=11.53 kcal mol^{-1} were not able to reproduce this vibrational cooling likely because the collision energy used in the calculations was too high, and the forming HF has enough translational energy to break the attractions with the rough liquid surface.[17] In addition, Fig. 6.1b shows that the original MSINDO Hamiltonian employed in that work does not show attractive intermolecular interactions between the forming HF molecule and the alkyl fragment, which further limits the amount of trapping.

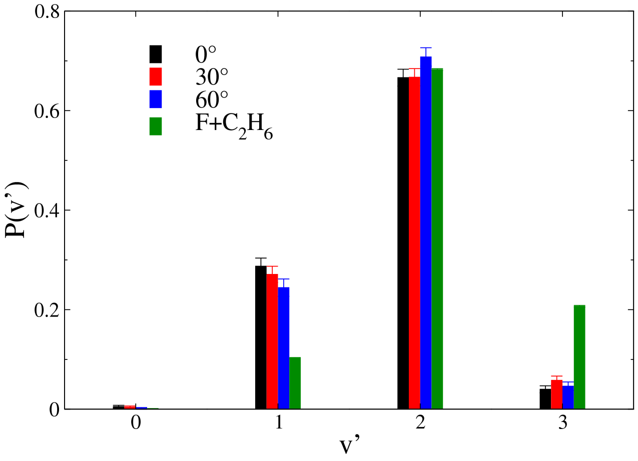

Figure 6.6: HF vibrational state distributions in F+SAM collisions as a function of the angle of incidence at E_{coll}=3.2 kcal mol^{-1} in comparison with calculations of the F+C_2H_6→HF+C_2H_5 reaction at the same collision energy.

While we observe some long trapping of HF in our F+SAM calculations (about 2% of the total trajectories calculated), its extent is limited by the smoothness of the SAM surface, which as nicely demonstrated in very recent measurements, impairs trapping in comparison with a squalane surface.[14] While the results for the F+C_2H_6→HF+C_2H_5 show that the SRP-MSINDO Hamiltonian predicts more energy in HF vibration than the experimental results of Nesbitt and co-workers, particularly the lack of population in ν'=0, the discrepancy between the gas-phase and F+SAM results might not only be a deficiency in the SRP-MSINDO method. Secondary collisions might play a major role in the final HF vibrational distributions as well. In order for the HF distributions obtained in this work on F+SAMs to match more quantitatively the experimental distributions obtained in the F+squalane system, about 25% of the reactive trajectories would need to exhibit trapping of the HF product on the surface for a long enough time to undergo vibrational decay from $\nu'=2$ to $\nu'=1$ and from $\nu'=1$ to the ground state.

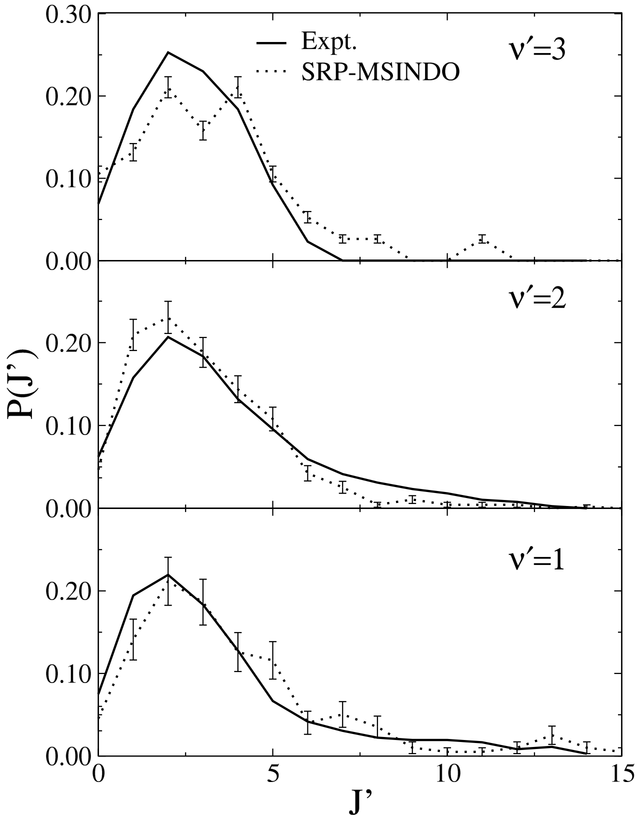

Figure 6.7: HF rotational state distributions for the F+SAM collisions at E_{coll}=0.8 kcal mol^{-1} and normal incidence in comparison with experiments of the F+squalane reaction at similar initial conditions (Ref. [2]).

Figure 6.7 shows the HF vibrational state distributions obtained in F+SAM collisions as a function of incident angle at E_{coll}=3.2 kcal mol^{-1} compared to the results of gas-phase $F+C_2H_6 \rightarrow HF+C_2H_5$ calculations with the same SRP-MSINDO Hamiltonian at the same collision energy. The gas/surface calculations reveal a very mild tendency to decrease HF vibrational excitation for more normal approaches to the surface, which is particularly appreciable in the populations of the $\nu'=1$ state. Average vibrational energies are shown in Table 6.4. More importantly, there is a significant difference between the F+SAM and $F+C_2H_6$ results, with the latter showing a considerably larger HF vibrational excitation. This result is a direct consequence of the involvement of more energy-absorbing modes of the alkane collision partner in a SAM and the presence of HF+SAM secondary collisions before HF desorption from the surface, and was anticipated in the comparison between gas-phase and gas/liquid experiments.[2]

6.3.2.3 HF Rotational Distributions

HF rotational state distributions for F+SAM collisions at E_{coll}=0.8 kcal mol^{-1} and normal incidence are shown in Figure 6.7 in comparison with the measurements on F+squalane at a comparable collision energy (0.7±0.3 kcal mol^{-1}). The simulations reproduce experiment very well, which is in contrast with the more qualitative agreement seen before in the HF vibrational distributions. These distinct levels of agreement between F+SAM calculations and F+squalane experiments suggest that the effect of long trapping of the formed HF product on the surface after reaction might have a more dramatic effect on the final vibrational energy of HF than on its rotational energy. Since, a small number of collisions are needed to cool the HF rotational degrees of freedom, the fact that there are substantially less collisions on a SAM than on squalane does not affect the comparison between HF rotational distributions in the F+SAM and F+squalane reactions as markedly as it does in the HF vibrational distributions. In fact, comparison of energy release in gas-phase and gas/surface reactions reveals that while the amount of energy going into HF rotation in the $F+C_2H_6 \rightarrow HF+C_2H_5$ gas-phase measurements is only about 1 kcal mol^{-1} larger than seen in the F+squalane measurements, there is an approximately ~7 kcal mol^{-1} loss of HF vibrational energy when going from $F+C_2H_6$ to F+squalane.[2]

Figure 6.8 exhibits the effect of the potential-energy surface used in the simulations on the HF rotational distributions by comparing the results obtained with the SRP-MSINDO Hamiltonian derived in this work and those of the original Hamiltonian. The figure shows HF(ν'=1) rotational distributions calculated at E_{coll}=3.2 kcal mol^{-1} and 0, 30, or 60° incident angles. Clearly, the SRP-MSINDO Hamiltonian predicts a much smaller energy release to HF rotation than the original Hamiltonian at all incident angles. Similar results are obtained also when comparing other HF vibrational states (not shown). In looking at Figure 6.1, one can see some of the differences in the potential-energy surfaces of these two electronic-structure methods for the representative $F+C_2H_6 \rightarrow HF+C_2H_5$ reaction. Even though the original MSINDO Hamiltonian is shown to predict a larger exothermicity than the SRP-MSINDO Hamiltonian, the larger energy available in the calculations with the original Hamiltonian is not solely responsible for the excessively hot HF rotational distributions obtained with this method; the description of the attraction between the forming HF and the alkyl fragment plays a role too. While the SRP-MSINDO Hamiltonian describes the attractive HF····alkyl intermolecular interactions reasonably well, this feature of the potential-energy surface is absent in the original Hamiltonian (see Fig. 6.1b). As mentioned above, the presence of this well limits the amount of rotational excitation of the recoiling HF species, which is consistent with the results seen in Figure 6.8. A second consequence of the presence of this attractive well is the potential for an increase in the amount of HF trapping on the surface. Analysis of the post-reaction dynamics of HF on the SAM with the original and SRP Hamiltonian corroborates this expectation. For instance, at E_{coll}=3.2 kcal mol^{-1} and normal incidence, the SRP MSINDO Hamiltonian predicts that the formed HF product collides approximately twice as many times with the surface as predicted by the original MSINDO Hamiltonian before desorption. A more detailed analysis of the post-reaction dynamics of HF will be presented below.

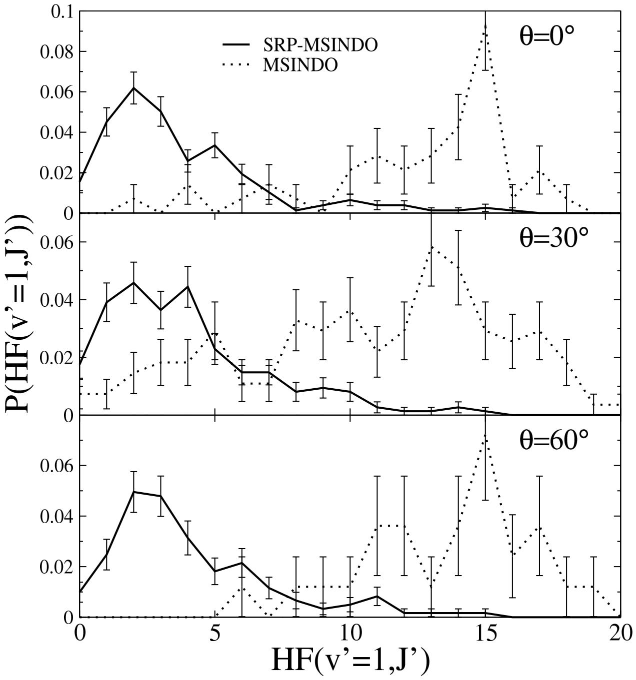

Figure 6.8: Calculated HF(ν'=1) rotational-state distributions in F+SAM collisions at 3.2 kcal mol^{-1} collision energy and (a) normal, (b) 30° and (c) 60° incidence.

A second point of interest in Figure 6.8 and Table 6.4 is the lack of dependence of the HF rotational distributions on the incidence angle, which has not been explored in the experiment yet. Since only a very few number of post-reaction secondary collisions are needed to cool the HF rotational modes, the rotational distributions not a sensitive enough probe of subtle changes in the reaction mechanism that one would expect to occur with varying incident angles.

The results in Figure 6.8 can also be used to rationalize the lack of quantitative agreement between the calculated HF rotational distributions in the F+squalane calculations of Radak *et al.*[17] at 11.53 kcal mol^{-1} and the F+squalane experiments. As the figure shows, the overexcitation seen in the calculations is tied to severe defects in the original MSINDO Hamiltonian used to obtain the atomic forces during the trajectory propagation. Other anticipated effects, such as the disparity in the collision energy of the calculations (11.53 kcal mol^{-1}) and experiment (0.7±0.3 kcal mol^{-1}) or in the incidence angles (normal in the experiment *vs.* 30, 45, and 60° in the calculations) play a role, but perhaps not as significant.

6.3.2.4 Reaction mechanism

We now present an analysis of the microscopic details of F+SAM collisions to provide fundamental insight into the mechanisms governing reactivity and product properties. First, we focus on the path traveled by the F atom before reaction, and then we detail the dynamics of the formed HF product before desorption from the surface.

A common feature of the reactive trajectories is that they predominantly occur when the F atom first collides with the surface. (In this work, we define that reaction has taken place when the distance between the incoming F atom and the reactive H atom reaches 2.5 bohr.) For collisions at a glancing incidence angle (30° and 60°) more than 80% of the reactions occur before the fluorine atom experiences a reversal of the component of its linear momentum perpendicular to the surface. For collisions where the fluorine atoms impinge with a normal incidence, between one-third and one-half react before the fluorine atom reverses its velocity in the surface-normal direction (z axis). In the trajectories in which F first collides inelastically with the surface before abstracting a hydrogen atom, the average number linear-momentum reversals in the z axis for all collision energies studied is always less than 1.4. Therefore, in most reactions that are not direct, the F atom only collides inelastically with the SAM surface just once. Furthermore, a negligible number of reactive trajectories are found in which a fluorine atom first thermally accommodates on the surface and then abstracts a hydrogen atom. The analysis of the post-reaction dynamics of HF is based on the examination of the evolution of its translational, rotational, and vibrational energy as a function of the number of its encounters with the SAM surface prior to desorption. Precedent for this type of analysis is provided by the numerous recent studies of inelastic collisions between closed-shell gases and SAMs.[51, 52] In this work, we define that the HF product has undergone a collision or encounter with the SAM surface if there is a reversal in any of the Cartesian components of its center-of-mass linear momentum. This analysis differs slightly from earlier work on inelastic atomic scattering from surfaces, which traditionally has only considered momentum reversals in the direction normal to the surface.[53] A difficulty in attributing gas/surface encounters to reversals in the center-of-mass linear momentum of a diatomic molecule like HF is that collisions of the H atom with the SAM might not necessarily lead to a linear-momentum reversal of the HF molecule. In effect, the location of the center of mass of HF implies that HF rotation can be viewed as a circular orbital motion of the peripheral H atom around the central F atom. To account for the possibility that the H atom collides with the SAM without recording a linear-momentum reversal of the HF center of mass, we have also examined reversals in any of the Cartesian components of the rotational angular momentum of the HF molecule. Figure 6.9 shows the probability distributions of the number of linear-momentum (a) and angular-momentum (b) reversals of the HF product in F+SAM collisions at E_{coll}=3.2 kcal mol^{-1} and various angles of incidence. The figure shows that in about half of the collisions, the HF experiences less than a handful of encounters before desorbing from the SAM surface. However, a noticeable result shown in the figure is that there is a substantial fraction of trajectories in which HF collides repeatedly with the surface before desorption. The figure also indicates that there are many more angular-momentum reversals than linear-momentum reversals. Again, this is expected because the peripheral H in an HF molecule experiences encounters with the SAM surface which might not substantially alter the direction of travel of the HF center of mass. Comparison of the post-reaction behavior of HF for various angles of incidence reveals an increase in the probability of desorption after a small number of reversals in the 0°< 30° < 60° sequence. This result indicates a

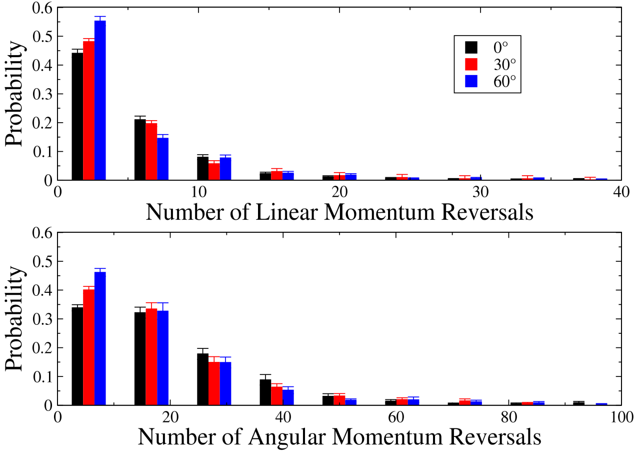

Figure 6.9: Calculated distributions of the number of (a) linear-momentum and (b) angular-momentum reversals for the HF molecule after reaction. E_{coll}=3.2 kcal mol^{-1}.

slight tendency for HF to desorb more promptly from the surface with more grazing F approaches.

To see the effect of these collisions of HF with the SAM surface on the amount of energy retained by this product, we show in Figure 6.10 average (a) translational and (b) rotational energy as a function of the number of linear-momentum reversals. The average energies in the figure clearly indicate that collisions with the SAM surface are effective in quenching both the translational and rotational energy of the HF product, which ends up absorbed by the surface. Similar analyses of the average HF vibrational energy do not reveal any quenching with the number of encounters in the time scales computed in this work (< 7.5 ps). Therefore, the F+SAM calculations concur with the traditional notion that both translational and rotational relaxation requires a much shorter time scale than vibrational relaxation. To probe the time scale needed for vibrational relaxation, we have computed model trajectories in which vibrationally excited HF (v=2) starts the trajectory trapped on a SAM surface and is not allowed to desorb. These model calculations indicate that approximately 50 ps are required for HF to lose one quantum of vibrational excitation.

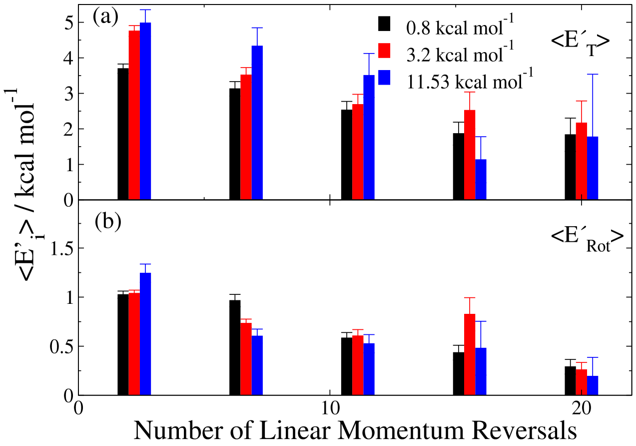

Figure 6.10: Calculated average (a) translational energy and (b) rotational energy in the desorbing HF molecules as a function of the number of linear momentum reversals that the HF molecule experiences after reaction. Data presented here represent collisions with normal incidence.

An ancillary consequence of the fast relaxation of HF rotation and translation on the surface observed in the F+squalane system is the positive correlation between HF translation and rotation. The experimental measurements determined that HF molecules recoiling fast from the squalane surface also were rotationally hotter than those which recoiled more slowly.[2] Figure 6.11 shows the correlation between HF translational and rotational energy in the F+SAM calculations performed in this work. The calculations nicely reproduce the experimental trend, and corroborate the mechanistic origin of the positive correlation between HF rotation and translation: HF products that receive a significant amount of translational energy can escape the attraction by the SAM surface and desorb without significant encounters with the alkane chains that might quench its rotational energy. On the other hand, if the amount of center-of-mass kinetic energy of the HF molecule in a direction normal to the surface is not large enough, HF might trap on the surface, which as shown in this work, leads to a decrease in both its rotational and translational energy in a short time scale.

6.4 Conclusions

We have studied the dynamics of F+SAM hydrogen-abstraction reactions using theoretical methods. Our approach has been based on propagating gas/surface classical trajectories employing a hybrid QM/MM potential-energy surface. While this approach is gaining momentum in the field of gas/organic-surface reactions, the novelty in the specific technology used in this work resides in the use of a specific-reaction-parameters semiempirical Hamiltonian derived from *ab initio* calculations of the potential-energy surface of exemplary F+alkane → HF+alkyl reactions. The SRP Hamiltonian captures reasonably accurately the main aspects of the *ab initio* calculations, including the absence of a barrier and the presence of a relatively deep intermolecular well in the products' asymptote. Energy profiles and reaction-dynamics calculations indicate that the SRP Hamiltonian has accuracy superior to commonly-used standard semiempirical Hamiltonians and even some first-principle methods.

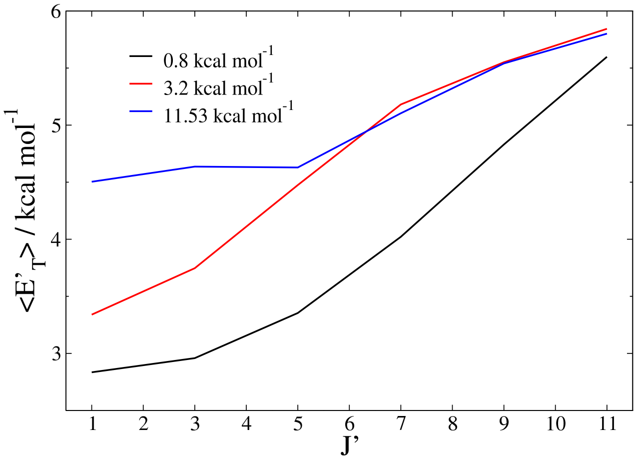

Figure 6.11: Calculated average HF translational energy as a function of HF rotational state for F+SAM reactions at normal incidence.

Employing the derived SRP-MSINDO Hamiltonian in our QM/MM scheme, we have carried out an extensive direct-dynamics study of fluorine atoms reacting with alkanethiol self-assembled monolayers at various collision energies and incident angles. The calculated HF rotational distributions are in very good agreement with recent measurements in the cousin F+squalane reaction at very low collision energies (~0.8 kcal mol^{-1}). On the other hand, while both theory and experiment produce inverted HF vibrational distributions, these distributions are slightly colder in the gas/liquid measurements, which seems to be a combination of the larger propensity of the HF product to undergo long trapping on the rougher squalane surface than on the smoother SAM surface used in this work and errors in the SRP-MSINDO method. Increasing collision energy decreases slightly the amount of energy channeled into HF vibration, increases even more slightly the amount of energy going into HF translation, and does not affect HF rotation. Investigation of the effect of the incident angle shows virtually no change in the energy partitioned to the HF product, suggesting that the amount of energy present in the desorbing HF product is largely controlled by the post-reaction interactions of this species with the surface.

We have put particular emphasis on examining the role of post-reaction HF-surface collisions on the energy of the desorbing HF product as a means to help elucidate the differences between gas-phase and gas/surface reactions. The analysis reveals that a substantial fraction of the formed HF products collide repeatedly with the SAM surface before desorption. These collisions are quite effective in quenching the rotational and translational excitation of the HF species. However, HF desorbs long before substantial vibrational deexcitation can occur in the F+SAM calculations. A consequence of post-reaction collisions is that HF products with high translational energy are also rotationally hot, corroborating the findings of recent F+squalane experiments.

A major conclusion of this work is that reparameterization of semiempirical Hamiltonians is an attractive strategy to enable dynamics studies of relatively large chemical reactions, including gas/organic-surface reactive collisions. Our study shows that by using relevant *ab initio* data from only the smallest members of a family of chemical reactions, one can generate electronic-structure methods to be used for a direct-dynamics simulation of atom/surface reactions. While the semiempirical Hamiltonians are not appropriate for extremely-precise studies, in which subchemical accuracy is required in the potential-energy surface, this work shows that a great degree of accuracy can be achieved relating to the energy of recoiling products.

The work presented in this chapter concludes our studies of reactive dynamics at the gas/organic-surface interface. We will use molecular-mechanics techniques similar to those implemented in the QM/MM scheme as a way to probe the nature of thin water films confined in hydrophobic environments. Chapter 7 will present our molecular-dynamics simulations in an effort to understand the mechanisms responsible for the hydrophobic effect.

References

1. E. S. Whitney, A. M. Zolot, A. B. McCoy, J. S. Francisco and D. J. Nesbitt, J Chem Phys **122** (12), 124310 (2005).
2. A. M. Zolot, P. J. Dagdigian and D. J. Nesbitt, J Chem Phys **129** (19), 194705 (2008).
3. F. Ausfelder and K. G. McKendrick, Prog React Kinet Mec **25** (4), 299-370 (2000).
4. C. Murray and A. J. Orr-Ewing, Int Rev Phys Chem **23** (3), 435-482 (2004).
5. D. Troya and G. C. Schatz, Int Rev Phys Chem **23** (3), 341-373 (2004).
6. D. J. Garton, T. K. Minton, M. Alagia, N. Balucani, P. Casavecchia and G. G. Volpi, J Chem Phys **112** (13), 5975-5984 (2000).
7. J. M. Zhang, D. J. Garton and T. K. Minton, J Chem Phys **117** (13), 6239-6251 (2002).
8. J. M. Zhang, H. P. Upadhyaya, A. L. Brunsvold and T. K. Minton, J Phys Chem B **110** (25), 12500-12511 (2006).
9. H. Kelso, S. P. K. Kohler, D. A. Henderson and K. G. McKendrick, J Chem Phys **119** (19), 9985-9988 (2003).
10. S. P. K. Kohler, M. Allan, H. Kelso, D. A. Henderson and K. G. McKendrick, J Chem Phys **122** (2), 024712 (2005).
11. S. P. K. Kohler, M. Allan, M. L. Costen and K. G. McKendrick, J Phys Chem B **110** (6), 2771-2776 (2006).
12. M. Allan, P. A. J. Bagot, S. P. K. Kohler, S. K. Reed, R. E. Westacott, M. L. Costen and K. G. McKendrick, Phys Scripta **76** (3), C42-C47 (2007).
13. M. Allan, P. A. J. Bagot, R. E. Westacott, M. L. Costen and K. G. McKendrick, J Phys Chem C **112** (5), 1524-1532 (2008).
14. C. Waring, P. A. J. Bagot, M. T. Raisanen, M. L. Costen and K. G. McKendrick, J Phys Chem A **113** (16), 4320-4329 (2009).
15. A. M. Zolot, W. W. Harper, B. G. Perkins, P. J. Dagdigian and D. J. Nesbitt, J Chem Phys **125** (2), 021101 (2006).
16. W. W. Harper, S. A. Nizkorodov and D. J. Nesbitt, J Chem Phys **113** (9), 3670-3680 (2000).
17. B. K. Radak, S. Yockel, D. Kim and G. C. Schatz, J Phys Chem A **113** (26), 7218-7226 (2009).
18. N. A. Kautz, D. P. Fogarty and S. A. Kandel, Surf Sci **601** (15), L86-L90 (2007).
19. N. A. Kautz and S. A. Kandel, J Am Chem Soc **130** (22), 6908-+ (2008).
20. M. Allan, P. A. J. Bagot, M. L. Costen and K. G. McKendrick, J Phys Chem C **111** (40), 14833-14842 (2007).
21. D. Troya, J Phys Chem A **111** (42), 10745-10753 (2007).
22. J. P. Layfield, A. F. Sweeney and D. Troya, J Phys Chem A **113** (16), 4294-4304 (2009).
23. D. Troya and G. C. Schatz, Esa Sp Publ **540**, 121-128
743 (2003).
24. G. Li, S. B. M. Bosio and W. L. Hase, J Mol Struct **556** (1-3), 43-57 (2000).
25. D. Troya and G. C. Schatz, J Chem Phys **120** (16), 7696-7707 (2004).
26. D. Kim and G. C. Schatz, J Phys Chem A **111** (23), 5019-5031 (2007).
27. B. Ahlswede and K. Jug, J Comput Chem **20** (6), 563-571 (1999).

28. B. Ahlswede and K. Jug, Journal of Computational Chemistry **20** (6), 572-578 (1999).
29. A. Gonzalezlafont, T. N. Truong and D. G. Truhlar, J Phys Chem-Us **95** (12), 4618-4627 (1991).
30. J. P. Layfield, M. D. Owens and D. Troya, J Chem Phys **128** (19), 194302 (2008).
31. J. P. Layfield and D. Troya, Chem Phys Lett **467** (4-6), 243-248 (2009).
32. D. Troya and E. Garcia-Molina, J Phys Chem A **109** (13), 3015-3023 (2005).
33. D. Troya and P. J. E. Weiss, J Chem Phys **124** (7), 074313 (2006).
34. G. H. Peslherbe and W. L. Hase, J Chem Phys **104** (20), 7882-7894 (1996).
35. T. D. Crawford and H. F. Schaefer, Rev Comp Ch **14**, 33-136 (2000).
36. D. E. Woon and T. H. Dunning, Journal of Chemical Physics **98** (2), 1358-1371 (1993).
37. B. Ahlswede and K. Jug, J. Comp. Chem. **20** (6), 572-578 (1999).
38. See http://webbook.nist.gov/chemistry for the experimental reaction energies calculated from the heats of formation of reagent and product species
39. "Chemical Kinetics and Photochemical Data for Use in Atmospheric Studies," JPL Publication No. 06-2.
40. N. Camillone, C. E. D. Chidsey, G. Y. Liu and G. Scoles, J Chem Phys **98** (4), 3503-3511 (1993).
41. D. Bakowies and W. Thiel, J Phys Chem-Us **100** (25), 10580-10594 (1996).
42. W. L. Jorgensen, J. D. Madura and C. J. Swenson, J Am Chem Soc **106** (22), 6638-6646 (1984).
43. W. L. Jorgensen, D. S. Maxwell and J. TiradoRives, J Am Chem Soc **118** (45), 11225-11236 (1996).
44. J. W. Ponder and F. M. Richards, J Comput Chem **8** (7), 1016-1024 (1987).
45. W. L. Hase, R. J. Duchovic, X. Hu, A. Komornicki, K. Lim, D. Lu, G. H. Peslherbe, K. N. Swamy, S. R. Vande Linde, A. J. C. Varandas, H. Wang and R. J. Wolf, Quantum Chemistry Program Exchange Bulletin, 55 (1996).
46. W. W. Harper, S. A. Nizkorodov and D. J. Nesbitt, Chem Phys Lett **335** (5-6), 381-387 (2001).
47. L. P. Sun and W. L. Hase, J Chem Phys **121** (18), 8831-8845 (2004).
48. Experimental reaction energies calculated from the heats of formation of reagent and product species in http://webbook.nist.gov/chemistry.
49. C. Murray, J. K. Pearce, S. Rudic, B. Retail and A. J. Orr-Ewing, J Phys Chem A **109** (49), 11093-11102 (2005).
50. J. G. Zhou, J. J. Lin, W. C. Shiu and K. P. Liu, J Chem Phys **119** (10), 4997-5000 (2003).
51. B. S. Day, J. R. Morris, W. A. Alexander and D. Troya, J Phys Chem A **110** (4), 1319-1326 (2006).
52. T. Y. Yan and W. L. Hase, Phys Chem Chem Phys **2** (4), 901-910 (2000).
53. W. A. Alexander, B. S. Day, H. J. Moore, T. R. Lee, J. R. Morris and D. Troya, J Chem Phys **128** (1), 084702 (2008).

Chapter 7
Dynamics of Water Confined Between Alkanethiolate Self-Assembled Monolayers

7.1 Introduction

The hydrophobic effect is the tendency for solutes which interact weakly with water to attract each other when placed in solution. The magnitude of these interactions and the length scales on which they occurs are not easily explained by basic chemical concepts. The hydrophobic effect is not only responsible for causing interesting phenomena in solutes and biological molecules, but also exhibits a strong influence on the structure and dynamics of water. Narrow channels found in biological membranes allow for the transport of water in and out of the cell, while their narrow diameters prevent ion transport. [1-3] Many of these channels are lined with non-polar groups, and the conduction of water is facilitated by strong water-water interactions and unfavorable water-channel interactions. Quasi-1D water bridges through carbon nanotubes (CNTs), which were used to mimic these membrane channels, demonstrate the strong water-water interactions that are induced by hydrophobic confinement.[4-6] These bridges are also important in proton-transport mechanisms, where it has been shown that proton conduction can be up to an order of magnitude larger through CNTs than in bulk water.[5] Additionally, confined water near the hydrophobic residues of a protein exhibits dynamics that are consistent with a super-cooled state even at room temperature.[7, 8]

The mutual structural and dynamics effects that water and hydrophobic surfaces can have on one another have lent them to extensive experimental and theoretical investigation. Parker *et al.* performed pioneering work in 1994 describing the attraction between curved surfaces covered with a hydrophobic layer submerged in water.[9] This work showed that hydrophobic attraction deviates sharply from the classical Derjaguin-Landau-Verwey-Overbeek (DLVO) theory, which only accounts for the attraction between two curved surfaces in terms of electrostatic and van der Waals forces, but it does not include any treatment of the intervening solvent-molecule effects.[10, 11] DLVO theory's deficiency in accounting for the hydrophobic interaction accurately leads to the conclusion that the solute-solvent effects are essential in this phenomenon.

Water is such a unique solvent that extensive investigation has illuminated many properties that do not exist for even other polar solvents. For instance, using thermodynamic arguments, Chandler has suggested that the solvation of hydrophobic species is not a universally entropically-driven process.[12] Instead, from his calculations, he concludes that while entropy controls solvation for small-radius hydrophobic solutes, this process is enthalpically driven for extended surfaces with a larger radius of curvature. Chandler's work serves as an example of the way that studies of the hydrophobic effect have challenged many of the previously held theories about the nature of solvation and aggregation of hydrophobic particles in aqueous environments.

7.2 Early investigations of the hydrophobic effect

While the theory of the hydrophobic effect had been phenomenologically linked to many important aspects of biomolecular conformation and colloid formation and interaction,[13] no experimental evidence of the distance dependence or magnitude of the forces between hydrophobic solutes in aqueous environments was available until the mid-1980s. For instance, in 1959 Kauzmann describes the role of 'hydrophobic bonding' in the structuring of proteins in their native configuration.[13] Ben-Naim *et al.* report the hydrophobic interaction of methane, ethane, *n*-butane, and benzene in H_2O and D_2O using a thermodynamic cycle to estimate the dimerization energy of the small molecules in water.[14] While Ben-Naim and co-workers were able to estimate the energetics of solution for the small molecules studied, they could not give an accurate description of the magnitude or length-scale of driving forces responsible for the dimerization processes.

Israelachvili and Pashley performed the first experimental measurement of the length-scale and magnitude of the attractive force between two hydrophobized mica surfaces submerged in water in 1982.[15] In that study, they reported an attractive force superior in magnitude and range to simple van der Waals forces acting between the surfaces. The long-range nature of this attractive force, 10-15 nm, gave definitive proof that the concept of a direct 'hydrophobic bond' between the surfaces, which was initially conceived to be analogous to a hydrogen bond, could be disproven[13, 16] as it had previously been challenged on a conceptual basis.[14]

The results of Israelachvili and Pashley using hydrophobized mica surfaces sharply deviated from two earlier studies on bare mica surfaces under the same experimental setup, which showed excellent agreement with the previously discussed water-neglecting DLVO theory.[17, 18] The discrepancy between the bare mica surface and the surfactant-covered surface studies led Israelachvili and Pashley to agree with the then contentious idea that the attractive force was the result of a rearrangement of the inter-surface water molecules.[15] Discrediting the "hydrophobic bond" mechanism led to extensive studies probing the nature of the attraction between hydrophobic surfaces in aqueous environments.

7.3 Theories of the hydrophobic interaction

This section includes a brief summary of the theory behind hydrophobic interaction in molecular solutes as explained by Ben-Naim in 1982.[19] The key concept found in Ben-Naim's work involves two spherical hydrophobic solutes being brought close together in a(n) (aqueous) solvent from infinite separation to a contact distance, designated σ. Assuming that this process is occurring under conditions of constant temperature (T) and pressure (P), Equation 7.1 describes the Gibbs free energy change of this process:

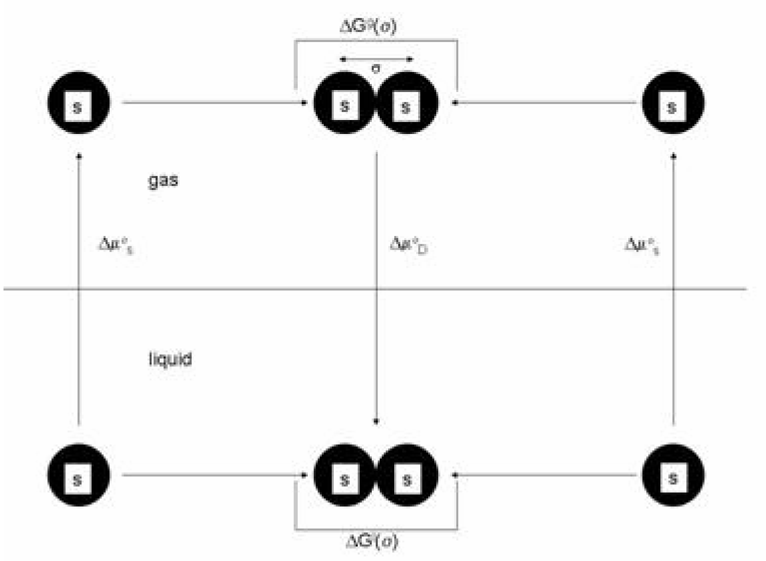

Figure 7.1: A thermodynamic cycle describing the process for hydrophobic aggregation in solution ΔG(R).

$$\Delta G(\infty \to \sigma)_{T,P} = G(T,P,solvent,R_{12}=\sigma) - G(T,P,solvent,R_{12}=\infty) \qquad (7.1)$$

where R_{12} is the separation between the hydrophobic solutes.

For simplicity sake, ΔG(∞ → σ) will be abbreviated as ΔG(σ) in the rest of this section. Using the thermodynamic cycle depicted in Figure 7.1, the quantity ΔG(σ) can be expressed as Equation 7.2:

$$\Delta G(\sigma) = \Delta\mu_D^O - 2\Delta\mu_S^O + \Delta G_D^g(\sigma) \tag{7.2}$$

where $\Delta\mu_X^O$ is the change in chemical potential of (X=S,solute and X=D,dimer) and ΔG^g_D is the gas-phase free energy of dimerization. If the solutes are approximated as structureless spherical particles, $\Delta G_D^g(\sigma)$=U_{SS}(R_{12}=σ), where U_{SS}(R_{12}=σ) is a direct interaction potential that can be expressed with a simple intermolecular potential such as a Lennard-Jones function.

Moving from the specific to the general, since $\Delta G_D^g(R)$=U_{SS}(R) for any value of R, and $\Delta\mu_D^O$ can be written as a function of R, Equation 7.2 can be re-written as:

$$\Delta G(R) = U_{SS}(R) + \delta G^{HI}(R) \tag{7.3}$$

where $U_{SS}(R)$ is the same interaction potential described above and $\delta G^{HI}(R)$ is the free energy of hydrophobic attraction expressed as a function of solute separation. Since $U_{SS}(R)$ is completely independent of choice or even presence of solvent, any solvent effects will be completely located in the $\delta G^{HI}(R)$ term in Equation 7.3.

Direct measurements of $\delta G^{HI}(R)$ are difficult by definition since it is a measure of the indirect work done by the solvent to bring two solutes to an intermolecular separation of distance R. One attempt to describe this indirect work quantity is through examination of the pair correlation function, $g_{SS}(R)$, which is the solute-solute pair-correlation function. The functional form of $g_{SS}(R)$ is found in Equation 7.4:

$$g_{SS}(R) = \exp[-\Delta G(R)/kT] \tag{7.4}$$

where k is the Boltzmann constant and T is temperature.[20] Combining Equations 7.3 and 7.4 we get:

$$g_{SS}(R) = \exp\{-[U_{SS}(R) + \delta G^{HI}(R)]/kT\} = \exp[-U_{SS}(R)/kT]\exp[-\delta G^{HI}(R)/kT] \tag{7.5}$$

which can finally be re-written as:

$$g_{SS}(R) = y_{SS}(R)\exp[-U_{SS}(R)/kT] \tag{7.6}$$

where $y_{SS}(R)$ is the pair-correlation function associated with only the $\delta G^{HI}(R)$ component of the total free energy. Practically speaking, the pair-correlation functions describe the probability of finding a solute molecule at a given distance from a point centered on another solute molecule.

Ben-Naim *et al.* have exploited an approximation that uses an ethane molecule to approximate a methane dimer at $R_{12}=\sigma_1=1.54$ Å, which is the equilibrium C-C bond distance for ethane. This approximation allowed them to close the thermodynamic cycle depicted in Figure 7.1 and calculate the quantity $\Delta G^{HI}(\sigma_1)$, and more importantly $\delta G^{HI}(\sigma_1)$, at a single distance $\sigma_1=1.54$ Å.[14]

Using this line of experimentation, the investigators provide a number of interesting results regarding the uniqueness of water as a solvent. The absolute magnitude of $\delta G^{HI}(\sigma_1)$ is on average more than 0.5 kcal mol^{-1} more exoergic than other solvents studied, which include cyclohexane, 1,4-dioxane, and a series of short-chain alcohols. The other major result of Ben-Naim *et al.'s* work is that the hydrophobic interaction in water has a strong dependence on the solution temperature. The strength of the hydrophobic interaction increases by ~15% from 10 to 30°C in water, but for all of the other solvents studied there was no appreciable effect over that same range.

Ben-Naim and co-workers later investigated the role that kinematics play on the hydrophobic effect by comparing the results of isotopically-substituted solvents.[14] At low temperatures (10°C) the hydrophobic effect in regular water is ~3% more exoergic than in D_2O. As the temperature is increased, the difference between the two solvents vanishes and the hydrophobic effect is essentially the same in the two solvents. While Ben-Naim *et al.* could offer no definitive mechanism for this phenomenon, they provide evidence that a simple treatment of the pairwise potential-induced structure of water is not able to describe the differences between H_2O and D_2O.

Major theoretical and experimental efforts have extended the theory of the hydrophobic effect to include a more robust treatment of the factors influencing small solute aggregation and the attraction between surfaces covered with hydrophobic, surfactant molecules.

7.4 Proposed mechanisms of the hydrophobic interaction

Building on the theoretical work of Ben-Naim and the experimental work of Israelachvili and Pashley, a number of researchers sought to study the nature of the experimentally measured attractive forces between hydrophobic surfaces in aqueous environments. Claesson and Christenson,[21] and Rabinovic and Derjaguin[22] both showed that the attractive force between hydrophobic surfaces extended nearly an order of magnitude beyond the 10-15 nm range first measured by Israelachvili and Pashley.[15] These new experiments led theorists to corroborate that the long-range attraction between hydrophobic surfaces cannot be a direct interaction between the surfaces; the intervening water film must play a role.

Three major mechanisms of attraction were proposed based on the results of these new experiments. The first mechanism, proposed by Pashley *et al.* states that the thermodynamically-stable state between hydrophobic surfaces is a vapor state with only gas-like water molecules present.[23] This mechanism is supported by the fact that a vapor layer persists between hydrophobic surfaces for distances up to a few hundred nanometers when they are separated from molecular contact. This mechanism also assumes that the barrier to water evaporation is too large to be energetically accessible until the surfaces are brought to near molecular contact. As the surfaces are brought near to one another, the barrier to evaporation is removed and a small density fluctuation in the confined region can result in drying between the surfaces (also termed dewetting). Lum *et al.* report a critical dewetting distance that can be estimated based on experimentally measured factors as:[24]

$$D_c \approx \frac{2\gamma}{n_l\left|\mu_l - \mu_g\right|} \tag{7.7}$$

where D_c is the critical dewetting distance, γ is the surface tension between the liquid/gas phases of water, μ_x is the chemical potential of the liquid (x=l) and gas (x=g) phase of water, and n_l is the number density of liquid water.

Determining the experimentally-controllable factors that govern this critical dewetting distance will be invaluable in helping to make a connection between theoretical simulations and experimental results. To this end, Debenedetti and co-workers have contributed a series of papers describing the effects that pressure, temperature, and surface topology have on the critical dewetting distance for water in between two silica-based hydrophobic plates, studied with molecular dynamics (MD) techniques.[25-27] The calculations show that as the temperature increases and the external pressure decreases, the critical dewetting distance becomes larger. The dewetting process implies that the hydrophobic surfaces will collapse if they are allowed to move during the simulation. At pressures of 1 bar and 300 K, the largest value of dewetting in the simulations by Debenedetti and co-workers is < 0.8 nm for the simulation times studied, which are all 1 ns or less. As the attractive forces measured in the experiment exist on much longer distance scales than the simulations predict, a dewetting mechanism cannot be solely responsible for the hydrophobic effect.

An MD study by Huang, Margulis, and Berne of water confined between two non-atomistic hydrophobic ellipsoids has shown that the critical dewetting distance depends strongly on the cross sectional area and shape of hydrophobic plates.[28] This result is particularly important in understanding the degree to which computational studies can be applied to understanding the experimental measurements on macroscopic systems of similar chemical composition. The size of the hydrophobic plates and the number of water molecules simulated represents a major limiting factor for MD simulations performed, in addition to the normal simulation-time limitations.

The complete dewetting/capillary-evaporation mechanism of attraction is a promising mechanism to explain attraction at close separation distances. However, the long-range attraction (≥100 nm) present in experimental studies cannot be fully explained by this mechanism. One possible explanation is that at long separation distances, the attraction is caused by a precursor state to capillary evaporation.[21, 29]

A second proposed mechanism for the attraction of hydrophobic surfaces in aqueous environments involves electrostatic forces. The electrostatic class of mechanisms encompasses many different possibilities, from double-layer surface forces[30] to charge-fluctuation forces,[31, 32] which create electrical bridges from one surface to the other. Each of these variations has been shown to not properly explain the force *vs.* distance curves seen in experimental studies of single-layer surfactant molecules. Yoon and co-workers have proposed a mechanism including the formation of a complete or partial micellar bi-layer that includes a component of electrostatic forces in the description.[33]

A third major mechanistic category involves the induction of structural changes in the intervening film of water between the hydrophobic surfaces. Marcelja and Radic proposed a mechanism based on the variational mean-field approximation in 1976 which hypothesized that small structural changes in the water film were responsible for the hydrophobic attraction.[34] Since these models were unable to properly describe the interaction free energy and experimental forces, they were extended by Cevc *et al.*[35] to include the effects of water orientation, and by Ostrowsky and Sornette,[36] with limited success. Eriksson, Ljunggren and Claesson proposed a model that expanded upon Marcelja and Radic's original mean-field approximations that explains the attractive forces between the hydrophobic surfaces as a result of increased ordering of water molecules, which produces enhanced hydrogen-bonding networks relative to bulk water.[37] Eriksson *et al.*'s variational mean force-based model balances the free-energy gain associated with reorganization of the water molecules near the hydrophobic surface and the free-energy cost associated with reducing entropy due to the constricted motion of water molecules in hydrogen-bonding networks not near the surfaces. This model estimated that the free energy related to the attractive forces is on the order of $10^{-3} – 10^{-5}$ kT per water molecule, which makes the subtle effects of the hydrophobic attraction difficult to study using MD or any other atomistic theoretical technique. Additionally, the investigators provided an alternate hypothesis to their findings, which proposes columns of water forming quasi-1D hydrogen-bonded bridges between the surfaces, and are precursors to capillary evaporation between the plates.

7.5 Experimental results

Parker, Claesson, and Attard used a surface-force apparatus (SFA) to measure the attractive forces between freshly formed glass surfaces that were covered in a partially fluorinated hydrocarbon silane molecules.[9] Their work investigated the role that temperature and electrolyte concentration had on the attractive forces between the two hydrophobic surfaces. The first result they present is the presence of discontinuities in the force *vs.* distance curves as the surfaces are initially brought together. The authors hypothesized that these discontinuities or steps in the force curves are the result of bubbles that span the gap between the two surfaces. These bridges form as a result of nanoscopic bubbles that are present on the hydrophobic surfaces even at infinite separation. The authors propose a model for bubble formation that assumes the sub-microscopic bubbles found in bulk water are stabilized when they come in contact with the hydrophobic surface.

The presence and stability of the nanobubbles present along the hydrophobic surfaces are crucial to Parker *et al.*'s mechanistic understanding of the hydrophobic effect. Ducker has recently written a letter[38] describing the stability of these bubbles at the water/hydrophobic-surface interface and he proposes a mechanism for their relatively high stability and low contact angles, which had been measured previously.[39, 40] Ducker's mechanism assumes that surfactant molecules desorb from the surface and insert themselves along the gas-liquid interfacial region. Hu, Fang, and co-workers have shown that there are three different stable formations of gas bubbles that can form at the liquid-solid interface and provide a thermodynamic understanding for these three types of bubble formation.[41]

Parker *et al's* bridging bubble mechanism proposes that each step or discontinuity in the measured force curve is the result of an additional bubble bridging the gap between the surfaces. To test the robustness of their bridging-bubble hypothesis, the authors investigated the effects of a number of experimentally controllable variables on their force *vs.* distance measurements. By increasing the temperature from 22°C to 41°C, the measured attractive forces increase by a factor 2 to 3. The mechanistic explanation for this temperature relationship is that the bridging process is an activated one and the increased temperature provides more thermal energy to overcome that barrier and increases the propensity for the bridges to form.

In addition to temperature effects, Parker *et al.* studied the effects of electrolyte concentration in the intervening water solution. The addition of NaBr and NaCl to the solution increases the attractive forces between the hydrophobic surfaces. This evidence provides further proof that the dominant mechanism for hydrophobic attraction cannot be explained by electrostatic forces alone, since the addition of electrolytes would screen the charge effects. Secondly, the slight increase in attraction between the hydrophobic surfaces is consistent with the bridging-bubble hypothesis since there is no appreciable difference in the surface tension of water with electrolyte concentrations in the range studied. Parker *et al.'s* work represents the earliest systematic study investigating the role that differing experimental conditions have on the hydrophobic effect.

The advent of atomic force microscopy (AFM) greatly expanded the study of hydrophobic interactions and has led to a wealth of new information,[42-60] which is summarized in a review by Christenson and Claesson.[61] The reviewers conclude that there is no consistent mechanism that can describe all of the measurements of the attractive forces between hydrophobic surfaces performed up to that point. They divide the experimental work into two different categories: 1) surfaces that are hydrophobized by chemical reactions (i.e. a covalent bond is formed between the surface and the surfactant molecule) and 2) surfaces where the hydrophobic surfactants are physisorbed onto the substrate. The authors conclude that for experiments that fall into the former case the mechanism is unequivocally dominated by gas-bubble bridging as previously described by Parker *et al.*[9] However, the mechanisms for those experiments in the second category are less clear, which was mostly due to the fact that those systems had not been studied with the same frequency at the time. The potential for mobility of surfactant molecules and exposed surface ions can lead to dramatically different mechanisms of hydrophobic attraction.

In an attempt to build a mechanistic understanding of the hydrophobic effect when the surfactant molecules are physically absorbed onto the substrate, Sakamoto *et al*. presented an experimental study of the hydrophobic effect acting between alkyl trimethyl-ammonium salts (C_nTAC, where n is the number of carbon atoms in the alkyl chain) adsorbed onto silica surfaces.[62] The investigators studied the role that molecular chain length and surfactant density have on the magnitude and range of the attractive forces between the surfaces. Sakamoto *et al*. report that increasing chain length in the C_nTAC increases the attractive forces between the hydrophobic surfaces monotonically, with no hydrophobic attraction measured for chain lengths shorter than C_{12}TAC. For the longest chains studied (C_{18}TAC), hydrophobic attraction force curves were reported to investigate the role that the density of the surfactant molecules plays in determining hydrophobic interaction. At low concentrations of C_{18}TAC ($1x10^{-5}$ M), hydrophobic attractive forces were measured, but the magnitude and length scale of attraction were both less than at $3x10^{-5}$ M, when the silica surfaces are completely covered. As the concentration of surfactant molecules increases to near the critical micellar concentration (cmc), the forces between the two surfaces are attractive at large separations and become repulsive as the surfaces are brought close to one another ($\leq$ 10 nm). At concentrations above the cmc, the force *vs.* distance curves measured are completely repulsive.

The discontinuities in the force *vs.* distance curves originally reported by Parker, Claesson, and Attard were also present in Sakamoto *et al.'s* study and the bridging-bubble mechanism was presumed to explain the attractive forces seen at large separations. To verify this assumption, Sakamoto *et al.* attempted to measure the forces between hydrophobic surfaces when the water has been degassed. The investigators first showed that general degassing procedures of boiling water for an hour, followed by freezing it in a sealed vessel with liquid nitrogen and then melting the water at reduced pressures is not enough to avoid formation of gas bubbles on the surfactant surface.

Even with these standard degassing procedures, nanoscopic bubbles formed on the surfactant surface and were imaged by Sakamoto *et al.* To ensure that no bubbles were present, surfactant powder was placed on a degassed block of ice in an evacuated vessel. As the ice melted, the surfactant molecules dissolved and the authors saw no bubbles on the surfactant surface with AFM. Using these degassing procedures to ensure no bubbles were present, these authors report no attractive forces between the hydrophobic surfaces, which further confirmed the bridging-bubble mechanism in their estimation.

The Ducker and Yoon groups report conflicting results using a similar methodology to Sakamoto *et al.* to study octadecyltrimethylammonium chloride (C_{18}TACl) adhered onto a silica surface. These authors have shown that in solutions where the C_{18}TACl concentration is below 1×10^{-5} M, smooth force *vs.* distance curves show long-range attractive behavior without the discontinuities reported by earlier investigation. Yoon and co-workers have shown that at smaller concentrations (10^{-6} M C_{18}TACl), there is only a slight difference in the length scale of attraction between degassed water solutions and air-equilibrated solutions. The authors propose a competing mechanistic understanding, which involves the pH change between air-equilibrated and degassed systems. Ducker, Yoon and co-workers propose that the major difference between air-equilibrated and degassed solutions is not the presence or absence of nanoscopic bubbles, but a change in the pH of the solution. By removing CO_2 from the solvent, the pH is raised dramatically and at the higher pH a micellar bilayer of the surfactant molecules forms. The outer layer of the micellar structure contains surfactant molecules having a reverse orientation with respect to the substrate surface, and thus has the positively charged ammonium side of the surfactant molecules exposed to the other surface. The positive charges repel one another and result in the repulsive force *vs.* distance curves reported. At low concentrations, there are not enough surfactant molecules in solution to form the bilayer with appreciable coverage and thus even at high pH values (degassed solutions), the differences in attraction are minimal.

To further support their hypothesis, Ducker, Yoon and co-workers report a screening of the attractive forces by the presence of NaCl in solution with salt concentrations as low as 10^{-4} M and almost complete attractive screening at $3x10^{-3}$ M NaCl concentration. The authors offer no additional mechanistic insight into the nature of this screening except to propose that electrostatic forces contribute to the surface attraction. McNamee *et al.* have investigated the role that ion screening has on the attraction between C_{18}-TACl covered mica surfaces.[63] While Ducker, Yoon, and co-workers found that the presence of NaCl effectively screens the long-range attraction between the surfaces, the presence of $NaNO_3$ does not screen these same forces. This finding indicates that the size and shape of the anion present can have an effect on the screening of the long-range attractions.

7.6 Measures of hydrophobicity

Sakamoto *et al.*[62] and Zhang *et al.*[33] have both independently shown that longer chain surfactant molecules exhibit greater attraction in AFM experiments when compared with shorter chain surfactants. Whether by screening the surface charges, inducing additional structure in the neighboring water molecules, or enhancing the presence and stability of surface-bound gas bubbles, all current experiments agree that the more hydrophobic a surface, the greater the magnitude of the hydrophobic effect in both AFM and SFA experiments. Quantification of the absolute or even relative hydrophobicity of different surfaces is a non-trivial matter. In an attempt to discern the relative hydrophobic character of surfaces, two major theoretical methods have emerged. Giovambattista *et al*.[27] have made use of a technique developed by Werder and co-workers in 2003[64] to compute the nanoscopic contact angle between a given surface and a water droplet comprised of $O(10^3)$ water molecules and surfaces of varying hydrophobicity. The calculations on these nanoscopic water droplets have been shown to correspond to macroscopic contact angle measurements, which are a good indication of the relative hydrophobicity of a surface for macroscopic systems.

Additionally, Garde[65-69] and Chandler[12, 24] have collaborated to expand the understanding of hydrophobicity near small spherical hydrocarbons and hydrophobic surfaces. These authors have shown that a better measure of the hydrophobicity of a surface or solute is the degree to which the density of water fluctuates near the hydrophobic particle.[65, 67] Chandler has shown that the probability distribution of the fluctuation of density near a hydrophobic surface can be fit to a Gaussian function and that the width of that function is an excellent indicator of the hydrophobicity of the surface.[12] Verifying the degree to which different surfaces present a hydrophobic environment will help to illuminate the different structural and dynamical effects that the intervening water molecules have on the hydrophobic effect.

7.7 Computational metrics of the hydrophobic effect

The use of MD to study molecular phenomena has led to a number of analytical techniques and metrics to probe the output of the simulations. While direct computational studies of the hydrophobic attractions are difficult to perform due to the aforementioned limitations of system size and simulation time scales, there are many different MD simulations that have shed light on the mechanisms and structural effects of water confined near hydrophobic surfaces. The first effect that has provided information about water structuring is the presence of water layering near hydrophobic surfaces.[70] The areas of high and low density provide insight into the cooperative aggregation of water molecules near the surface, as shown in Figure 7.2. Density layering occurs because the hydrophobic surface or solute interrupts the hydrogen-bonding networks that exist in bulk water. This interruption induces aggregation of water molecules into layers of high and low density by increasing the number and strength of hydrogen bonds as a function of distance from the hydrophobic surface.

The layering of density leads to regions where water molecules are aggregated to the degree that no strong order exists in the water structure. Conversely, regions of low density provide the opportunity for water molecules to order into tetrahedral formations, which are similar to ice crystals. Errington and Debenedetti created the concept of a structural order parameter, q, defined as

$$q \equiv 1 - \frac{3}{8}\sum_{j=1}^{3}\sum_{k=j+1}^{4}(\cos\psi_{jk} + \frac{1}{3})^2 \tag{7.8}$$

where ψ_{jk} is the angle formed between the O-O bond vectors of the four nearest neighbors of each individual water molecule.[71] In a perfectly tetrahedral environment (all ∠(O-O-O)=109.5°) q=1, and if the particles have no defined structure relative to one another (as in a sufficiently high temperature ideal gas) q≈0. The degree of tetrahedral structuring is indicative of the balance between the enthalpic gains from hydrogen bond formation and the entropic penalty paid for reduced water motion.

Another major metric for describing the structure of liquids is the radial distribution function (RDF). The RDF provides a measure of the relative density of water molecules from a point centered on either the center of mass or the oxygen atom in each water molecule. The features of the peaks in the RDF give an indication of the degree to which the individual liquid molecules have a structure regular to each other. A RDF with sharp peaks indicates a liquid with a very regular structure and distinct spacing of one water molecule relative to its nearest neighbors, whereas a smooth featureless RDF indicates a disordered liquid without a regular structure. As shown earlier in Equation 7.5, the RDF, $\gamma_{SS}(R)$, for dissolved species in a solvent can provide a direct measure of the hydrophobic effect.

All of the previous computational metrics have included either static or steady-state measurements, but an indication of the dynamical effects can expressed by measuring the diffusion coefficient of the water molecules as a function of their distance from hydrophobic surfaces. Measurements of the dynamical relationships of water molecules are particularly important because

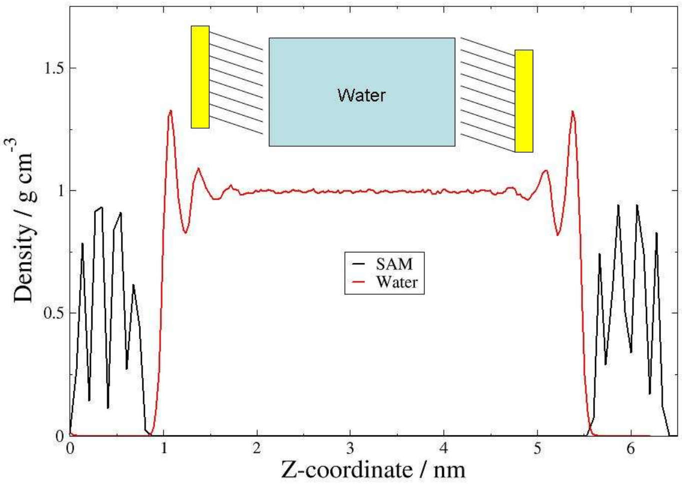

Figure 7.2: Density profile for a 2.0nm-thick film of TIP5P water confined between hydrophobic SAM surfaces at 300 K.

the formation of nanoscopic bubbles could be directly tied to the dynamics of water at the interface.

MD simulations can be analyzed to provide diffusion coefficients as a function of distance from the hydrophobic surface. The Einstein relationship is used to calculate diffusion coefficients as expressed in Equation 7.9:

$$D = \frac{< \Delta r(\tau)^2 >}{2d\tau} \tag{7.9}$$

where D is the diffusion coefficient, $< \Delta r(\tau)^2 >$ is the mean-squared displacement of each particle for the time period τ, and d is the spatial dimensionality of the system (e.g. d=3, for a three-dimensional system). Wick and Dang have provided a more sophisticated treatment of diffusion coefficients near an interface which divides the lateral and perpendicular diffusion coefficients into two separate components, which we have implemented in this work to determine the lateral diffusion behavior of confined water.[72]

A final computational variable that will be important in quantifying the structure and dynamics of water near hydrophobic surfaces is investigating the orientation of water molecules with respect to the surface. The wetting or dewetting of a hydrophobic surface is crucial to understanding the water dynamics near surfaces and other hydrophobic solutes. Calculating the degree to which O-H bonds point towards the surface gives an indication of the types of solute-solvent interactions that are involved in the hydrophobic effect and their range.

7.8 Water Models/Molecular Dynamics Simulations

Using many of the same techniques that have been described before, MD simulations have provided a unique level of information about the nature of water near hydrophobic and hydrophilic surfaces. The distinctive properties and ubiquitous presence of water in many different biologically and technologically relevant environments makes it particularly difficult to model it without a very sophisticated treatment of the electronic structure.[73] Many molecular-mechanics (MM) based models have been proposed and tested extensively for water at varying conditions. The ST2 model of water[74] was the gold standard for MD simulation of water properties until the TIP3P and TIP4P models were developed by Jorgensen and co-workers in 1983.[75, 76] These water models were all parameterized using experimental data of water under ambient conditions and treat water molecules as internally static molecules. For the relatively small range of experimental data used in the parameterization of these models, they are able to give qualitatively correct descriptions of water behavior in interfacial regions and over a relatively wide range of temperatures.

More recently, two models have emerged as the preferred methods for performing MD simulations of water. The first is the single point charge-extended (SPC/E)[77] model of water which was introduced in 1987 and is an improved version of the earlier single point charge model (SPC)[78] that includes a self-energy correction. The SPC/E model improved agreement between experimental and calculated water bulk radial distribution functions, density and self diffusion coefficients over the SPC model. SPC/E model water molecules have a rigid structure with a fixed O-H bond distance of 0.9572Å and a H-O-H bond angle of 104.52°. The effective pair potential in the SPC/E model implicitly includes some polarization effects without explicitly including polarization terms into the potential. One theoretical limit of the SPC/E model is that it only models the three atomic centers for each water molecule and does not explicitly include the lone-pair electrons on the oxygen center.

Although the SPC/E model of water is the most widely used model for MD simulation today,[8, 25-27, 79] there are some properties of the model that are not desirable, especially over relevant temperature ranges, for simulations of interfacial water behavior. A simulation of the co-existence of I_h ice and liquid water to determine the melting point of a wide variety of water models predicts the bulk melting point for SPC/E water to be 213±2 K, or ~60 K below the experimental freezing point at ambient pressure.

A more sophisticated water potential that can ameliorate some of the deficiencies of SPC/E is the TIP5P[80] model. Briefly, TIP5P explicitly considers all three atomic centers and the two lone electron pairs. The model shows remarkable accuracy in the predicted density of water over the range from -35°C to 75°C (238 K - 348 K) and predicts the appropriate temperature of maximum density in comparison to other water models. One of the most striking improvements of the TIP5P model over SPC/E is that the predicted melting point of water is 271±2 K.[80] However the TIP5P model's major drawback is that the 5-site model tends to over-predict the tetrahedral nature of liquid water. This will be an important factor to consider as we use the TIP5P model, in conjuction with SPC/E, to investigate the nature of water interacting with hydrophobic surfaces in this work.

Let us return to the MD simulations performed by Debenedetti and co-workers on the effects of pressure and temperature on the nature of water confined between two atomically defined plates.[25, 27] A major conclusion of their work investigating the effects of pressure for water confined between hydrophobic plates that are separated by a distance of 1.6 nm is that as the pressure is increased, the water between the plates begins to form more well defined layers.[25] The density near the plates increases as more water molecules accumulate in the first water layer. Additionally, that first water layer moves closer to the plates. This density increase with increasing pressure indicates that the effective hydrophobic nature of the plates is reduced. As a metric of this phenomenon, the coordination number, the number of other water molecules within 0.3 nm, increases to ~4 at the interface. External pressure also increases the coordinated nature in the water that is confined between the plates, but not at the interface. Debenedetti and co-workers also probed the tetrahedral nature of the confined water. Increasing the external pressure does not in fact alter the maximum of the tetrahedral-order distribution of the confined water, but it does extend the range of water that is similar to bulk water when using tetrahedricity as a way of comparison.

The other major work relevant to this study is a complementary MD study by Debenedetti and co-workers that investigated the effects that changing temperature has on water confined between hydrophobic plates.[27] The trends seen as the temperature increases are all similar to those when the pressure is decreased except for the behavior of the tetrahedral order of the confined water. While the maximum order parameter of the confined water is unaffected by the external pressure of the simulation, the water near the plates is more ordered, and the range of maximal ordering extends to within 0.3 nm of the hydrophobic plates. When the temperature is lowered during the simulation, the increase in the range of the maximum ordering is still seen, but the degree of ordering increases monotonically from a maximum of ~0.625 at 300 K to ~0.75 at 220 K. One issue of note for these simulations is that the water model used (SPC/E) has a freezing point of 213±6 K[81] and the dynamics exhibited below the physical freezing point of water can exhibit artifacts of the water models and do not necessarily correspond to reality. Even with this caveat, these simulations provide the most complete description of water confined in both hydrophobic and hydrophilic surfaces available.[25-27, 79, 82, 83] A final conclusion from this series of papers is that at low temperature and high pressure, the differences between the types of surfaces are minimized.

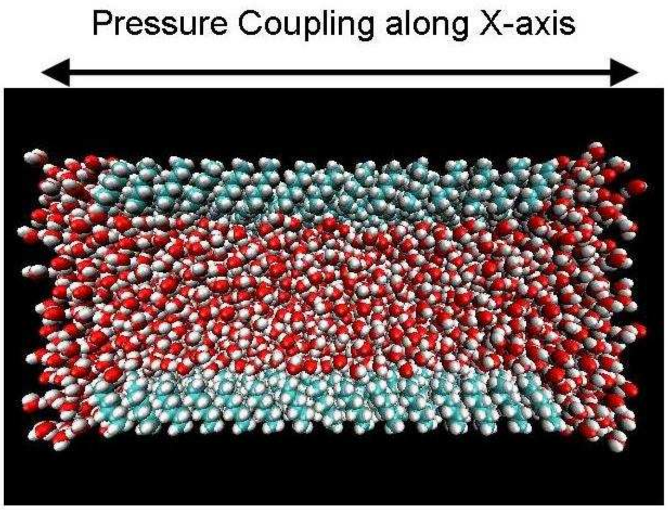

Figure 7.3:A schematic representation of the NPT molecular dynamics simulation of water confined between hydrophobic SAM surfaces.

While the simulations just described represent state-of-the-art calculations in the field, the authors propose further studies which include semi-crystalline and amorphous solids. These types of surfaces are similar to the surfactant molecules used in all of the experimental studies reported previously and represent the basis for our simulations.

In summary, we have presented in this section the historical and theoretical background of the hydrophobic effect. The rest of this work is organized as follows. First we present the details of the computer simulations of bulk water and water confined near hydrophobic surfaces. We then present the results of our simulations using the metrics described above. Finally, we compare our results with previous MD simulations and with prevailing theories of hydrophobic interaction.

7.9 Simulation details

In an attempt to model realistic hydrophobic surfaces, we have employed in all simulations alkanethiolate self-assembled monolayers (SAMs), which are commonly used in the experiment to hydrophobize gold surfaces. The SAM surfaces are composed of hexanethiolate molecules arranged in a hexagonal pattern with an inter-chain spacing of 4.98Å and a chain tilt angle of 30°. These SAM conditions correspond to the experimental equilibrium conditions of a SAM on a Au(111) surface.[84] The forces acting on all of the atoms are described by the all-atom version of the OPLS force field.[85] Our choice of this force field was informed by its satisfactory reproduction of the experimental tilt angle of the alkanethiol SAM surfaces on gold (~30°).[86]

In the simulations, two SAM surfaces are placed along the *xz*-plane so that the separation between them can be controlled by modifying their coordinates along the y axis only. The confined water is in equilibrium with reservoirs of water along the x direction of the box. In our simulations we vary the length of the inter-surface water film from 0.8 to 5.0 nm. The analysis of the structure and dynamics of water is performed only for those molecules of water that are in between the two surfaces.

All of our simulations have been performed using the GROMACS molecular dynamics program.[87] The long-range Coulombic interactions are modeled using the particle mesh Ewald (PME) sum technique.[88] To facilitate the simulations, the positions of the non-hydrogen atoms of the SAM surfaces were restrained by a force constant of 1000 kJ mol^{-1} nm^{-2} using the LINear Constraint Solver (LINCS) algorithm[89] also implemented in GROMACS.

Most of the MD simulations were performed in a semi-isotropic NPT (isothermal, isobaric) ensemble in which the pressure was controlled by a Berendsen barostat[90] and the atomic velocities were scaled to maintain temperatures over the course of each MD simulation.[91] The external pressure for all MD simulations was 1 bar along the x-direction, while the lengths of the box were frozen along the y- and z-axes. Figure 7.3 shows a cartoon depiction of the simulation. A subset of calculations where performed in the NVT (constant temperature and volume) ensemble with an average water density of 1 g cm^{-3} to check the generality of the results presented in this work. We did not find any significant differences between the results of the NPT and NVT ensembles.

7.10 Results

7.10.1 Density layering

Thin water films that are confined in hydrophobic environments have been shown to organize in such a way that water layers form in the density across the film, as shown in Figure 7.2. The magnitude and number of these density layers depends on the relative hydrophobicity of the confining surfaces and the thickness of the film itself. Figure 7.4 shows the density profiles across the thin film of water for a number of films of varying thickness. As the film thickness increases, the number of layers increases from two layers

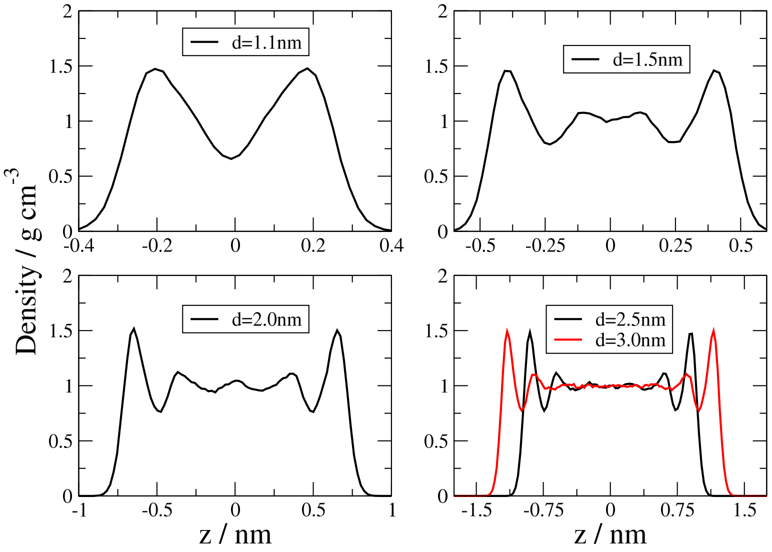

Figure 7.4: Density profiles for TIP5P thin water films of thicknesses varying from 1.1-3.0nm and 300 K.

for plate separations of 1.1 nm up to five layers at 2.0 nm. For all films thicknesses >2.0 nm, there is a distinct pattern that develops in the density distributions with two apparent layers formed near SAM surfaces. Beyond this initial interfacial region, which extends approximately 0.5 nm into the film, the water density approaches that of bulk water. This can be fully appreciated in the density profiles of 2.5 and 3.0 nm films, where the central region of the film clearly exhibits bulk density.

While these water density layers influence the structure and dynamics of water in the interfacial region, there is no indication that they can account for the distance scale of water structuring required to explain the experimental measurements of the hydrophobic effect (>> 10 nm). Debenedetti and co-workers have shown that these characteristic water layers are unique to hydrophobic confinement and that the degree to which the confining surfaces present a hydrophobic environment is important to determining the degree of water layering in similar thin films.[82]

7.10.2 Contact angle

Sakamoto *et al.*[62] and Zhang *et al.*[33] have both independently shown that longer chain surfactant molecules exhibit greater attraction in AFM experiments when compared with shorter chain alkyl surfactant changes. All current experiments agree that the more hydrophobic a surface, the greater the magnitude of the hydrophobic effect in both AFM and SFA experiments. Quantification of the absolute or even relative hydrophobicity of different surfaces is non-trivial and has warranted extensive study in the past.[24, 67, 68]

To investigate the relative hydrophobicity of the SAM surfaces in this work, we have performed MD simulations of nanoscopic water droplets (~2500 water molecules) located on top of different infinite hydrophobic surfaces and over a range of temperatures. From these simulations, we calculate the contact angle of the droplet over a range of temperatures and with a number of substrates to determine the effects of temperature on surface hydrophobicity. We use a methodology similar to that used by Debenedetti, Rossky, and co-workers[25, 27, 82] to calculate the contact angle between the water droplet and the surface. Figure 7.5a shows an initial snapshot of the simulations and Figure 7.5b is an equilibrated snapshot during the simulation that clearly shows that the SAM surface used in this work is hydrophobic. Quantitatively, the calculated contact angle is 132° at 300 K, employing the TIP5P water mode and a hexanethiol SAM. This result is in very good agreement with the result by Dalvi and Rossky (129°), using an *n*-dodecanethiol surface and a water droplet of approximately the same size as that used in this work but modeled with the SPC/E model, and using a slightly different calculation procedure that assumes that the droplet is spherical.[92] Both calculations slightly overestimate the contact angle measured in macroscopic experiments,[93] presumably due to the fact that experimental SAMs commonly contain defects at the gold surface and contain multiple boundaries between alkanethiol domains.

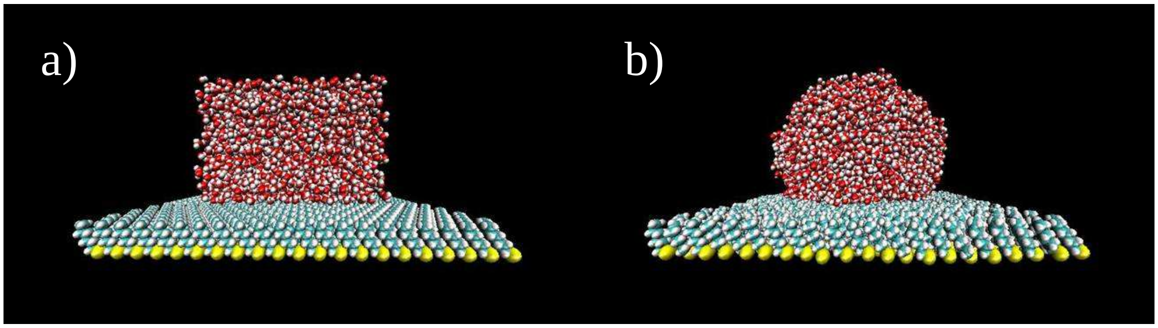

Figure 7.5: Snapshots of TIP5P water nanodroplets on SAM surfaces at 300 K a) Initial water configuration at t=0 b)Equilibrated nanodroplet at t=5 ns.

Additional calculations were performed for a shorter-chain, reduced-dimensionality model of the surface consisting of just the ethane terminus of the hexanethiol SAM. The ethane molecules have the C atoms frozen to their positions in regular SAM so that the average separation between the SAM chains (4.98 Å) is maintained throughout the simulations. The contact angle of water for this ethane surface is identical to that using the fully-dimensional hexanethiol SAM, suggesting that the ethane surface is a time-saving representation of the full SAM. In the experiments referred to above, the hydrophobicity of short-chain SAMs was found to be smaller than that of longer-chain SAMs likely because surfaces made with alkanethiol molecules with less than 6 methylene units do not possess enough inter-chain dispersive attraction to form a regular self-assembled monolayer.[94] In our work, we do not see this loss of hydrophobicity with decreasing chain length because we deliberately freeze the non-hydrogen atoms for simplicity. The calculated contact angles provide verification that these surfaces present a hydrophobic environment in which to model the properties and dynamics of confined water.

7.10.3 Interfacial orientation

The orientation of water molecules confined near an interface provides another metric to describe the degree of hydrophobicity of a surface. In 1984, Lee *at al.* showed that water confined near a flat hydrophobic wall tends to orient itself in such a way as to have one of its O-H bond vectors pointing directly towards the hard-wall surface.[70] This orientational structure minimizes the interactions between a water molecule and the hard wall, thereby allowing the other three hydrogen-bonding vectors to actively participate in hydrogen bonds with either interfacial water molecules or water molecules deeper into the film. A decade later, Lee and Rossky showed that the exact opposite case is true for hydrophilic surfaces, where an O-H bond preferentially points away from a hydroxylated silica surface, allowing the other three hydrogen bonding vectors to interact with the hydroxyl sites on the silica.[95] Using a similar confining surface, Giovambattista *et al*. have shown that as they artificially vary the local dipole moment of hydroxyl sites on the surface there is a smooth transition from hydrophobic to hydrophilic character in the orientational structure of water at the interface.[82] This smooth transition in orientational structure provides a metric by which the relative hydrophobicity of the confining can be probed. Figure 7.6 shows the distribution of O-H bond angles relative to a vector normal to the SAM surface and pointing away from it over a range of distances from the surface.

Figure 7.6(a) shows the orientations of water in the first layer of water (0-0.3 nm, where 0 is the z-coordinate of the terminal carbon layer). The figure indicates a strong propensity for the water molecules to orient themselves with one of their O-H bonds

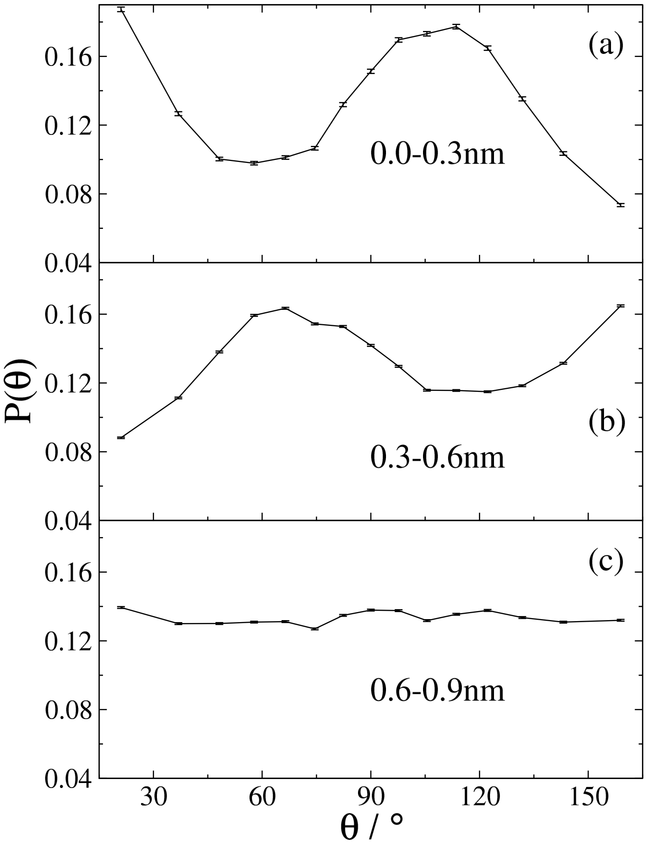

Figure 7.6 Distribution of O-H bond angular distributions between water molecules and the normal vector pointing away from the SAM surface over a range of distances from the SAM surface. Simulations are for 5.0 nm thick TIP5P water films at 300 K.

pointing towards the surface, while the other O-H bond points back into the water film to establish hydrogen bonds. The next water layer (0.3-0.6 nm) shows water molecules preferentially located in a complementary orientation to those in the interfacial layer. Molecules in this layer form an enhanced hydrogen bonding network with the interfacial layer when compared with bulk water. However, the height of the peaks in the distribution is slightly smaller than in the purely interfacial data, suggesting a small loss in the anisotropy of the orientation distribution. The third layer (0.6-0.9 nm) shows a largely isotropic distribution, implying no preference for any particular orientation of O-H bond vectors relative to the surface. (This is corroborated by analysis performed at longer distances from the surface.) Therefore, while the hydrophobic SAM surface has a dramatic effect on the orientation of water close to the surface, its effects disappear well before reaching a depth of 1 nm within the film. The lack of preferred O-H bond orientations deep into the water film provides another piece of evidence from the simulations that long-range structuring does not seem like a possible explanation for the experimentally-measured range of hydrophobic attraction.

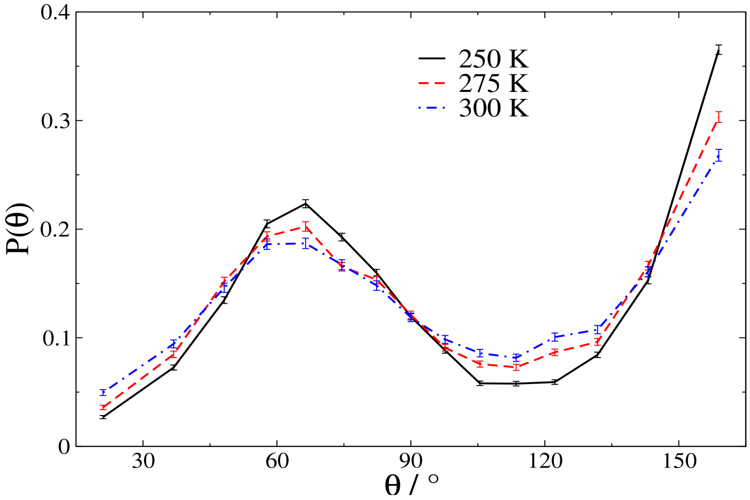

Figure 7.7: Distribution of O-H bond angular distributions between water molecules and the normal vector pointing away from the SAM surface over a range of temperatures. Distributions are calculated from all water molecules that are within 0.2nm of the terminal carbons atoms in simulations of 5.0 nm thick TIP5P water films at 300 K.

To investigate the role that temperature plays on thin water films we present temperature dependent interfacial O-H orientational profiles in Figure 7.7. Over the range of temperatures studied, the interfacial distributions are all qualitatively similar. The sharpness of the peaks at lower temperatures indicates increased orientation that is associated with a reduction in the entropic penalty at lower temperatures.

7.10.4 Structural ordering

The strong interfacial orientation seen in the prior section can serve as a template to structurally order the water molecules. Tetrahedral ordering of water molecules in a thin film occurs as a function of water's ability to form four different hydrogen bonds. The formation of these hydrogen-bonding networks is the result of a balance between the enthalpic gains as a result of bond formation and the entropic penalty that is paid due to the restricted motion of water molecules in a hydrogen-bonding network.

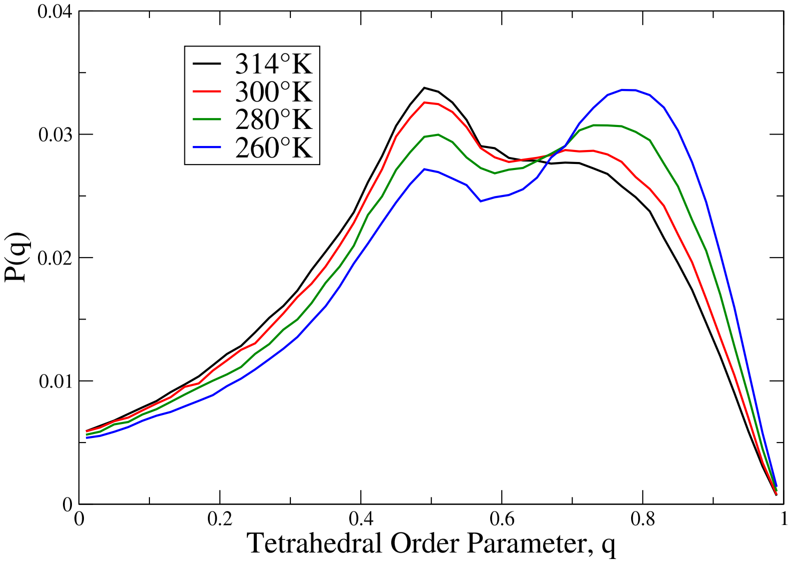

Figure 7.8: Distribution of the order parameter, q, for bulk water simulations at temperatures ranging from 260-314K. Simulations were performed for 10ns and used the SPC/E water model.

The temperature dependence on the tetrahedral order parameter is exhibited in Figure 7.8 where we present the order parameter for bulk water simulations from 260-314 K using the SPC/E water model. The order-parameter distribution is shown to be bimodal over the range of temperatures studied, with a smooth transition from high-temperature disorder to more ordered systems at lower temperature. Note that even if some of the explored temperatures are below the normal freezing point of water, we do not observe ice formation because the freezing point for the SPC/E water model is 213 K.

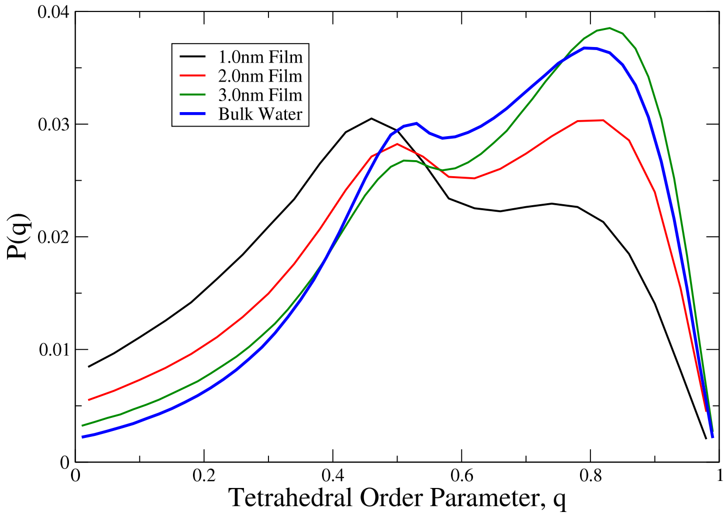

Figure 7.9: Distribution of the order parameter for thin water films ranging from 1.0-3.0nm thicknesses. Simulations were performed using the TIP5P water model at 300K.

The effects on confinement on the ordering of water films are shown in Figure 7.9, where we exhibit the order parameter distribution of all water molecules confined in films with thicknesses ranging from 1 to 3 nm. The bulk water distribution is also plotted as a reference. All simulations in Figure 7.9 were run at 300K and used the TIP5P water model. The figure indicates that there is a significant level of disorder induced by narrow confinement, but films with thickness of 3 nm approach that of bulk water. Simulations of confined water with thicknesses larger than 3 nm (not shown) are nearly coincident with the bulk water and provide no insight into the mechanisms responsible for the hydrophobic effect at the long hydrophobic-plate separation distances explored in the experiments.

We confirm this conclusion by investigating the average order parameter as a function of location in the film. Figure 7.10 shows the water density profile (left axis) and average order parameter (right axis) as a function of the inter-surface coordinate across a 5.0 nm-thick water film using the TIP5P model at 300 K. There is a very slight enhancement of the tetrahedral ordering parameter beyond the first water layer but this enhancement does not extend beyond 0.5 nm into the film, where the order parameter falls to its bulk value. Near the interface, the tetrahedral order parameter becomes zero due to the absence of neighbors in a tetrahedral environment in the vicinity of the hydrophobic surface.

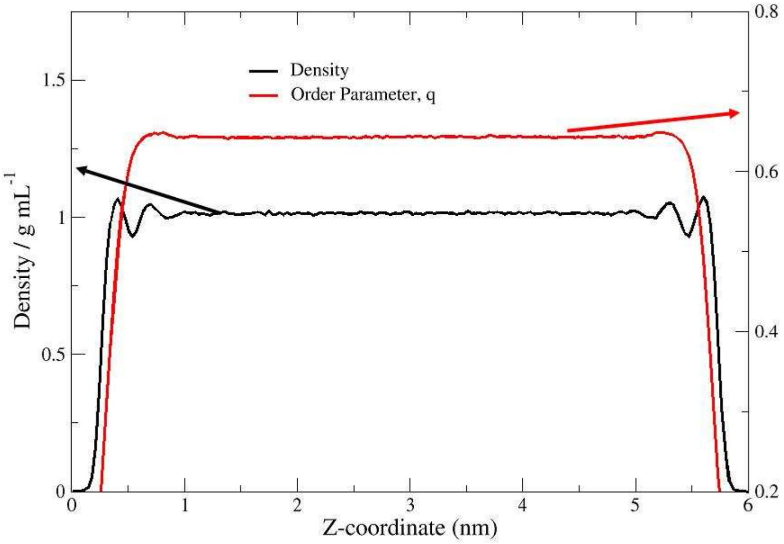

Figure 7.10: Density distribution and average order parameter for a 5.0nm thick film confined between hydrophobic SAM surfaces. Water film is modeled using the TIP5P water model at 300K.

7.10.5 Diffusion coefficients

One consequence of the depletion layer that forms at the interface between extended hydrophobic surfaces and water is the presence of enhanced water mobility in the surface plane. Our final characterization of the thin films of water under hydrophobic confinement is an analysis of diffusion coefficients of water parallel to the hydrophobic plates. The diffusion coefficients are calculated by means of a modified version of the

Einstein relationship. We calculate the survival probability, P(τ), for molecules that are located in a given slab for a period of time τ.

$$P(\tau) = \frac{N(0,\tau)}{N(0)} \quad (7.10)$$

Molecules that enter the box after the initial time step or leave the box and return are not counted in the analysis. The next step is calculating the mean-squared change in position in the surface (xy) plane.

$$\left\langle \Delta r_{xy}(\tau)^2 \right\rangle_{\mathbf{R}_k} = \frac{1}{N(0)} \sum_{i \in \mathbf{R}_k} \left[(x(\tau) - x(0))^2 + (y(\tau) - y(0))^2 \right] \quad (7.11)$$

Where $\mathbf{R}_k$ represents the set of all molecules that remain in a particular slab centered at z from time t=0 through t=τ. The diffusion coefficients are then calculated using Equation 7.12

$$D_{xy}(z) = \frac{\left\langle \Delta r_{xy}(\tau)^2 \right\rangle_{\mathbf{R}_k}}{4\tau P(\tau)} \quad (7.12)$$

For this work we have chosen a value of τ=6 ps and slabs that are 0.25 nm thick in the z-direction. These chosen values need to be balanced with the total simulation time to give the desired level of precision, since smaller slabs and longer values of τ both decrease the survival probability.

Castrillón *et al.* have sought to describe the length-scale along which interfacial water ceases to exhibit characteristics that are distinguishable from bulk water in the vicinity of hydrophilic surfaces.[83] To illustrate the evolution of water from interfacial to bulk-like conditions they present distance-dependent diffusion coefficients and rotational relaxation times. These authors have shown that there is depressed translational dynamics of water on the length scale where density layering occurs but no differences from bulk behavior beyond the distance where density layering occurs.

In Figure 7.11, we present parallel diffusion coefficients for the TIP5P water molecules as a function of distance from the hydrophobic surface at 300 K. The results show that water closest to the hydrophobic surface moves substantially faster than water more removed from the interface. The figure also shows that this fast lateral motion of water persists relatively deeper into the water film than the prior structural metrics described earlier in this paper. In effect, the diffusion coefficients of the confined water

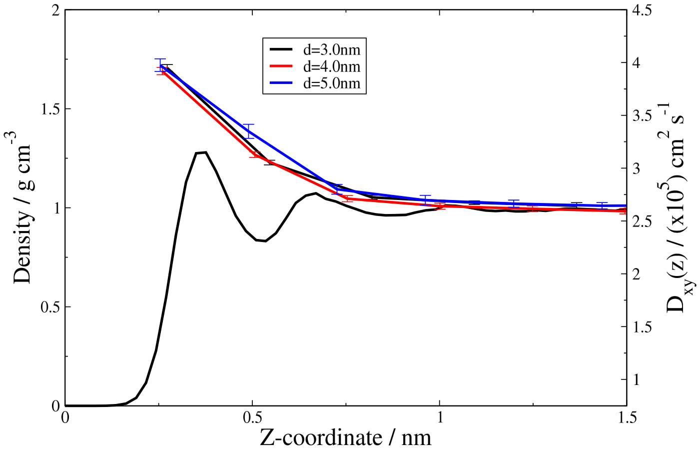

Figure 7.11: Parallel diffusion coefficients as a function of the distance from the hydrophobic SAM surfaces over a number of film thicknesses. The films considered in these simulations use the TIP5P water model at 300K.

do not become independent of the distance from the surface until approximately 1.5 nm separation from the surface.

Another conclusion that can be obtained from Figure 7.11 is that the diffusion coefficient is independent of film thickness for films thicker than 2.0 nm. The previous work done on hydrophilic surfaces found that this behavior was showed the same result, but for all plate separations greater than just 1.0 nm, which is also the distance where density layers extend into the thin water film in that work. The water model used to describe the motions of water molecules is important to describe the accurate lateral translations of confined water molecules.

Figure 7.12 shows a comparison of lateral diffusion coefficients of water predicted by the TIP5P and SPC/E water models normalized to their respective bulk values. The simulations correspond to films 5.0 nm thick and were run for 10.0 ns. Clearly, water modeled by TIP5P shows much more enhanced diffusion that SPC/E at the interface. This discrepancy between the two water models further illuminates the need for high-quality molecular mechanics force fields that are able to correctly describe the structure and dynamics in a wide range of

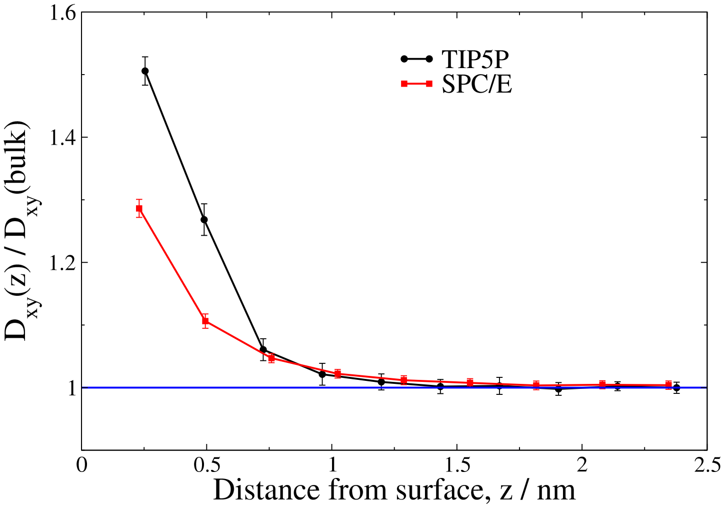

Figure 7.12: Parallel diffusion coefficients for TIP5P and SPC/E water molecules as a function of distance from the SAM surface. Diffusion coefficients are normalized to the bulk water diffusion coefficients for the given water model. Simulations are performed at 300K and have film thicknesses of 5.0nm.

environments. An interesting result of the comparison is that the range over which a difference from bulk behavior can be ascertained is very similar for both models.

To investigate whether the range of enhanced diffusion of water is correlated to density layering, we have investigated the effect of temperature on both of this metrics using TIP5P water. In Figure 7.13 we show distributions of lateral diffusion coefficients as a function of distance from the SAM surfaces. Since the diffusion coefficient is greatly dependent on the temperature, the distributions in Figure 7.13 are normalized to the bulk diffusion coefficient for each temperature. The length scale for enhanced water translational motion is much larger at 250 K than at 300 K. This trend is faithfully followed in density layering occurs, as shown in the inset. The obvious conclusion is that the enhanced water structuring that occurs with decreasing temperatures is correlated with an increase in the range with which hydrophobic surfaces influence the dynamics of a water film.

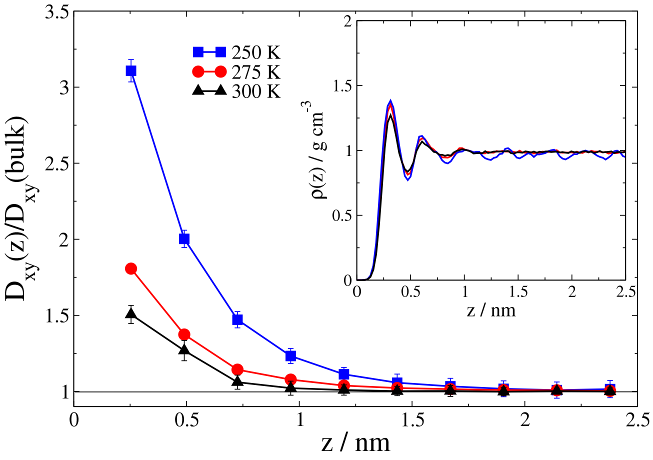

Figure 7.13: Parallel diffusion coefficients for TIP5P water molecules as a function of distance from the SAM surface over a range of temperatures. Diffusion coefficients are normalized to the bulk water diffusion coefficients for the given temperature. Simulations are performed for film thicknesses of 3.0nm. Inset: The water density profiles as a function of distance from the SAM surface for the given temperatures.

Finally, our MD study shows a connection between the lateral diffusion coefficients of water and the density fluctuations that have been described by Garde and co-workers to quantify the degree to which a surface is hydrophobic.[65-67, 96-98] The Garde group has shown that for a spherical cavity near a hydrophobic surface, the degree to which the density in that sphere fluctuates directly corresponds to the degree of hydrophobicity of the surface. The length-scale of these density fluctuations for a sphere with radius of 7.5 Å actually is remarkably similar to that of the lateral diffusion coefficient enhancement that we have presented in this work. Figure 7.14 shows this comparison between the density fluctuations and the lateral diffusion coefficients for films of thicknesses from 3-5 nm. The correlation between the density fluctuations and lateral diffusion coefficients provides evidence that the density fluctuations can be explained by the enhanced lateral diffusion.

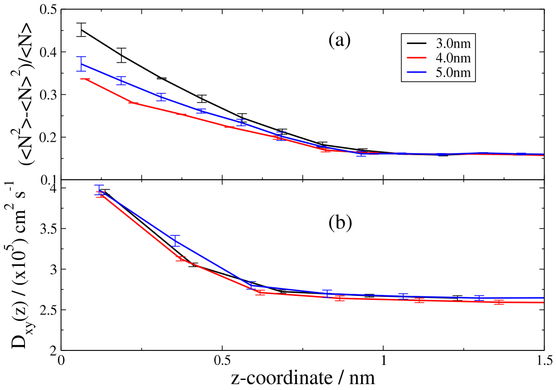

Figure 7.14: A comparison of the (a) density fluctuations for a spherical cavity, measured as ($\langle N^2\rangle$-$\langle N\rangle^2$)/$\langle N\rangle$ where N is the number of molecules in the cavity and (b) the lateral diffusion coefficient as a function of distance from the SAM surface for three different film thicknesses. Simulations were performed on a 5.0 nm thick film with the TIP5P water model at 300 K.

7.11 Conclusions

We have investigated the extent to which hydrophobic confinement can influence both the structure and dynamics of water via calculation of density profiles, interfacial O-H bond orientation, and diffusion coefficients from MD simulations. In agreement with previous work, we have shown that an alkanethiol SAM surface perturbs the density profile and tetrahedricity of water in direct proximity for the surface and favors an orientation of water molecules with O-H bonds pointing at the surface. However, we see in this work that all of these structural effects are short-ranged, and do not extend very far into the thin water film, i.e., less than 1 nm at room temperature. We have also shown that the lateral diffusion coefficient of water near hydrophobic plates is enhanced with respect to bulk water, and extends deeper (>1nm) into the film than any other metric of hydrophobicity we have examined in this work. Lower temperatures increase the range of the effect of the surface on the oscillations of the density profile of water and the lateral diffusion coefficients. The enhanced water mobility exhibited in this work correlates directly to the density fluctuations that have so thoroughly been studied by Garde and co-workers, but present a more detailed understanding due to their two-dimensional nature.

A somewhat dissatisfying conclusion of this work is that even if this work has been able to reveal that the effect of a hydrophobic surface on the dynamics of water extends further than previously thought from MD simulations, the range of the effect is still about two orders of magnitude smaller than seen in the experiment. However, the turbulent behavior of water near hydrophobic surfaces might lend support to one of the disputed theories that try to explain the long range of interaction between hydrophobic plates: bubble formation. In effect, the enhanced water motion seen in this paper, coupled with the dissolved gas bubbles that are known to form on hydrophobic surfaces in aqueous environments,[38] could provide an insight into precursor events that are responsible for bridging-bubble formation in experimental investigations of the hydrophobic effect. This effect could be further exacerbated by the imperfect nature of common hydrophobic surfaces used in the experiment, such as alkanethiol SAMs on gold. Steps, vacancies, and boundaries between alkanethiol domains which are rotated with respect to one another could provide nucleation sites for bubble formation. Since the hydrophobic surfaces used in theoretical work lack those imperfections, in the future it will be interesting to learn how the presence of common defects in the hydrophobic surfaces affect the results of the simulations.

References

1. K. Murata, K. Mitsuoka, T. Hirai, T. Walz, P. Agre, J. B. Heymann, A. Engel and Y. Fujiyoshi, Nature **407** (6804), 599-605 (2000).
2. H. X. Sui, B. G. Han, J. K. Lee, P. Walian and B. K. Jap, Nature **414** (6866), 872-878 (2001).
3. D. X. Fu, A. Libson, L. J. W. Miercke, C. Weitzman, P. Nollert, J. Krucinski and R. M. Stroud, Science **290** (5491), 481-486 (2000).
4. C. Dellago, M. M. Naor and G. Hummer, Physical Review Letters **90** (10), - (2003).
5. C. Dellago and G. Hummer, Physical Review Letters **97** (24), - (2006).
6. S. A. Hassan, G. Hummer and Y. S. Lee, J. Chem. Phys. **124** (20), - (2006).
7. D. Russo, P. Baglioni, E. Peroni and J. Teixeira, Chem. Phys. **292** (2-3), 235-245 (2003).
8. A. R. Bizzarri and S. Cannistraro, J. Phys. Chem. B **106** (26), 6617-6633 (2002).
9. J. L. Parker, P. M. Claesson and P. Attard, J. Phys. Chem. **98** (34), 8468-8480 (1994).
10. E. J. Verwey and J. T. G. Overbeek, *Theory of the Stability of Lyophobic Colloids* (Elsevier, New York, 1947).
11. B. Derjaguin and L. Landau, Prog Surf Sci **43** (1-4), 30-59 (1993).
12. D. Chandler, Nature **437** (7059), 640-647 (2005).
13. W. Kauzmann, Adv. Protein Chemistry **14**, 1-63 (1959).
14. A. Ben-Naim, J. Wilf and M. Yaacobi, J. Phys. Chem. **77** (1), 95-102 (1973).
15. J. Israelachvili and R. Pashley, Nature **300** (5890), 341-342 (1982).
16. G. Némethy and H. A. Scheraga, The Journal of Physical Chemistry **66** (10), 1773-1789 (1962).
17. J. N. Israelachvili and G. E. Adams, Nature **262** (5571), 773-776 (1976).
18. J. N. Israelachvili and G. E. Adams, J Chem Soc Farad T 1 **74**, 975-& (1978).
19. A. Ben-Naim, (Plenum Press, New York and London, 1982).
20. A. Ben-Naim, *Water and Aqueous Solutions: Introduction to a Molecular Theory*. (Plenum Press, New York, 1974).
21. H. K. Christenson, P. M. Claesson and R. M. Pashley, P Indian as-Chem Sci **98** (5-6), 379-389 (1987).
22. Y. I. Rabinovich and B. V. Derjaguin, Colloid Surface **30** (3-4), 243-251 (1988).
23. R. M. Pashley, P. M. Mcguiggan, B. W. Ninham and D. F. Evans, Science **229** (4718), 1088-1089 (1985).
24. K. Lum, D. Chandler and J. D. Weeks, Journal of Physical Chemistry B **103** (22), 4570-4577 (1999).
25. N. Giovambattista, P. J. Rossky and P. G. Debenedetti, Phys. Rev. E **73** (4) (2006).
26. N. Giovambattista, P. J. Rossky and P. G. Debenedetti, Phys. Rev. Lett. **102** (5) (2009).
27. N. Giovambattista, P. J. Rossky and P. G. Debenedetti, J. Phys. Chem. B **113** (42), 13723-13734 (2009).
28. X. Huang, C. J. Margulis and B. J. Berne, PNAS **100** (21), 11953-11958 (2003).
29. P. M. Claesson and H. K. Christenson, J. Phys. Chem. **92** (6), 1650-1655 (1988).

30. H. K. Christenson and P. M. Claesson, Science **239** (4838), 390-392 (1988).
31. P. Attard and D. J. Mitchell, Chem Phys Lett **133** (4), 347-352 (1987).
32. P. Attard, R. Kjellander and D. J. Mitchell, Chem Phys Lett **139** (2), 219-224 (1987).
33. J. Zhang, R.-H. Yoon, M. Mao and W. A. Ducker, Langmuir **21** (13), 5831-5841 (2005).
34. S. Marcelja and N. Radic, Chem Phys Lett **42** (1), 129-130 (1976).
35. G. Cevc, R. Podgornik and B. Zeks, Chem Phys Lett **91** (3), 193-196 (1982).
36. N. Ostrowsky and D. Sornette, Chem Scripta **25** (1), 108-111 (1985).
37. J. C. Eriksson, S. Ljunggren and P. M. Claesson, J Chem Soc Farad T 2 **85**, 163-176 (1989).
38. W. A. Ducker, Langmuir **25** (16), 8907-8910 (2009).
39. X. H. Zhang, X. D. Zhang, S. T. Lou, Z. X. Zhang, J. L. Sun and J. Hu, Langmuir **20** (9), 3813-3815 (2004).
40. X. H. Zhang, A. Quinn and W. A. Ducker, Langmuir **24** (9), 4756-4764 (2008).
41. Z. X. Li, X. H. Zhang, L. J. Zhang, X. C. Zeng, J. Hu and H. Fang, Journal of Physical Chemistry B **111** (31), 9325-9329 (2007).
42. P. Kekicheff and O. Spalla, Phys. Rev. Lett. **75** (Copyright (C) 2010 American Chemical Society (ACS). All Rights Reserved.), 1851-1854 (1995).
43. J. Wood and R. Sharma, Langmuir **11** (Copyright (C) 2010 American Chemical Society (ACS). All Rights Reserved.), 4797-4802 (1995).
44. M. L. Fielden, R. A. Hayes and J. Ralston, Langmuir **12** (Copyright (C) 2010 American Chemical Society (ACS). All Rights Reserved.), 3721-3727 (1996).
45. M. Hato, J. Phys. Chem. **100** (Copyright (C) 2010 American Chemical Society (ACS). All Rights Reserved.), 18530-18538 (1996).
46. M. E. Karaman, B. W. Ninham and R. M. Pashley, J. Phys. Chem. **100** (Copyright (C) 2010 American Chemical Society (ACS). All Rights Reserved.), 15503-15507 (1996).
47. J. Tamayo and R. Garcia, Langmuir **12** (Copyright (C) 2010 American Chemical Society (ACS). All Rights Reserved.), 4430-4435 (1996).
48. V. V. Yaminsky, B. W. Ninham, H. K. Christenson and R. M. Pashley, Langmuir **12** (Copyright (C) 2010 American Chemical Society (ACS). All Rights Reserved.), 1936-1943 (1996).
49. V. Yaminsky, C. Jones, F. Yaminsky and B. W. Ninham, Langmuir **12** (Copyright (C) 2010 American Chemical Society (ACS). All Rights Reserved.), 3531-3535 (1996).
50. G. Bar, Y. Thomann, R. Brandsch, H. J. Cantow and M. H. Whangbo, Langmuir **13** (Copyright (C) 2010 American Chemical Society (ACS). All Rights Reserved.), 3807-3812 (1997).
51. A. Kuhle, A. H. Sorensen and J. Bohr, J. Appl. Phys. **81** (Copyright (C) 2010 American Chemical Society (ACS). All Rights Reserved.), 6562-6569 (1997).
52. A. Carambassis, L. C. Jonker, P. Attard and M. W. Rutland, Phys. Rev. Lett. **80** (Copyright (C) 2010 American Chemical Society (ACS). All Rights Reserved.), 5357-5360 (1998).

53. V. S. J. Craig, B. W. Ninham and R. M. Pashley, Langmuir **14** (Copyright (C) 2010 American Chemical Society (ACS). All Rights Reserved.), 3326-3332 (1998).
54. M. Preuss and H.-J. Butt, Langmuir **14** (Copyright (C) 2010 American Chemical Society (ACS). All Rights Reserved.), 3164-3174 (1998).
55. R. F. Considine, R. A. Hayes and R. G. Horn, Langmuir **15** (Copyright (C) 2010 American Chemical Society (ACS). All Rights Reserved.), 1657-1659 (1999).
56. V. S. J. Craig, B. W. Ninham and R. M. Pashley, Langmuir **15** (Copyright (C) 2010 American Chemical Society (ACS). All Rights Reserved.), 1562-1569 (1999).
57. G. Haugstad and R. R. Jones, Ultramicroscopy **76** (Copyright (C) 2010 American Chemical Society (ACS). All Rights Reserved.), 77-86 (1999).
58. N. Ishida, M. Sakamoto, M. Miyahara and K. Higashitani, Langmuir **16** (Copyright (C) 2010 American Chemical Society (ACS). All Rights Reserved.), 5681-5687 (2000).
59. N. Ishida, N. Kinoshita, M. Miyahara and K. Higashitani, J. Colloid Interface Sci. **216** (Copyright (C) 2010 American Chemical Society (ACS). All Rights Reserved.), 387-393 (1999).
60. N. Ishida, T. Inoue, M. Miyahara and K. Higashitani, Langmuir **16** (Copyright (C) 2010 American Chemical Society (ACS). All Rights Reserved.), 6377-6380 (2000).
61. H. K. Christenson and P. M. Claesson, Adv Colloid Interfac **91** (3), 391-436 (2001).
62. M. Sakamoto, Y. Kanda, M. Miyahara and K. Higashitani, Langmuir **18** (15), 5713-5719 (2002).
63. C. E. McNamee, H. J. Butt, K. Higashitani, I. U. Vakarelski and M. Kappl, Langmuir **25** (19), 11509-11515 (2009).
64. T. Werder, J. H. Walther, R. L. Jaffe, T. Halicioglu and P. Koumoutsakos, Journal of Physical Chemistry B **107** (6), 1345-1352 (2003).
65. R. H. Coridan, N. W. Schmidt, G. H. Lai, R. Godawat, M. Krisch, S. Garde, P. Abbamonte and G. C. L. Wong, Physical Review Letters **103** (23), - (2009).
66. S. Sarupria and S. Garde, Physical Review Letters **103** (3), - (2009).
67. R. Godawat, S. N. Jamadagni and S. Garde, Proceedings of the National Academy of Sciences of the United States of America **106** (36), 15119-15124 (2009).
68. G. Hummer and S. Garde, Physical Review Letters **80** (19), 4193-4196 (1998).
69. S. Garde, G. Hummer, A. E. Garcia, M. E. Paulaitis and L. R. Pratt, Physical Review Letters **77** (24), 4966-4968 (1996).
70. C.-Y. Lee, J. A. McCammon and P. J. Rossky, The Journal of Chemical Physics **80** (9), 4448-4455 (1984).
71. J. R. Errington and P. G. Debenedetti, Nature **409** (6818), 318-321 (2001).
72. C. D. Wick and L. X. Dang, Journal of Physical Chemistry B **109** (32), 15574-15579 (2005).
73. J. L. Finney, Philosophical Transactions of the Royal Society B-Biological Sciences **359** (1448), 1145-1163 (2004).
74. F. H. Stillinger and A. Rahman, J. Chem. Phys. **60** (4), 1545-1557 (1974).

75. W. L. Jorgensen, J. Chandrasekhar, J. D. Madura, R. W. Impey and M. L. Klein, J. Chem. Phys. **79** (2), 926-935 (1983).
76. W. L. Jorgensen and J. D. Madura, Mol. Phys. **56** (6), 1381-1392 (1985).
77. H. J. C. Berendsen, J. R. Grigera and T. P. Straatsma, J. Phys. Chem. **91** (24), 6269-6271 (1987).
78. H. J. C. Berendsen, J. P. M. Postma, W. F. van Gunsteren and J. Hermans, in *Intermolecular Forces*, edited by B. Pullmann (Dordrecht, 1981), pp. 331.
79. N. Giovambattista, C. F. Lopez, P. J. Rossky and P. G. Debenedetti, PNAS **105** (7), 2274-2279 (2008).
80. M. W. Mahoney and W. L. Jorgensen, J. Chem. Phys. **112** (20), 8910-8922 (2000).
81. R. G. Fernandez, J. L. F. Abascal and C. Vega, The Journal of Chemical Physics **124** (14), 144506-144511 (2006).
82. N. Giovambattista, P. G. Debenedetti and P. J. Rossky, J. Phys. Chem. B **111** (32), 9581-9587 (2007).
83. S. Romero-Vargas Castrillón, N. s. Giovambattista, I. A. Aksay and P. G. Debenedetti, The Journal of Physical Chemistry B **113** (23), 7973-7976 (2009).
84. L. Zhang, W. A. Goddard Iii and S. Jiang, The Journal of Chemical Physics **117** (15), 7342-7349 (2002).
85. W. L. Jorgensen, J. D. Madura and C. J. Swenson, J. Am. Chem. Soc. **106** (22), 6638-6646 (1984).
86. J. Hautman and M. L. Klein, The Journal of Chemical Physics **91** (8), 4994-5001 (1989).
87. B. Hess, C. Kutzner, D. van der Spoel and E. Lindahl, J. Chem. Theory Comput. **4** (3), 435-447 (2008).
88. T. Darden, D. York and L. Pedersen, The Journal of Chemical Physics **98** (12), 10089-10092 (1993).
89. B. Hess, H. Bekker, H. J. C. Berendsen and J. Fraaije, J. Comp. Chem. **18** (12), 1463-1472 (1997).
90. H. J. C. Berendsen, J. P. M. Postma, W. F. van Gunsteren, A. DiNola and J. R. Haak, The Journal of Chemical Physics **81** (8), 3684-3690 (1984).
91. G. Bussi, D. Donadio and M. Parrinello, The Journal of Chemical Physics **126** (1), 014101-014107 (2007).
92. V. H. Dalvi and P. J. Rossky, Proceedings of the National Academy of Sciences of the United States of America **107** (31), 13603-13607 (2010).
93. M. Graupe, M. Takenaga, T. Koini, R. Colorado and T. R. Lee, Journal of the American Chemical Society **121** (13), 3222-3223 (1999).
94. B. S. Day and J. R. Morris, Journal of Chemical Physics **122** (23), - (2005).
95. S. H. Lee and P. J. Rossky, The Journal of Chemical Physics **100** (4), 3334-3345 (1994).
96. N. Shenogina, R. Godawat, P. Keblinski and S. Garde, Physical Review Letters **102** (15), - (2009).
97. S. N. Jamadagni, R. Godawat and S. Garde, Langmuir **25** (22), 13092-13099 (2009).
98. S. N. Jamadagni, R. Godawat, J. S. Dordick and S. Garde, Journal of Physical Chemistry B **113** (13), 4093-4101 (2009).

Chapter 8
Concluding Remarks

8.1 General comments

The goal of the research presented in this dissertation is to study reactions in both the gas phase and at gas/organic-surface interfaces and the structure and dynamics of water confined near hydrophobic surfaces. To this end we have performed theoretical reactive dynamics studies on a variety of chemical systems in the atomic-radical+alkane reaction class. In Chapters 3 and 4, we have presented direct-dynamics quasi-classical trajectory studies of the first few reactions in the H+alkane family using a Hamiltonian developed in our group. While the F+alkane reaction class exhibits a dramatically different potential energy surface from the H+alkane reactions, we have used a similar methodology to study these reactions in Chapter 5.

Moving beyond the gas phase, we have extended our investigations of F+alkane reactions to explore the dynamics of hydrogen abstraction from alkanethiolate self-assembled monolayers (SAMs) by fluorine atoms. Using a hybrid quantum-mechanics/molecular-mechanics (QM/MM) scheme, we have utilized the Hamiltonian that we developed for gas-phase reactions to study reactions at the gas/organic-surface interface in Chapter 6.

Finally, in Chapter 7, we have presented the behavior of water films under hydrophobic confinement. Employing classical molecular-mechanics simulation techniques, we sought to gain insight into the mechanisms responsible for the magnitude and length scale of attraction between hydrophobic surfaces seen in some experiments.

8.2 Gas-phase reaction dynamics

Classical trajectory simulations require an accurate description of the potential energy surface if quantitative dynamics results are to be achieved. In our work on gas-phase reaction dynamics, we demonstrated that specific-reaction-parameters (SRP) Hamiltonians can be used to provide such accuracy. Specifically, the work presented in this dissertation has extended the SRP-Hamiltonian technique from describing only a single reaction to the first few reactions in a homologous reaction family.

SRP-Hamiltonians have shown that they can provide at least semi-quantitative agreement with experimental dynamics results when they are used to propagate direct classical trajectories. While maintaining this demonstrated level of accuracy, the simplifications that have been made in the semiempirical methods afford the opportunity to study reactions that have previously been inaccessible to accurate theoretical simulation.

8.2.1 H+Alkanes

For the H+alkane class of reactions, we have shown that by using high-level *ab initio* data from only the H+CH_4 and H+C_2H_6 systems we can build a SRP-Hamiltonian that is suitable to describe the dynamics of those reactions as well as the H+propane reaction. Our SRP-MSINDO Hamiltonian has shown dynamics results for the H+CH_4 and H+C_2H_6 reactions that reproduce the methyl product lab frame speed distributions, excitation functions, and H_2/HD vibrational and rotational state distributions over a wide range of collision energies. Our results compare favorably with a state-of-the-art analytical potential energy surface that has been developed for the H+CH_4 reaction, but we are able to study other reactions without the need to derive a new Hamiltonian.

Our comparative dynamics study of the H+alkane family of reactions reveals a number of distinct mechanistic trends that emerge when we compare the nature of the alkane reactant and the relative collision energy of the reactants. Larger alkanes tend to absorb more of the available energy after reaction due to the increased presence of low-frequency vibrational modes. This partitioning of energy into the alkyl radical comes at the expense of product relative translational energy, which is still the dominant energy channel for all of the reaction conditions studied. There is also a consistent trend of increased stripping dynamics as the collision energy increases for all three alkane reactants studied. Stripping dynamics is the result of enhanced reactivity at large impact parameters that lead to enhanced forward scattering of the H_2 product. Although we have not calculated the dynamics of larger alkane molecules reacting with hydrogen radicals, our SRP-MSINDO Hamiltonian should be able to at least semi-quantitatively describe the dynamics of these reactions.

8.2.2 F+Alkanes

The hydrogen abstraction reactions from methane, ethane, propane and isobutane by fluorine atoms have been studied using a different SRP-MSINDO Hamiltonian to propagate direct trajectories. Our simulations of the $F+CH_4 \rightarrow HF+CH_3$ reaction reproduce the general trends of HF vibrational and rotational distributions and product energy partitioning found in experiments. We have also shown that there is a positive correlation between DF vibrational excitation and forward scattering of this diatomic product in the F+CD_4 reaction. Our classical trajectories proved that this result can be explained as a feature of the potential energy surface and is not necessarily evidence of a reactive resonance in the dynamics as had been hypothesized.

The comparative study of the dynamics of hydrogen abstraction reactions from different gas-phase alkanes exhibits a number of mechanistic trends. Some of these trends are similar to those found in the H+alkane system, despite the dramatically different potential energy surfaces governing these reactions. As the size of the alkane reactant increases, there is an increased percentage of the available energy partitioned into the alkyl product. As in the case of H+alkane reactions, this partitioning is the result of increased low-frequency vibrational modes in the alkyl fragment. In this family of reactions the increased energy in the alkyl fragment comes predominantly at the expense of HF vibration, which is the major energy sink for the reactions studied. The major result from our study of F+alkane reactions is the use of SRP Hamiltonians to efficiently model relatively large chemical reactions that again could extend beyond those studied in our work.

8.3 Gas/organic-surface collisions

By employing a QM/MM scheme, we have studied the reactions of fluorine atoms with alkanethiolate SAMs. Our hybrid potential energy surface employs both the OPLS MM force field to provide structural support for the reactive region of the SAM surface and the QM SRP-MSINDO Hamiltonian to describe bond breaking and forming in the reactive region. As we have demonstrated, the improvement of the SRP-MSINDO when compared with the original MSINDO Hamiltonian, this represents a major step forward in the computational modeling of gas/organic-surface reactions.

Our simulations reproduce the major trends of the HF vibrational state distributions and provide quantitative agreement with the rotational state distributions measured in F+squalane experiments. We have also investigated the role that secondary collisions have on the final rotational state and translational energy. However, HF molecules leaving the SAM surface. Within a few post-reaction collisions, there is an effective cooling of the HF rotational and translational energy but HF vibrations are not significantly affected by secondary collisions during the residence times of the HF molecules on the surface.

8.4 Confined water simulations

Our final set of MD simulations investigated the nature of water confined between hydrophobic SAM surfaces. The motivation for these simulations was to determine the physical phenomena responsible for the hydrophobic effect. We calculated density profiles, interfacial O-H bond orientations, and diffusion coefficients for water molecules in confined thin films. Our simulations demonstrate that water density and structuring are only affected near the SAM surfaces and cannot begin to explain the length scale of attraction measured in experiments. In accordance with other simulations of water confined near extended hydrophobic surfaces, our simulations show O-H bonds that preferentially point toward the surface at the interface. While these hydrophobic surfaces perturb the water proximal to the SAMs, neither density layering, water structuring, nor O-H bond orientation extend deep into the water films. We have demonstrated that the diffusion coefficients parallel to the SAM surfaces show enhanced water motion compared to bulk water simulations. This enhanced diffusion of water parallel to the confining surface can extend >1nm into the water film and could potentially lead to the formation of bubbles that bridge between the SAM surfaces. Some experimentalists have hypothesized that bubbles such as these might be responsible for the attraction between two hydrophobic surfaces in aqueous environments, known as the hydrophobic effect.

8.5 Future directions

To build upon the work presented in this dissertation, there are a number of directions that these lines of investigations can take in the future. In the area of gas-phase reaction dynamics, a number of other types of reactions can be studied to investigate the breadth of reaction mechanisms that can be accurately described by using SRP Hamiltonians to propagate direct trajectories.

In the area of gas/organic-surface reactions, it will be interesting to investigate the reaction of hydroxyl radicals with alkanethiolate SAMs. Motivated by recent inelastic scattering measurements of OH radicals from SAM surfaces, these reactive simulations would represent an advance in the complexity of reactions that can be studied at the gas/organic-surface interface.

Finally, in the field of molecular simulations of water in hydrophobic confinement, adding dissolved gases into our system would be a logical next step. The existence of nanoscopic bubbles composed of dissolved gases has been verified on SAM surfaces when they are submerged in water, and determining their role in promoting or suppressing the diffusion of water parallel to the hydrophobic surfaces should provide insight into the mechanisms of the hydrophobic effect.